Characterizing North American Biomass Burning Layers in the Free Troposphere with a Single Particle Soot Photometer

Katharina Elisabeth Heimerl

München 2018

Characterizing North American Biomass Burning Layers in the Free Troposphere with a Single Particle Soot Photometer

Katharina Elisabeth Heimerl

Dissertation der Fakultät für Physik

der Ludwig-Maximilians-Universität München

vorgelegt von

Katharina Elisabeth Heimerl

aus Nürnberg

München, den 22.01.2018

Erstgutachter:	Prof. Dr. Bernadett Weinzierl
Zweitgutachter:	Prof. Dr. Bernhard Mayer
Datum der Abgabe:	22.01.2018
Datum der mündlichen Prüfung:	26.02.2018

Zusammenfassung

Waldbrände sind eine Hauptquelle von Ruß, der schwarzen Kohlenstoff enthält, den am stärksten absorbierendem Partikeltyp in der Atmosphäre. Durch Vertikaltransport können Waldbrandaerosolschichten die obere Troposphäre erreichen, was ihre Klimawirkung noch verstärken kann, da die Lebenszeit von Aerosolpartikeln in der Atmosphäre mit der Höhe zunimmt. Diese Arbeit befasst sich mit der Charakterisierung von schwarzem Ruß in Waldbrandaerosolschichten in der freien und oberen Troposphäre anhand von Messdaten, die 2012 bei der Deep Convective Clouds and Chemistry (DC3) Flugzeugmesskampagne mit einem SP2 gewonnen wurden. Die Rußpartikel, die in diesen in Waldbrandaerosolschichten gemessen wurden, unterscheiden sich zwischen Schichten in unterschiedlichen Höhen. Anhand einer Fallstudie vom 11. Juni 2012, bei der Rußmassenkonzentrationen von bis zu 2 µg /m³ gemessen wurden, werden Waldbrandaerosolschichten in der freien Troposphäre unterhalb von etwa 8 km Höhe exemplarisch dargestellt. Diese Schichten enthalten Rußpartikel mit einem Massenmediandurchmesser von 160-200 nm, etwa 60-80% dieser Rußpartikel weisen dicke Ummantelungen aus anderem Material auf. In den meisten dieser Schichten war die Konzentration von Partikeln größer 2 µm, wie Staub, erhöht, auf Werte bis zu 1 cm³. Die Waldbrandaerosolschichten, die in der oberen Troposphäre gemessen wurden, unterschieden sich in den Rußpartikeleigenschaften von den schichten unterhalb von 8 km Höhe. Am 17. Juni wurde eine Waldbrandaerosolschicht in der oberen Troposphäre, auf 11 km Höhe, vermessen, die durch ein Gewitter nach oben transportiert wurde. Das Verhältnis von CO und Rußmassenkonzentration in der Schicht weist auf eine geringere Auswaschung hin, als sie im Ausfluss von Gewitterambossen beobachtet wurde. Auch erhöhte Ozonkonzentrationen deuten darauf hin, dass die Waldbrandaerosolschicht nicht im Hauptaufwindbereich sondern in schwächeren Aufwinden unterhalb des Ambosses transportiert wurde und sich mit stratosphärischer Luft vermischte. Waldbrandaerosolschichten in der oberen Troposphäre enthielten Rußpartikel, deren Massenmediandurchmessern mit 145 nm etwas kleiner waren als in Waldbrandaerosolschichten der mittleren Troposphäre. Etwa 50% der Rußpartikel waren intern gemischt. Diese Massengrößenverteilung von Rußpartikeln war nicht nur in allen bei DC3 beobachteten Waldbrandaerosolschichten nahezu identisch, sondern gleicht auch anderen Beobachtungsdaten von Rußpartikeln in Waldbrandaerosolschichten in der oberen Troposphäre, was auf eine stabile Gleichgewichtsverteilung hindeutet. Das Verhältnis von Rußmassenkonzentration und CO, 4.05 (ng/m³)/ppb in der freien Troposphäre und 1.43 (ng/m³)/ppb in der oberen Troposphäre, zeigt, dass bis zu zwei Drittel der Rußmasse beim Transport ausgewaschen wurden. Durch die große horizontale Ausdehnung der Schichten konnte eine dieser nur wenige hundert Meter dicken Schicht immer noch Ruß in Größenordnung von 2 Mg enthalten, was etwa einem Achtel der täglichen Flugzeugemissionen in der oberen Troposphäre entspricht.

Abstract

Biomass burning is the largest natural source of black carbon, the most absorbing particle type in the atmosphere. Layers containing biomass burning aerosol that are lifted into the upper troposphere have an increased atmospheric lifetime which can enhance their effect on climate. Biomass burning layers were measured during the Deep Convective Clouds and Chemistry (DC3) campaign with an airborne SP2 in the free and upper troposphere. Two case studies show the properties of black carbon particles in biomass burning layers at different altitudes. On June 11, 2012, biomass burning layers in Oklahoma and Missouri at 3-8 km altitude contained high concentrations, up to 2 μg/m³, of large, thickly coated black carbon particles. Biomass burning layers measured on June 17, 2012, over Kansas and Arkansas were located in the upper troposphere, at about 11 km altitude. The mass size distribution of black carbon particles and the rBC/CO ratio indicate that the biomass burning layers underwent cloud processing by a large thunderstorm on the previous day. Washout was less strong than for anvil outflow, leading to the conclusion that the layer was not transported in the main updrafts but in weaker updrafts that mixed with stratospheric air in the anvil region. Black carbon in layers up to 9 km altitude contain large particles with a mass median diameter of about 160-200 nm with 60-80% of the particles being thickly coated. Concentrations of large particles, possibly dust, were elevated above background in biomass burning layers up to 1 cm^{-3}. Biomass burning layers in the upper troposphere (UT-BB) are vertically often only thin, several hundred meters thick, but can horizontally stretch over about thousand kilometers. The estimated total amount of black carbon in one biomass burning layer is about 2 Mg, which corresponds to roughly one eighth of daily global aviation emissions. Black carbon particles in upper tropospheric biomass burning layers showed a nearly constant, probably steady-state, mass size distribution with mass median diameters of 145 nm, (160-200 nm in the middle troposphere). The O_3 concentrations in the UT-BB layers were elevated, with values above 200 ppb. The lower rBC/CO ratio of the UT-BB layers, 1.43 (ng/m³)/ppb in contrast to 4.05 (ng/m³)/ppb in the middle troposphere, indicates that up to two thirds of black carbon particles were removed during transport.

_____

Index

1   Introduction: Black Carbon from Wildfires in the Atmosphere

Wildfires have always been an important factor for humans, wildlife and the atmosphere (Bowman et al., 2009). Wildfires can influence the life cycle of plants by facilitating the survival of certain species (e.g. Clewell, 2014) or reducing the fertility of seeds (e.g. Zimmerman and Laven, 1987). Large, destructive wildfires can threaten the lives of humans and animals and can cause high economic damages (e.g. Cohen, 2000). Especially black carbon emitted from wildfires, and also from traffic, is known to influence human health as it is linked to an increase in respiratory and cardiovascular diseases (Naeher et al., 2007; Janssen et al., 2011). The influence of wildfires on human lives and economy stresses the importance of forest fire management policies (e.g. Stephens and Ruth, 2005). By wildfire management, humans can influence the size, patterns, frequency, and severity of fires (Bowman et al., 2011).

As the main natural source of CO_2 and black carbon particles, wildfires influence the carbon cycle by releasing large amounts of carbon from vegetation into the atmosphere (Bowman et al., 2009). Figure 1 shows a global map of the total carbon emissions from biomass burning (van der Werf et al., 2017). Wildfires release huge smoke plumes containing a large variety of trace gases and particles (e.g. Andreae and Merlet, 2001). Due to their potential to act as nuclei for water condensation, particles can affect the formation of clouds (e.g. Bougiatioti et al., 2016). The emission of large amounts of trace gases and particles influences the Earth's radiative budget (Bond and Bergstrom, 2006). Black carbon has a special role since it is responsible for most of the aerosol-related light absorption in the atmosphere due to its strong absorption efficiency (e.g. Moosmüller et al., 2009). The warming effect of the light absorption by black carbon is the second most important warming factor in climate after CO_2 and has a similar order of magnitude as the cooling effect of the particle light scattering (IPCC, 2013).
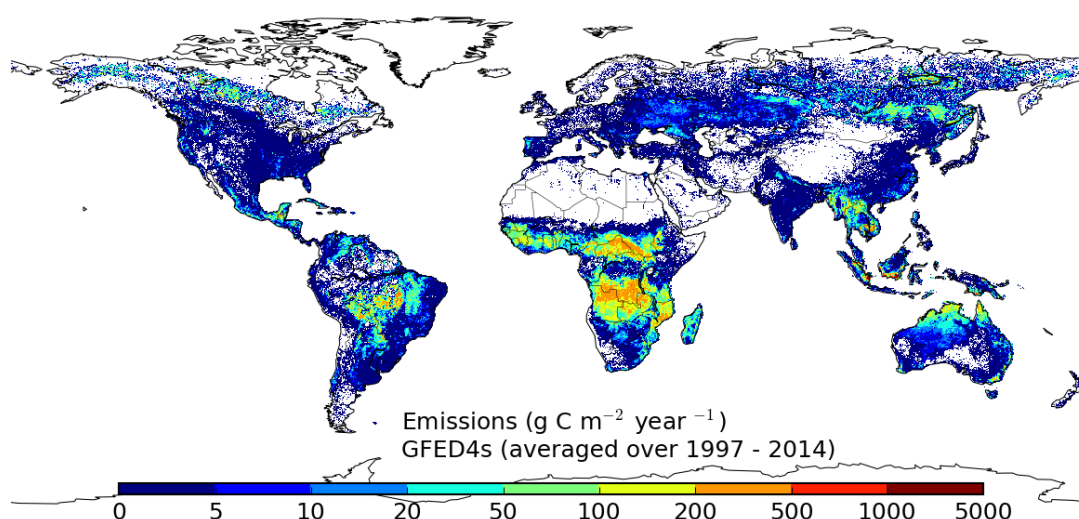

Figure 1: Fire emissions of total carbon. From http://www.globalfiredata.org (van der Werf et al., 2017).

_____

Particles influence the atmosphere not only at the place where they are emitted but they can be transported also into regions far away from their source (e.g. AMAP, 2015). During transport, particle properties like hygroscopicity and light absorption can change due to aging effects (e.g. Oshima et al., 2009a). Vertical transport has an influence on the climate effect as the particle residence time increases with increasing altitude (Jaenicke, 1980). The lifetime of black carbon in the atmosphere varies from hours to several weeks because the removal rates depend strongly on precipitation (Ogren and Charlson, 1983). Vertical transport brings particles from the sources in the boundary layer to higher altitudes, influencing the vertical distribution of particles in the atmosphere. The influence of transport processes on particle composition, concentration and lifetime makes it important to study vertical transport processes to understand the life cycle of aerosol.

Black carbon occurs in strongly variable concentrations, varying by three orders of magnitude from less than 1 ng over the remote Pacific (e.g. Schwarz et al., 2010b) to several micrograms per m³ in polluted regions (e.g. Subramanian et al., 2010; Kondo et al., 2011a). However, comparisons between measurements and a range of global aerosol models have shown that models tend to overestimate black carbon in the upper troposphere by up to a factor of 10 (Koch et al., 2009; Schwarz et al., 2013), indicating that relevant processes of vertical transport and deposition are not well represented in the models. In order to identify and improve the understanding of possible transport pathways into the upper troposphere, this work aims to quantify black carbon in biomass burning layers at different altitudes. The focus here is on emissions from wildfires in the central United States in early summer. This work will investigate black carbon in biomass burning layers in the central United States, focusing on the characterization of particle size and mixing state. With the potential increase of the number of intense wildfires in a changing climate (e.g. Barbero et al., 2015), the emission of black carbon from wildfires could also increase in the future. The fire season in the western United States lasts from April to October (Westerling et al., 2003). The early part of the fire season coincides with a peak in the occurrence of thunderstorms with overshooting tops that penetrate the tropopause and influence stratosphere-troposphere exchange in May (Solomon et al., 2016). As thunderstorms and wildfires can occur at the same time in the same region, they can influence each other. This work aims to investigate the influence of thunderstorms on the transport of black carbon from biomass burning emissions.

1.1　Sources and Sinks of Black Carbon Particles

The main sources for black carbon particles in the atmosphere are combustion processes, mainly from industry, traffic and, as already mentioned, open biomass burning at the surface. Nearly all these sources are located at the Earth's surface, only aircraft emit black carbon directly into the free troposphere. Figure 2 summarizes all these black carbon sources and illustrates the interactions between black carbon particles and the atmosphere as well as the main sinks for black carbon particles (Bond et al., 2013). Open biomass burning is one of the largest contributors to the total black carbon emissions. Burning forests, woodlands and grass emitted an estimated amount of 2760 Gg black carbon in the year 2000

(Schultz et al., 2008), which is more than one third of the total emitted black carbon from all sources in that year (Bond et al., 2013). Wildfire emissions are derived from satellite images of the burned area (Wooster et al., 2005), estimates of the fuel load (van der Werf et al., 2010) and emission factors for burning vegetation (Andreae and Merlet, 2001). In the United States, about 578 Gg black carbon were emitted into the atmosphere in 2005, of which 35% originate from open biomass burning and wildfires (EPA, 2012). This is similar to the total black carbon mass emitted by traffic in the United States. Traffic emissions, however, come from a large amount of small, widely spread point sources, while wildfires are more confined in time and space.
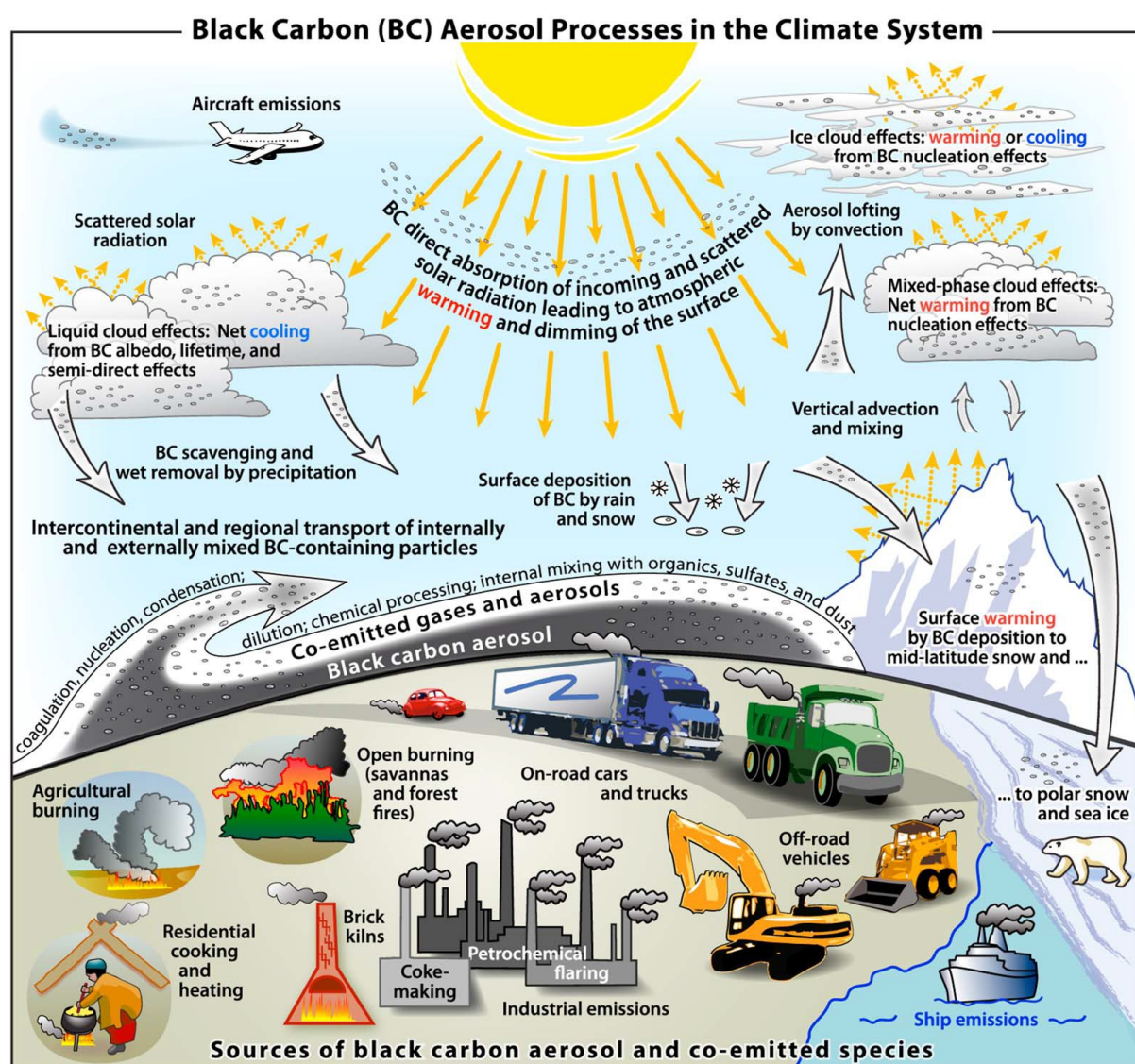
Figure 2: Sources and sinks of black carbon particles in the Earth's atmosphere (from Bond et al., 2013).

Wildfires emit also a wide range of other species (e.g. Andreae and Merlet, 2001; Akagi et al., 2011), so black carbon particles in wildfire emissions are found in mixtures with other substances. These co-emitted substances are other products of combustion like CO_2, CO and other trace gases or organic materials, with the latter often found mixed into black carbon particles (e.g. Lee et al., 2016a). Unlike

industrial and traffic emissions, wildfire emissions show also large variations depending on the year. These variations can be strong enough to affect global concentrations in CO_2 (Simmonds et al., 2005). The strong local and seasonal variations of wildfire activity can lead to CO emissions from wildfires exceeding anthropogenic CO even in areas with strong anthropogenic sources (Wotawa and Trainer, 2000). Ratios between the concentration of black carbon and trace gases can give indications of the source of pollution or ageing processes. Depending on the burned fuel, concentrations of trace gases like SO_2 vary as fossil fuel contains more sulfate than forests (e.g. Kaufman et al., 1991).

The main sink for black carbon particles are dry and wet deposition processes. Dry deposition of black carbon can lead to a dark cover of surfaces like the greyish to black cover of pollution on snow (e.g. Hansen and Nazarenko, 2004). Wet removal mechanisms for black carbon are interactions with clouds and precipitation. Black carbon particles can act as cloud nuclei and be removed from the atmosphere by washout (e.g. Ogren and Charlson, 1983). Cloud processing and washout strongly influence aerosol concentration while they have only little effect on insoluble trace gases like CO. Studying black carbon particles in context with other trace species can therefore give valuable information on source and history of the black carbon population in an air mass.

1.2   Influence of Black Carbon on Climate

Climate effects of black carbon particles in the atmosphere are both direct, because of interaction with solar radiation, and indirect, from interaction with clouds and albedo. While the majority of particle mass in the atmosphere causes a cooling effect due to the scattering of light, black carbon particles can counteract this effect since it absorbs solar radiation efficiently (IPCC, 2013). High concentrations of black carbon particles in the atmosphere, which appear like thin, brown layers to the observer, can decrease the reflection of sunlight back to space if they are located above a brighter surface, and, due to the strong absorption of solar radiation, can warm the surrounding air (Ramanathan and Carmichael, 2008). This direct effect of aerosol on the atmosphere's energy budget is part of the effect of aerosol-radiation interactions (left part of Figure 3). The semi-direct effect of black carbon particles on clouds is strongly influenced by the altitude of the particles relative to the clouds and the cloud type (Koch and Del Genio, 2010). Light-absorbing particles located in the proximity of clouds cause warming of the surrounding air, increasing the capability of air to take up moisture (Hansen et al., 1997; Hill and Dobbie, 2008).This can lead to inhibition of cloud formation or "cloud burn-off" as the cloud droplets tend to form later and evaporate sooner in a warmer environment. If located above clouds, black carbon layers can change the cloud regime, e.g. from stratocumulus decks to more patchy cumulus clouds (Yamaguchi et al., 2015). Black carbon caused warming can also increase the stability of the atmosphere, and suppress turbulence in the boundary layer (Wilcox et al., 2016).
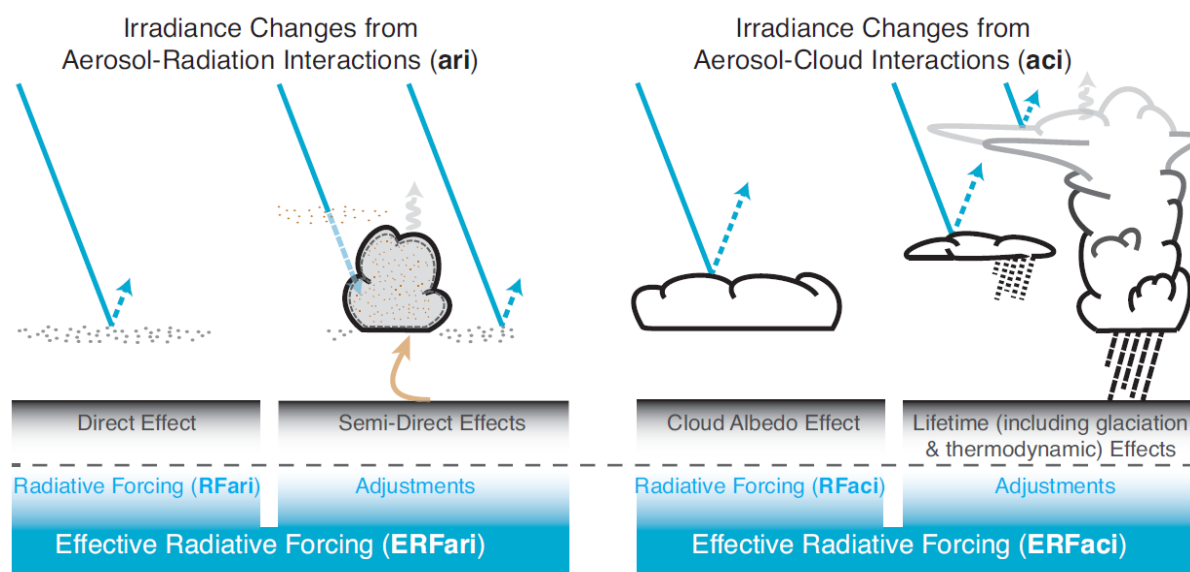
Figure 3: Influence of aerosol on radiative forcing. From Boucher et al. (2013) in IPCC (2013).

Also, their ability to act as cloud or ice condensation nuclei makes aerosol particles an important factor in cloud formation processes. Changes in concentration or size distribution will therefore also affect clouds (e.g. Spracklen et al., 2011). The number concentration of particles acting as cloud condensation nuclei influences the cloud albedo (Twomey, 1977), as a higher concentration of cloud droplets makes the cloud appear brighter. It reflects more solar light back into space leading to a cooling of the atmosphere underneath the cloud top (cloud albedo effect in Figure 3). A change in particle concentration can also influence the lifetime and precipitation of clouds (e.g. Small et al., 2009). In a heavily polluted region over China, Guo et al. (2016) found a delay in the diurnal cycle of convection caused by high particle concentrations, partly because the increased stability suppresses convection until noon (Lee et al., 2016b). For deep convective clouds, Fan et al. (2013) showed that a polluted environment can cause a larger anvil size, increasing cloud cover and cloud top height. In the Amazon region, Goncalves et al. (2015) found that the atmospheric stability influenced how increased black carbon concentrations affect the change in precipitation, enhancing it in unstable cases.

Interactions with clouds can also lead to a washout of the particles, which is the main removal mechanism for particles in the atmosphere (e.g. Bond et al., 2013; Seinfeld and Pandis, 2016). Black carbon particles can influence the climate even after being removed from the atmosphere. When they are deposited on a very light ground, especially on snow or ice, they lead to a darkening of the surface which may enhance snow and ice melt (e.g. Hansen and Nazarenko, 2004; Kaspari et al., 2015).

The influence of black carbon on climate can also feedback on the natural sources of black carbon. Wildfires, the major natural contributor to black carbon emissions, can also change in amount and intensity due to climate change (e.g. Sommers et al., 2014). To evaluate the effect of black carbon on

the atmosphere, it is therefore necessary to know the distribution of black carbon concentrations, which are not only affected by sources and sinks, but also by various transport processes.

1.3   Transport and Vertical Distribution of Black Carbon from Biomass Burning in the Atmosphere

Global models tend to overestimate the rBC mass concentrations, especially in the upper troposphere and lower stratosphere, like comparisons between measurements and the AeroCom atmospheric model ensemble shows (Schwarz et al., 2013; 2017). Black carbon emitted from wildfires can be transported over large distances and to high altitudes. Damoah et al. (2004) show that a Russian forest fire smoke plume can be transported across the northern hemisphere within 17 days. During transport, processes like ageing and both wet and dry removal change the black carbon aerosol distribution, leading to differences in climate forcing, and cloud activity between young and aged, transported populations making aerosol transport an important topic of research (e.g. AMAP, 2015).

Long-range transport of forest fire aerosol from North America to Europe was studied intensively for example in the ICARTT-ITOP campaign (Petzold et al., 2007) for layers at 3-7 km altitude. Most of these layers were transported over the Atlantic very efficiently with little dilution. First in-situ measurements in a biomass burning layer in the upper troposphere were made by Jost et al. (2004), who found a biomass burning layer at 15 km altitude over Florida, originating from Canadian forest fires. Dahlkötter et al. (2014) show measurements of a single biomass burning layer in the upper troposphere and lower stratosphere that was transported over the Atlantic from Canada to Europe. The total black carbon content of this upper tropospheric layer was in the same range as the total daily black carbon emissions of global aviation. Black carbon particles in this layer were thickly coated, which is typical for aged particles.

Black carbon mass concentrations in the atmosphere span more than three orders of magnitude, from about 1 ng/m^{-3} in remote regions to several micrograms per m^3 in heavily polluted regions and dense biomass burning plumes (e.g. Schwarz et al., 2017). In the northern hemisphere, black carbon is most abundant in the lowermost troposphere, decreases with altitude above the planetary boundary layer and reaches a stratospheric background level of around 1 ng/kg above the tropopause (Schwarz et al., 2006; 2010b). This decrease in concentration reflects that the main sources of black carbon are at the ground and reach the free and upper troposphere by vertical transport. As the residence time of black carbon in the atmosphere increases with increasing altitude, vertical transport of black carbon influences its residence time in the atmosphere (e.g. Petzold and Kärcher in Schumann, 2012), and also its effect on climate (Samset and Myhre, 2015).

Vertical transport of biomass burning emissions in the atmosphere can happen in different ways. The heat release of the burning fire induces pyroconvection, causing the plume to rise into the free troposphere (e.g. Fromm et al., 2010). Other vertical transport mechanisms are related to meteorology.

Prominent examples of meteorological systems that transport air masses vertically through the atmosphere are low pressure systems and thunderstorms. Both systems involve cloud formation, which can influence concentration, mixing state and size distribution of black carbon particles.

In low pressure systems, warm, moist air is transported upward at frontal zones, forming a warm conveyor belt (e.g. Harrold, 1973; Schemm et al., 2013). Warm conveyor belts cross the troposphere vertically in about two days and play an important role in the transport of water vapor to the upper troposphere (Eckhardt et al., 2004).

Thunderstorms transport air masses vertically even faster, air from the planetary boundary layer can reach the tropopause and in some cases even the stratosphere within less than one hour (e.g. Byers and Braham, 1948; Emanuel, 1994). In the tropics, thunderstorms are known to be involved in the stratosphere-troposphere exchange (e.g. Frey et al., 2015). Tropical thunderstorms are also known to transport biomass burning emissions into the upper troposphere (e.g. Andreae et al., 2001; Huntrieser et al., 2011; Reid et al., 2015). In the northern hemisphere midlatitudes, a hot spot of thunderstorms that reach the tropopause, and occasionally also the lower stratosphere, is located in North America (Liu and Liu, 2016; Solomon et al., 2016). This is also a region of wildfire activity, which makes it interesting to study the influence of thunderstorms on the transport of biomass burning. As 2012 was an intense fire year (Jolly et al., 2015), this year provided a great opportunity to study the interactions between wildfires and thunderstorms.

Black carbon in biomass burning plumes was the main research topic in several field campaigns. ARCTAS (Arctic Research of the Composition of the Troposphere from Aircraft and Satellite) and ARCPAC (Aerosol, Radiation, and Cloud Processes affecting Arctic Climate) were conducted in the Arctic and the western US (Spackman et al., 2010; Kondo et al., 2011a). Both campaigns quantified biomass burning layers and their influence on the Arctic climate. The BORTAS (Quantifying the impact of BOReal forest fires on Tropospheric oxidants over the Atlantic using Aircraft and Satellite) campaign 2011 in Canada analyzed ageing of boreal fire plumes with a multi-platform approach (Palmer et al., 2013). Biomass burning plumes containing large concentrations of rBC particles were also observed over Texas during TexAQS (Schwarz et al., 2008a; Spackman et al., 2008), where the differences in rBC properties between biomass burning and industrial and urban pollution were studied. Dahlkötter et al. (2014) discussed in detail rBC in a biomass burning layer in the upper troposphere after long-range transport from Canada to Europe measured during the 2011 CONCERT campaign. All these studies have focused either on biomass burning plumes advected in the lower and middle troposphere or on single layers that were lifted into the upper troposphere and lower stratosphere by e.g. pyroconvection. As so far only two case studies report on properties of rBC in biomass burning layers in the upper troposphere, Dahlkötter et al. (2014) and Taylor et al. (2014), the data set of upper tropospheric biomass burning layers presented in the present work can improve the understanding of upper tropospheric biomass burning layers.

1.4   Questions and Outline

The present work aims to study and compare refractory black carbon (rBC) in biomass burning plumes found both in the lower and in the upper troposphere. A unique dataset with extensive measurement in both lower and upper tropospheric biomass burning layers from the same source gives the possibility to investigate black carbon properties in layers at different altitudes. This can help to improve the understanding of the vertical transport of biomass burning layers and its effect on the size distribution and mixing state of black carbon particles. Encountering rBC-rich biomass burning layers at different altitudes throughout the troposphere, both close to and far away from the wildfire they originate from, brings up questions concerning the properties of these layers and their transport pathways:

- What are the properties of rBC particles in the tropospheric biomass burning layers and do these depend on altitude?

- Are the rBC particle properties measured in May and June 2012 representative for this type of biomass burning layers or do they differ from other observations?

- Which vertical transport processes can bring the biomass burning layers to the altitudes they were observed at and do these processes influence particle properties?

These questions will be answered in this work based on the data set acquired during the Deep Convective clouds and Chemistry (DC3) field campaign in 2012, focusing on rBC measurements.

The next four chapters of this thesis are organized as follows: Chapter 2 gives an overview of the physical background of the measurements of rBC mass and a short description of vertical transport processes. The measurement campaign, DC3, the core instrument, the Single Particle Soot Photometer (SP2), and data analysis methods are the topics of chapter 3. Chapter 4 shows and discusses the results of the measurements, focusing on the three questions above. The last chapter, chapter 5, summarizes the thesis and the main conclusions.

After a short overview of the physical background of the measurements in chapter 2, chapter 3 gives more details on the measurements themselves. The general situation and the meteorological background of the DC3 field campaign, during which the data were acquired, are shown. A large part of this chapter contains descriptions of alignment and calibration procedures for the SP2 that are crucial for data quality assurance and long-term stability of the rBC mass concentration measurements. Chapter 3 closes with a short description of the data evaluation methods used to process the data presented in the following chapters. Chapter 4 starts with the description of two case studies that represent two different types of biomass burning layers measured during DC3, June 11, 2012 (chapter 4.1), as an example for biomass burning layers in the free troposphere, and June 17, 2012, (chapter 4.2) as an example of a biomass burning layer in the upper troposphere. The third part, chapter 4.3, summarizes all the observations of biomass burning layers made during DC3 to characterize the properties of refractory black carbon particles, especially size and mixing state, in the biomass burning layers. Co-emitted species, with a

focus on dust and CO, are the topic of chapter 4.4. The last part of this chapter, chapter 4.5, is dedicated to the discussion of the third question, vertical transport processes and their influence on the properties of upper tropospheric biomass burning layers. It also contains a discussion of the contribution of biomass burning to black carbon in the upper troposphere, and of the mixing between upper tropospheric biomass burning layers and stratospheric air. The thesis closes with a summary of the main findings of this work in chapter 5.

2   Theoretical Background

Aerosols play an important role in many atmospheric processes. They influence the Earth's radiative budget by absorption and scattering of solar radiation. Individual particles can be classified according to their physical characteristics like size, shape, material, or optical properties. The variability of sizes and composition in particles makes it necessary to parameterize particle properties in order to condense information on particle size and properties. Measurements of particle size is often based on the interaction between particles and light. Material and size of particles are crucial parameters for the interaction with light and the particle's ability to act as cloud or ice nucleus. This chapter describes in the first part shortly the physical characteristics of aerosol particles. The second part of this chapter gives an overview of vertical transport processes in the atmosphere. Since most pollution sources, also wildfires, are located at the ground, vertical transport processes are responsible for the redistribution of particles and trace gases which can be found all over the atmosphere in different concentrations. The vertical distribution of these trace species influences their lifetime and so their effect on climate. Interactions between particles and physical processes during transport can also influence properties and concentration of aerosol.

2.1   Physical Properties of Aerosol Particles

The term *Aeroso*l describes a suspension of solid particles in a gaseous medium (Hinds, 1999). The size of these particles ranges from agglomerates of molecules of only few nanometers to large dust particles of tens of micrometers in diameter. The wide range of sizes can be separated into size modes with the *Nucleation mode* containing the very small particles below 10 nm, the *Aitken mode* describing particles between 10 nm and 100 nm, the A*ccumulation mode* covering the range 100-1000 nm, and *Coarse mode* aerosol having a diameter of more than 1 μm (Hinds, 2011; John, 2011).

The composition of aerosol particles varies, depending on their source and processes in the atmosphere. The most abundant type of aerosol by mass is sea salt (e.g. Dentener et al., 2006), emitted from the oceans that cover a large fraction of the earth, followed by dust from soil mobilization, especially in the large deserts of the northern hemisphere like the Sahara (Prospero et al., 2002; Mahowald et al., 2009). Mineral dust particles are composed of non-absorbing materials like quartz and absorbing materials like hematite (Sokolik and Toon, 1999). Though dust is the most abundant absorbing aerosol type, black carbon dominates the aerosol light absorption (IPCC, 2013). Another type of absorbing aerosol is brown carbon (Moosmüller et al., 2009). As their name suggests, brown carbon and black carbon both contain carbon, the sixth element in the periodic table. Black carbon strongly absorbs light of all wavelengths and therefore appears black to the human eye while the light absorption of brown carbon is wavelength-dependent, which makes the material appear in colors from brown over orange to yellow (Moosmüller et al., 2009).

A variety of definitions exists for the term black carbon, based on the material's optical properties, the measurement method or the melting point temperature (Bond et al., 2013; Petzold et al., 2013). The term "soot" describes all kinds of carbon-containing particles produced by combustion processes. It is very unspecific about the nature of these particles and will therefore not be used in this work. Petzold et al. (2013) discuss the various definitions of black carbon found in the literature. As different measurement methods produce different results, it is also necessary to make this clear when naming the measured quantity. Following these recommendations, black carbon measured by laser-induced incandescence in a Single Particle Soot Photometer (SP2) is here referred to as *refractory black carbon*, abbreviated as *rBC*. This includes only that part of black carbon that strongly absorbs light and has a boiling point temperature around 4000 K (Schwarz et al., 2006). Other instruments that measure black carbon properties, like the Particle Soot Absorption Photometer, use slightly different definitions of black carbon. Therefore, it is crucial to consider that different measurement techniques may give slightly different results, which should be reflected in the terms used (see recommendations in Petzold et al., 2013).

Black carbon particles are found mainly in the Aitken and Accumulation mode. They are emitted as small spherules of graphitic material with diameters of 30-60 nm (e.g. Heidenreich et al., 1968). Within a short time after emission, they coagulate to fractal structures containing hundreds of primary spherules (e.g. van Poppel et al., 2005). Black carbon particles freshly emitted from fossil fuel combustion are found mainly in the Aitken mode below 100 nm diameter while black carbon from wildfires often shows larger particle diameters (e.g. Schwarz et al., 2008a; Costabile et al., 2015). Volatile compounds can condense on the black carbon particles during ageing, which may lead to the collapse of the fractal aggregates into a more compact shape (e.g. electron microscope images in Slowik et al., 2007). The mixing state of black carbon particles allows to draw conclusions about the history of the particle population as they acquire coatings during ageing processes (e.g. Moteki et al., 2007). These coatings can change the surface properties of the particle and improve the abilities of black carbon particles to act as cloud or ice condensation nuclei (e.g. DeMott et al., 1999; McMeeking et al., 2011). The morphology of black carbon particles is therefore an indicator of atmospheric processes and an important quantity when measuring black carbon.

Figure 4 shows examples for different types of particle mixing states of black carbon with non-absorbing substances. External mixtures contain different types of homogeneous particles (Figure 4, left). Internal mixtures can contain homogeneous particles composed of different materials (Figure 4, middle), or inhomogeneous particles of the same type, for example particles coated with a different material (Figure 4, right). External mixtures occur if air masses containing different aerosol types are mixed, or if particles are emitted into an air mass already containing a different type of particles (e.g. Weinzierl et al., 2011), if a source emits different types of particles (e.g. Kondo et al., 2011a).

Wildfires emit not only black carbon, but also a wide range of trace gases and organic substances as particulate matter (e.g. Sahu et al., 2012). In very intense wildfires, the turbulence and heat in the fire causes particulate matter from the ground to be mobilized and dispersed. The soil particles that are whirled up can be mixed into the smoke plume emerging from the fire. Soja et al. (2004) found signatures of soil dust particles in Siberian forest fire plumes. Dust from the surface was also found in biomass burning plumes over Cyprus (Nisantzi et al., 2014). Mixtures between dust and biomass burning aerosol occur also off the western coast of Africa if Saharan dust is mixed into the biomass burning emissions from central Africa (Weinzierl et al., 2011).

| External Mixture | Internal Mixture | Internal Mixture |
| Homogeneous Particles | | Coated Particles |
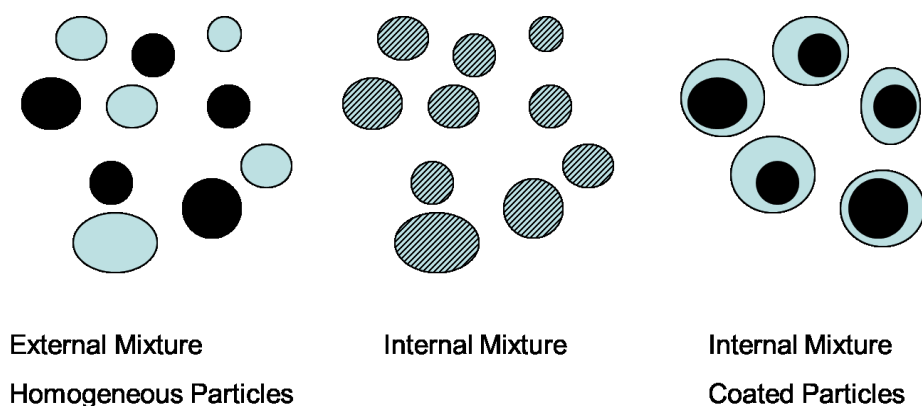
Figure 4: Mixing state of particles containing absorbing and non-absorbing materials (adapted from Bond and Bergstrom, 2006).

A homogeneous or inhomogeneous internal mixture of absorbing and non-absorbing materials within particles can be found in some dust particles composed of different materials containing non-absorbing quartz and absorbing iron oxides (e.g. Kandler et al., 2009). Coated black carbon particles are a specific type of internally mixed particles. The absorbing black carbon particles are coated with a non-absorbing material. This type of particles is typically found in aerosol populations of aged black carbon (e.g. Dahlkötter et al., 2014).

Acquiring a coating of a different material can change a black carbon particle's properties with respect to light scattering and absorption (Schwarz et al., 2008b) or water solubility (e.g. Zhang et al., 2008; Ohata et al., 2016). While pure black carbon particles are hydrophobic, they may become hydrophilic when coated with a hydrophilic substance like organics (e.g. Lee et al., 2010).

Even if the coating material on black carbon particles is non-absorbing, the absorption by thickly coated black carbon particles (Figure 4, right) is enhanced by more than 30% up to 100% compared to uncoated particles (e.g. Schwarz et al., 2008b; Shiraiwa et al., 2010; McMeeking et al., 2014). While these studies assume a core-shell model with a black carbon core and a concentric non-absorbing coating, Dahlkötter et al. (2014) and Sedlacek et al. (2012) presented evidence of internally mixed black carbon particles that do not correspond to the concentric core-shell model.

2.1.1 The Lognormal Aerosol Size Distribution

In a polydisperse aerosol, as it is usually found in the atmosphere, particles span a wide range of sizes. Particle size is an important factor affecting health, as deposition of particles in the lung depends on particle size (e.g. Hofmann, 2011). The effect of particles on radiation also depends on particle size (e.g. Bohren and Huffman, 1998). Larger particles can also more efficiently get water to condense on them to act as nuclei for cloud droplets and ice crystals (e.g. Kreidenweis et al., 2005; Hoose and Möhler, 2012). Atmospheric processes like ageing can change the size distribution of aerosol (e.g. Oshima et al., 2009a). For these reasons, it is crucial to identify particle size distribution in an aerosol population. Since particle size distributions found in atmospheric aerosol tend to have a peak with a long tail towards larger sizes, the lognormal distribution has proven to be a useful parameterization for particle size, volume and mass distributions (e.g. Whitby, 1978). This section introduces the most commonly used parameterization for aerosol size distributions, which is the lognormal distribution. It is only a short summary of the more detailed explanations found in Hinds (1999) and Kulkarni et al. (2011). Why the size distribution of aerosol follows a lognormal function is not entirely clarified (e.g. Hinds, 1999). Previous studies have found that a lognormal function can be the result of breakup and coagulation processes on an originally monodisperse distribution (e.g. Brown and Wohletz, 1995). The shape of the particle size distribution in an atmospheric polydisperse aerosol population often follows a superposition of several lognormal functions (e.g. Whitby et al., 1972).

For lognormally distributed particles, the part of the total number concentration N_0 of particles, dN, that falls into the infinitesimal size interval $d\ln d$ of the diameter d is parameterized as

$$\frac{dN}{d\ln d} = \frac{N_0}{\sqrt{2\pi}\ln GSD}e^{-\frac{(\ln d - \ln CMD)^2}{2(\ln GSD)^2}} \tag{2-1}$$

where the count median diameter (*CMD*) marks also the peak of the distribution. The geometric standard deviation (*GSD*) represents how strong particle sizes vary in the aerosol. An example of a lognormal number size distribution with a CMD of 80 nm and a GSD of 1.7 is shown in Figure 5. The usefulness of the lognormal size distribution does not only lie in the representation of the peak at small and the tail at large sizes, but also in the easy convertibility between median diameters of number, surface and volume or mass (Hatch and Choate, 1929). The Hatch-Choate conversion for count and mass median diameter (*MMD)* is:

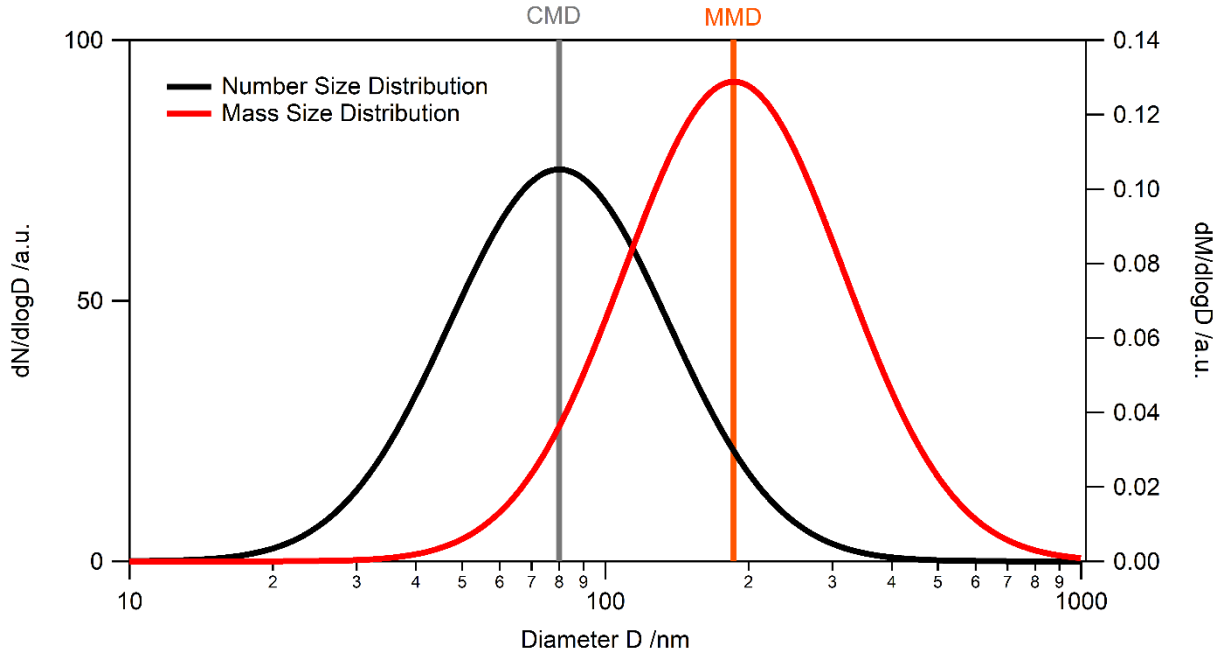$$MMD = CMD \cdot e^{3(\ln GSD)^2} \tag{2-2}$$

Figure 5: Example for the number size distribution (black) and the mass size distribution (red) of a sample of particles with lognormally distributed particle size.

The equation for the mass size distribution can be written in analogy for the mass concentration M with the MMD and the total mass concentration M_0. It is also possible to convert the lognormal number size distribution directly to a lognormal mass size distribution.

$$\frac{dM}{d\ln d} = \frac{M_0}{\sqrt{2\pi}\ln GSD}\, e^{-\frac{(\ln d - \ln MMD)^2}{2(\ln GSD)^2}} = \frac{dN}{d\ln d}\frac{\pi}{6}d^3\rho \qquad (2\text{-}3)$$

The corresponding mass size distribution to the black number size distribution is shown in Figure 5 in red. CMD and MMD are marked as vertical lines. The total number or mass concentration can be calculated by integrating the respective lognormal function.

2.1.2 Scattering and Absorption of Light by Small Particles

To measure particle size, a large variety of measurement techniques is employed in atmospheric aerosol sciences (e.g. Baumgardner et al., 2011; Kulkarni et al., 2011). In this study, the measurement of particle size and particle mass is based on the interaction between a single particle and electromagnetic waves, i.e. the scattering, absorption and emission of light by each particle.

Light falling onto a particle induces secondary radiation into all directions, the scattered light, which depends on incoming radiation and particle type and size. The incident light can also be absorbed by the particle and transferred into another type of energy, like heat. The physical principles are shortly described in this section. A more detailed description of this topic can be found in Hulst (1981) or Bohren

and Huffman (1998). Textbooks on aerosol measurement techniques, like Hinds (1999) or Kulkarni et al. (2011), also treat the scattering and absorption of light by particles.

A simple approach to estimate the effect of a particle in a beam of light is to look at the energy rates of the incoming and outgoing radiation. The intensity of the incoming light, the incident irradiance I_i in W/m², is the energy per time crossing a plane perpendicular to the direction of light propagation. The surrounding medium, usually air in the case of atmospheric particles, is neglected here. The change in direction and energy flux of the incoming radiation due to the interaction with the particle is the extinguished radiation. The rate of energy that is scattered and absorbed by the particle, W_{ext}, can be separated into a scattered, W_{sca}, and an absorbed part, W_{abs}. The ratio of the scattered or absorbed energy rate relative to the incident irradiance has units of an area, and is called the scattering cross section, C_{sca}, or absorption cross section, C_{abs}. The sum of scattering and absorption cross section, the extinction cross section C_{ext}, can be interpreted as the area of the shadow that is casted by the particle. The scattering cross section refers to the light that is scattered into all directions in space. If the light scattered only into a certain solid angle is of interest, the differential scattering cross section dC_{sca} for a differential angle $d\Omega$ is used instead. Integrated over the full solid angle of 4π (see equation (2-4)), it is identical with the scattering cross section C_{sca}.

$$C_{sca} = \frac{W_{sca}}{I_i} = \int_{4\pi} \frac{dC_{sca}}{d\Omega} d\Omega \tag{2-4}$$

$$C_{abs} = \frac{W_{abs}}{I_i} \tag{2-5}$$

$$C_{ext} = \frac{W_{sca} + W_{abs}}{I_i} = \frac{W_{ext}}{I_i} = C_{sca} + C_{abs} \tag{2-6}$$

Though the scattering, absorption and extinction cross sections have the unit of an area, they are not identical to the particle's geometric cross section. The relationship between the scattering cross section and the geometrical cross section is called the scattering efficiency Q_{sca}. The absorption efficiency, Q_{abs}, is defined in analogy.

$$Q_{sca} = \frac{C_{sca}}{C_{geometric}} \qquad \text{and} \qquad Q_{abs} = \frac{C_{abs}}{C_{geometric}} \tag{2-7}$$

Similar to the extinction cross section, the extinction efficiency is the sum of the scattering and absorption efficiency.

$$Q_{ext} = \frac{C_{ext}}{C_{geometric}} = \frac{C_{sca} + C_{abs}}{C_{geometric}} \tag{2-8}$$

The scattering and absorption cross sections C_{sca} and C_{abs} depend on material, shape and size of the particle and the wavelength of the incident light. Since the relation between particle radius a and

wavelength λ of the incident light determines the optical regime, the size parameter x is often used instead.

$$x = 2\pi a/\lambda \tag{2-9}$$

Particles much larger than the wavelength of the incident electromagnetic radiation ($x>>1$) fall into the geometrical regime, the other side of the size range ($x<<1$) is called the Rayleigh regime. The intermediate regime, where particle size is the same order of magnitude as the wavelength of light ($x\approx1$), is called the Mie regime. For very large and very small x, the calculation of scattering and absorption cross sections can be simplified, while for the Mie regime, explicit calculations are necessary (Mie, 1908; Bohren and Huffman, 1998).

For particles much smaller than the wavelength of the incident light, the relations between size, wavelength and scattering and absorption efficiency can be derived from dimensional considerations (e.g. Kulkarni et al., 2011). Being smaller than the wavelength of light, the whole particle experiences the same phase of the electromagnetic wave's oscillation. Rayleigh scattering and absorption are therefore independent of particle shape. As all infinitesimal subvolumes of the particle absorb equally, the absorption cross section must be proportional to the volume of the particle. Dimensions require a proportionality factor, which must depend on wavelength and have the units of inverse length, i.e. the absorption cross section must be proportional to λ^{-1}.

In the Mie range, these assumptions do not hold, and the relations between size, wavelength and scattering and absorption cross section become more complicated. For a particle with known size, shape and refractive index, the Maxwell equations can be solved explicitly, as shown first by Mie (1908) for spherical particles.

To calculate the scattering and absorption for one particle like the examples shown in Figure 4, a spherical shape is often assumed for simplicity. In case of the internally mixed, coated particles, the simple sphere approximation has to be expanded. For this particle type, the assumed model particle consists of a spherical core with a concentric, spherical shell of a different material around. The Rayleigh regime is a special case of Mie theory for small x. For homogeneous spherical particles in the Rayleigh regime, the scattering and absorption efficiencies are

$$Q_{sca} = \frac{8}{3} x^4 \left| \frac{m^2 - 1}{m^2 + 2} \right|^2 \qquad \text{and} \qquad Q_{abs} = 4x Im\left\{ \frac{m^2 - 1}{m^2 + 2} \right\} \tag{2-10}$$

where m is the complex refractive index relative to the surrounding medium. The real part of the refractive index describes how much the light is slowed when passing through a medium compared to vacuum. The complex part, associated with the absorption of light, describes the dampening of the electromagnetic wave in a medium.

Optical instruments measure particle size by detecting the light from a known source, usually a laser, that is scattered by a particle. The light source provides light of a known wavelength. The detector usually does not measure the total scattered light, but covers only a specific solid angle *ΔΩ* from the particle's point of view. The scattered light that reaches the detector depends on particle size and material. For the measurement instrument shown in this work, the light source is a 1064 nm laser, and the scattering detector covers a cone at an angle of 15-75° forward and 105-165° backward relative to the direction of the laser beam (Gysel, 2012, pers. comm.). For this detector geometry and wavelength of light, the scattered light intensity is shown in Figure 6 for several absorbing and non-absorbing particle types in the size range of interest for this work.
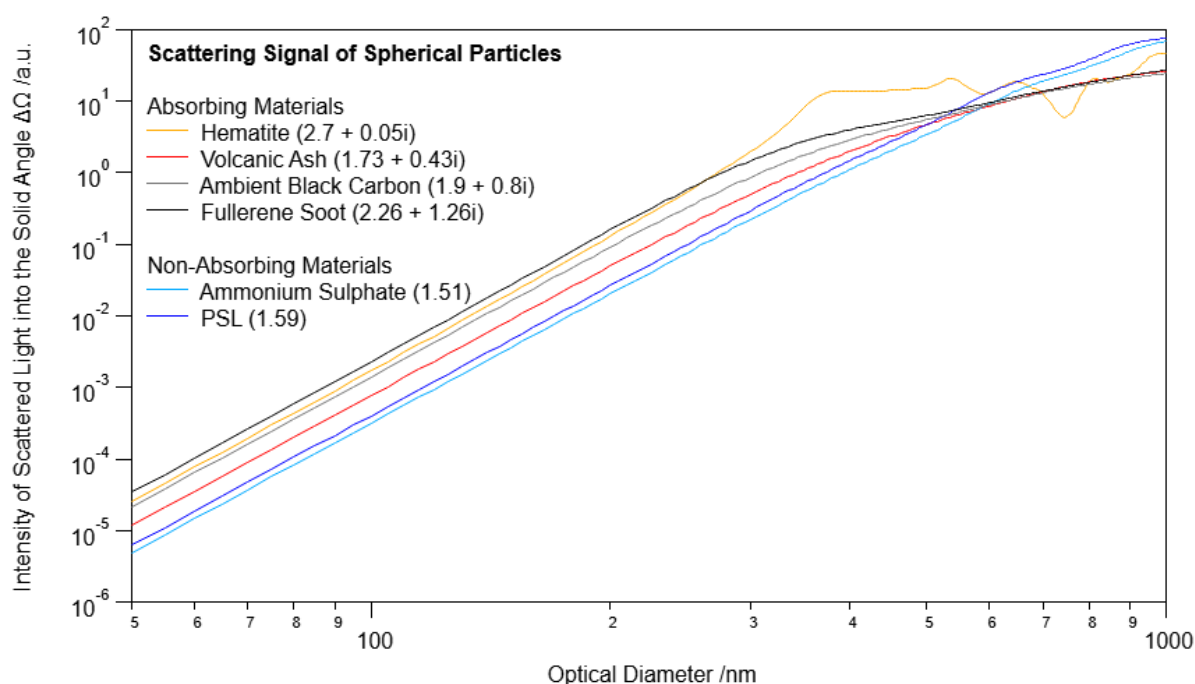

Figure 6: Relative intensity of scattered laser light (1064 nm) seen by a scattering detector at 15-75° to the laser beam for a variety of atmospheric and laboratory spherical particles of different sizes and materials.

The range of the size parameter for the materials shown in Figure 6 is about 0.15 to 3, covering the transition from the Rayleigh regime to the Mie regime. At smaller sizes, the curve shows the Rayleigh regime power law, which changes, depending on refractive index, into the wiggles typical for the Mie regime at larger sizes.

2.1.3 Emission of Light by Small Particles and Incandescence

So far, the interaction between a particle and light was described for light from an external source. Particles act also as a source of electromagnetic radiation due to the thermal radiation emitted from a body of matter with a temperature above 0 K. For particles in thermal equilibrium, the emitted thermal radiation is usually in balance with the absorbed thermal radiation from the surroundings. In the SP2,

refractory particles are heated to temperatures much higher than ambient temperatures. At their boiling point, refractory particles emit measurable amounts of thermal radiation as visible light. The maximum possible energy emitted at a certain wavelength into a solid angle, the wavelength-dependent spectral irradiance $B(\lambda)$, is given by Planck's law, equation (2-11) (Planck, 1901; Seinfeld and Pandis, 2016) and depends only on the temperature T of the body of mass.

$$B(\lambda, T) = \frac{2\pi hc^2}{\lambda^5 (e^{hc/k_B \lambda T} - 1)} \tag{2-11}$$

Here, h is Planck's constant, k_B is Boltzmann's constant and c is the speed of light in vacuum. For several example temperatures, the Planck curve is shown in Figure 7. The integration of equation (2-11) over all wavelengths gives the total emissive power of a blackbody, which is related to the fourth power of the temperature by the Stefan-Boltzmann constant, $\sigma_{sb.}$

$$B(T) = \sigma_{sb} T^4 \tag{2-12}$$

The maximum temperature a particle can reach is the boiling point, above which it will evaporate. Some materials like metals or black carbon have their boiling point at several thousand Kelvin, so the peak of the Planck curve falls into the spectral range of visible light (approximately 380-780 nm). The thermal emission of electromagnetic radiation at visible wavelengths is often referred to as incandescence.

At incandescence, the strongly light-absorbing particles the SP2 measures have temperatures around 3700 – 4300 K (Schwarz et al., 2006). The emitted thermal radiation follows approximately the yellow curve (4000 K) in Figure 7. The figure also shows the wavelength bands used for incandescence measurements, indicated as a light blue shading. Violet lines mark the limits of the sensitivity of the narrowband detector, which coincides with the maximum of the 4000 K curve.
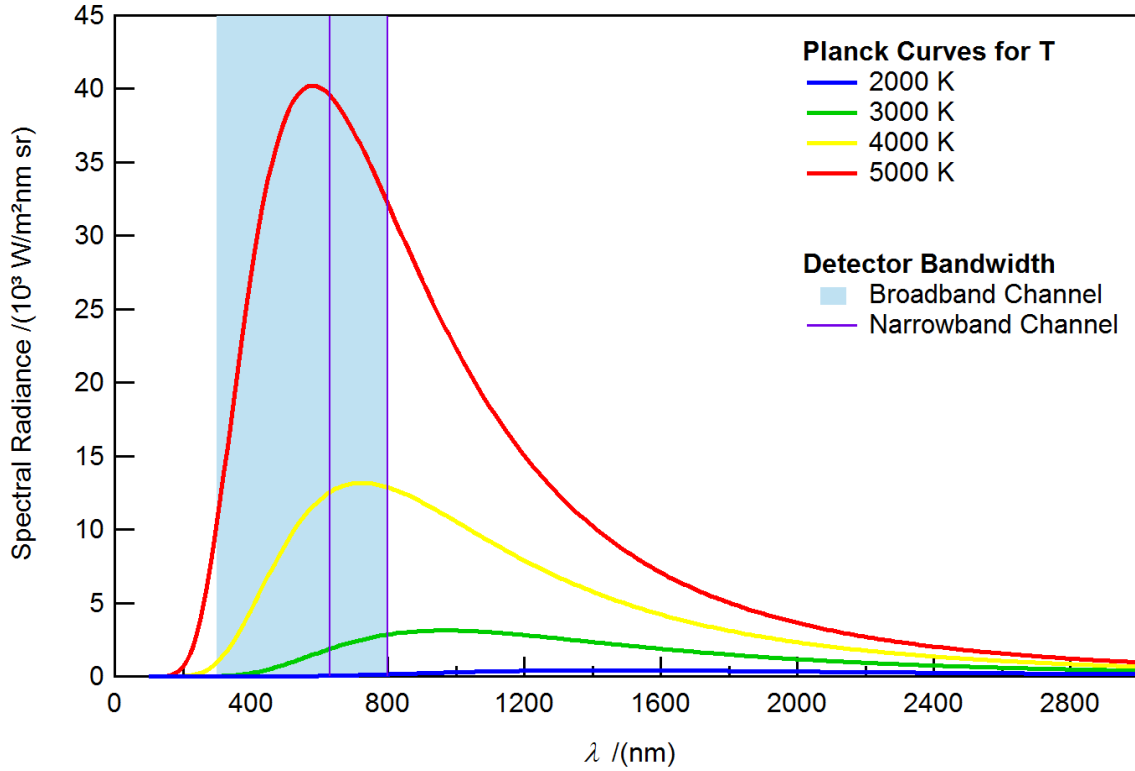
Figure 7: Wavelength-dependent spectral radiance for different temperatures. The light blue shaded area corresponds to the bandwidth of the broadband incandescence detector in the SP2. The narrowband detector is restricted approximately to the bandwidth marked by vertical violet lines.

In the real world, bodies of matter are rarely perfect blackbodies, not even if they consist of strongly light absorbing black carbon. The deviation of the real emission from the ideal blackbody emission is described by the emissivity ε. The emissivity often depends on wavelength and, as Moteki and Kondo (2007) pointed out, can also depend on particle size.

To heat a particle to its boiling point and evaporate it, the energy uptake must be larger than the energy loss, mainly due to heat conduction to the surrounding air and thermal emission. The processes in the heating particle are described by equation (2-13) in e.g. Melton (1984) and Stephens et al. (2003).

$$Q_{abs}(a)\pi a^2 I(t) = \quad h_N(T-T_0)\pi a^2 + \frac{H_V}{W_V}\frac{dm_P}{dt} + \sigma_{sb}4\pi a^2(T^4-T_0^4) + \frac{4}{3}\pi a^3\rho C_S\frac{dT}{dt} \qquad (2\text{-}13)$$

$$\text{I} \qquad\qquad\qquad \text{II} \qquad\qquad \text{III} \qquad\qquad \text{IV} \qquad\qquad\qquad \text{V}$$

The absorbed energy (term I) is used to heat up the particle (term V) and eventually evaporate it (term III). As soon as the particle's temperature T is larger than the temperature T_0 of the surroundings, it will lose energy due to conduction of heat (term II) and thermal emission (term IV, see also equation (2-12)). The terms that are critical for determining whether a particle will reach incandescence, are the energy gain due to absorption (term I) and the energy loss due to heat conduction (term II). As the absorption efficiency Q_{abs} is related linearly to the particle radius a as shown in equation (2-10) (Bohren and

Huffman, 1998; Stephens et al., 2003), the absorbed energy is proportional to the volume of the particle. The ratio between term I and term II therefore is proportional to the ratio between volume and surface of the particle. The larger the particle, the larger is the volume-to-surface ratio. Therefore, for small particles, the heat loss due to conduction is dominant, while the absorption dominates for larger particles. The particle size threshold above which absorption dominates determines therefore the minimum possible lower detection limit of particle sizing by laser-induced incandescence.

Term IV is the difference between thermal emission and absorption due to the particle's temperature being warmer than the surroundings', T_0 (see also equation (2-12)). The thermal radiation, is detected by the incandescence detectors if the temperature is high enough for sufficient radiation to be emitted within the detectors' bandwidth. Assuming that the thermal emissions are independent of direction, the detected signal in the incandescence detectors is proportional to the detector's solid angle of view, $\Delta\Omega$, the wavelength-integrated emitted thermal radiation, weighted by emissivity and wavelength-dependent detector sensitivity $R(\lambda)$, and the particle's surface, $4a^2\pi$.

$$S \sim \frac{\Delta\Omega}{4\pi} 4a^2\pi \int_0^\infty \varepsilon B(T,\lambda)\, R(\lambda) d\lambda \tag{2-14}$$

However, experiments indicate that the detected signal is related linearly to the particle's mass rather than the surface. This might be an effect of the emissivity which depends not only on wavelength but also on particle size, as Moteki and Kondo (2007) show for small graphite particles. While equation (2-14) assumes that the emissions are spatially uniform, Moteki et al. (2009) showed that incandescence of particles with very irregular shapes, like graphite and Aquadag, do have a directional dependence.

A characteristic of Planck's law (equation (2-11)) is that the color ratio, the relationship between two integrals over two different wavelength bands depends on temperature only, not on the wavelength bands the function is integrated over.

$$ColorRatio = \frac{\int_{broadband} \varepsilon B(\lambda) d\lambda}{\int_{narrowband} \varepsilon B(\lambda) d\lambda} \tag{2-15}$$

This is valid for ideal particles only, with an emissivity that is independent of wavelength. For a non-ideal particles with a wavelength-dependent emissivity, the color ratio will also depend on the choice of the narrowband and the broadband wavelength bands. To reduce the effects of a wavelength-dependent emissivity, overlapping wavelength bands can be chosen, as indicated in Figure 7 with blue shading for the broadband detector bandwidth and violet lines for the borders of the narrowband detector bandwidth.

The color ratio can be used as an indicator for particle temperature at incandescence. Different color ratios indicate different incandescence temperatures. As the incandescence temperature is specific for the material, the color ratio differs between materials, as shown for several types of metal (Stephens et al., 2003; Schwarz et al., 2006) and for iron oxides (Moteki et al., 2017). The difference in color ratio

between black carbon and mineral dust or volcanic ash can, to some extent, be used to distinguish the different materials due to the lower incandescence temperature of the latter (Heimerl, 2011). However, the efficiency of incandescence is very low for both volcanic ash and hematite, the strongest absorbing component of mineral dust.

2.2 Vertical Transport in the Atmosphere

The previous sections described the physical properties of particles, size distributions and optical properties, which do not only depend on particle type, but also the processes that a population of aerosol particles has experienced in the atmosphere. Transport processes are also responsible for the horizontal and vertical distribution of aerosol in the atmosphere. With the exception of air traffic, black carbon aerosol sources are located at the surface of the Earth, within the planetary boundary layer (PBL). Black carbon found above that level, in the middle and upper troposphere, must have undergone vertical transport to reach this altitude. Several types of vertical transport mechanisms are described in this section following explanations found in Holton and Hakim (2013), Stull (1988) and Emanuel (1994).

2.2.1 Stability of the Atmosphere

The atmospheric stability is an indicator of the type of vertical motion that is possible in the atmosphere. For the calculations here, is considered to be in hydrostatic equilibrium, e.g. the gravity force per unit mass, $-\rho g$, acting on an air parcel is balanced by the vertical gradient of the pressure p.

$$\frac{\partial p}{\partial z} = -\rho g \tag{2-16}$$

According to the first law of thermodynamics, the change of internal energy of an air parcel is equal to the difference between heat added to the system and work done by the system (Holton and Hakim, 2013). In adiabatic processes, no heat is exchanged between the parcel and the surroundings. The energy changes due to changes in temperature T and pressure p will then cancel each other and the first law of thermodynamics can be written in this form:

$$c_p \frac{D \ln T}{Dt} - R \frac{D \ln p}{Dt} = \frac{D(c_p \ln T - R \ln p)}{Dt} = 0 \tag{2-17}$$

Here, c_p is the specific heat of dry air at constant pressure and R is the gas constant for dry air. Integration of equation (2-17) leads to the definition of the potential temperature, θ. The reference pressure p_0 is usually 1000 hPa.

$$\theta = T * (p_0/p)^{\frac{R}{c_p}} \tag{2-18}$$

The potential temperature θ, the temperature an air parcel would have if it was brought adiabatically to the reference pressure level p_0, is conserved in all adiabatic processes and is a measure for the parcel's

internal energy. If an air parcel is displaced adiabatically from its original position, the vertical profile of potential temperature determines whether it is more or less buoyant than the surrounding air and whether it will continue its way or return to the initial position. The vertical gradient of the potential temperature is therefore a good description of the static stability of the atmosphere (Table 1).

Table 1: Criteria for stability of atmospheric stratification (adopted from Holton and Hakim, 2013).

$\frac{\partial \theta}{\partial z} > 0$	*statically stable*
$\frac{\partial \theta}{\partial z} = 0$	*statically neutral*
$\frac{\partial \theta}{\partial z} < 0$	*statically instable*

In a statically stable atmosphere, vertical motion cannot happen on its own account. Topography, like mountains, can force the air to rise, when it flows over the obstacle. A statically stable atmosphere can be dynamically instable, e.g. due to vertical wind shear. In this case, vertical motion is triggered by the dynamics in the atmosphere. An example for rapid vertical motion in a dynamically instable atmosphere is the warm conveyor belt (WCB), described in the next section, 2.2.2. Section 2.2.3 describes convection, the vertical motion in an instable atmosphere, focusing on thunderstorms.

2.2.2 Vertical Motion in Low Pressure Systems and the Warm Conveyor Belt

In the midlatiudes, dynamic instabilities in a statically stable atmosphere lead to the development of extratropical cyclones (Holton and Hakim, 2013). These low pressure systems consist of sectors of warm and cold air, separated by fronts. Warm, moist air rises ahead of the cold front from the boundary layer to the upper troposphere (e.g. Harrold, 1973; Schemm et al., 2013). Figure 8 shows an example of an extratropical cyclone with the major pathways of air stream indicated (Schultz, 2001). Thick arrows mark the three main quasi-Lagrangian streams of air, two upward moving, the warm (WCB) and the cold conveyor belt (CCB) and the downward intrusion of cold air (dry airstream). The strength of WCBs is correlated with the strength of the cyclone (Binder et al., 2016). Strong WCBs move boundary layer air upward relatively fast as they can reach the altitude of the tropopause within two days (e.g. Stohl, 2001).
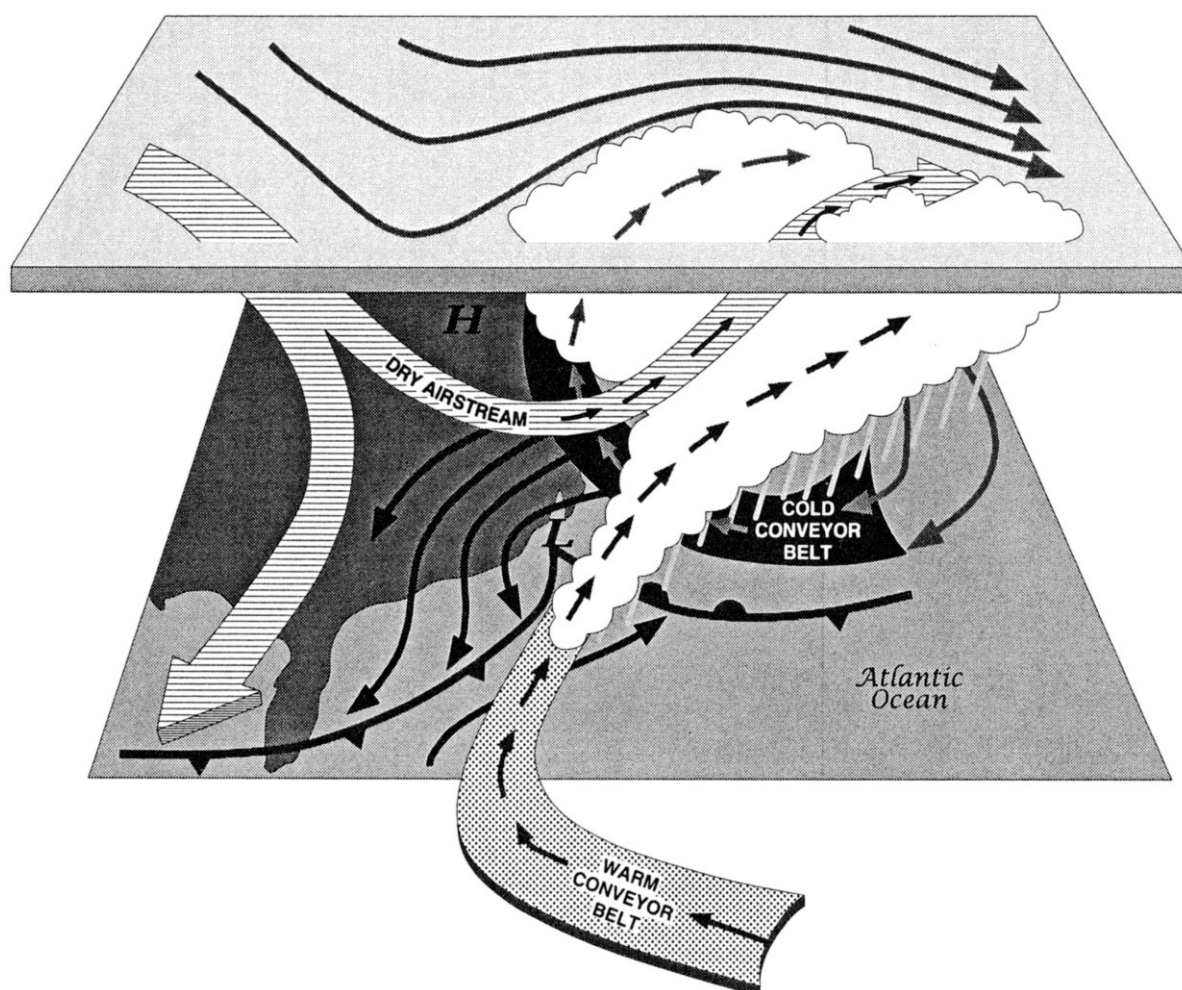
Figure 8: Schematics of air pathways in an extratropical cyclone (from Schultz, 2001; Republished with permission of American Meteorological Society, from Monthly weather review; permission conveyed through Copyright Clearance Center, Inc.).

The WCB's ascent is associated with cloud formation and precipitating cloud bands (Houze, 2014), causing wet deposition of particles. Matsui et al. (2011) show for the transport of Asian pollution to the North American Arctic that most black carbon, up to 99%, was removed from the air masses found in the upper troposphere due to cloud processing. WCB hotspots in the northern hemisphere are at the western sides of the Atlantic and Pacific oceans. They occur more frequently in the winter months (Eckhardt et al., 2004). In the summer months, thunderstorms, associated with convection, are more frequent.

2.2.3 Convection

The term convection describes the vertical motion due to buoyancy differences in the atmosphere. This section gives a short overview of the topic on the basis of Emanuel (1994) and Houze (2014), which give both a more detailed and in-depth descriptions of atmospheric convection.

In an instable atmosphere, an air parcel that is displaced out of its balanced state will continue its path. Over land, destabilization of the atmosphere is often caused by radiative heating at the ground. A parcel of air with temperature T will rise as long as it is warmer than the surrounding air ($\overline{T}$). The lowest layer of air warms up and then ascends adiabatically as thermals. If the top of the thermal reaches the lifting condensation level, the level where the thermal's temperature reaches its dew point, cloud formation starts. The released latent heat from the condensing water vapor can support further ascent. The maximum altitude, to which these thermals can rise, depends on the vertical structure of the atmosphere. In the case of shallow convection, the thermals reach only altitudes smaller than the height of the troposphere, e.g. the top of the boundary layer. The typical clouds that form in this case are fair weather cumuli or stratocumulus decks. Deep convection reaches throughout the whole troposphere, from the boundary layer to the tropopause (e.g. Ogura and Phillips, 1962). Whether convection is enhanced or suppressed in the atmosphere is determined by the stratification and the convective available potential energy (CAPE). The CAPE is the energy gained by a parcel of air by rising from the level of free convection (LFC), the altitude where the parcel becomes buoyant, to the level of zero buoyancy (LZB), where it has the same temperature as the surroundings (Houze, 2014).

$$CAPE = g \int_{LFC}^{LZB} \frac{T(z) - \overline{T}(z)}{\overline{T}(z)} dz \tag{2-19}$$

High values of CAPE indicate an unstable atmosphere, which makes the occurrence of strong convection more likely. Before the air parcel reaches the LFC, it sometimes has to overcome an inversion layer (e.g. Carlson et al., 1983). The energy needed to rise to the LFC is called the convective inhibition (CIN). High values of CIN can prevent convection, even in case of high CAPE. In the midlatitudes, CAPE can be stored and then released in very strong convective storms (Doswell, 2001). These severe convective storms can produce strong gusts, large hail and occasionally tornadoes. Strong updrafts in large thunderstorms can even penetrate the tropopause. These overshooting tops contribute to the troposphere-stratosphere exchange (e.g. Frey et al., 2015). In the tropics, the atmospheric destabilization by the large-scale flow is in quasi-equilibrium with the local convection that stabilizes the atmosphere (Arakawa and Schubert, 1974). About 1% of tropical thunderstorms reach above the tropopause with the stronger ones located over land (Liu and Zipser, 2005; Liu et al., 2007).

The development of a convective cell can be described in three phases, illustrated in Figure 9. In the first stage, a towering cloud evolves and grows in height with a strong updraft in the center. The towering cloud can continue to grow until it reaches the level of neutral buoyancy. For deep convection, this is often at the level of the tropopause where thunderstorms spread and form an anvil, in cases of very strong updrafts with an overshooting top. Inside the cloud, the condensing water vapor forms droplets and ice crystals, which results in rain and hail in the mature stage (Figure 9, center). The cooling due to precipitation forms a gust front on the ground. The downdrafts associated with precipitation counteract

the updrafts inside the cloud and lead to a weakening and dissipation of the thunderstorm (third stage in Figure 9).
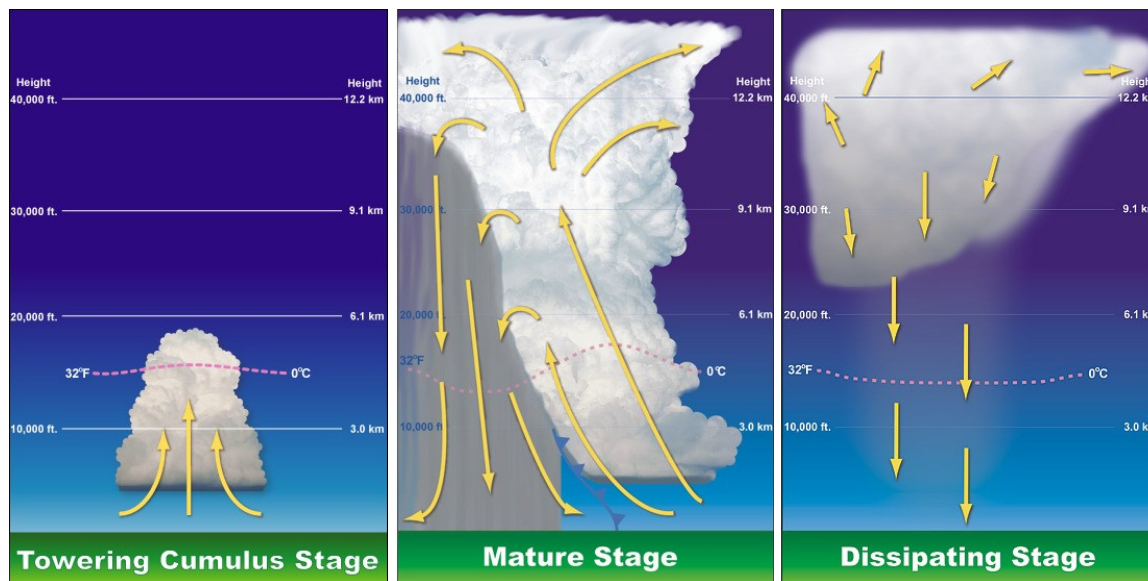

Figure 9: Stages of thunderstorm development (from: National Weather Service, http://www.weather.gov/jetstream/life).

This describes roughly the evolution of a single convective cell with a lifetime of about 1 hour. In an environment with low shear, this is the typical thunderstorm with a horizontal extent in the order of ten kilometers. In favorable meteorological conditions with high CAPE and very strong wind shear, this convection cell can develop into a supercell. Supercell storms often produce strong gust fronts, large hail and can develop tornadoes, all possibly resulting in high damage. The development of supercells is driven by vorticity dynamics and do not always produce heavy precipitation. Updrafts in supercells are so strong that newly-forming ice particles are lifted up before they grow large enough to be detected by cloud radars, causing a "vault", seen in the radar echo as a hole in the cloud. Rotation in supercells can lead to tornado formation at the base of the main updraft. Supercell storms occur often in the US Midwest, where the hot, dry air from the desert is situated over colder, moist air from the Gulf of Mexico. This stratification favors the formation of strong thunderstorms. In an environment with strong CAPE and moderate shear, the gust front can initiate further convection so that a new cell forms next to the original one. Convective cells developing next to each other can form organized *Mesoscale Convective Systems* (MCS). An MCS is characterized by cold cloud top covering more than 100.000 km² and large areas of convective and stratiform precipitation (Maddox, 1980). A specific type of these systems is the *squall line*, where the convective cells form a curved band.

While squall lines form under a variety of atmospheric conditions, a more circular shaped *mesoscale convective complex* forms preferably in the ascent regions of midlatitudinal troughs or in the intertropical convergence zone and occurs more frequently downwind of mountain ranges. The mesoscale convective

complex forms in the afternoon and can last until the morning hours, with the maximum extent at some time in the early morning hours. Typical parameters for the three different types of thunderstorms shortly described here are listed in Table 2.

Table 2: Types of thunderstorms with typical scale, duration and updraft speed. The vertical extent of all three thunderstorm types is from boundary layer to the tropopause region, with the stronger ones producing overshooting tops into the lower stratosphere. (Data from Emanuel, 1994; Houze, 2014)

	Horizontal Scale	*Duration*	*Updraft Speed*
Isolated Thunderstorm	~ 10 km	~ 1 h	~ 10-15 m/s
Supercell	~ 10-50 km	~ 1-15 h	~ 10-40 m/s
Mesoscale Convective System	~ 100-1000 km	~ 6-15 h	~ 1-20 m/s

A specific case of convection associated with biomass burning is pyroconvection. In this case, the energy source for the rise of an air parcel is the heat of the fire (Fromm et al., 2010). Pyroconvection plays a role in vertical transport of pollutants and has been identified as a source for stratospheric aerosol (e.g. Fromm et al., 2005; 2008).

Biomass burning aerosol can also be lifted into the upper troposphere by thunderstorms, as several studies of tropical thunderstorms in regions with strong biomass burning showed (Andreae et al., 2001; Huntrieser et al., 2011; Reid et al., 2015). Hotspots for thunderstorm development are the tropics and the summertime northern hemisphere (Liu and Liu, 2016). In the northern hemisphere, the Great Plains in the US are an area which favor the development of strong thunderstorms, frequently with overshooting tops, due to the geographic and meteorological conditions. This was the motivation to conduct a measurement campaign there to study processes associated with deep convection. Details on this measurement campaign that provided most data for this study are described in the next chapter.

3   Methods

This chapter gives an overview of the data and measurement methods used in this study. The first part of this chapter, section 3.1, introduces the aircraft measurement campaign during which the data shown in this work were acquired. As the aim of this work is investigating refractory black carbon, the instrument used to measure it, the Single Particle Soot Photometer (SP2), is described in detail in the following part, section 3.2, giving details on calibration procedures and data quality assurance methods. The last part of this chapter, section 3.3, describes the data analysis methods used here.

3.1   Deep Convective Clouds and Chemistry (DC3): Campaign Overview

The Deep Convective Clouds and Chemistry Campaign (DC3) was a field experiment conducted in May and June 2012 in the U.S. Midwest with three aircraft and a wide range of ground-based measurements to study deep convection (http://www.eol.ucar.edu/field_projects/dc3). The main objective of this field campaign was to investigate dynamical, physical, chemical and electrical processes in deep convection in the midlatitudes to improve the scientific understanding of the influence of deep convection on the upper troposphere (UT). The focus was on the quantification of transport of water and trace species to the UT and the chemical reactions in the fresh and aged thunderstorm outflow. The three aircraft that participated in the campaign, the NASA DC-8 (https://www.nasa.gov/centers/armstrong/aircraft/DC-8/index.html), the NSF GV and the DLR Falcon 20E were equipped with a range of in-situ and remote sensing instruments for the detection of trace gases and particles and probed thunderstorm inflow and both fresh and aged outflow. Ground-based measurements like radiosondes, mobile radars and lightning detection networks provided valuable input for the flight planning during the field campaign. A wide range of models and operational satellite observations, available in the DC3 field catalog (http://catalog.eol.ucar.edu/dc3_2012/), supported both flight planning and post-campaign analysis. The main DC3 campaign lasted from May 18 to June 30 2012. Both the NASA DC-8 and the NSF GV were present at the flight operation base in Salina in Kansas (KS) during this whole period. For three weeks, the DLR Falcon (Figure 10) joined the field campaign, conducting 13 research flights between May 29 and June 14. A summary of the whole campaign period can also be found in Barth et al. (2015) and Huntrieser et al. (2016b).

Figure 10: Picture of the DLR Falcon in front of the hangar in Salina/KS with spectrometer probes under the wings and inlets on the roof. The large nose boom is used for meteorological measurements outside of the aircraft's own boundary layer.

The focus of this study is on black carbon data acquired on board of the Falcon aircraft (Figure 10). Altogether, the Falcon conducted 26 flights between May 25 and June 19, 2012, all listed in Table 3 and illustrated in Figure 11 and Figure 12. Due to the limited flight duration of the aircraft of three to four flight hours, half of the flights (13) were needed for the transfer from Oberpfaffenhofen to the campaign base in Salina and back. During the campaign, the Falcon performed 13 research flights starting from the operation base in Salina. Due to the distance between the operation areas and the base in Salina, the Falcon had to refuel at a different airport between two flights on most of the days. All flights conducted by the Falcon during the DC3 campaign are listed in Table 3 with their flight number and scientific objective The Falcon flights are all named by a six-digit number consisting of the flight date with year, month and day, followed by a letter enumerating the flights of one day. For flights measuring in air masses influenced by biomass burning, the third column gives the names of the corresponding active fires.

Table 3: List of Falcon flights during the DC3 campaign with their scientific targets and major fires that influenced the measurements on these flights. The last column indicates availability of the rBC data measured with the SP2 and data gaps due to laser overheating and power failures.

Flight Number	Flight Objective	Biomass Burning plumes from fires	SP2 Data Availability
120525a	Transfer flight		full flight
120525b	Transfer flight		full flight
120525c	Transfer flight		full flight
120526a	Transfer flight		full flight
120526b	Transfer flight		full flight
120527a	Transfer flight	Fires at Great Lakes	full flight
120527b	Transfer flight		full flight
120529a	Whitewater-Baldy fire plume	Whitewater-Baldy Fire	full flight
120529b	OK/TX thunderstorm		no data (overheating)
120530a	Whitewater-Baldy fire plume	Whitewater-Baldy Fire	full flight
120530b	OK/TX thunderstorm		major data gaps (overheating)
120605a	convection over OK/TX		major data gaps (power failure)
120605b	convection over OK/TX		major data gaps (power failure)
120606a	convection over CO	Fires in Canada, Cheyenne Fires in WY	full flight
120608a	Aged thunderstorm outflow from CO	Fires in CO	full flight
120608b	Aged thunderstorm outflow from CO	Fires in CO	full flight
120611a	convection over AR/MO	Little Bear and High Park Fire	full flight
120611b	convection over AR/MO	Little Bear and High Park Fire	full flight
120612a	convection over CO	Little Bear Fire and Colorado Fires	full flight
120614a	Aged thunderstorm outflow from CO/KS	Little Bear Fire and Colorado Fires	full flight
120617a	Transfer flight	High Park Fire	full flight
120617b	Transfer flight		full flight
120618a	Transfer flight	High Park Fire and Canadian Fires	full flight
120618b	Transfer flight		full flight
120619a	Transfer flight		full flight
120619b	Transfer flight		full flight

Since the main target of this campaign was studying thunderstorms, most flights were conducted in and around the anvil region of thunderstorms. The targeted thunderstorms are also listed in Table 3 and described in more detail in Huntrieser et al. (2016a). This study focuses on the biomass burning plumes that were measured during the DC3 campaign. For all flights during which plumes were encountered, the major fires from which the plumes originated are also listed. The map in Figure 11 shows all the

flight tracks corresponding to all flights listed in Table 3. A close-up of the local flights performed from the Salina/KS operation base is shown in Figure 12.
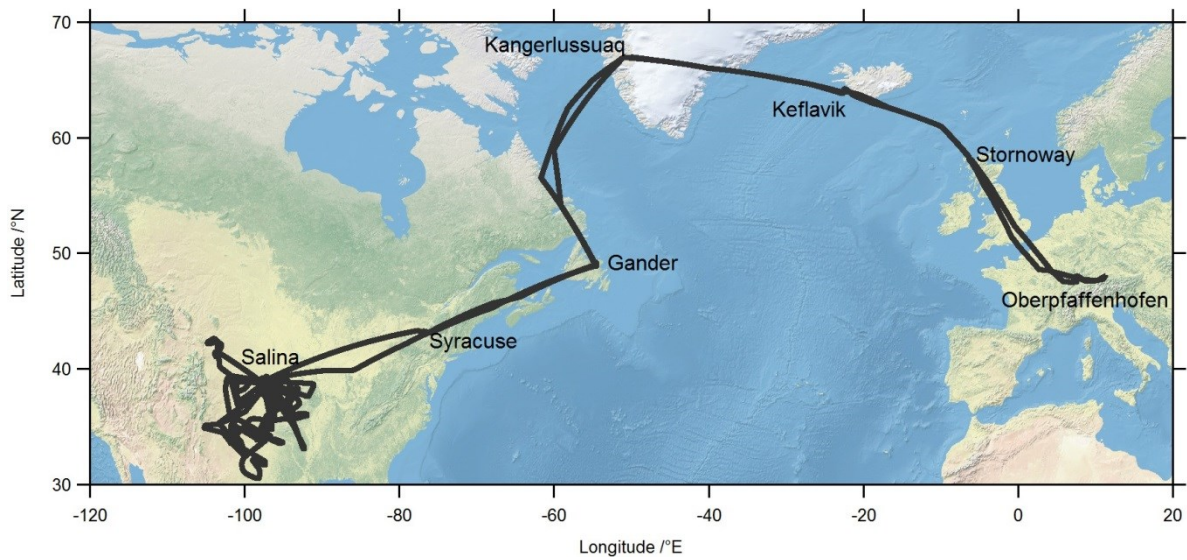

Figure 11: Map of all flights during the DC3 campaign. Shown are also the refuel stop airports of the transfer flights. The local flights are shown in more detail in Figure 12.
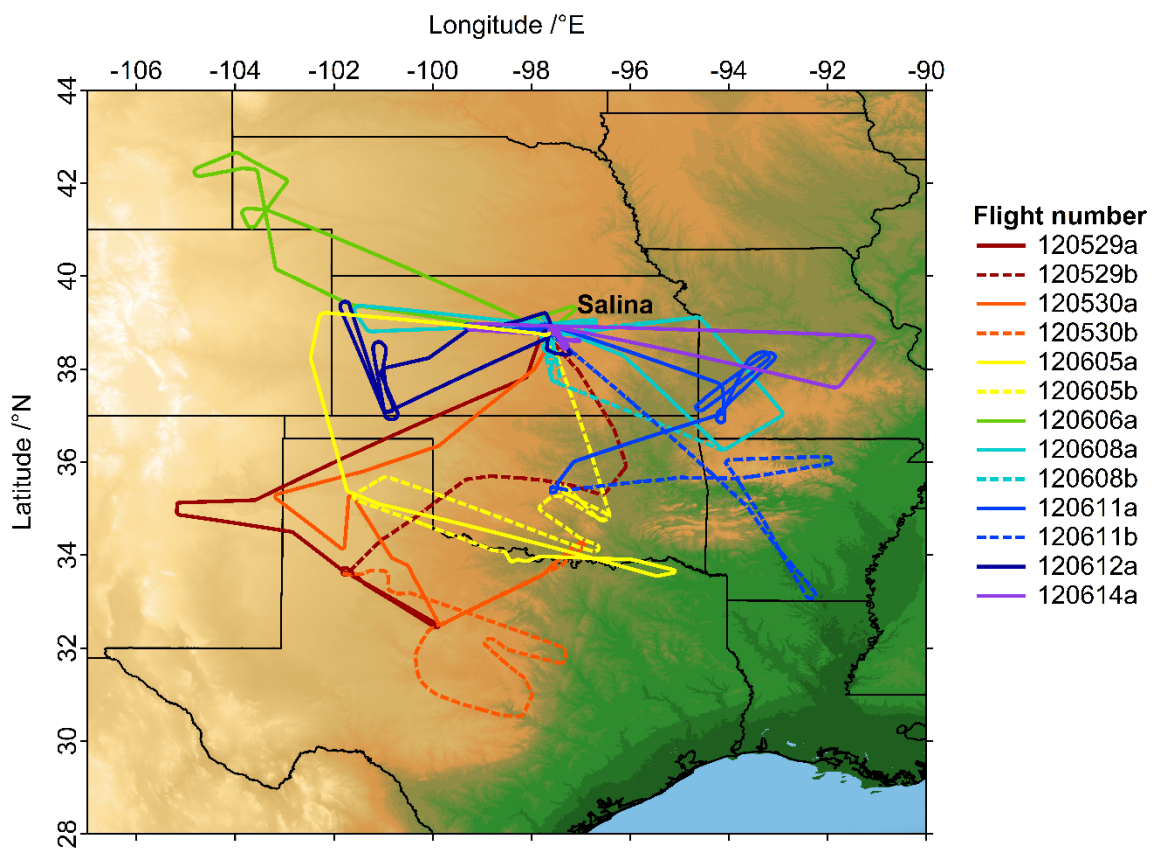

Figure 12: Map of local flights of the DC3 campaign. The operation base in Salina/Kansas is marked.

As a research aircraft, the Falcon has a range of sensors built in to measure meteorological data like wind speed and direction, pressure, temperature, and relative humidity, and position data like GPS (Global Positioning System) coordinates and the angle of the plane in the air. The Falcon was also equipped with a range of in-situ measurement instruments for particle and trace gas detection, listed in Table 4 and also described in the campaign overview paper (Huntrieser et al., 2016b). For the detection of larger particles, four Knollenberg mounts, situated under the wings, housed optical probes for particle detection; namely an FSSP-100 (Forward Scattering Spectrometer Probe, Particle Measuring Systems, Boulder/Colorado, USA), an FSSP-300 (Forward Scattering Spectrometer Probe, Droplet Measurement Technologies, Boulder/Colorado, USA), a PCASP-100X (Passive Cavity Aerosol Spectrometer Probe, formerly manufactured by Particle Measuring Systems, Boulder/Colorado, USA, now maintained by Droplet Measurement Technologies, Boulder/Colorado, USA), and an airborne UHSAS (Ultra-High Sensitivity Aerosol Spectrometer, Droplet Measurement Technologies, Boulder/Colorado, USA).

To provide air samples for the cabin instrument, air was drawn into the cabin via an isokinetic aerosol inlet on the Falcon rooftop (large black inlet on roof top over the first side window in Figure 10). This inlet is designed to decelerate the air flow when drawing it into the aircraft without changing the particle size distribution by enhancing or decreasing the amount of particles in a certain size range. The upper cut-off of the aerosol inlet lies at roughly 1.5-2 μm, depending on altitude (Fiebig, 2001). The aerosol instrumentation inside the cabin included two CPCs (Condensation Particle Counter, TSI), three CPSAs (Condensation Particle Size Analyzer), a PSAP (Particle Soot Absorption Photometer), two OPCs (Optical Particle Counter, Grimm, Germany), and an SP2 (Single Particle Soot Photometer, Droplet Measurement Technologies, Boulder/Colorado, USA). Data taken with the latter will be the focus of this study. Two CPCs and two CPSAs were set to different lower cut-offs to study Aitken-mode aerosol. A thermal denuder, set to 250 °C was integrated into the inlet of one of the CPSAs and one of the OPCs to study non-volatile aerosol.

The optical instruments, the OPCs and the wing probes, measure scattered light from particles passing through a laser beam. Though these instruments all use different sensors and lasers at different wavelength, the measurement principle is always based on the dependence of backscattered light on particle size for known detector geometry and assumptions about the particle's refractive index. The SP2 also uses this technique for measuring non-refractory particles, but its main purpose is the measurement of rBC particle mass by detecting the emitted light from incandescing rBC particles. In the condensation particle counters (CPC and CPSA), the aerosol is led over a heated working fluid with a low boiling point, here 1-Butanol and subsequently cooled so the Butanol condenses on the particles. Particles with only a few nanometers in size grow through the condensation so they are large enough to be counted by an optical detector.

Table 4: Selected Instrumentation of the DLR Falcon during DC3 for the Data shown in this work (for more details, see Huntrieser et al., 2016b). If no upper detection limit is given for cabin instruments, the aerosol inlet cutoff applies. In addition to the listed instruments, position and meteorological data were provided by the Falcon measurement system.

Instrument	*Measured Species*	*Nominal Size Range or Detection Limits*
Wing Station		
Forward Scattering Spectrometer Probe (FSSP100)	Size-resolved Particle Concentration	2-32 µm
Cabin Instruments behind Aerosol Inlet (Upper Cut-Off 1.5-2 µm)		
Condensation Particle Counter (CPC) Condensation Particle Size Analyzer (CPSA)	Total Non-Volatile Particle Concentration	> 5 nm > 10 nm
Condensation Particle Size Analyzer (CPSA) with Thermodenuder	Total Non-Volatile Particle Concentration	> 10 nm
Single Particle Soot Photometer (SP2)	Black Carbon Mass Concentration and Mixing State	80-485 nm
Cabin Instruments behind Rosemount Trace Gas inlet		
CO Analysator AL 5001	CO	$2\text{-}10^5$ ppb
UV-Ozone-photometer TE49	O_3	1-700 ppb
CLD Ecophysics 790 SR with modifications	NO, NO_x, NO_y	20-50000 ppt

Rosemount inlets provided sample air for trace gas measurement instruments inside the Falcon's cabin (small orange inlets on the aircraft's rooftop in Figure 10). The measured trace gas species were CO, O_3, CO_2, CH_4, SO_2 and the nitrous oxides NO, NO_x and NO_y (see Table 4). The DC-8 was equipped with a wide range of different in-situ and remote sensing instruments. Here, data from the DIAL (Differential Absorption Lidar) and from an SP2 are used. The DC-8 SP2 was part of a system consisting of two SP2s, one measuring dried air, the other humidified air, to study humidity effects on rBC particles (Schwarz et al., 2015). In this study, only data from the dry SP2 are shown. The DIAL is a high spectral resolution lidar, which measures aerosol backscatter and depolarization at 532, 1064 and 355 nm and

aerosol   extinction   at   532 nm   (Hair   et   al.,   2008;   Burton   et   al.,   2015).

Figure 13: MODIS fire map for May 20 to June 18. The blue circles mark the three largest fires during DC3, the High Park (north), the Whitewater-Baldy (west), and the Little Bear (east) fire. (http://rapidfire.sci.gsfc.nasa.gov/cgi-bin/imagery/firemaps.cgi)

As the 2012 fire season was more intense than usual (Jolly et al., 2015), the DC3 campaign was influenced by many large wildfires. Figure 13, showing fire data from MODIS (Moderate Resolution Imaging Spectroradiometer on the Terra and Aqua satellites) for the whole campaign period, gives an impression of the ubiquity of fires during DC3. The unusually dry conditions of 2012 (Hoerling et al., 2014) may be a reason for the increased wildfire activity of that year. The three largest fires that influenced the DC3 measurements are marked with blue circles in the MODIS fire map in Figure 13.

Huntrieser et al. (2016b) give some details on the three largest fires occurring during the campaign period. The Whitewater-Baldy wildfire, the Little Bear wildfire in New Mexico and the High Park wildfire in Colorado are all counted among the largest and most destructive wildfires in the respective state's history.

Table 5: List of the three largest wildfires burning during DC3 (adapted from Huntrieser et al., 2016b).

Fire	Area Burned	Time Burning	Comments
Whitewater-Baldy Fire	~121·10³ ha	Started on May 9, 2012 by lightning 95% contained on July 23, 2012	merged from Whitewater and Baldy fire on May 23, largest wildfire in New Mexico state history
Little Bear Fire	~18·10³ ha	Started by lightning on June 4, 201 90% contained on June 26, 2012	most destructive wildfire in New Mexico state history
High Park Fire	~35·10³ ha	Started by lightning on June 9, 2012 100% contained on July 1, 2012	second largest wildfire in Colorado state history at that time

The plume from the Whitewater-Baldy wildfire was probed intensively on May 29 and 30, 2012. On both days, the conditions were similar with the plume between 3 and 5 km altitude. In Figure 14, the Whitewater-Baldy wildfire in the Gila Wilderness, marked by red dots, can be spotted easily as it was the only larger fire in this area at the beginning of the campaign. The smoke plume from this fire, visible in the satellite image as a greyish cloud, extends far downwind and spreads from New Mexico to Texas and Oklahoma over a distance of about 1000 km.
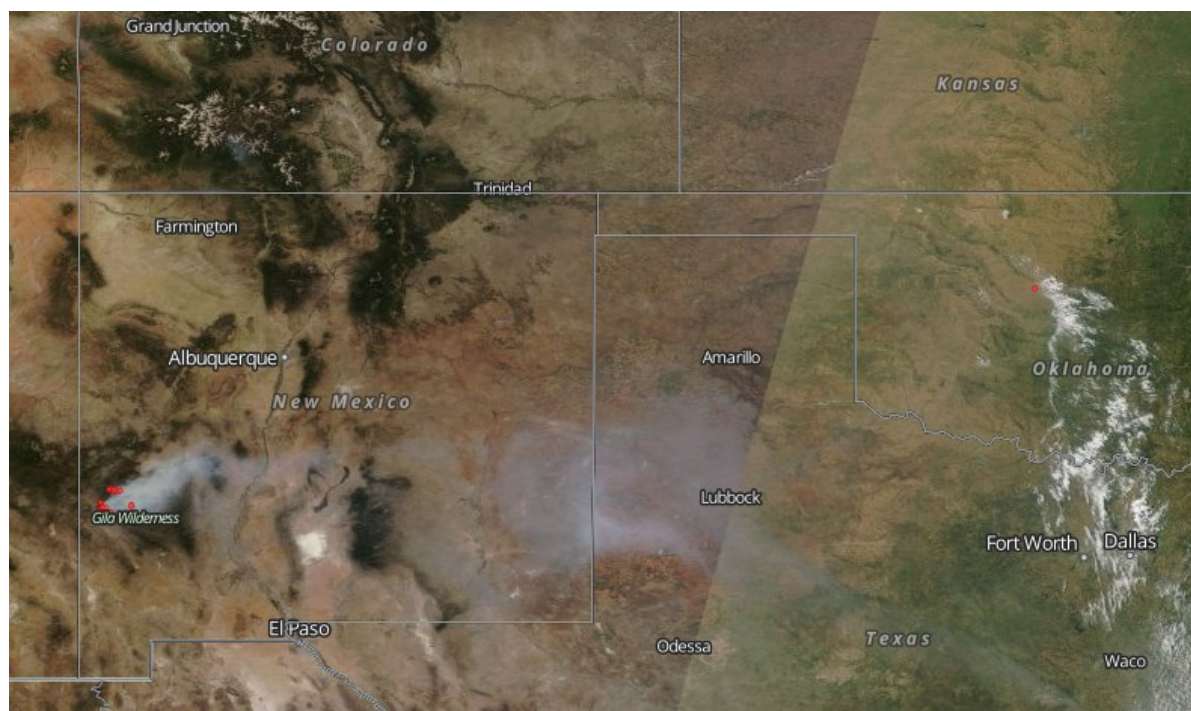
Figure 14: MODIS images of May 29, 2012 showing the Whitewater-Baldy wildfire in the Gila Wilderness in western New Mexico. The thick smoke plume is clearly visible downwind of the fire. Falcon measurements on that day were performed in the thick smoke layer in eastern New Mexico and northern Texas. (NASA EOSDIS World view screenshot with Terra/Aqua temperature anomalies overlay; https://worldview.earthdata.nasa.gov/)

Later during the campaign, after June 10, wildfires were more frequent. Fires in Colorado and New Mexico produced plumes that were measured during every flight of the second part of the campaign. Plumes from several smaller fires also influenced the measdurements, since many fires burned all over North and Middle America , especially during the second part of the campaign (see Figure 13).

3.2 Measuring Black Carbon Particles with a Single Particle Soot Photometer (SP2)

Quantifying the impact of black carbon from wildfires like these on atmosphere and climate requires reliable measurements of black carbon particles. A variety of measurement techniques have been developed and improved over the years (Moosmüller et al., 2009), The first measurements of black carbon were made by collecting particles on filters (e.g. Hill, 1936) and observing the change in optical properties when particles are deposited from air containing particles is sucked through it. Filter-based measurements of the optical properties of black carbon particles are still widely used today, employing instruments like the Aethalometer (Hansen et al., 1984) or the Particle Soot Absorption Photometer (Bond et al., 1999). They measure the change in light transmission of a filter when particles are collected onto it and compare it to a clean filter. The Multi-Angle Absorption Photometer (Petzold et al., 2005) is

based on the same technique, but uses several detectors to avoid high biased measurements from scattering particles and coatings (e.g. Lack et al., 2009). Off-line filter-based measurements rely on post-sampling analysis of the particle-loaded filter by heating it to high temperatures to evaporate volatile particles (e.g. Birch and Cary, 1996) in order to distinguish organic and black carbon. .

Another way to deal with the issue of bias due to mixing of black carbon with other substances is to use a heated inlet which removes volatile particles (e.g. Burtscher et al., 2001) as black carbon has a very high melting point and measuring the number concentration of the remaining sample. However, this also applies to dust and sea salt which can make up a large fraction of aerosol, especially in the coarse mode (e.g. Weinzierl et al., 2009).

The optical properties of aerosol are also used in remote sensing techniques both from ground and from space. Active remote sensing techniques, like lidar instruments, provide their own light source, usually with a laser. The lidar uses a laser pulse as light source and measure the backscattered light. High resolution of time, frequency and polarization make it possible to study aerosol properties at different altitudes (e.g. Groß et al., 2013). They are used widely as ground-based or airborne instruments (Schumann, 2012) and from space with the CALIOP (Cloud-Aerosol Lidar with Orthogonal Polarization) on the CALIPSO (Cloud-Aerosol Lidar and Infrared Pathfinder Satellite Observation) satellite (https://www-calipso.larc.nasa.gov/).

Passive remote sensing techniques, for example the MODIS instrument (Remer et al., 2005), use the sunlight as light source to measure aerosol properties like the aerosol optical thickness. The drawback of passive remote sensing techniques is that they are limited to column-integrated values and cannot detect black carbon mass or number concentrations alone without making many assumptions like the refractive index or the size distribution.

Other in-situ techniques rely on the heating of black carbon particles due to strong light absorption to measure black carbon independent of other substances. Photoacoustic instruments measures the pressure wave induced by a heated particle with a very sensitive microphone (Arnott et al., 1999). Laser-induced incandescence uses strong light absorption of particles to heat them to evaporation. At evaporation temperature, refractory particles emit thermal radiation at the wavelength of visible light. This has been used for many years with pulsed lasers to study particle formation and combustion processes in flames (e.g. Eckbreth, 1977; Melton, 1984). While the pulsed laser technique is used to quantify particle ensembles at high concentrations, the commercially available Single Particle Soot Photometer (SP2) uses a continuous laser for measuring the mass of single black carbon particles at low concentrations (Stephens et al., 2003). It detects mainly particles in the accumulation mode, which makes it a suitable instrument to study black carbon from wildfires and ageing effects. Due to its capability of measuring small quantities of rBC mass, the SP2 is also widely used for measuring the rBC content in ice cores (e.g Kaspari et al., 2011) and snow samples (e.g. Bisiaux et al., 2012). Studies by Slowik et al. (2007) and Cross et al. (2010) show that the SP2 measures black carbon mass

concentrations very well without being biased by the particles' mixing state by comparing nascent soot with a fractal shape to more compact particles which were coated and subsequently thermally denuded, so their fractal shape collapsed in the process. Moteki and Kondo (2010) and Laborde et al. (2012a) show that SP2 detects well most types of ambient and commercially available black carbon types. The only black carbon type not detected efficiently are particles generated with the PALAS soot generator, as Gysel et al. (2012) found out, probably due to a low effective density. As the SP2 combines incandescence technique with optical particle detection, it is a favorable instrument to study also the mixing state of rBC particles (Gao et al., 2007). From an intercomparison between six SP2s with different setups, Laborde et al. (2012b) concluded that detailed knowledge of the varying detection limits and detection efficiency is crucial for comparable results. The following chapter gives details on the setup of the specific SP2 used to obtain the data shown in this work. Alignment and calibration of the instrument and their influence on detection limits and detection efficiency are shown as well.

3.2.1 Instrument Setup and Alignment of the SP2

The SP2 contains two PMTs (Photomultiplier tubes) with different optical filters for the detection of the thermal radiation emitted by the incandescing particles and two detectors measuring scattered laser light for optical particle sizing. The components of the SP2 can be seen in Figure 15, which shows the open SP2 instrument. The core of the instrument is the black optical block, containing laser crystal and mirrors in the left and right housings. The laser consists of an 808 nm pump laser (not visible here behind the black optical block) and a Nd:YAG crystal providing the 1064 nm wavelength. Highly reflecting surfaces on the laser crystal and the output coupler increase the laser intensity inside the cavity to values in the order of 10^7 W/cm² (Schwarz et al., 2010a). The measurement chamber with the four detectors is mounted movable in the middle of the optical block. The SP2 housing also contains a computer for data acquisition, visible behind the detector block. Not included in the housing is a pump for sucking the sample air through and pushing the sheath airflow into the instrument.
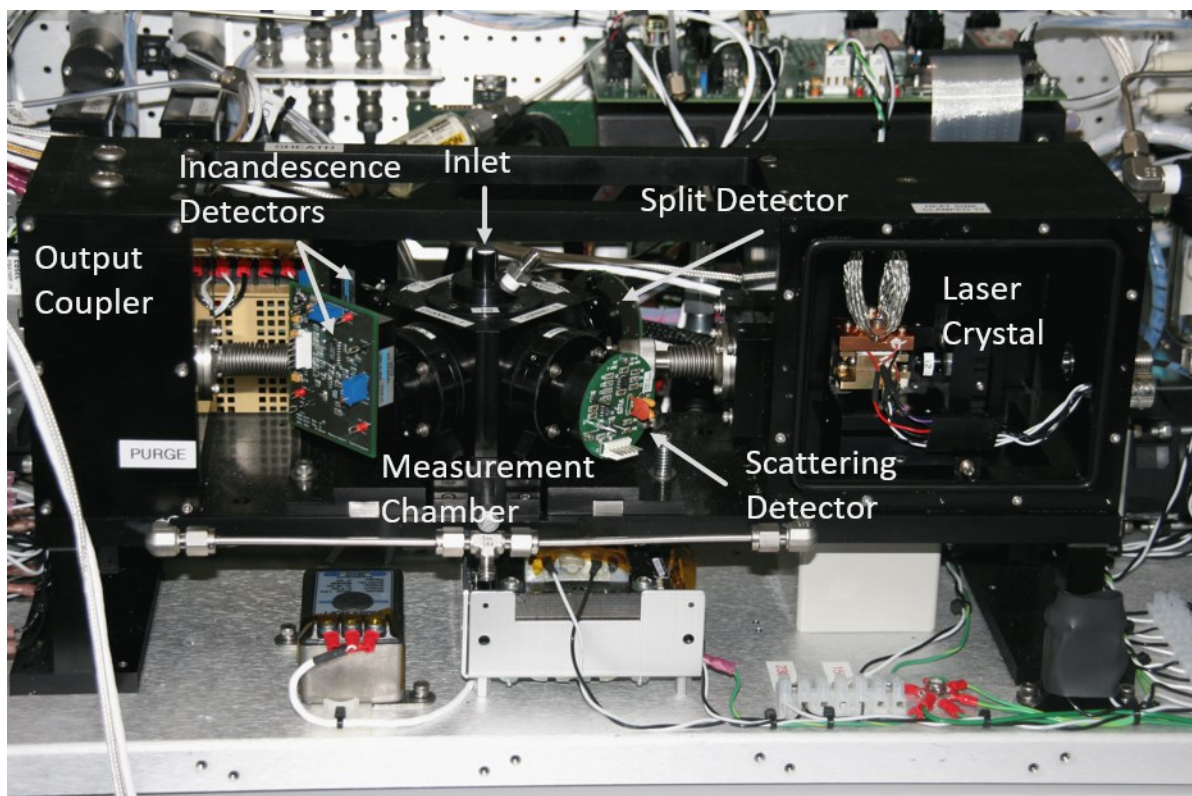
Figure 15: Image of the SP2 with open housing. The black optical block is seen in the front with the measurement chamber in the middle and the YAG crystal in the opened right part of the block.

The sampled air is introduced into the measurement chamber from the top (Figure 15). It is surrounded by a sheath flow and focused into a thin stream in the measurement chamber where it crosses the center of the Gaussian shaped laser beam at its maximum intensity. Particles in the laser beam scatter light which is detected by the scattering detector, an avalanche photodiode (APD) with a filter (RG850) to exclude most of the visible light emitted from incandescing particles. The four detectors are mounted into the measurement chamber as shown in Figure 15.

High gain channel signals from all four detectors are shown in Figure 16 for two example particles, on the left an rBC particle with coating, on the right a purely scattering, non-absorbing particle. The scattering (dark green) and the split detectors' (black) signals start to rise as soon as the particle enters the laser beam, following the Gaussian shape of the laser intensity profile. When the absorbing particle starts to heat up, the coating evaporates and the scattering signal decreases with decreasing particle size. The rBC core of the particle keeps absorbing laser light and heats up even further until it reaches incandescence, seen as a rise in the broadband (blue) and narrowband (red) incandescence signals. Subsequently, the incandescing particle evaporates and the signals in all four channels decrease to the baseline. The purely scattering particle passes the laser beam unaltered and the signal shape of the scattering signal represents the Gaussian shape of the laser beam intensity profile.
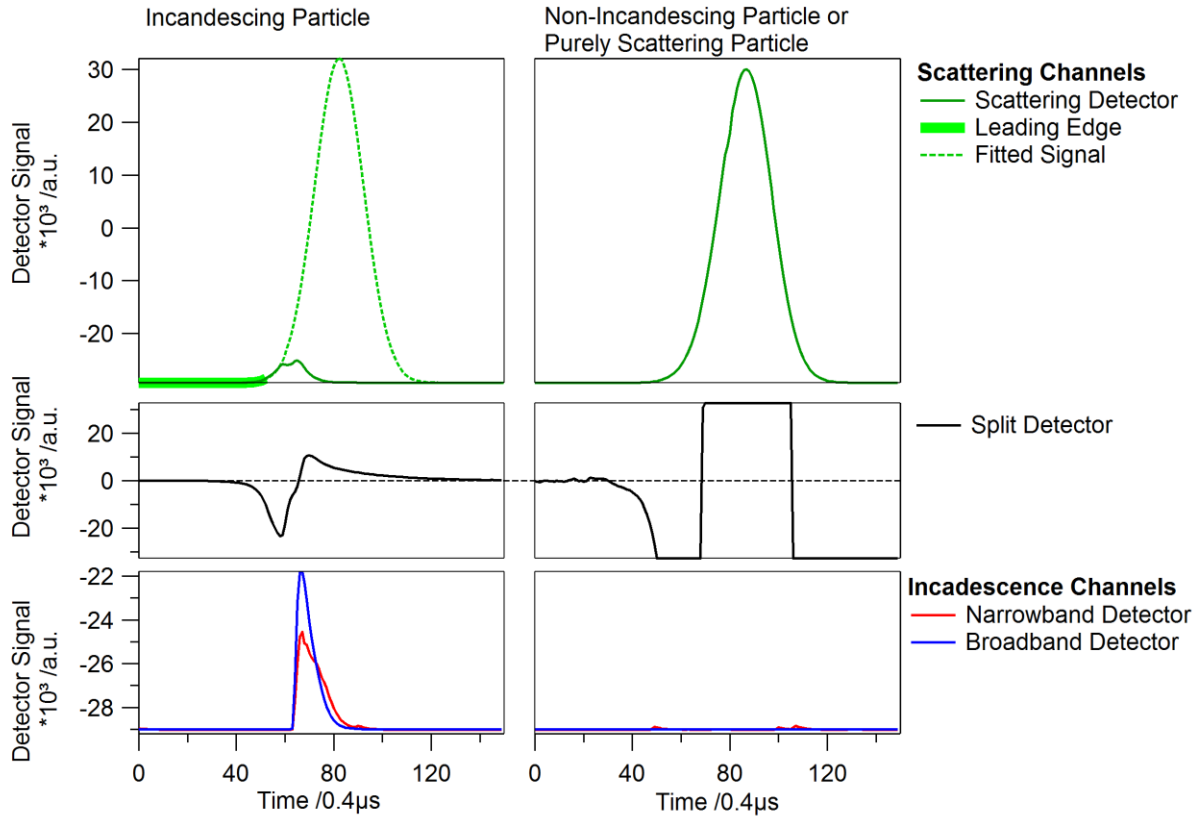
Figure 16: Signals from all four detectors of the SP2 for two different particles of roughly the same scattering cross section, an incandescing particle which evaporates in the laser beam (left) and a purely scattering particle that passes the laser beam unchanged (right). Shown are the high gain channels of the 8-channel SP2, the low gain channel signals show the same signal shape, but with different values. The signals are the scattering signal (green, see text for different line types in left figure), the incandescence signals (blue: broadband, red: narrowband) and the split detector signal (black). The split detector signal is enhanced to properly detect the evaporating rBC particles, which has the side effect that the detector is saturated even for particles well within the scattering detector's detection limit.

As the evaporation temperature of the rBC particles typically measured with the SP2 lies around 4000 K (Schwarz et al., 2006; Moteki and Kondo, 2007; Moteki and Kondo, 2010), the particles emit thermal radiation at wavelengths in the visible range. This visible light is detected by two PMTs with optical filters (KG5) excluding the detection of scattered laser light. One detector, the broadband incandescence detector, samples light in the range of 300-800 nm (shown in blue in Figure 16). The second detector, the narrowband incandescence detector, has an additional optical filter (RG630) to restrict the detected wavelengths to a range of 630-800 nm (shown in red in Figure 16). Using two incandescence detectors that are sensitive on two slightly different wavelength bands makes it possible to determine the color ratio, which can be used as an indicator of the temperature at which the particle evaporates (see also chapter 2.1.2).

The scattering signal of the incandescing particle also follows the Gaussian shape of the laser beam intensity profile, however, only until evaporation starts. Identifying the optical size of the coated rBC particle is not as straight forward as the rBC core mass because the peak of scattering signal is masked by the decrease in signal due to the particle's evaporation. For reconstructing the scattering signal's peak height from the undisturbed signal of the whole particle before the onset of evaporation, Gao et al. (2007) have introduced a method called the Leading Edge Only fit (LEO-fit). It uses the Gaussian shape of the laser beam intensity profile, which is also the scattering signal shape for a non-evaporating particle, to fit a Gaussian function to the undisturbed leading edge of the signal (marked by a thick green line in the left panel of Figure 16). The fitted Gaussian represents the theoretical scattering signal of the whole particle if it would not evaporate in the laser beam. Since a Gaussian function is determined by the four parameters baseline, peak position, width and peak height, the peak height can be determined from, in theory, only one point of the signal if the other three parameters are known. Of these four parameters of the Gaussian function, only the peak height depends on the particle's scattering cross section. The baseline can be determined from the recorded signal before and after the particle is inside the laser beam. The width depends on the laser beam and the particle speed and can be assumed as constant for a particle ensemble containing both evaporating and non-evaporating particles measured at constant pressure within short time. The position of the peak is identified with the help of the position-sensitive split detector (Gao et al., 2007), a four element APD with only two active elements that also detects scattered laser light. The position of the particle in the laser beam has to be measured independently as the recorded 150 points every 0.2 or 0.4 µs (shown on the horizontal axis in Figure 16) are relative to the size-dependent trigger point, where the signal gets larger than the baseline, rather than the particle position relative to the laser beam. The traces shown in Figure 16 were recorded with 50 pre-trigger points.
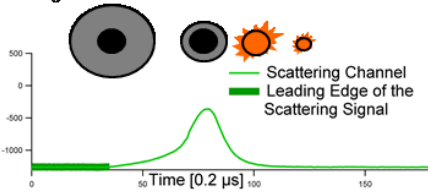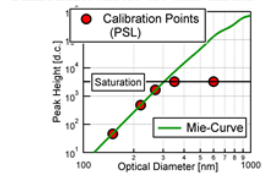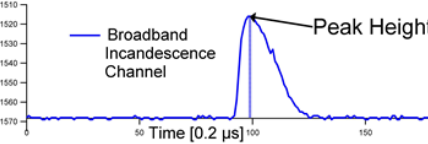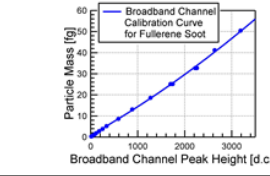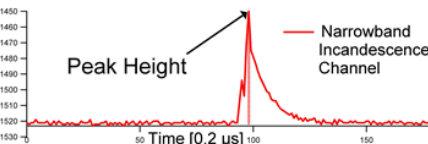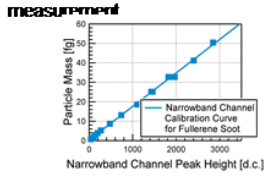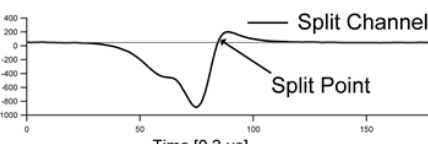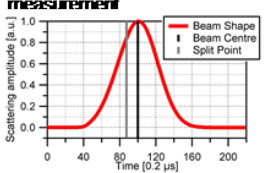
The scattering signal at the center of the laser beam, directly derived from the signal trace or calculated with the LEO-fit, is converted with a look-up table calculated with the Bohren-Huffman Mie code (Bohren and Huffman, 1998) by assuming homogeneous spheres for non-incandescing particles. For incandescing particles, the conversion table for optical size assumes that particles are coated spheres. The coating thickness is then derived from the LEO-fit peak height and the core size, which is the mass equivalent diameter, calculated from the measured incandescence mass assuming a spherical particle with a bulk density of 1800 kg/m³.

While in the first SP2 versions, one signal was tapped from each of the four detectors, the newer versions tap two signals from each detector with one of the two signals amplified by a factor of 10. Table 6 lists the names of the channels and their corresponding abbreviations that are used in text and figures here. The amplified signal is referred to as high gain signal in contrast to the low gain signal, which has no extra amplification. The signals are tapped in turns, reducing the time resolution for each individual channel from 0.2 µs to 0.4 µs. The SP2, as it was used during the DC3 campaign, was the 4-channels

version, i.e. one signal was taken from each detector. In January 2014, the DLR SP2 instrument, originally designed as 4-channel SP2, was upgraded to an 8-channel version. A summary of all the detector signals and the derived parameters is also shown in Table 7.

Table 6: Detection wavelength bands and channel names corresponding to the four detectors in the SP2. Low gain channels are only recorded in the 8-channel SP2.

Detector	Wavelength	Channel (Abbreviation)	Additional Low Gain Channel in 8-Channel SP2
Scattering Detector	> 850 nm	Scattering High Gain Channel (SCHG)	Scattering Low Gain Channel (SCLG)
Broadband Incandescence Detector	300 – 800 nm	Broadband High Gain Incandescence Channel (BBHG)	Broadband Low Gain Incandescence Channel (BBLG)
Narrowband Incandescence Detector	630 – 800 nm	Narrowband High Gain Incandescence Channel (NBHG)	Narrowband Low Gain Incandescence Channel (NBLG)
Split Detector	> 850 nm	Split High Gain Channel (SPHG)	Split Low Gain Channel (SPLG)

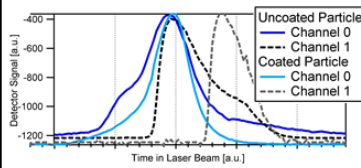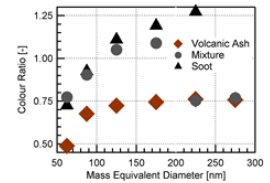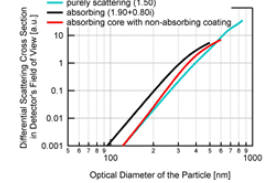| Channel & Time-dependent Signal from Detector	Primary Measured Quantity	Calibration	Assumption	Quantity Derived from a Single Detector (Range of Detection)	What has to be taken care of for good performance
Channel 0 Scattering Detector	Peak Height	•PSL-Calibration for purely scattering particles -> Calibration factor for Mie-tables	•Mie-Data look-up table for several refractive indices of non-absorbing aerosol	•Optical size of purely scattering particles (detection range: about 150–300 nm equivalent to PSL-particles with a refractive index of 1.59+0i)	•Gaussian shape of laser beam •Laser power stable •Baseline below threshold •Noise below trigger level •Calibration with low uncertainty
Channel 1 Broadband Incandescence Detector	Peak Height	•Calibration: particles of known size from DMA •Density from mass measurement	•Assumed particle density for MED	•Mass of refractory black carbon particles (detection range: 0.2 – 55 fg) •Mass Equivalent Diameter (75 – 390 nm for an assumed density of 1800 kg/m³)	•Laser power stable and high enough (Colour Ratio as indicator for sufficient laser intensity) •Baseline below threshold •Noise below trigger level •Calibration with low uncertainty •Gain setting appropriate for measurement objectives •Properties of measured material similar to calibration material •Mass of calibration material known
Channel 2 Narrowband Incandescence Detector	Peak Height	•Calibration: particles of known size from DMA •Density from mass measurement	•Assumed particle density for MED	•Mass of refractory black carbon particles (detection range: 1 – 60 fg) •Mass Equivalent Diameter (100 – 400 nm for an assumed density of 1800 kg/m³)	•Laser Power high enough (Colour Ratio as indicator for sufficient laser intensity) •Calibration with low uncertainty •Gain setting appropriate for measurement objectives •Properties of measured material similar to calibration material •Mass of calibration material known
Channel 3 Split Detector	Zero-crossing Point (Split Point)	•Beam shape from room air measurement	•All particles reach zero-crossing at the same position in the laser beam	•Position of the particle in the laser beam	•Split Point well aligned •Flow stable
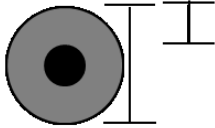
Combination of Detectors	Quantities used	Assumptions	Calculation	Derived Quantity
Scattering and Broadband Incandescence Detector (Channels 0 and 1)	•Position of signal peaks	•Coated particle: Maximum of scattering signal occurs before coating is evaporated, (before maximum of incandescence signal) •Uncoated particle: Maximum of scattering and incandescence signal occur at the same time	•Delay Time = Peak Position from Broadband Incandescence Channel – Peak Position from Scattering Channel	•First guess on mixing state
Broadband and Narrowband Incandescence Detector (Channels 1 and 2)	•Peak heights	•Different materials have different colour ratios	• Colour Ratio = $\dfrac{\text{Broadband Peak Height}}{\text{Narrowband Peak Height}}$	•Material of the incandescent particle
Scattering, Split and Broadband Incandescence Detector (Channels 0, 1 and 3)	•Leading edge of the scatter signal (from Channel 0) •Position of the particle in the laser beam (from Channel 3) • Diameter of the incandescent core (from Channel 1)	•Constant width of laser beam •All particles move with the same speed •First part of scatter signal not influenced by evaporation	•Fit to the leading edge of the scatter signal (LEO-Fit) •Calculation of the optical size with look-up tables for Mie-data of coated spheres and core size from broadband channel	•Optical size of the whole particle •Thickness of the coating •Mixing state of the particle •Volume fraction of refractory black carbon

Table 7: Detector signal of the SP2 and derived particle properties (from Heimerl, 2011).

The method for fitting the leading edge can be extended to other parts of the signal trace, as described by Laborde et al. (2012a), for example to get the optical size of the incandescing core just before the onset of incandescence. Dahlkötter et al. (2014) describe a similar method to derive particle morphology from the scattering trace of coated particles. If in a mixed particle, the rBC core is much smaller than the whole particle and located close to the rim of the coating material, the non-absorbing coating material does not always evaporate before the incandescence of the rBC core, but still scatters light after the rBC core is completely evaporated due to incandescence.

Several studies have been performed to test the performance of the SP2 and the necessary calibration procedures as well as the reproducibility of measurements with different SP2 instruments. Especially the intercomparison of six SP2s which all had a slightly different setup (Laborde et al., 2012b) stresses the need for a good calibration and alignment of the instrument to achieve reliable and comparable results. Laborde et al. (2012b) also show that different SP2s can have slightly different detection efficiencies at the lower end of the detection range, which have to be known in order to compare concentrations measured by different SP2s. The lower limit of the detection range can differ up to 40 nm and even more for instruments that are not aligned well.

Schwarz et al. (2010a) discuss in their study several ways to characterize and optimize the detection efficiency of the SP2. They show that the incandescence channel peak height of an rBC particle is independent of laser intensity as long as the intensity lies above a threshold required for sufficient heating and incandescence. A similar evaluation of sufficient laser intensity is done regularly for the DLR SP2, which will be addressed in section 3.2.2. The recommended steps for calibration are listed in Table 8.

While the data from the DC3 campaign are the main focus of this work, the following sections on calibration include also data from other campaigns and laboratory tests to illustrate the stability and drift of calibrations over time and between different instrument setups. A list of all the calibration data sets can be found in the appendix (Table A 1, page 178). Calibrations before January 2014 were performed with the 4-channel SP2, those after this point with the upgraded 8-channel version.

Table 8: Recommended steps for SP2 calibration, which measurement parameter they influence and where they are described in detail here.

Calibration Step	Influenced Measurement Parameter	Chapter
Laser Alignment	Detection Efficiency; Coating Thickness	3.2.1.1 Alignment of Laser and Sample Flow Jet
Laser Intensity	Detection Efficiency; Detection Limits	3.2.2 Calibration and Detection Limits of the Incandescence Channels
Laminar Flow Element	Particle Concentration	3.2.1.2 Calibration of the Linear Flow Element
Sample Flow Jet Alignment	Detection Efficiency; Optical Size; Coating Thickness	3.2.1.1 Alignment of Laser and Sample Flow Jet
Split Detector Alignment	Optical Size; Coating Thickness	3.2.1.3 Split Detector Alignment
Incandescence Channels	rBC Mass Concentration; rBC Mass Size Distribution	3.2.2 Calibration and Detection Limits of the Incandescence Channels
Counting Efficiency	Detection Limits	3.2.2 Calibration and Detection Limits of the Incandescence Channels
Scattering Channels	Optical Size	3.2.3 Calibration and Detection Limits of the Scattering Channels

For the alignment procedures and calibrations described in the following sections, standard particles were used as reference. For optical particle detection, polystyrene latex spheres (PSL) of different standard sizes were used. PSL are commercially available as suspensions of monodisperse particles with a very narrow size distribution and well-known optical properties. The most commonly used PSL standard here, 200 nm, has a standard deviation in size of 2 nm, according to the NIST (National Institute of Standards and Technology) certificate supplied with the bottled particles. Incandescence detection calibration was performed with fullerene soot particles. Fullerene soot is a black carbon material with

known density and the recommended calibration material for the SP2 (Moteki and Kondo, 2010). The standard particle sample was dissolved in distilled water and nebulized. As the fullerene soot sample is polydisperse, it has to be size-selected for calibration. Details and the specific setup for each type of alignment or calibration listed in Table 8 are shortly described in the corresponding section.

3.2.1.1 Alignment of Laser and Sample Flow Jet

The laser beam is reflected on both sides of the measurement chamber, on the surface of the Nd:YAG crystal and on the output coupler on the opposing side of measurement chamber (Figure 15). To ensure that the laser beam is in a Gaussian shape, as it is needed for the SP2 measurements, the output coupler can be adjusted. The adjustment is monitored with an infrared camera, called beam camera, which replaces the laser power monitor (left of output coupler in Figure 15) during the alignment procedure. A well aligned laser shows as a circular shape with symmetrical Gaussian intensity distribution in the beam camera. Example images are shown in Figure 17 (left). The Gaussian shape of the laser beam is a crucial parameter for determining the optical size of incandescing particles.
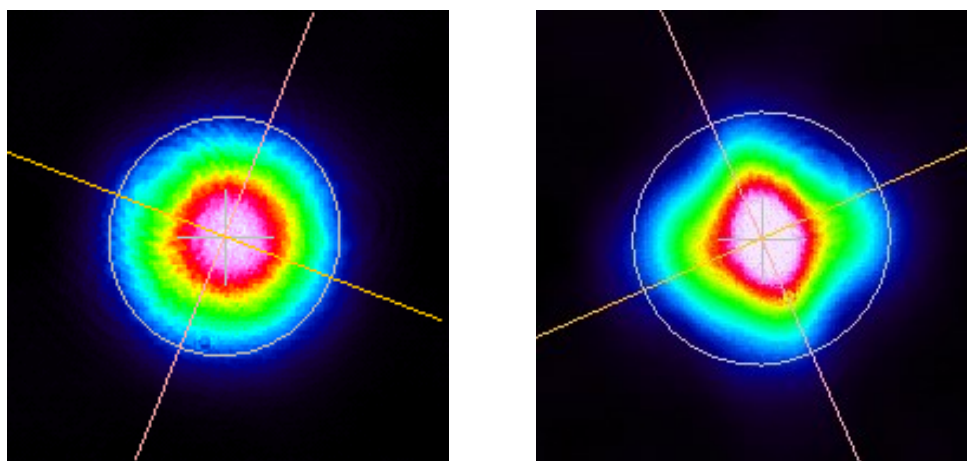

Figure 17: Images of the SP2's laser, taken with the beam camera, as examples for a good (left, June 21, 2012) and a bad (right, April 28, 2014) alignment.

To ensure that the sample flow passes the laser beam exactly in the middle, where the highest laser intensity is found, the sample flow jet has to be aligned properly. The sample flow nozzle is fixed to the top of the measurement chamber, which is mounted movable on rails (Figure 15, middle). For alignment, the measurement chamber is moved forward and backward while sampling PSL particles of known size so that the sample flow crosses the fixed laser in different positions. The signals of these PSL particles are recorded and the optimum chamber position is determined by finding the chamber position with the maximum signal, which is the position where the sample flow jet crosses the laser beam at its maximum.
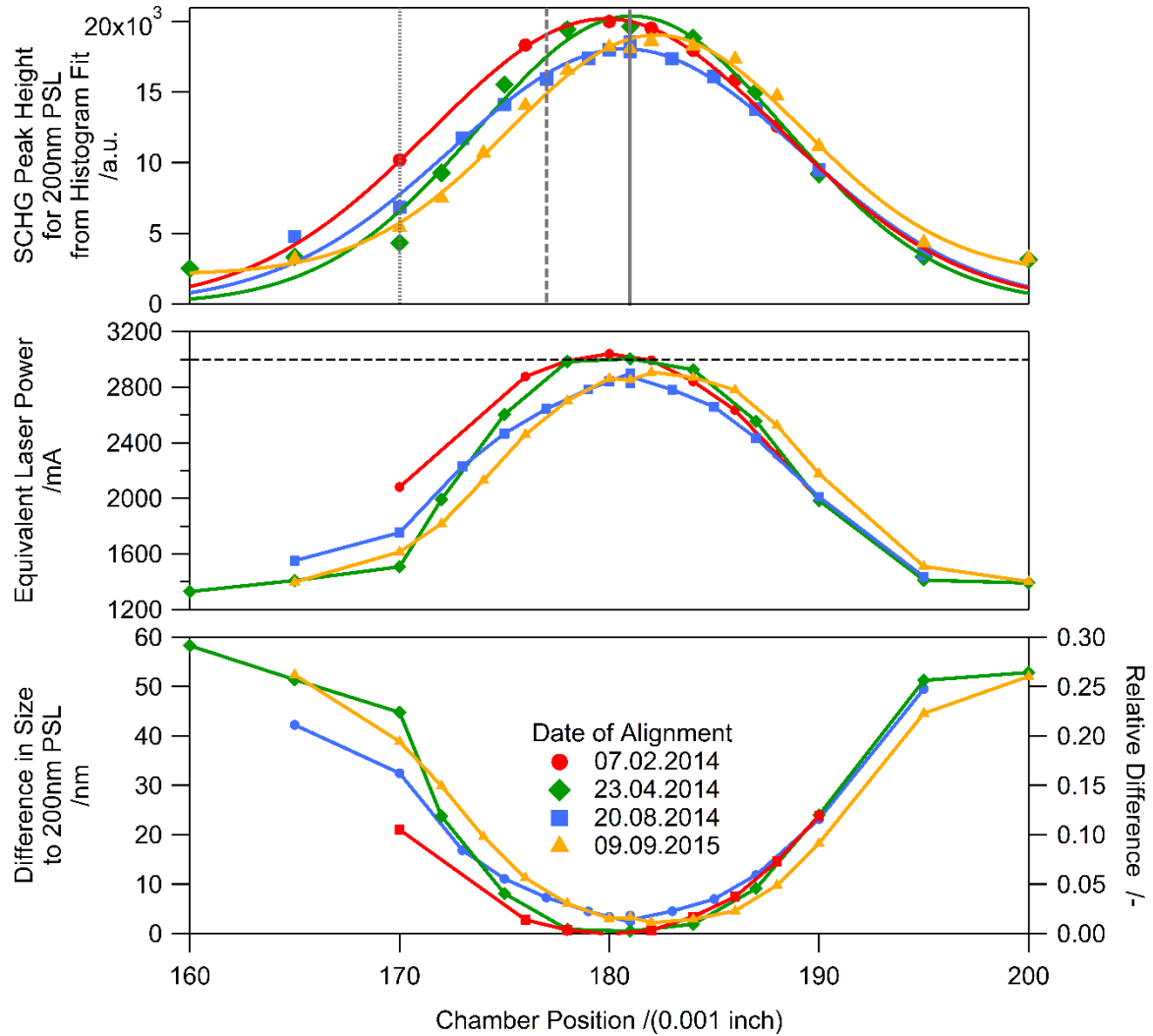
Figure 18: Measurements of 200 nm PSL particles at different position in the laser beam. Top: peak height of 200 nm PSL particles, the vertical grey lines refer to Figure 19; Middle: equivalent laser intensity calculated from PSL measurements at different laser current settings, the grey horizontal dashed line marks the actual laser current value; Bottom: absolute and relative difference between the nominal 200 nm PSL particle size and the optical diameter calculated from the scattering signal peak height.

The top part of Figure 18 shows the results of four different alignment procedures that were necessary after adjusting the output coupler to get a circular laser shape. For the four dates shown, the optimal chamber positions were 0.180" (07.02.2014), 0.181" (23.04.2014 and 20.08.2014) and 0.182" (09.09.2014), indicating a slight drift in laser position. If this drift was not be compensated for by adjusting the chamber position accordingly, in September 2015, the laser intensity at the 0.180" position (February 2014 alignment) would be about 2% lower than at the actual center, the 0.182" position. This also applies to the optical size, if the drift is not accounted for by regular calibration.

The PSL sizes at the different positions in the laser beam were calculated by applying the calibration factor derived for the center position for each date. Details on the calculation of the scattering channel calibration factor can be found in section 3.2.3.

The middle panel of Figure 18 shows the equivalent laser power, a proxy for the laser intensity at the corresponding position of the sample flow jet in the laser beam, To obtain the equivalent laser power, the linear relationship between scattering signal peak heights of 200 nm PSL particles and laser power settings was calculated from an independent measurement. The equivalent laser power at different positions in the laser beam is then the laser power setting that would result in the same scattering peak height in the center of the laser beam for 200 nm particles as the laser power setting of 2800 mV at the corresponding chamber position.

Another important point to note is the increase in variability of measured peak heights with increasing distance from the beam center. Figure 19 shows number size distributions, normalized by the total concentration, for 200 nm PSL particles at three different positions in the laser beam, marked by dashed vertical lines in the top panel of Figure 18. The measurements were made during the alignment on August 20, 2014 with the beam center being at 0.181". The measurements made with the sample flow jet positioned at the center of the laser beam are marked by "Center" and drawn as a continuous line in Figure 19. For comparison, two PSL number size distributions measured at positions more distant from the beam center are added. Long dashes refer to a position close to the center of the laser beam (0.177"); short dashes indicate a position on the flank (0.170") of the laser intensity profile in Figure 18.
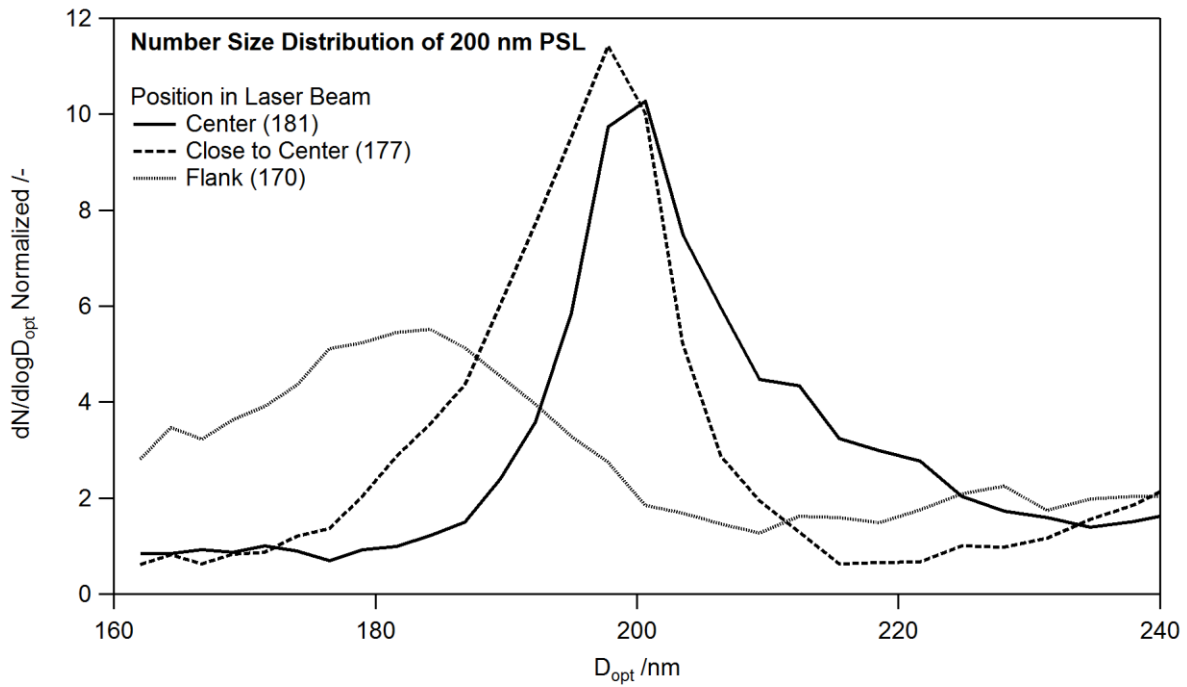
Figure 19: Normalized number size distributions for samples of 200 nm PSL particles measured during chamber alignment on August 20, 2014. The different positions of the sample flow with respect to the laser beam shape are listed in the legend and are marked in the top panel of Figure 18 by vertical grey bars with the same dash type. The number size distributions were normalized by the total number concentration.

The width of the size distribution increases rapidly if the position of the sample flow jet is not exactly in the middle of the laser beam, as Figure 19 shows. This leads to a higher uncertainty of the optical particle size. As the intensity decreases, the peak height and so the calculated optical size of particles decrease with increasing distance from the middle. Due to the lower laser intensity at the edge of the laser, a misalignment of the sample flow jet can also compromise the counting efficiency of the SP2 (see also section 3.2.2).

As the position of the laser beam center relative to the measurement chamber can change slightly when the output coupler is readjusted or, even more, when the whole laser is realigned, it is important to also realign the measurement chamber with the sample flow jet to reduce the possible measurement uncertainties and errors resulting from a misaligned sample flow jet.

3.2.1.2 Calibration of the Linear Flow Element

The linear flow element is situated in the SP2's inlet to measure the sample flow before it enters the measurement chamber. The measured flow is directly used to derive the particle number and mass

concentration. Therefore, the calibration of the laminar flow element is crucial for a reliable calculation of the measured concentrations. To check the calibration, it is usually sufficient to measure the sample flow at several settings with a flow meter.

The recorded flow is calculated from the measured voltage as a linear relation with the parameters set in the SP2 software's configuration file. Figure 20 shows the measurement points from two calibrations (markers) with their linear fits (line) and lists the calibration parameters for each linear fit in the legend.
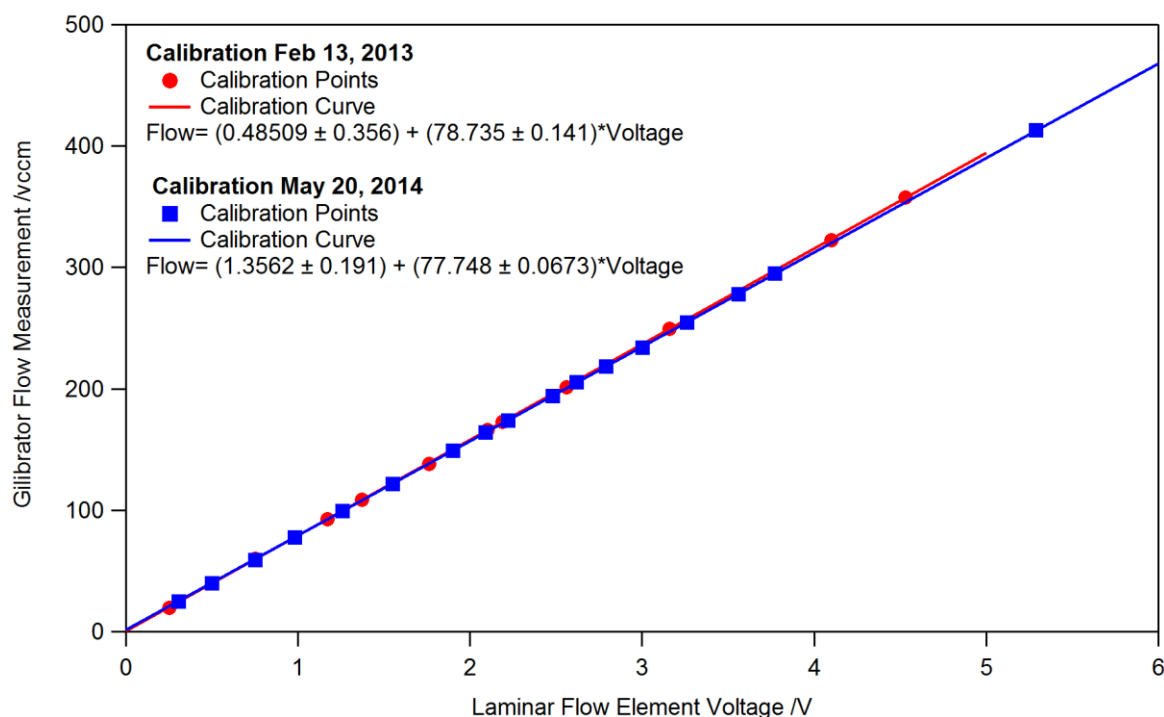

Figure 20: Calibration curves for the linear flow element for two calibrations on May 20 2013 (blue) and February 14 2014 (red) with the measured calibration points and the parameters of the linear fit.

The calibration of the linear flow element is similar for the calibrations on May 20, 2013 (blue) and February 14, 2014 (red), with a deviation of less than 1% at a flow setting of 120 cm³/min, the flow set point mainly used for this SP2.

The sample flow is kept stable by adjusting a valve controlling the exhaust flow. In the laboratory at stable conditions, the variations of the sample flow are below 0.8 % for a measurement interval of 5 minutes at a sample flow settings above 80 cm³/min, decreasing with increasing sample flow. This deviation is larger when measuring in the plane as sudden changes in pressure, like starting, landing or changing from ascent or descent into a constant altitude flight level, induce flow variations. These flow variations are in the range of 10% of the total flow while variations on constant flight levels are about 1% of total flow. For the calculation of number and mass concentrations, the measured flow in the instrument is used to reduce biases from flow variations. For time series, data are shown as 10 s values

to smooth out most of the fluctuations. This is also the averaging time interval used for time series stored in the DC3 data base.

3.2.1.3 Split Detector Alignment

The position-sensitive split detector measures scattered light to provide a reference point relative to the particle's position in the laser beam. When a particle enters the laser beam from the top, the scattered light is projected through a lens onto the lower sector (see Figure 21). As the particle moves through the laser beam, the signal moves from the lower to the upper segment. When the particle signal is projected onto the part of the detector, which is not assigned to one of the segments, the detector sees less light, visible as a dip in the signal shown as second from right in the lower part of Figure 21. To identify this point more clearly, the signal from the lower segment is inverted electronically before adding the signals from the single segments, so the split point can be identified as the zero crossing point in the split detector signal (see the split detector signal traces in Figure 16 and Figure 21).

The quality and detection limit of the split point is determined by the relative position of the split point in the laser beam. To capture incandescing particles that evaporate very early, the split point must be very early in the laser beam, but close enough to the center so that the first part, the negative signal peak, is large enough even for small particles to rise above the baseline noise. Since the split point is an essential parameter in deriving the optical size of incandescing particles, the alignment of the split detector is crucial for the SP2's potential to measure rBC particle coating thickness.
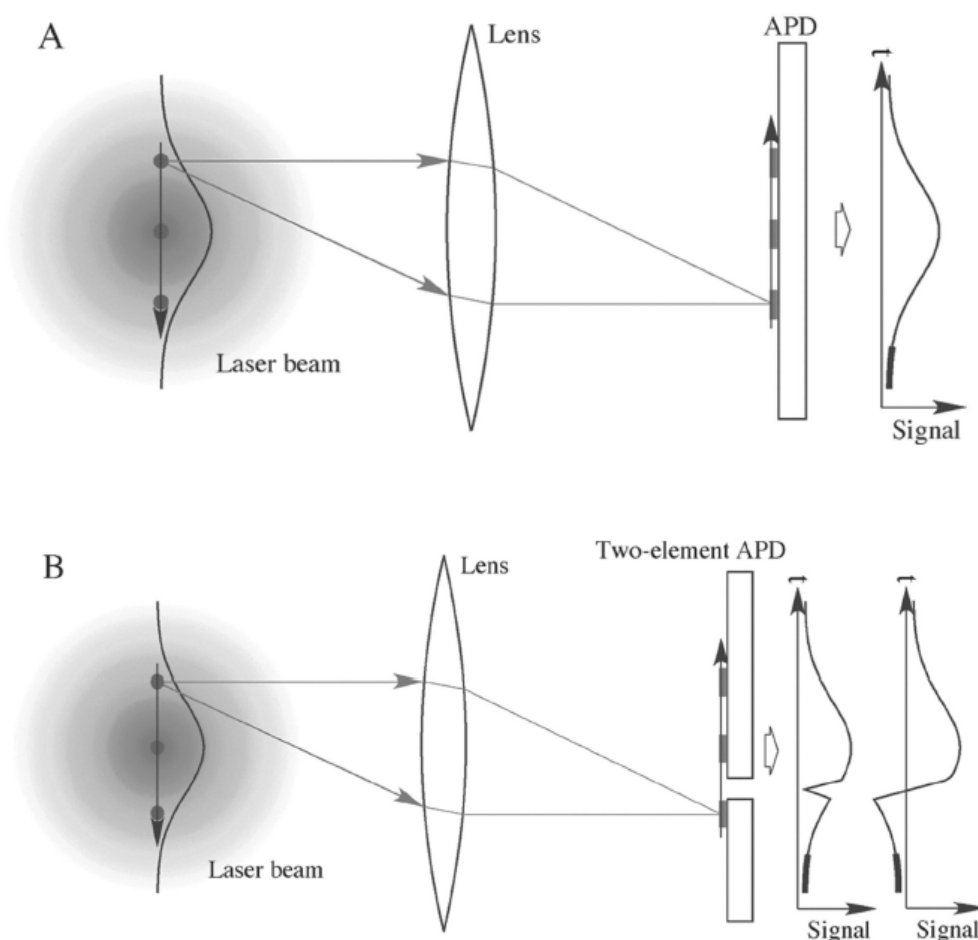
Figure 21: Sketch of a non-incandescing particle crossing the SP2's laser beam (left) and producing the scattering (top, A) and the split detector (bottom, B) signal (adopted from Gao et al., 2007; reprinted by permission of The American Association for Aerosol Research, www.aaar.org). The two-element APD mentioned in the description corresponds to the four-element APD with only two active sectors.

According to the schematic drawing in Figure 21, the split detector signal should have one positive and one negative peak, with one zero crossing in between. This was the case for the original split detector in the 4-channel instrument, which failed in September 2011. It was then replaced by a different version of the 4-element APD. The new detector, however, has an "overshooting" effect. It gives an output signal even after the particle has evaporated or left the laser beam. Depending on the positioning of the split detector, the signal exhibits then two or three peaks. The example trace for a non-evaporating particle at the beginning of this chapter (Figure 16, right) and the beam shape example here (Figure 22, bottom panels) illustrate this behavior. The split detector signal does not return to the baseline together with the scattering signal, but remains negative for a longer time. If the split point falls together with the decline

in the scattering signal due to evaporation of incandescing particles, the overshooting signal will produce an artificial split point at this position instead of the correct one slightly later.
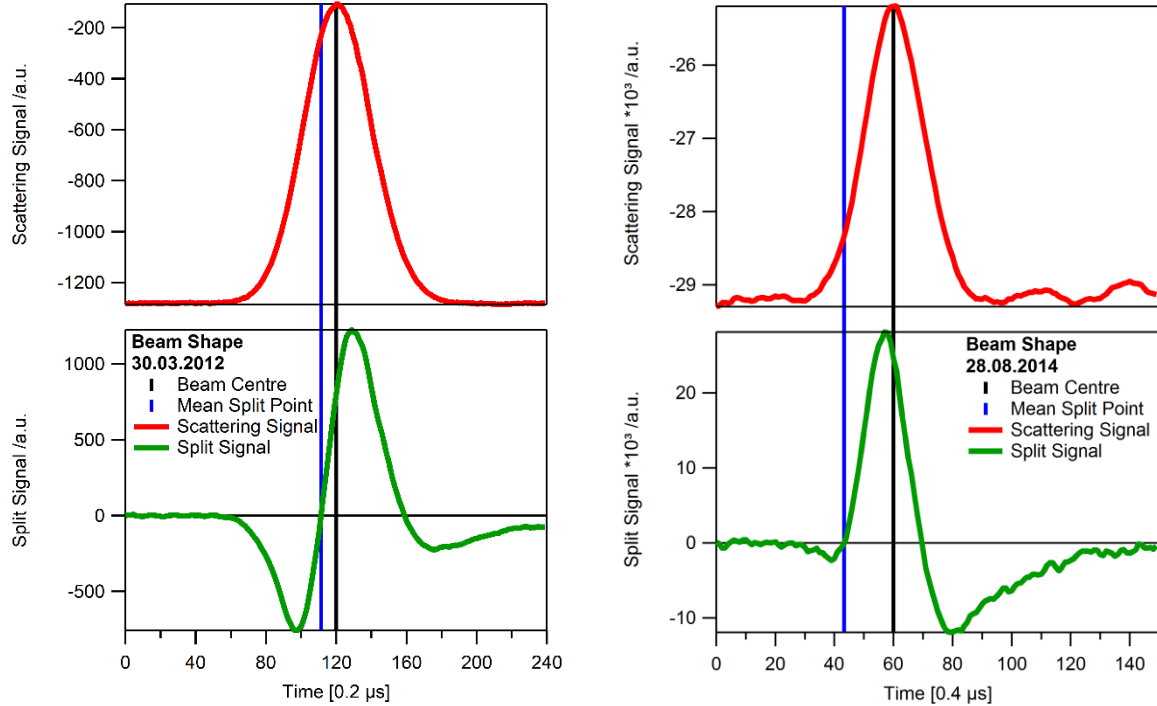

Figure 22: Beam shape (red) with beam center (black line) and split point (blue line) for the DC3 setup (left) and the setup in August 2014 (right). Corresponding split detector signals are shown in green. Both example particles are non-incandescing.

The location of the split point relative to the beam center can be changed by moving the detector in its fitting vertically. The fitting is equipped with two screws to adjust the detector's position. As it was not possible to get the detector in the desired position by adjusting these screws only, the split detector mounted in this specific SP2 has additional tape at the bottom since August 2014. Trying to align the new split detector in the same way as the original one, so that the signal shows only one zero crossing with one negative and one positive peak, gives a split position very close to the center of the laser beam (Figure 22, left). This alignment was done during the preparation for the DC3 campaign, when the new detector was aligned with the same procedures as the original one. The post-campaign data analysis then showed that the positioning of the new split detector's split point had to be done differently than for the old one. The new split detector produced a third, artificial peak that was not present in the old version, which led to a second, erroneous split point. This chapter compares the split detector alignment as it was during the DC3 campaign according to the alignment procedures for the old 4-channel split detector (pre-campaign alignment on March 30, 2012), with a later alignment (August 28, 2014). The shown

ambient air samples were in both cases measured in a laboratory facing a parking lot close to the Oberpfaffenhofen airport, so they contain mainly small rBC particles with little coating.

The signal traces from the March 30, 2012 alignment (Figure 22, left) show that the split detector signal has the two-peak structure as it was desired to minimize problems of the data evaluation software to correctly identify the split point. The right part of Figure 22 shows the three-peak structure of the split detector signal. Due to the very small first peak, the split point is often not determined correctly for smaller incandescing particles.

To aid with the alignment procedure, DMT provides a software, the split detector alignment tool (SPAT). The SPAT software derives four check plots correlating parameters of single particle signal traces for non-incandescing particles immediately from raw data on the SP2's data acquisition computer. Two of the SPAT plots focus on the correct determination of the fixed parameters for the LEO-fit, the width of the Gaussian and the center position. The correlation plot and the frequency distribution histogram are here combined into one plot for each of the alignments (Figure 23 for the May 2012 alignment and Figure 24 for the August 2014 alignment). As both parameters are assumed to be constant for all particles when applying the LEO-fit, both parameters, the full width at half maximum (FWHM) of the scattering signal (top, green) and the distance between center and split point (right, black) should vary as little as possible, and show very narrow distributions. The correlation between the two parameters (center, blue) varies around the average (red dot), which is used for the fit. Both signal width and split-to-center-distance depend actually on the residence time of the particle in the laser beam, and are affected by slight variations in the sample flow (see previous subchapter 3.2.1.2). The FWHM is also influenced by how close to the center the particle actually passes the beam, which also varies due to the non-zero diameter of the sample flow air stream.

_____
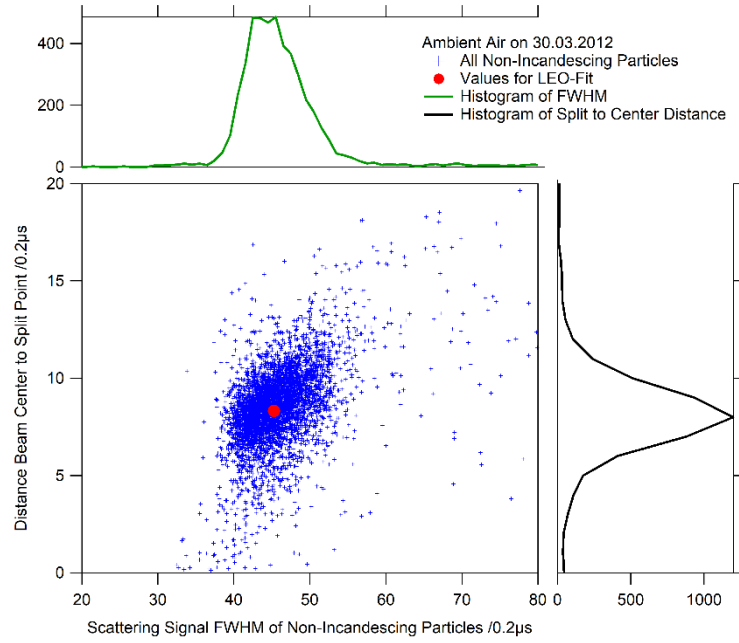
Figure 23: Comparison of the full width at half maximum of the scattering signal trace and the distance between split point and beam center for non-incandescing particles for the DC3 setup. The histograms at the top and at the left correspond to the distributions of the two correlated parameters.

Figure 24: Same as Figure 23, but for the August 2014 setup and alignment. LG indicates parameters derived from the low gain channels of the 8-channel SP2.

The two other SPAT plots are correlations between the split signal peak heights and the scattering peak height for non-incandescing particles to verify the stability and reliability of the split detector signal.

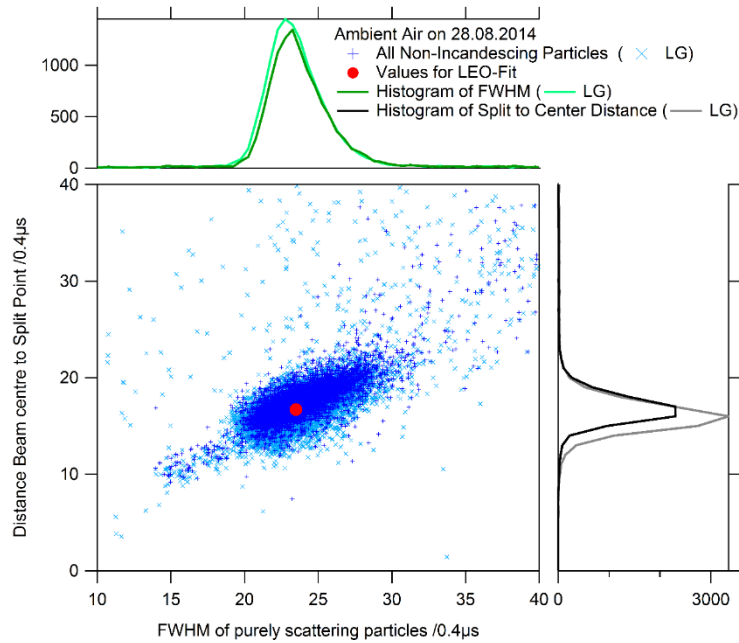The correlation between the scattering signal peak height and the peak height of the first, negative, peak of the split detector signal is shown in the appendix (Figure A 1, page 180) for both alignment cases. The SPAT software also compares the first and second peak of the split detector signal of non-incandescing particles, which is not shown here. If these signal peak correlation scatterplots do not show a clear correlation, the split detector alignment should be redone.
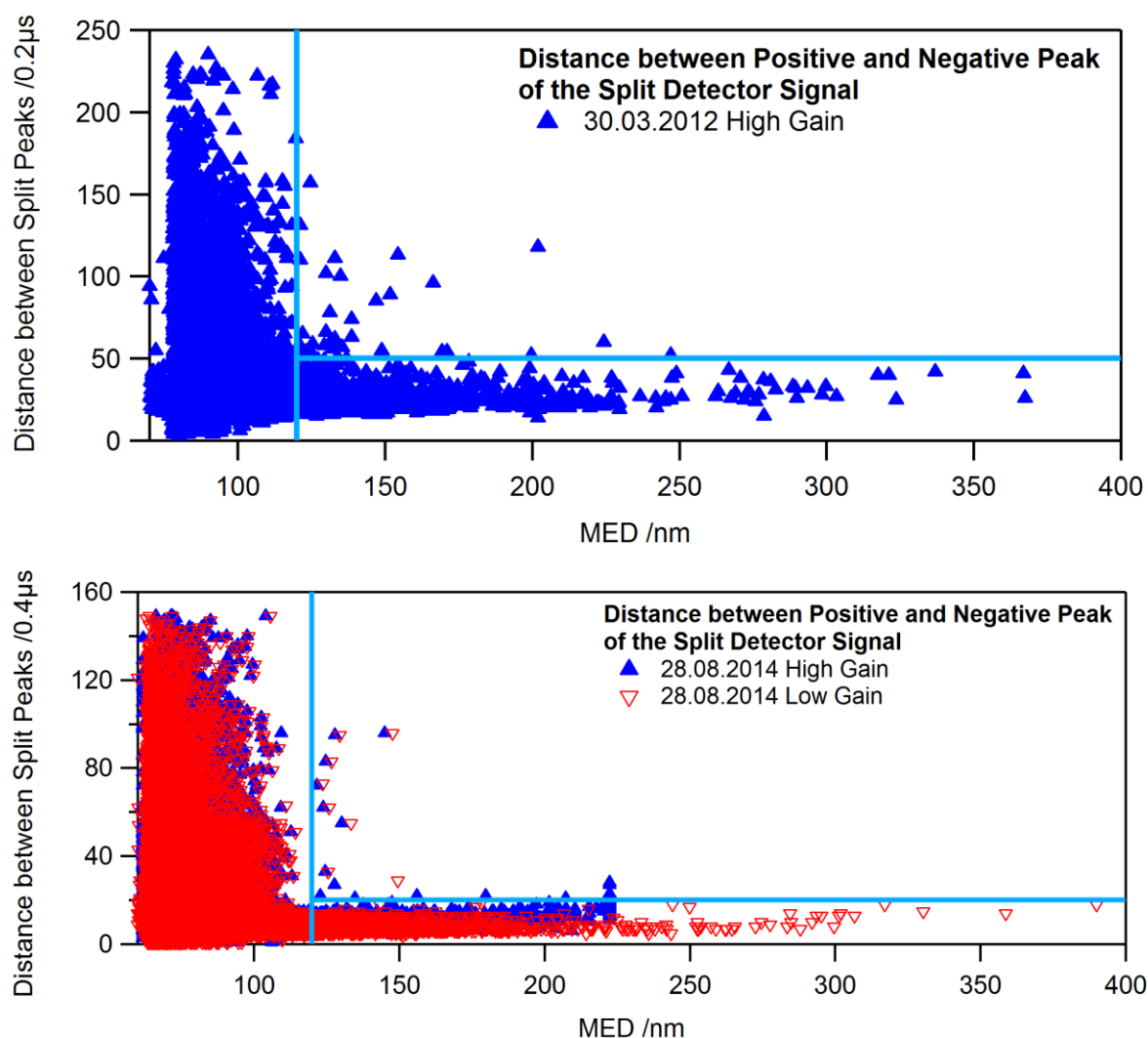
Figure 25: Identification of the lower incandescence size limit for valid split point determination. Top: Ambient air sample measured during DC3 preparation. Bottom: Ambient air sample measured with the August 2014 alignment. Light blue lines mark the upper limit for particle size (vertical line) and distance between split peaks for reasonable split detector signals (horizontal line).

Besides the SPAT plots, some more tests can be useful when evaluating the split detector performance. To identify the lower threshold for rBC particles, for which the LEO-fit is possible, the distance between the first positive and the first negative peak of the split detector signal is shown for the mass equivalent

_____

diameter that is derived from the incandescence channels (Figure 25). The distance between split peaks is used here as a proxy for how reliable the data evaluation software can distinguish the peaks in the split detector signal from signal baseline noise. For particles larger than 120 nm mass equivalent diameter, this time distance is in a narrow range below 10 µs. Smaller particles do not scatter enough light to produce a signal that can be distinguished reliably from noise by the data evaluation software.
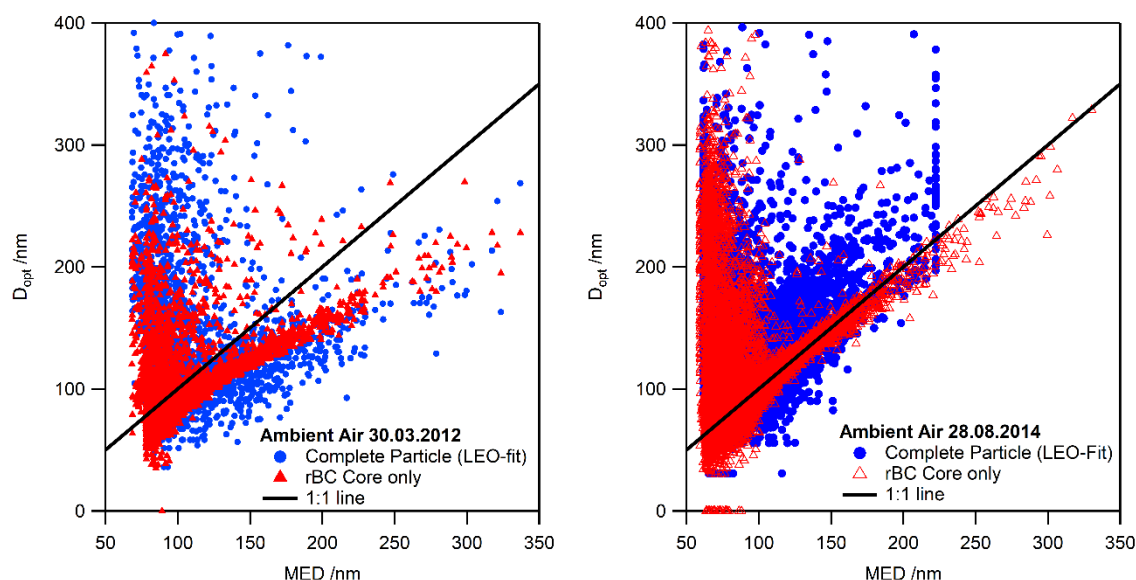

Figure 26: Comparison of incandescing size and optical size to evaluate the reliability of the LEO-fit and the calculation of the optical size of the rBC core. Left: Ambient air sample during DC3 preparation. Right: Ambient air sample during ACRIDICON preparation (high gain channels only).

Figure 26 shows a direct comparison of the sizes for individual incandescing particles of the ambient samples derived from the incandescence detector and the LEO-fit. In addition to the LEO-fitted size of the complete particles (blue), the optical size of the incandescing core (red) is shown. While the particles larger than about 120 nm group along the 1:1 line (black) in case of the August 2014 alignment (right), in case of the May 2012 alignment (left) the optical size of the particles is systematically underestimated. The LEO-fitted scattering peak height was converted into an optical diameter (D_{opt}) by assuming a refractive index of $1.9 + 0.8i$ in both cases. Using a refractive index with a lower real part would result in larger optical diameters for the same LEO-fitted peak height, and mask the underestimation of optical particle size for the May 2012 alignment. The optical particle size of the core shows a smaller spread while the LEO-fitted particle size shows a large spread towards bigger sizes since this size includes coatings on the particles. The effect of the coating is small in this case as both samples contain mainly fresh black carbon particles with little coating. The spread would be larger for samples of aged and heavily coated black carbon particles.
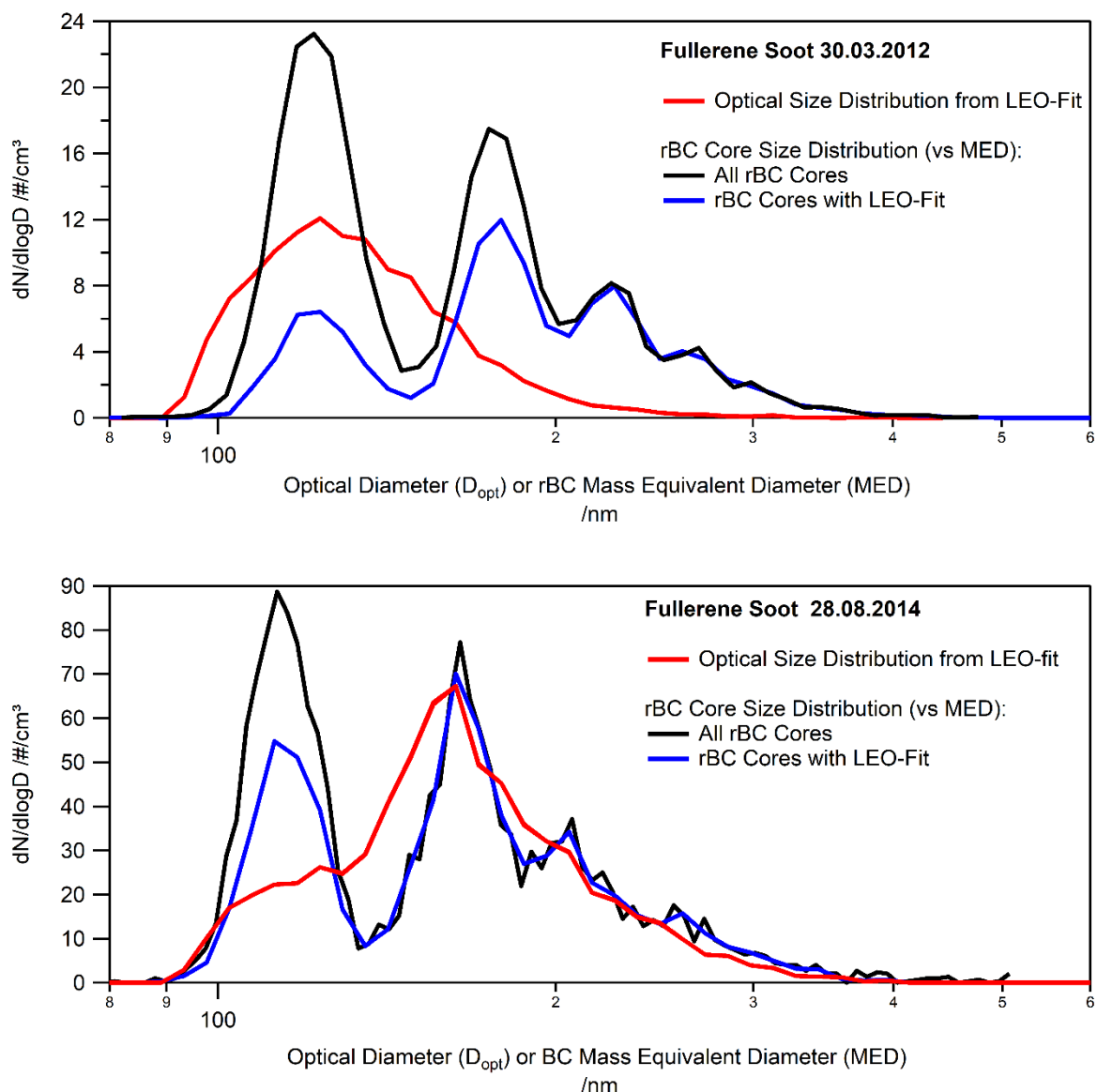
Figure 27: Number size distribution of fullerene soot samples with 1.35 fg or 150 nm mobility diameter for the May 2012 (top) and the August 2014 alignment (bottom) derived from the incandescence channel (black) and the LEO-fit (red). The number size distribution derived from the incandescence channel for the particles with LEO-fit only is drawn in blue.

To evaluate whether the refractive index was chosen appropriately, resulting number size distribution for samples of size-selected fullerene soot are shown in Figure 27 for the DC3 alignment (left) and the ACRIDICON alignment (right). The number size distribution derived from the broadband incandescence channel measurements (black) shows the typical peaks representing particles with one, two or three charges after size-selecting particles with a DMA. Note that the peaks of the size distribution do not appear at the mobility diameter of 150 nm, since the DMA size-selects it, but at the slightly lower

mass equivalent diameter (MED) of 113 nm, calculated from the measured particle mass, 1.35 fg. For all particles for which a LEO-fit was made, the number size distribution from the broadband incandescence channel is shown in blue. The increasing difference between the blue and the black size distribution towards smaller sizes represents the decreasing detection efficiency of the scattering and the split detector for smaller particles.

The rBC number size distribution derived from the incandescence channel measurements are shown in black in Figure 27 for the May 2012 (top) and the August 2014 (bottom) alignment. The number size distribution plotted in red is derived from the particle sizes acquired from the LEO-fit. The LEO-fit number size distribution (red) for the 150 nm particles for the DC3 alignment (top) peaks at 150 nm, but it has no similarities with the number size distribution derived from the same particles' mass equivalent diameter, shown in blue. For the August 2014 alignment in the bottom panel, the lower detection limit for the scattering and split detector is at smaller sizes, as already shown in , so the difference between the number size distributions derived from the incandescence channels for all particles (black) and for particles with LEO-fit (blue) is smaller. The shape of the LEO-fit number size distribution follows roughly the shape of the incandescence channel number size distribution for particles above about 150 nm.

This underestimation of particle size of the May 2012 sample is an effect of a misalignment of the split detector due to the artificial third peak in the split detector signal. While this poses no problem for non-evaporating particles that show a signal throughout the whole laser beam, incandescing particles evaporate and their real optical signal fades away with them. If the particle evaporates very close to or past the split point, the second peak is not produced by laser light scattered onto the detector by the particle but by the electronical overshooting of the signal. The resulting split point in this case is at an earlier point in the laser beam than the real split point would be. The leading edge of the scattering signal and the center of the laser beam, both derived from non-incandescing particles, are then placed too early in time. Instead of the actual leading edge, the LEO-fit is fitted on an earlier part of the signal which is smaller than the actual leading edge, resulting in the underestimation of the fitted signal peak and therewith the optical particle size.

3.2.2 Calibration and Detection Limits of the Incandescence Channels

As described before, the mass of an individual black carbon particle is related to the emitted light of the incandescing particle. This emitted light is gathered onto the PMTs and converted into an electrical signal. The approximately linear relationship between a particle's mass and the detector signal is determined by calibration. For calibrating the SP2's incandescence channels, a size-selected refractory black carbon material standard is fed into the instrument. For several different particle sizes, signal peaks are recorded and related to the particle mass to obtain the final calibration curve.

A variety of materials has been discussed as standard material for calibration, mainly Aquadag, which was originally recommended by the manufacturer DMT, and fullerene soot. Several studies investigated the SP2's sensitivity to different calibration standard particles and ambient, thermally denuded aerosol (Moteki and Kondo, 2010; Laborde et al., 2012a; Laborde et al., 2012b).

Laborde et al. (2012a) have found that the most representative calibration material is thermally denuded diesel exhaust which is then mass-selected by an aerosol particle mass analyzer. Since the latter is not often available for calibration, a differential mobility analyzer (DMA) is used instead to select particles by mobility diameter (Reischl, 1991). In that case, fullerene soot is the standard material that resembles ambient rBC best (e.g. Baumgardner et al., 2012). Fullerene soot contains fractal aggregates of black carbon spherules, similar to fractal aggregates of combustion-produced rBC found in the atmosphere. Following these recommendation, fullerene soot is used as calibration material here. The dry fullerene soot powder is mixed with distilled water and nebulized in a nebulizer (DMT AG-100) to produce the air sample, which is then size-selected. Due to the limited solubility of fullerene soot in water, the mixture of fullerene soot and distilled water was treated in an ultrasonic bath prior to being nebulized. To reduce artefacts from water coating on the particles, the sample was dried before size selection.

The two mainly used instruments for size selecting the fullerene soot particles for SP2 calibration are a particle mass analyzer to size-select particles by mass, and a differential mobility analyzer (DMA), to size-select particles by aerodynamic diameter. Since a particle mass analyzer is not available at the DLR, particles were size-selected by a DMA, which makes it necessary to know the relationship between particle mass and aerodynamic diameter. This relationship is not constant, but a size-dependent effective density which also varies slightly between different production lots of the fullerene soot (Gysel et al., 2011). Gysel et al. (2011) describe in detail the decrease of effective density with particle size for both Aquadag and fullerene soot, of which only the latter is used here. The size-dependent effective density of the fullerene soot sample used at DLR for SP2 calibration is slightly different from the one reported by Gysel et al. (2011). This curve was measured in 2011 and is described in detail in Heimerl (2011). The calibrations reported here were all performed with the DLR fullerene soot standard with the exception of the calibration done on June 5, 2012, during the DC3 campaign. For this calibration, NOAA's fullerene soot standard was used and its specific density was applied for evaluating the calibration curve (Markovic, 2012, pers. comm.). Due to the varying density of black carbon, and since the SP2 measures single particle mass, the particle size is given here as the mass equivalent diameter unless stated otherwise. The mass equivalent diameter is derived from the measured particle mass by assuming spherical particles with a density of 1.8 g/cm³, a value which is also used in other studies as it represents well the density of different black carbon types (Moteki and Kondo, 2010; Laborde et al., 2012b). This represents the bulk density of the calibration material, fullerene soot, which is

1.718 ± 0.004 g/cm³ (Kondo et al., 2011b). It does not account for the fractal structure some rBC particles in the atmosphere have, but it gives an impression of particle size.

For each calibration point, data from one size-selected fullerene soot sample are recorded to get the peaks of the incandescence channels for all particles. The measured signal peaks are binned into histograms. Since the DMA sorts by the mobility diameter to charge ratio, the incandescence peak heights histogram exhibits several peaks as heavier multiply charged particles are recorded as well. An example histogram is shown in Figure 28.

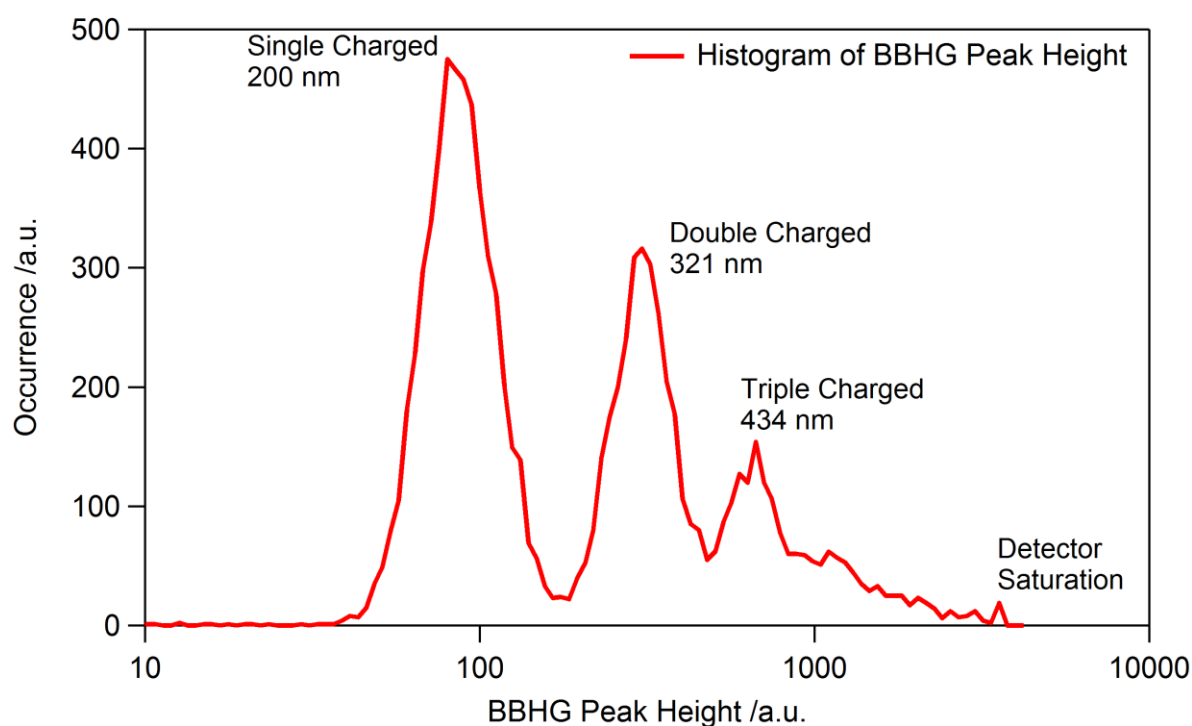*Figure 28: Example histogram for the BBHG peak height distribution of a fullerene soot sample size-selected by a DMA set to 200 nm.*

The single charged mass histogram peaks are correlated with the particle mass as shown in Figure 29 for the broadband channel for the calibration curve used to evaluate the DC3 data set. The corresponding calibration curve for the narrowband channel is shown in Figure 30.
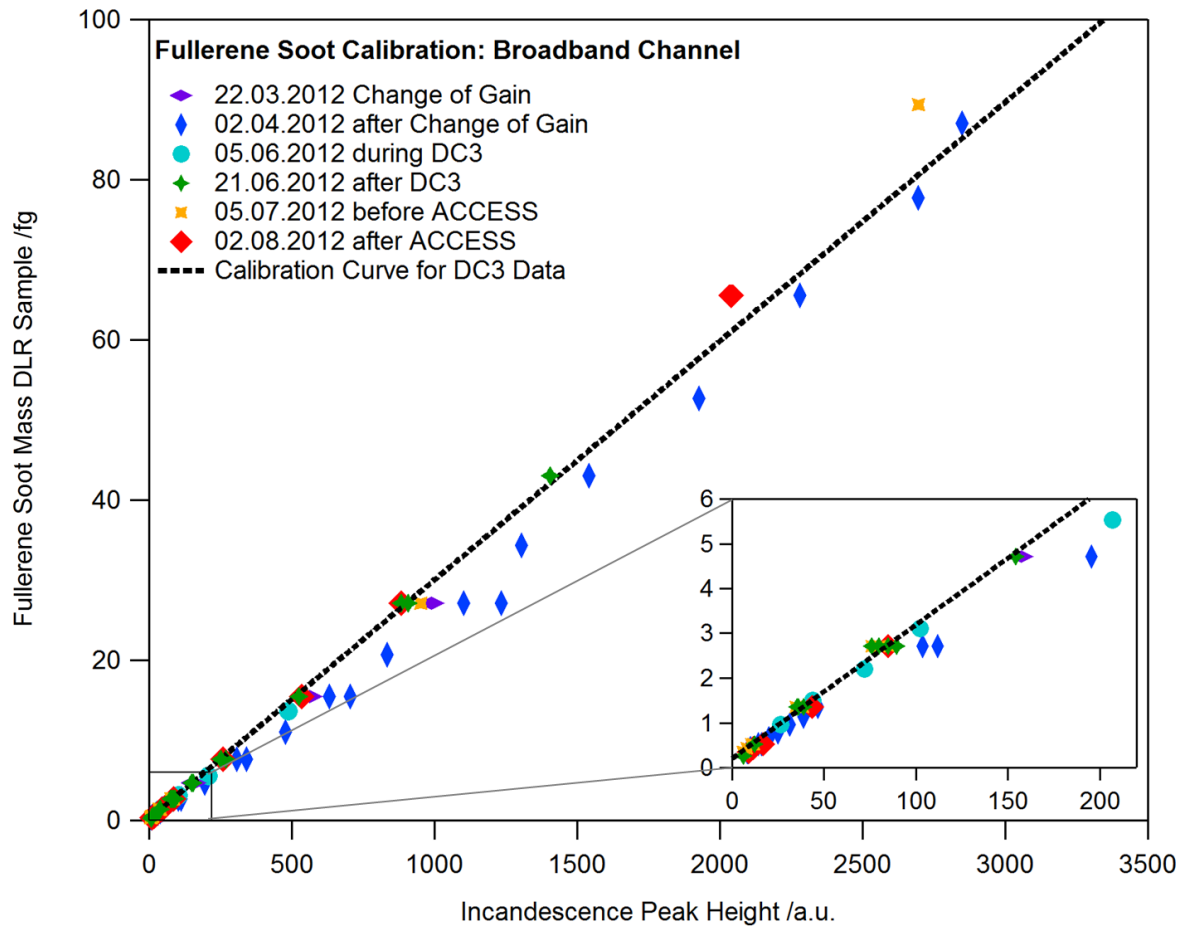
Figure 29: Calibration points for all calibrations in 2012 after the change of the gain stage setting to 0.512V and the calibration curve used for the evaluation of the DC3 data. The inset graph is an enlarged picture of the calibration points for the small sizes part of the calibration curve, marked in black in the bottom left corner.

The slope of the calibration curve can be changed by adjusting the detector gain. This was done before the start of the DC3 campaign when the broadband channel was decreased from 0.574 V to 0.512 V to decrease the signal and thereby increase the upper detection limit. As Figure 29 shows, the calibration points taken directly after the change in gain setting differ from all other calibration points that were taken before adjusting the gain stage potentiometer again in spring 2013. When measuring the detector gain again after the DC3 campaign on June 28, 2012, the reading had increased to 0.513V. The narrowband detector gain was changed to 0.848 V on April 2, 2012. At the test measurement after the campaign, it had changed to 0.849 V. This slight change in gain setting could be a reason for the slight difference between the calibrations in April 2012 and the calibrations performed during and after the DC3 campaign. Considering that the calibrations during and after DC3 agree very well while the pre-

campaign calibration differs, this could mean that the gain setting was not stable directly after changing it, but remained stable afterwards.
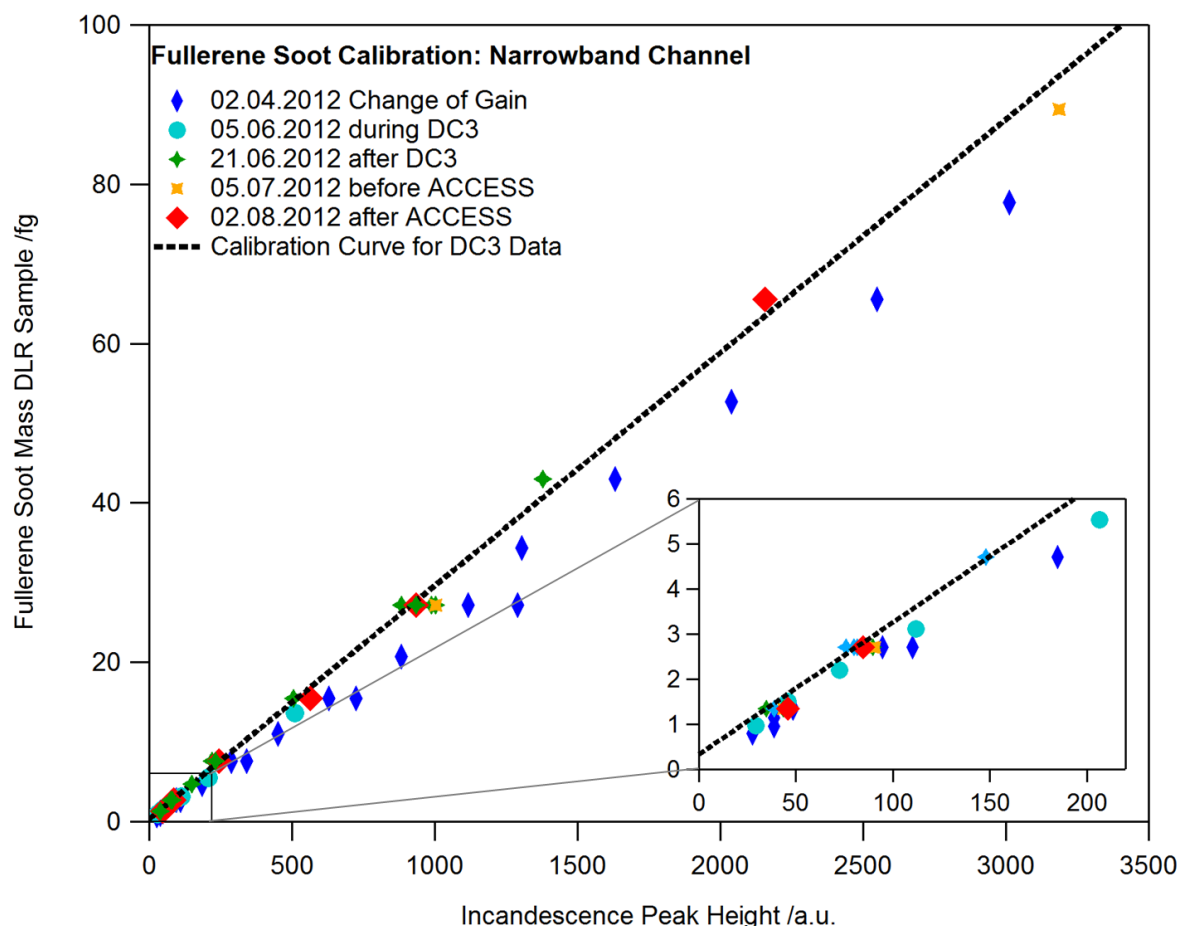
Figure 30: Same as Figure 29, but for the narrowband channel. The calibration data from March 30 2012 are not included since the gain settings of the narrowband channel were changed on April 4, 2012.

The DC3 calibration curve was acquired by linearly fitting the calibration points measured during and directly after DC3, while the ACCESS2012 calibration points served as validation. The calibration coefficients are given in Table 9. After showing how the calibration curve is derived from calibration data, the following paragraphs contain an evaluation of the accuracy and stability of the calibration.

Table 9: *Incandescence channel calibration coefficients used for the DC3 data evaluation. The numbers correspond to the linear fits shown in Figure 29 for the broadband channel and Figure 30 for the narrowband channel.*

Channel	Offset	Slope	Detector Saturation
Broadband Channel	0.21	0.0298	485 nm or 107 fg
Narrowband Channel	0.34	0.0293	480 nm or 104 fg

There are several potential error sources which lead to an uncertainty of the calibration curve and thereby an uncertainty of the derived particle mass, which influences the uncertainty of the total mass concentration. The error sources addressed here are the size-dependent density curve, the accuracy of the histogram peak determination, and detector noise.

The size-dependent density of the fullerene soot samples was evaluated in my Diploma Thesis (Heimerl, 2011). The error of the density from these measurements was estimated to be smaller than 10%. Comparing calibration results performed with different fullerene soot samples (e.g. the calibrations on June 5, 2012 with the NOAA sample and the calibration on June 21, 2012 with the DLR sample) suggests that this uncertainty is lower than 10%. For the following estimates and calculations, an error of 10% in calibration material mass is assumed as a maximum deviation.

In addition to the size-dependent density, Gysel et al. (2011) also address different techniques to mobilize the black carbon calibration aerosol as a potential source for errors. They found a systematic deviation between different mobilization techniques of up to 6%, while the variations were small for different measurements of particles mobilized with the same technique. Here, all samples of fullerene soot were mobilized in the same way, by nebulizing an aqueous suspension, both for the determination of the sample's individual density curve as well as for all the incandescence channel calibration. The nebulization technique is therefore not regarded specifically as an additional error source here.

Peak height might also be influenced by detector noise, as this can obscure the baseline and might bias the peak height. Detector noise is very low in the broadband channel (about ±2 digital detector counts). The narrowband channel tends to be more noisy and occasionally shows random spikes unconnected to particles (up to +40 digital detector counts) which makes it impossible to distinguish between noise and signal for small particles. These large spikes increase the uncertainty in narrowband channel peak height determination, making it nearly impossible to determine reliable peak heights for particles below 150 nm.
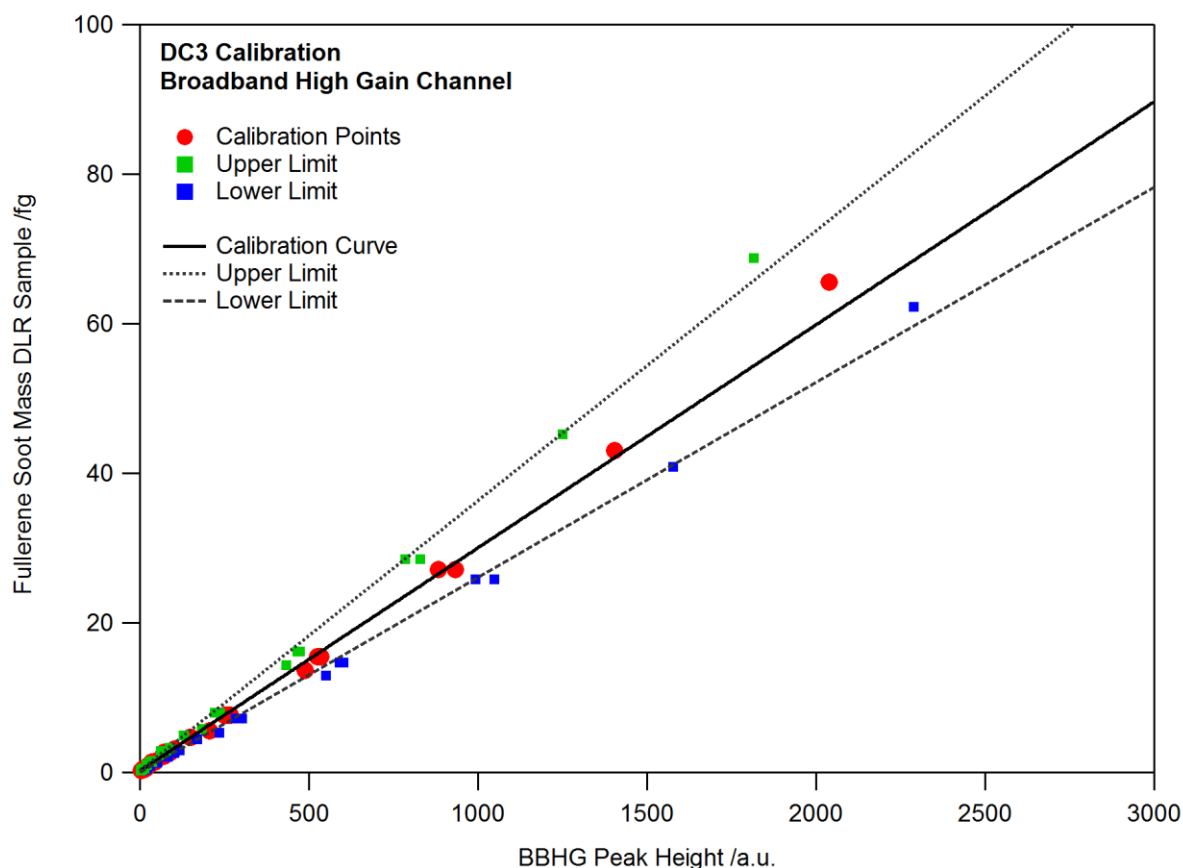
Figure 31: Calibration curve for DC3 (black unbroken line) and calibration points (red). Green and blue dots represent the upper and lower limit due to all possible error sources listed in the text. The corresponding upper and lower calibration curves are shown as lines with short and long dashes.

To assess an approximate uncertainty of the incandescence measurements, all potential error sources listed in the previous paragraphs were added up to get a maximum error estimate. The maximum error estimate includes the uncertainty of the mass to diameter conversion by considering the density measurement inaccuracy (as in Heimerl, 2011), as well as the uncertainty in deriving the peak height. Here this is shown for the broadband channel only. Figure 31 shows again the same broadband channel calibration points and curve as Figure 29 (red dots and solid line). By summing all positive errors or subtracting all negative errors, respectively, the upper (green) and lower (blue) limit of the errors in the calibration points are calculated. The broken lines are the corresponding calibration curves fitted to the upper and lower limit of the calibration points, the same method as applied for the "real" calibration curve. To assess the error in rBC mass concentration, the upper and lower estimate of the calibration curve are applied to a sample of ambient air with varying concentrations.
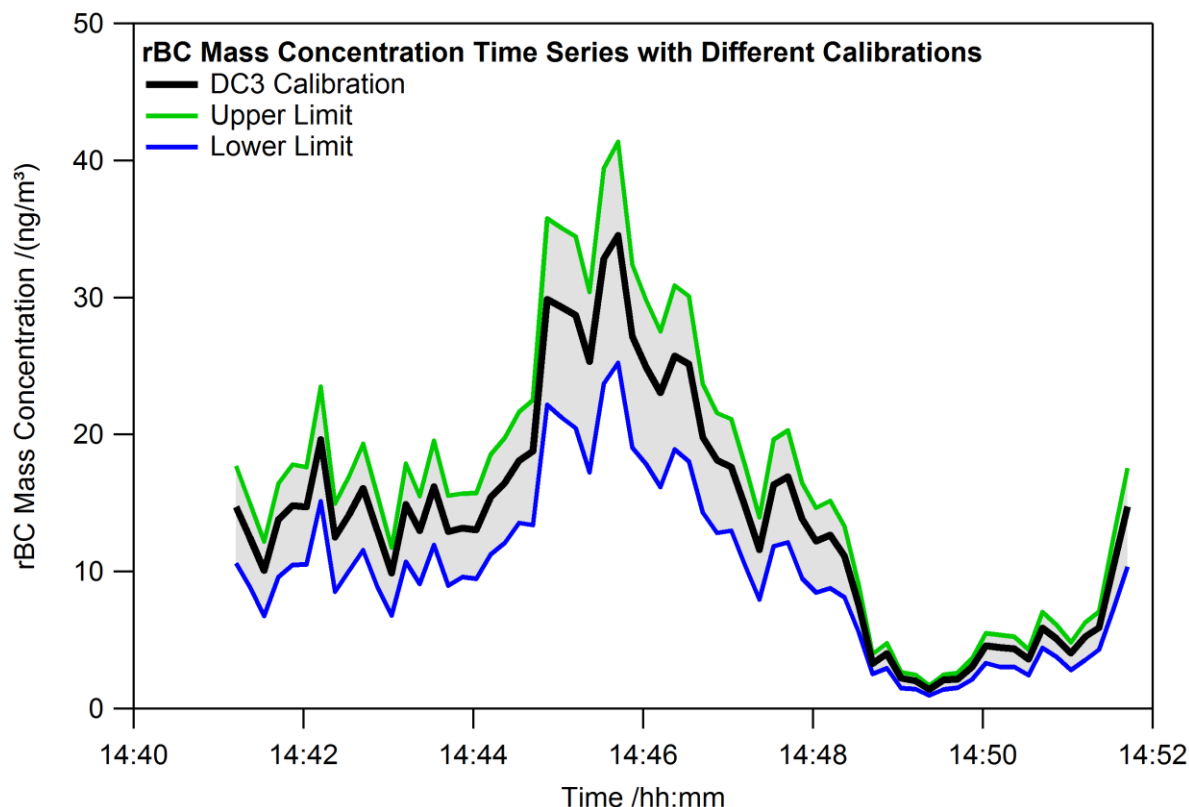
Figure 32: Time series of rBC mass concentration of an ambient air sample with varying concentrations, evaluated with the DC3 calibration curve (black) and the upper (green) and lower (blue) maximum error estimate calibration curve.

Applying the upper or lower calibration curve to measured data of an air sample (Figure 32) gives an rBC mass concentration in the SP2's detection range which is 20% higher or 29% lower than the rBC mass concentrations obtained with the best-estimate calibration curve, independent of concentration. This is within the range of estimations for rBC mass concentration errors given in the literature which reaches from 10% (e.g. Kondo et al., 2011b) to 30% (e.g. McMeeking et al., 2010). The error is asymmetric as both the upper and lower limit concentrations were calculated from calibration curves. The different slopes of the lower and upper estimate of the calibration curve lead to different results for single particle mass, resulting in the asymmetric upper and lower estimate of the measured rBC mass concentration.

The different slopes of the calibration curve error limit estimates also influence the rBC mass size distribution. The upper and lower estimates of single particle rBC mass can be used to calculate an upper and lower mass size distribution (Figure 33) and evaluate the influence on the shape of the distribution. It shows that the total rBC mass concentrations can be up to 50% higher or lower than the total concentration acquired with the actual calibration curve. The size distribution of a particle sample

_____

calculated with the upper or lower calibration curve can be shifted by nearly 10 nm. That both the lower and the upper limit mass size distributions show mass median diameters larger than the one with the actual calibration is probably an effect of the different offsets of the calibration curves (Figure 31).
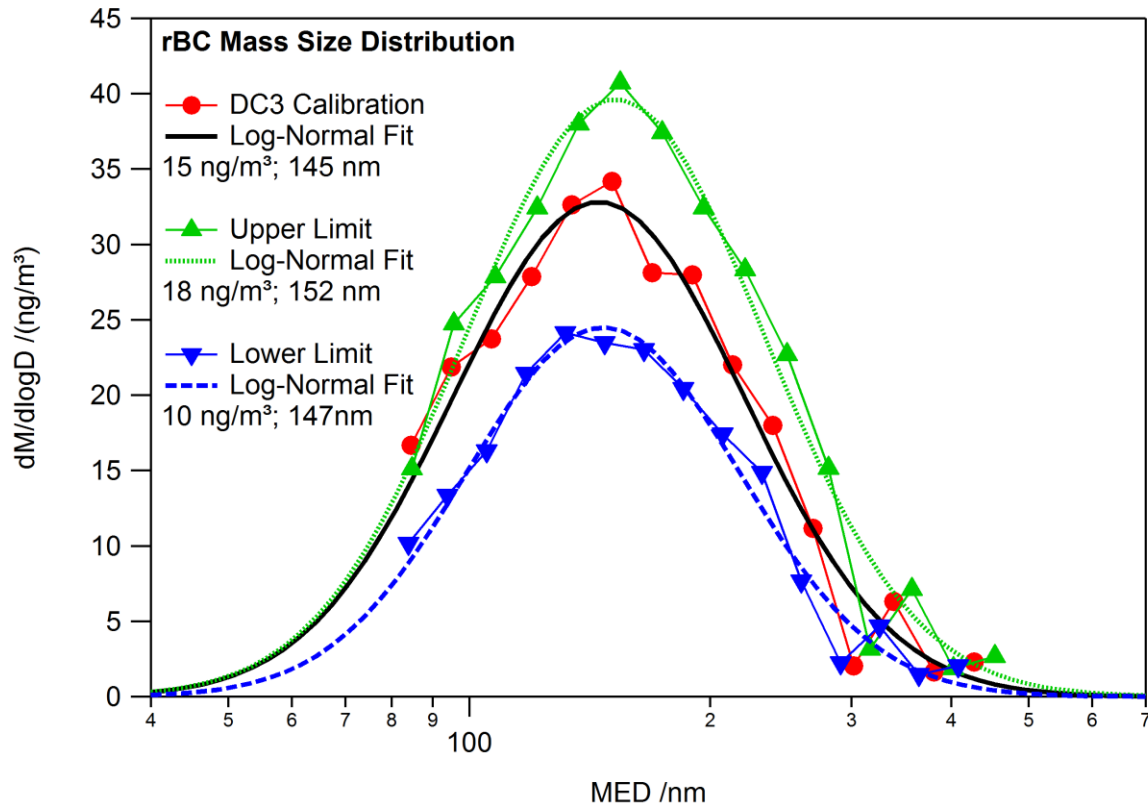

Figure 33: Mass size distributions for one ambient rBC sample evaluated with the three different calibration curves shown in Figure 31. Shown are the measured mass size distribution (symbols connected with thin lines) with the corresponding log-normal fit (thick lines) evaluated with the DC3 calibration curve (black and red) and with the upper (green) and lower (blue) limit of the calibration curve (see text for details). The numbers given in the legend are the corresponding total mass concentration and mass median diameter from the log-normal fit to the measured mass size distribution.

As this is an estimate of the maximum possible error, the actual deviations are smaller. During an intercomparison of different SP2s (Laborde et al., 2012b), our instrument deviated by less than 15% from the average of all SP2s. This was the largest deviation from the average of all instruments participating in the study and can partly be attributed to a misalignment of the laser. For the field campaign discussed in this work, an in-flight intercomparison during a wing-by-wing flight was performed during one of the mission flights. The two SP2 instruments deviated by about 5% in mass concentration. Figure 34 shows rBC mass concentrations measured by the two SP2s during a wing-by-wing intercomparison between the two aircraft.
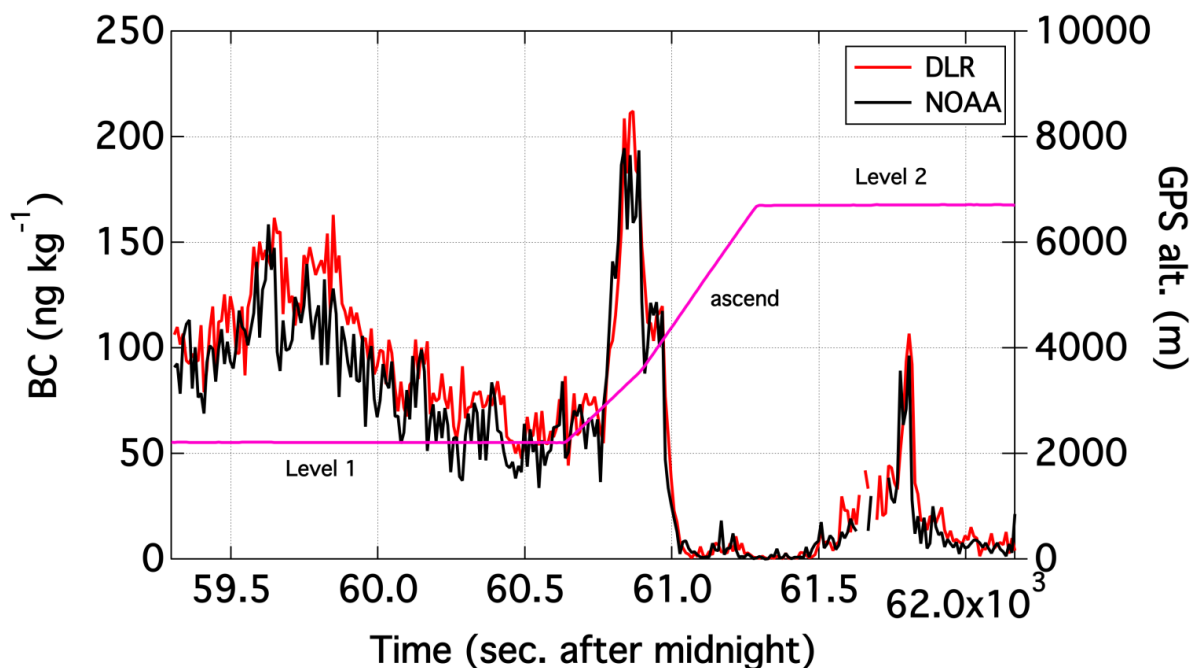
Figure 34: Mass concentration of rBC particles during a DC3 intercomparison flight at different altitude levels (pink) for the DLR SP2 on board of the Falcon (red) and the NOAA SP2 on board of the DC-8 (black) (Figure provided by M. Z. Markovic for Heimerl et al., 2013).

The upgrade to 8 channels in January 2014 influenced the calibration curves to some extent. As the digital resolution was changed, the mass-to-peak-height relationship calibration curves cannot be compared directly between the 4 and the 8 channel versions. The realization of the 8 channel upgrade was done by taking turns in tapping the signal from each single detector via two different amplifiers. This gives half the time resolution for each of the eight channels (0.4 µs instead of the 0.2 µs for the 4 channel version). Due to the signal for the high gain channels being amplified ten times over the low gain channel signal, this gives a better resolution for the smaller particles without having to make compromises regarding the upper detection limit, as it was the case with the 4 channel set-up.

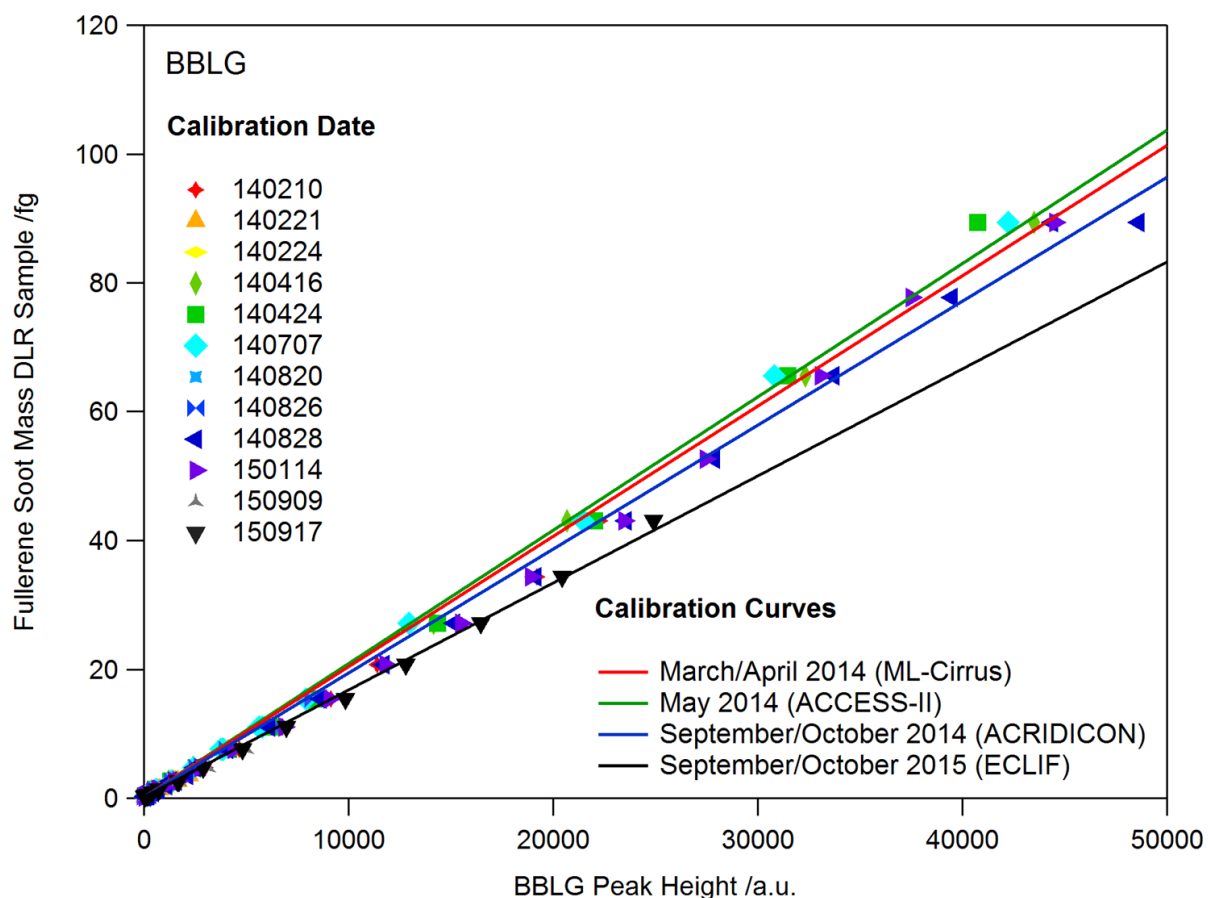*Figure 35: Calibration points for the Broadband Low Gain Channel for all calibrations performed in 2014 and 201 after the 8-channel upgrade. Calibration curves for all field campaigns in 2014 and 2015 are added.*

The broadband low gain channel calibrations are shown in Figure 35 together with the calibration curves used for data evaluation of field campaign data in 2014 and 2015. Similar calibration curve plots for all four incandescence channels of the 8 channel SP2 are shown in the appendix (Table A 2, Figure A 2, page 181ff). No changes were made to the instrument setup during that time, so all calibration points were taken with the same gain stage settings and should be comparable.

The calibration point for the largest mass often shows a larger spread than other calibration points. This mass is close to the detection limit of the high gain channels, so the peak is often only half visible in the peak height histogram. In the low gain channels, the highest calibration point is the largest value for size in the DMA system. This could be the reason for a larger spread in size from size-selection, resulting in a larger spread between the calibration points.

The average deviation from the calibration curve for all points is between 4% and 7% of the mass. This is much smaller than the maximum error estimation derived earlier in this section. A slight drift can be

seen in the data from the 2014 values (green and blue colors) to the 2015 values (violet, pink and black colors), increasing the deviation systematically from less than ±10% to nearly +30% if this effect is not taken into account. It is therefore crucial for reliable data to calibrate the incandescence channels regularly.

Comparing the original 4-channel SP2 with the 8-channel upgrade shows that the low gain channels give a slightly higher upper detection limit, which is only determined by detector saturation. Particles with a mass above this detection limit are still counted by the SP2, but their mass cannot be determined. With the 4-channel version, increasing the upper detection limit by changing detector gain always caused a loss in resolution that compromised the accurate sizing of particles close to the lower limit of the detector. The downside of the upgrade is the reduced time resolution from 0.2 μs to 0.4 μs of the single particle trace recording. For the DC3 campaign, which is of primary interest here, the gain settings of the 4 channel SP2 were adjusted to maximize the detection range without losing the resolution for small particles. The detection limits of the two incandescence channels are listed in Table 9.

The lower detection limit is not influenced by the upgrade directly, as it is a physical limit rather than a detector limit, depending on how efficient the particles are heated in the laser beam. If the laser power is sufficiently high to heat particles to incandescence (see description of particle heating in section 2.1.2), the incandescence peaks are independent of laser intensity. Figure 36 shows peak height histograms for fullerene soot particles of 75 nm mobility diameter with 0.2 fg (= $0.2 \cdot 10^{-15}$ g), corresponding to a mass equivalent diameter of 62 nm (similar to Figure 28).
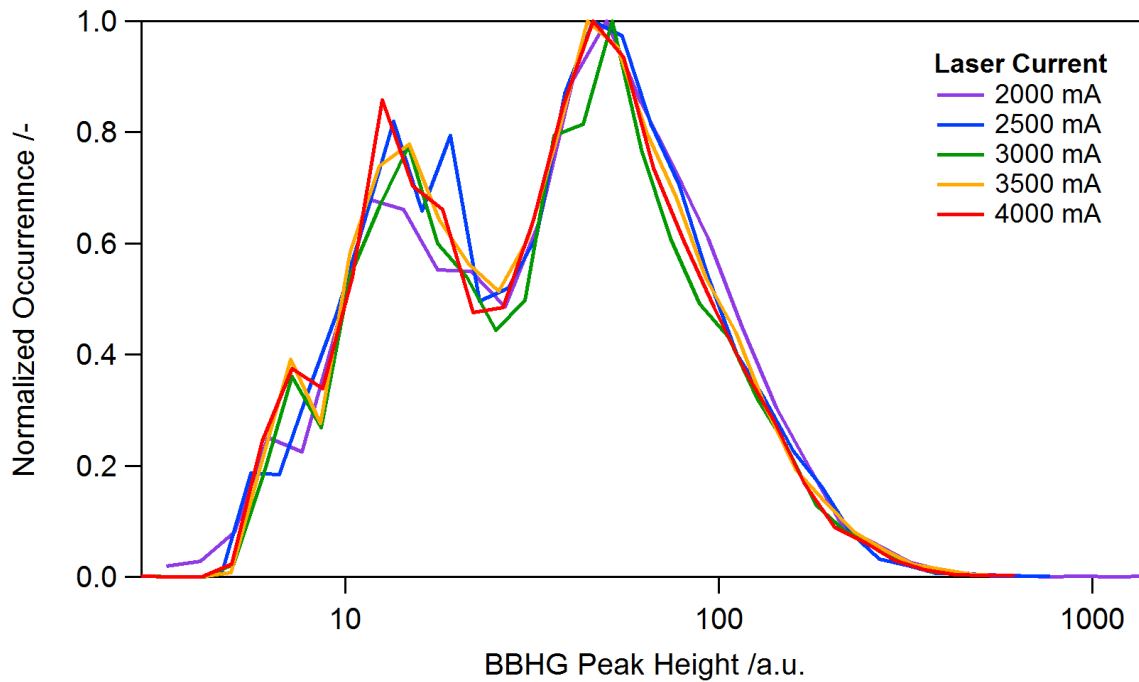
Figure 36: Histogram of broadband channel peak height of fullerene soot particles with a mobility diameter of 75 nm and a mass of 0.2 fg for different laser current settings. The peak height of the first peak is reduced due to the 75 nm particles having a detection efficiency below 50%.

In the case shown in Figure 36, the first peak is smaller than the second peak, unlike the example shown in Figure 28. The shown size, 75 nm is detected with a detection efficiency below 50% in the incandescence channels. The lower detection limit of the detector itself is well below this size. The slightly smaller peak for 2000 mA laser current is a result of less efficient heating of these particles. Schwarz et al. (2010a) have shown that the actual detection efficiency improves with increasing laser power up to a certain amount. Increasing the laser power even further does not result in a further improvement, corresponding to the similarity between the peak height histograms for higher laser current settings.

A simple way to determine the minimum laser power for sufficient detection of rBC particles is varying the laser current when measuring ambient air to find a minimum laser current setting which detects as much ambient rBC particles as possible. Setting the laser current to the maximum possible level is not desirable due to saturation of the scattering and split detectors and the YAG monitor. When using this method, the ambient air must contain a sufficient amount of small rBC particles with a mass around the detection limit at a more or less stable concentration. This is usually the case if rBC particle sources like cities, road traffic or airports are close by and the measurements are performed within short time. Figure 37 shows 30-second averages of rBC number concentration measured at different laser current settings within 10 minutes. The measured rBC number concentrations increase steeply with increasing laser

___

current below 2000 mA and only little above 2500 mA. For the DC3 campaign, the laser current was first set to 2500 mA and later increased to 2800 mA in the course of the campaign.
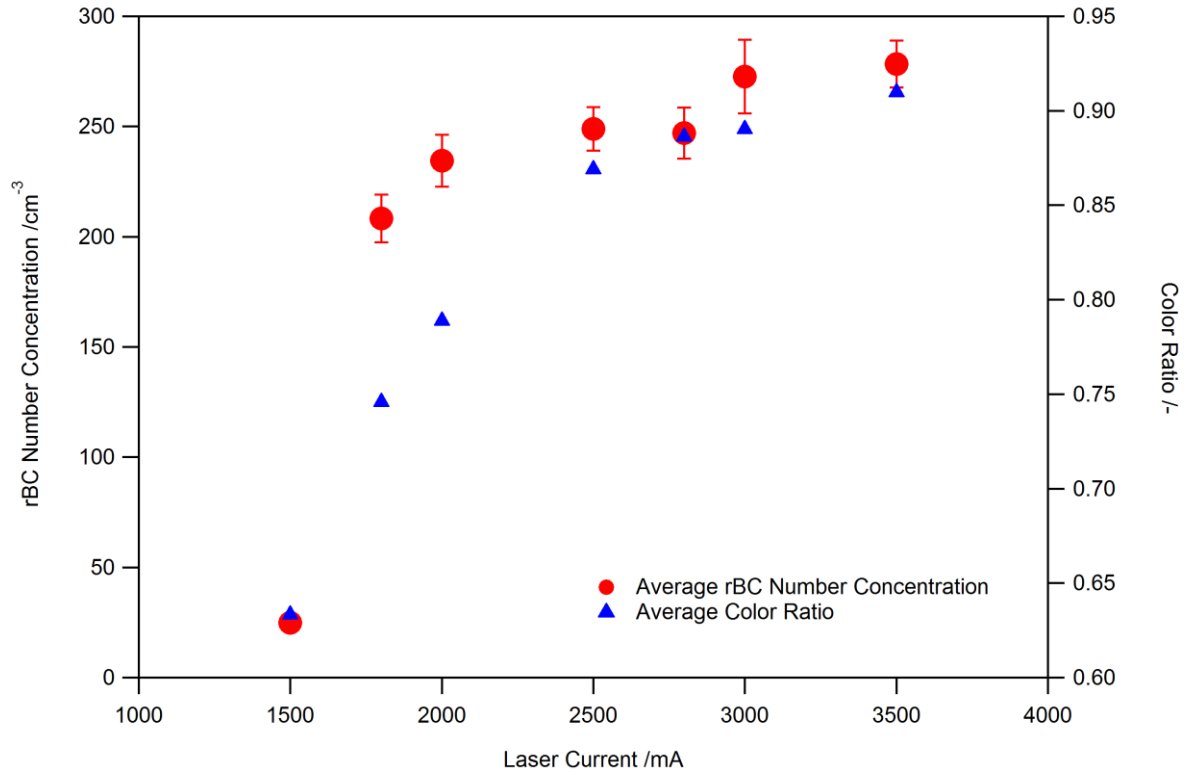

Figure 37: Ambient rBC number concentration (red) and average color ratio (blue) measured at different laser current settings during a lab test on July 2, 2012. Vertical error bars represent one standard deviation of the concentration.

Schwarz et al. (2010a) also describe a method to test for sufficient laser intensity using the ratio between the incandescence peak heights from the broadband and the narrowband channel, the color ratio. 30 s averages of the color ratio are shown in Figure 37 for the same 10-minute sampling period as the number concentrations in the same figure. Since the color ratio is a measure for particle temperature, an increase in color ratio with increasing laser intensity indicates that the particles do not reach their maximum temperature. Similar to the concentration method, the color ratio increases with laser current at settings below 2500 mA and reaches a plateau above that value (Figure 37). In contrast to the rBC number concentration, the color ratio reaches the plateau at higher laser current settings, above 2500 mA. As the color ratio is also slightly size-dependent (Moteki and Kondo, 2010; Heimerl, 2011), the increase in detection efficiency of small particles with increasing laser intensity could influence the average color ratio as well, due to the abundance of rBC particles with sizes around the detection limit in this sample of fresh rBC.

Testing the sufficient laser power by checking the rBC concentration and the color ratio has the advantages to be very fast and to work without any additional instruments. However, this cannot give a quantitative measure of the lower detection limit. To determine the size-dependent counting efficiency, a reference instrument is used, which has a detection efficiency of 100% over the full range of the SP2's detection range and beyond. The most commonly used method, also employed here, is to use a Condensation Particle Counter (CPC) as a reference to determine the total particle concentration of size-selected aerosol. This concentration is then compared to the concentration measured by the SP2. The ratio between the concentration measured by the SP2 and the concentration measured by the CPC for each size setting of the DMA is the size-resolved counting efficiency. The lower detection limit is then defined as the diameter with 50% counting efficiency.

Figure 38 shows the size-dependent counting efficiency for both incandescence channels of the 4-channel SP2 for the DC3 campaign. The broadband channel counts all particles above a mobility diameter of 150 nm, which corresponds to a mass equivalent diameter of 113 nm. The lower detection limit is at 90 nm mobility diameter, corresponding to a mass equivalent diameter of 77 nm. The counting efficiency of the narrowband incandescence channel is slightly lower than that of the broadband channel. The decrease in counting efficiency of the 8-channel setup (green stars in Figure 38, marked as ACRIDICON) is shifted to slightly smaller diameters than the 4-channel setup. For the broadband low gain channel, the 50% cut off is at 63 nm (64 nm mass equivalent diameter) and 100% detection is reached at 100 nm mobility diameter (82 nm mass equivalent diameter). A similar effect could be observed in Laborde et al. (2012b) where the only participating 8-channel SP2 also had the detection limit at a lower diameter than the participating 4-channel SP2s.
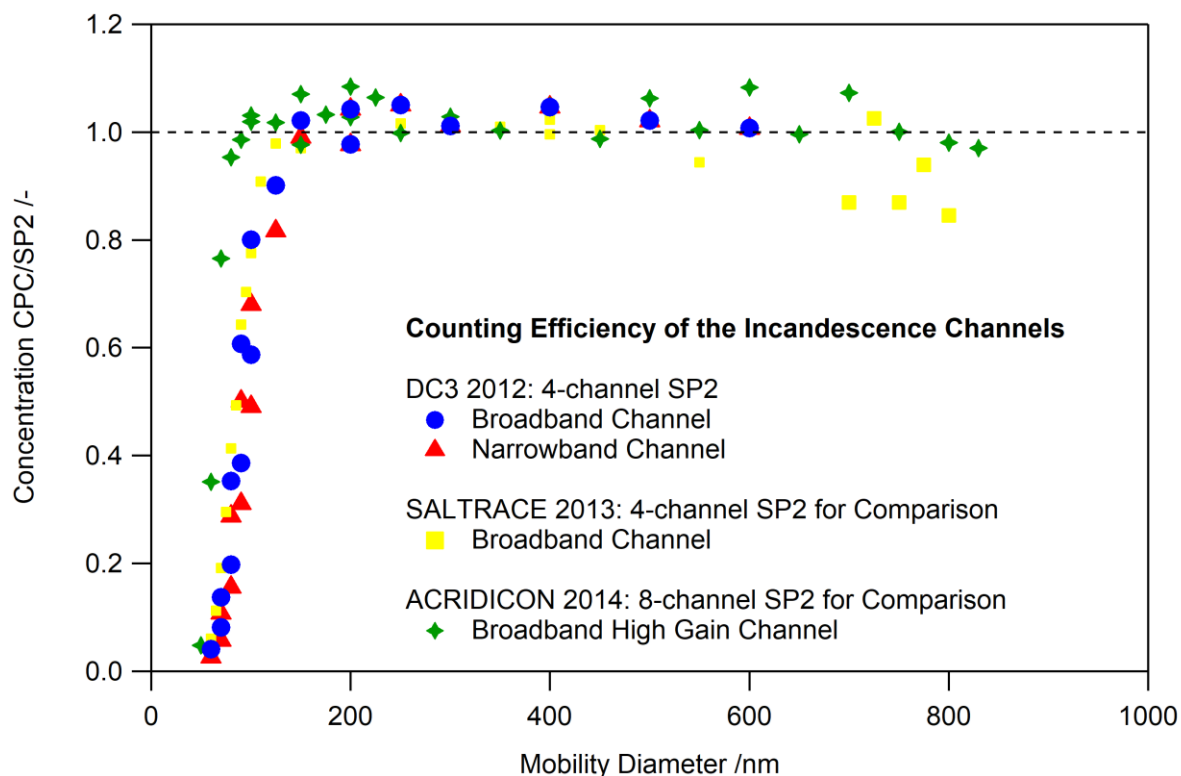
Figure 38: Size-resolved counting efficiency for the SP2's incandescence channels for the 4-channel version used during DC3 (blue circles: broadband, red open squares: narrowband), one year later (yellow squares marked as SALTRACE), and after the upgrade to 8 channels (green stars: broadband low gain channel). The dashed black line marks a detection efficiency of 100%.

Concentration of rBC mass given in this work is the mass concentration of rBC particles in the size range of 80-480 nm. When referring to the total concentration of rBC particles, including particles outside of this size range, the term "total mass concentration" is used. The derivation of the total rBC mass concentration from the SP2 measurements is described in section 3.3.3.

3.2.3 Calibration and Detection Limits of the Scattering Channels

In addition to the incandescence detectors for the emitted thermal radiation, the SP2 is equipped with a detector to measure the scattered laser light. The detector signal is recorded in one or two channels in the 4 and the 8 channel version, respectively. The recorded signal represents the differential scattering cross section, which depends on optical particle size and the refractive index (see section 2.1.2).

In instruments which use scattered laser light to determine optical size, the detectors on which the light is collected capture only a part of the total scattered light. In the SP2, the scattering detector covers a conical solid angel of 60° seen from the particle's position in the laser beam. The center of the scattering detector is located at an angle of 45° to the line of the laser. With the laser wavelength of 1064 nm being

in the same size range as the larger particles detectable with the scattering detector, the particle size range measured by the SP2 falls into the transition between Rayleigh and Mie regime. The Bohren-Huffman Mie-code (Bohren and Huffman, 1998) was employed to calculate the scattering cross sections for spherical particles and coated spheres for the SP2's scattering detector's filters and detector geometry. These calculations are available as lookup tables in the data evaluation software. Examples of the resulting scattering cross sections for several refractive indices are shown in Figure 39.
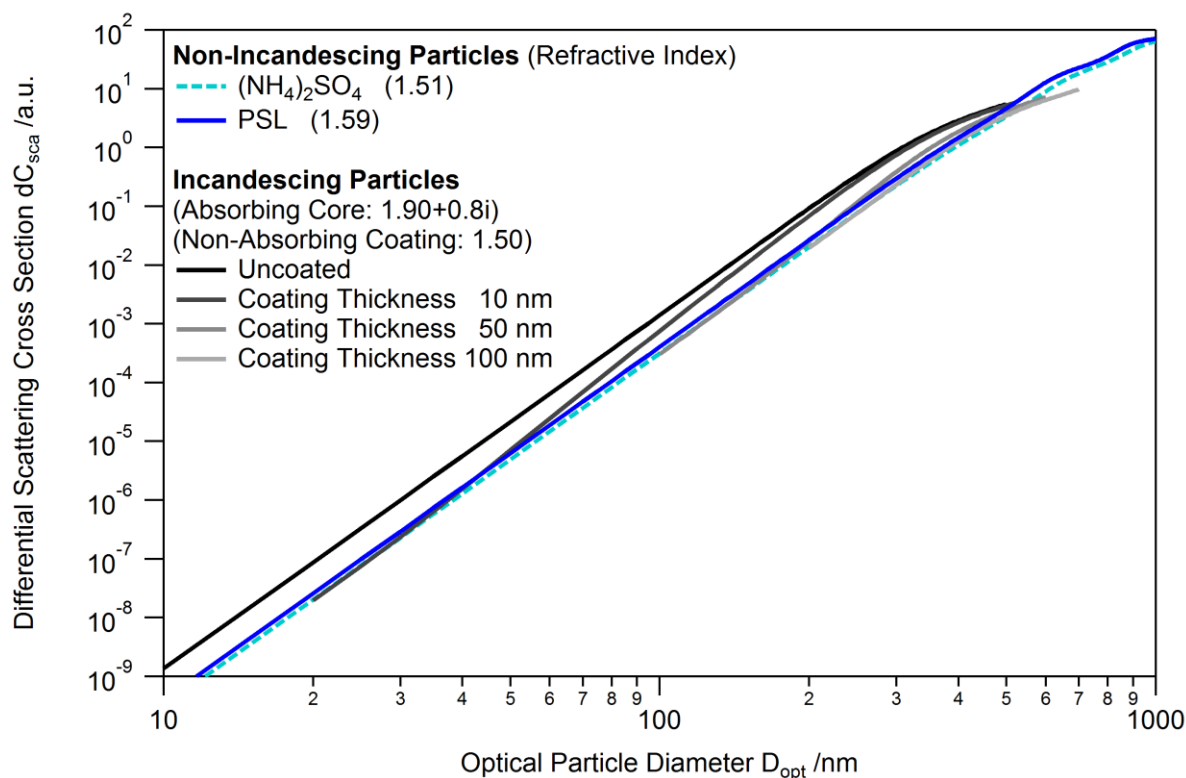
Figure 39: Differential scattering cross sections for the laser light wavelength of 1064 nm and the SP2's scattering detector geometry for different particle types in the SP2's size range. The refractive indices for the different materials are 1.51 for $(NH_4)_2SO_4$, 1.59 for PSL, 1.9 + 0.8i for incandescing rBC particles and 1.51 for the coating material.

The relationship between the measured signal and the optical size is determined by calibration with particles of known refractive index and size. Here, PSL particles with a refractive index of 1.59 + 0i and a size of 200 nm and 220 nm are used, the same as used for the alignment procedures in the previous sections. Figure 40 shows the same curve as the light blue one in Figure 39, scaled with the calibration factor to the 200 nm calibration point. The 220 nm calibration points served as validation. A third PSL size, 300 nm, is also shown, but lies already above detector saturation (thin grey line), which marks also the upper detection limit.

Table 10: Upper and lower detection limit of the scattering detector for the DC3 data.

Material (Refractive Index)	Lower Detection Limit	Upper Detection Limit
PSL (1.59+0i)	127 nm	277 nm
Ammonium Sulfate (1.51+0i)	131 nm	290 nm

To test the performance of the scattering detector and to verify its calibration, several tests with the same PSL standard size, 200 nm, were performed during the DC3 campaign and the following ACCESS2012 campaign. Schwarz et al. (2010a) mention that the scattering detector might be sensitive to changes in temperature but give no quantitative values.
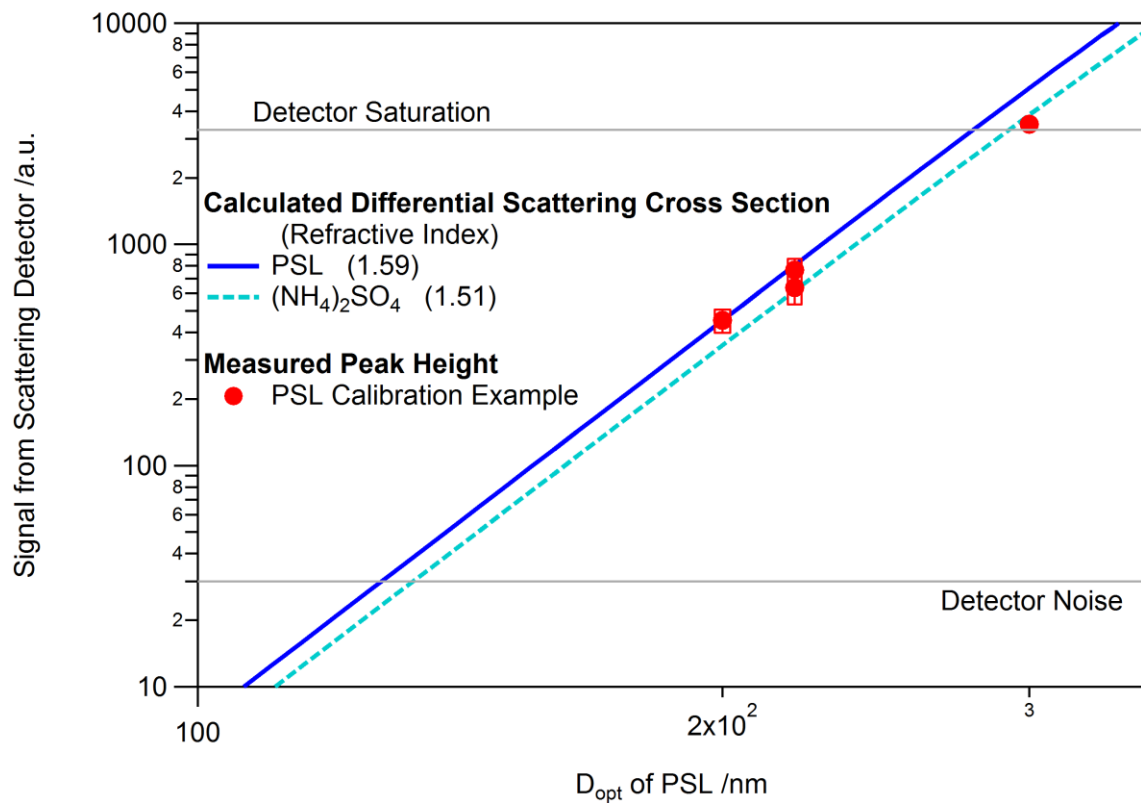
Figure 40: Calibration curve for the scattering detector with calibration points from one example calibration. Error boxes represent the standard deviation of the measured peak heights in the vertical direction and the standard deviation of the PSL calibration standard as given by the manufacturer in the horizontal direction.

Since the DC3 campaign took place in the subtropics while a following field campaign was situated at the Arctic Circle, the instrument was operated at a range of ambient temperatures in 2012. Though it is

recommended to keep the SP2 at a more or less constant temperature with little variation, this is hardly possible in the Falcon aircraft as the air condition is not adapted to the scientific equipment. The temperature in the SP2's measurement chamber varies therefore strongly, from about 10°C to nearly 50°C. This temperature variation is reflected in a temperature dependence of the scattering signal. Measured scattering signal peak heights of 200 nm PSL particles are shown in Figure 41 for the temperature range at which the SP2 was operated in 2012. The graph shows a linear decrease in scattering signal peak height with increasing temperature. Applying a scattering size calibration measured at 25°C to peak heights measured at other temperatures would result in the optical sizes indicated on the right axis. In the temperature range the SP2 was operated at in 2012, this temperature-induced bias can be as large as 10% if the temperature during the calibration deviates strongly from the temperature during the measurement.
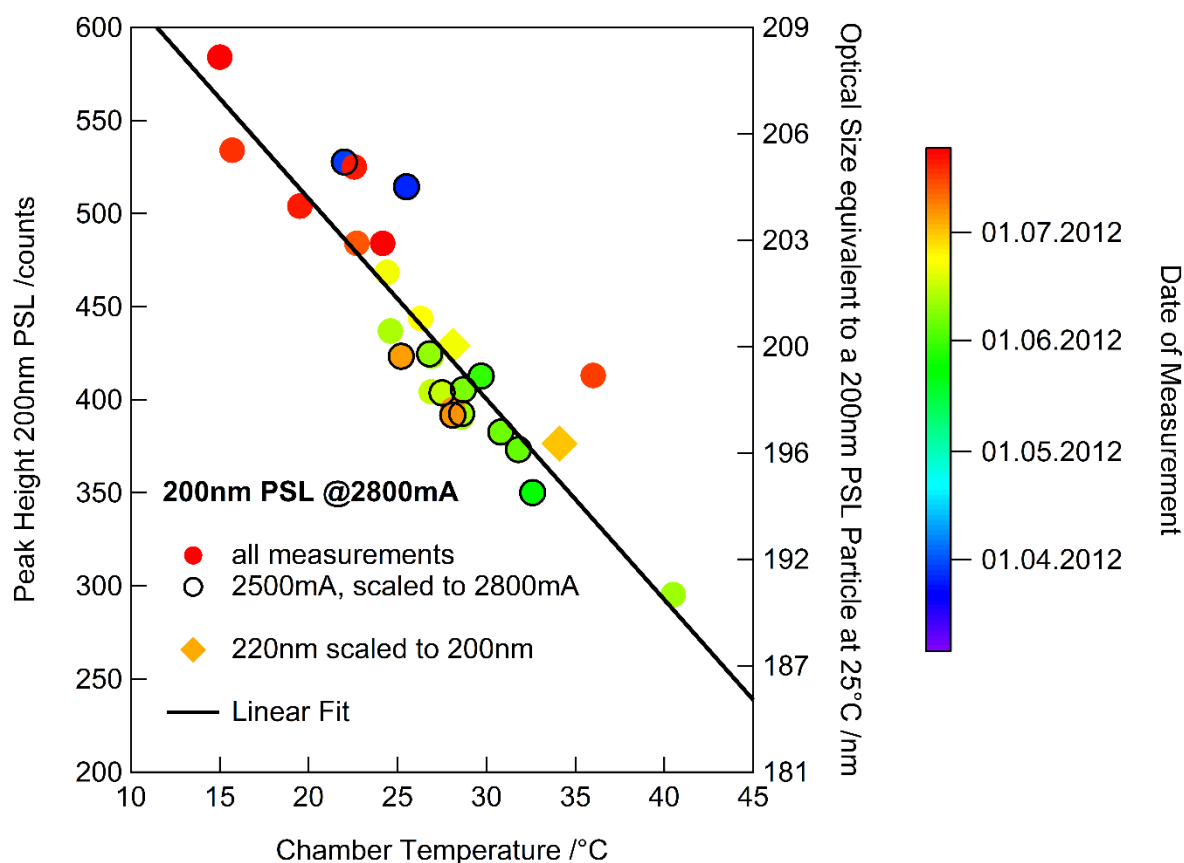
Figure 41: Temperature dependence of the scattering signal. The measured peak height for 200 nm PSL particles is shown for different temperatures; different colors refer to the date of the calibration. As the calibrations were performed at two different laser current settings, peak heights taken at 2500 mA laser current were scaled to a laser current setting of 2800 mA for better comparability. Data from the ACCESS2012 campaign in July 2012 were measured and evaluated by Florian Dahlkötter.

Fitting a linear curve to the 200 nm PSL peak heights between March 27 and July 24 gives the black line in Figure 41. The fit curve, with one sigma confidence interval, is:

$$\text{Peak Height} = (722.85 \pm 28.6) - (10.761 \pm 1.05) \cdot \text{Temperature}$$

(3-1)

The uncertainty of the optical size can be reduced by correcting for temperature and laser intensity deviations to avoid systematic errors. The main source for errors left after these corrections is the potentially non-spherical shape and unknown refractive index of the scattering particles in the sample.

3.3   Data Analysis

This chapter summarizes analysis methods applied to the DC3 data set to get the results shown in the following chapters.

The time stamps of the cabin instruments were corrected for inlet line length by comparing their concentration measurements to measurements made by the wing probes. These have no time delay as they are located outside of the airplane and sample directly into the instrument without an inlet line. Even if the aerosol inlet and the wing probes are not located at the same position on the aircraft's outside, the time delay between them is only minor, as the phenomena observed and discussed in this work have scales much larger than the distance between the roof and the wing of the aircraft. The time difference between wing probes and the SP2 was estimated to be 6 s for the DC3 Falcon configuration and used for all flights.

The SP2 raw data were evaluated with the SP2 Toolkit, provided by Martin Gysel of the Paul-Scherrer Institute, Villigen, Switzerland. It is a data analysis tool specialized on SP2 data running on IGOR (Wavemetrics, Inc.). As the SP2 Toolkit functions are mostly intended for general data evaluation, it was necessary to develop additional functions for the specific use of aircraft data.

To compare particle concentrations measured at different altitudes, it is necessary to correct for the pressure differences. Particle concentrations are therefore often normalized to standard conditions, either standard volume with a temperature of 273.15 K and a pressure of 1013.25 hPa (mass concentration reported as ng/m³), or the mass of dry air (mass mixing ratio reported as ng/kg). Here, concentrations are shown as relative to standard volume. This is the number or mass of particles per unit volume in a parcel of air that was brought adiabatically to standard conditions.

Both the mass concentration per standard volume and the mixing ratio can be converted into each other as their ratio is equivalent to the mass of 1 m³ of dry air at the atmospheric standard conditions (273.15 K, 1013.25 hPa). Falcon SP2 rBC mass is stored on the DC3 data base (http://data.eol.ucar.edu/master_list/?project=DC3) both as mass concentration per standard volume and mass mixing ratio per kg dry air.

3.3.1 Treatment of In-Cloud Data

The Falcon aerosol inlet has an upper cut-off in the range of 1.5 - 2.5 µm, depending on ambient pressure (Fiebig, 2001). Cloud droplets and ice particles are often larger than this. When flying in clouds, these large particles can produce artificial particles from shattering of large particles and mobilization of particles that accumulated on the inlet walls. Therefore the data measured by instruments in the cabin behind the aerosol inlet were checked for in-cloud sequences. In-cloud data were excluded from all further data analysis to avoid sampling artefacts induced by large cloud and ice particles impacting on the aerosol inlet (Murphy et al., 2004).

Cloud sequences were identified according to measurements of the FSSP-100 wing probe and notes taken during the flights. The FSSP-100 measures coarse mode particles in the range of 2-30 µm at the setting used during most of the DC3 flights. The notes about cloud passages coincided with particle number concentrations in the FSSP-100 exceeding about 1 cm^{-3}. This value was taken as the threshold for cloud passages as a first step. In a second step, the identified sequences with coarse mode particle concentrations (N_{coarse}) exceeding 1 cm^{-3} were discarded as cloud passages if the relative humidity was lower than 60%. As the relative humidity measurements retrieved from the Falcon data system are unreliable at high altitudes, in-cloud sequences at high altitudes were only compared to the notes about anvil crossings taken during the flights. Sequences with N_{coarse}<1 cm^{-3} that coincided with reports of cloud crossing in the flight observation protocols were added to the cloud flag.

As a cross validation, the rBC mass concentrations were compared to the CO concentrations, which are uninfluenced by clouds, and the coarse mode concentrations. This is shown in Figure 42, a correlation plot of rBC mass and CO concentration color-coded by coarse mode particle number concentration. In-cloud sequences, marked by violet and blue colors, are characterized by very high, artificial, rBC mass concentrations which are uncorrelated to the CO concentrations. Sequences with low concentrations of large particles, shown in green, show a positive correlation.
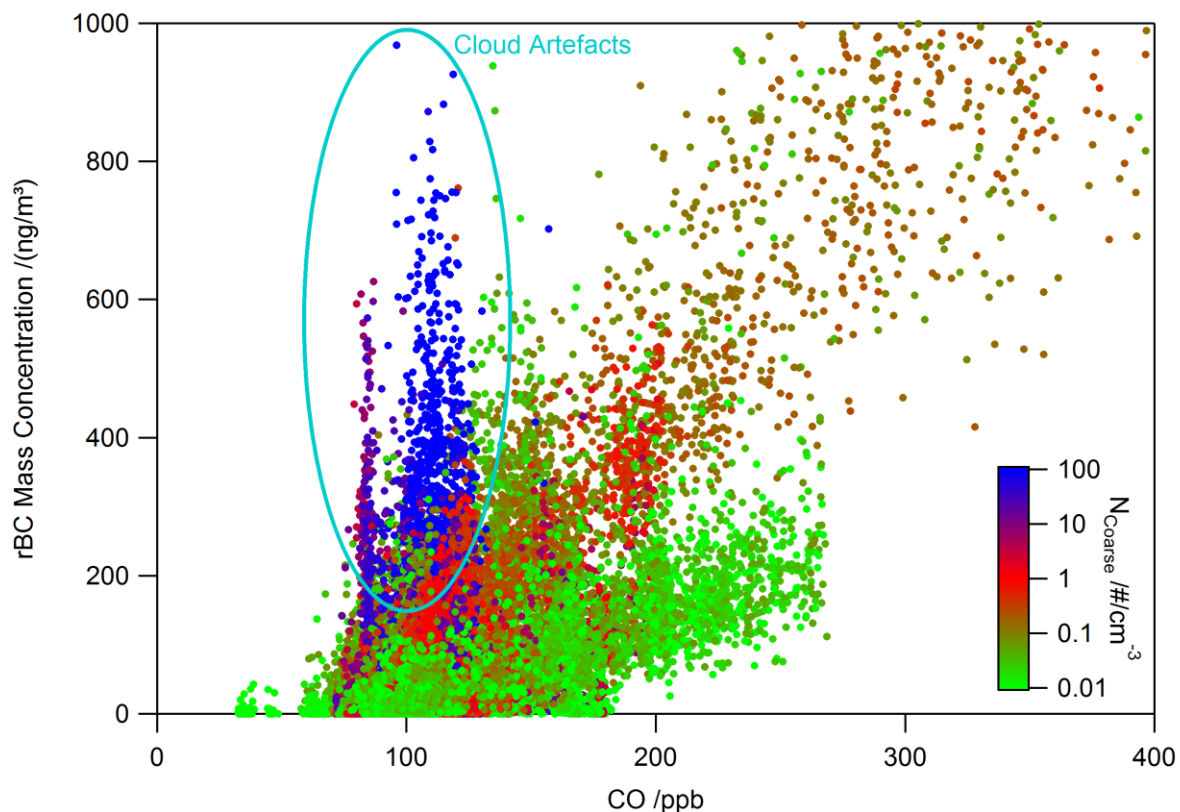
Figure 42: Comparison of 1 s measurements of rBC mass concentration and CO concentration out of the PBL in and out of clouds color-coded by number concentration of particles larger than 2 μm.

Coarse mode concentrations also exceed the 1 cm^{-3} threshold in some cases where rBC mass and CO concentrations are well correlated (positively correlated branch in reddish colors in Figure 42). These sequences were measured in biomass burning layers and characterized by low humidity, indicating the absence of cloud particles.

About 13% of all data points were excluded from further analysis according to the cloud flag criteria of coarse mode particle concentration exceeding 1 cm^{-3} with the additional cross checking with relative humidity and in-flight observations. The cloud flag is also included in the Falcon SP2 data files on the DC3 data base (http://data.eol.ucar.edu/master_list/?project=DC3).

Sequences out of clouds were classified into five categories: planetary boundary layer, biomass burning, pollution, thunderstorm outflow (both fresh and aged), free tropospheric background and industrial pollution.

3.3.2 Identification of Biomass Burning Layers

The term *Biomass Burning Layer* refers in this work to an air mass, often found as a vertically thin and horizontally extended layer, which contains high concentrations of aerosol originating from fires fueled

by organic matter (wood, grass, dry leaves, etc.). In the cases described in this work, these fires are wildfires in forested areas, where the fuel consisted mainly of pine trees, understory and grass (http://inciweb.nwcg.gov/incident/2870; http://inciweb.nwcg.gov/incident/2903; http://inciweb.nwcg.gov/incident/2904). The term *Biomass Burning Plume* is used here to refer to the visible smoke clouds above such fires that are transported downwind, still connected to the fire.

To identify biomass burning (BB) encounters, the DC3 data set was in a first step searched for sequences with an increase in rBC mass concentration together with a simultaneous rise in CO concentration. The start and end times of each sequence are defined here as the time when rBC mass and CO concentration rise above and decay back to background level, respectively. For CO, the background level was around 80-100 ppb for most cases. The background level for rBC mass concentration was around 100 ng/m³ in the lower troposphere and decreased with altitude to 1-10 ng/m³ in the upper troposphere. These sequences were defined as BB when backward trajectory analysis of the flight sequence resulted in a source fire. Other sequences were classified as planetary boundary layer (PBL) or other pollution plumes, judging by altitude and total particle concentrations. The PBL is defined here as the lowermost well-mixed layer of the atmosphere with high number concentrations of total particles and an upper boundary above which total particle number concentration decreases (Stull, 1988). This decrease in total number concentration can also be seen in cases which have a BB layer directly on top or mixed into the boundary layer, leading to several cases of BB layers containing a fraction of PBL air.

In the upper troposphere, thunderstorm outflow was measured. The corresponding time steps of these sequences, both in and out of clouds, are listed in Huntrieser et al. (2016a; 2016b). Aerosol measurements in thunderstorm outflow are only shown here if they were measured out of clouds in aged dissipating outflow, due to the in-cloud sampling biases.

Background sequences in the upper troposphere serve as reference for the measurements of thunderstorm outflow and BB in the upper troposphere. These background sequences are measurements at a flight altitude of approximately 11 km during transfers from Salina/KS to the targeted area. The sequence is identified as background if CO concentration was below 80 ppb and no other trace species like NO_x, total particle concentration or O_3 were elevated to exclude measurements of aged outflow or stratospheric air.

To assess the extent of BB layers, the coordinates of start and end point of the sequence were used to calculate the extension of the crossed layer. The distance was calculated as the minimum distance on a sphere from the position data and does not correspond to the actual flight track to avoid a positive bias in length.

For all sequences, average values of rBC number and mass concentrations and trace gas concentrations were calculated. For calculating ratios between two measured concentrations, here rBC mass and CO,

the 1 s data were fitted with a linear regression. The derivation of the average rBC mass size distribution and its parameters for each sequence is described in the next section.

3.3.3 Mass Size Distribution and Correction for Particles Beyond the Detection Limits

The size distribution of total aerosol can often be described in a good approximation by a superposition of log-normal fits for the four modes, nucleation, Aitken, accumulation, and coarse mode (e.g. Whitby et al., 1972; Hinds, 1999; Weinzierl et al., 2011). Since the SP2's detection range only covers the accumulation mode, ambient rBC particle sizes show a lognormal distribution with one mode in the SP2's detection range in most observed cases (e.g. Schwarz et al., 2006; Oshima et al., 2009b; Liu et al., 2010; Subramanian et al., 2010; Dahlkötter et al., 2014). For an SP2 with a larger detection range, Huang et al. (2011) find a small second mode at larger sizes for ambient rBC in a polluted air mass over China. Lognormal size distributions are also used to represent black carbon in models (e.g. Oshima et al., 2009b; Aquila et al., 2011; Kaiser et al., 2014).

To get the parameters of the lognormal mass size distribution, described in chapter 2.1.1, the measured and binned mass size distribution is fitted with the IGOR build-in lognormal function using a least-squares fit. As the SP2 detects the mass of individual rBC particles only in the size range above the lower detection limit (80 nm during DC3) and below the saturation of the incandescence detector (480 nm during DC3), the total rBC mass concentration cannot be measured directly. However, it can be derived from the fitted lognormal distribution, if most of the mass size distribution fall into the detection range.

The rBC mass size distribution for an exemplary sample is shown in Figure 43 in red (marked as BB). The solid line steps show the measured distribution, with a peak around 180 nm. The lognormal fit to this distribution (dotted line) gives a mass median diameter of 179 nm and a calculated total mass concentration of 214 ng/m³. The fraction of the total mass concentration measured by the SP2 corresponds to the shaded area underneath the lognormal distribution. The mass concentration measured by the SP2 was 198 ng/m³, so in this case, the SP2 measurements covered 93% of the total mass.
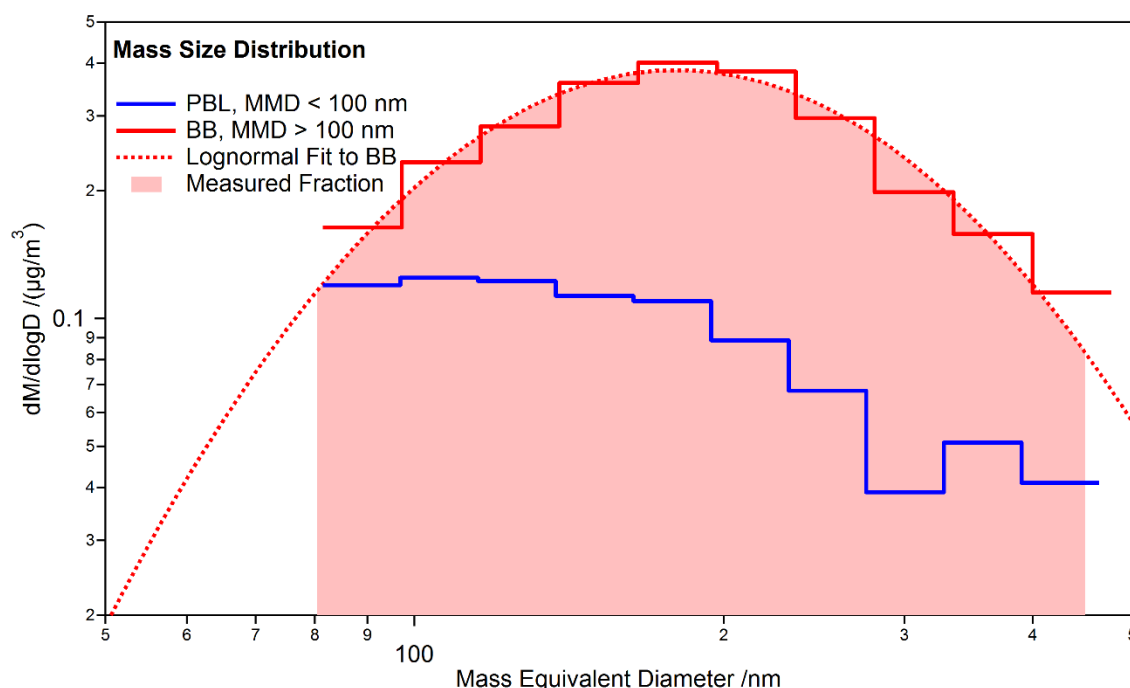
Figure 43: Two examples of rBC mass size distributions without log-normal fit (blue) and with log-normal fit (red). The shaded area corresponds to the fraction of the total mass concentration that was measured. The total area underneath the broken red line corresponds to the total mass concentration for the BB (biomass burning) sequence. Both sequences were measured during the flight 120530a.

Calculating the total rBC mass concentration from the measured rBC mass size distribution does not work for all cases. If less than 50% of the particle mass lies within detection limits, the measured rBC mass size distribution will not show a distinct peak and the lognormal fit is unreliable. This is the case for the second example in Figure 43, shown as PBL in blue. As the PBL sequence contains many particles below the detection limit of 80 nm, the measured mass size distribution shows no peak, only the falling right flank of the lognormal distribution. Without a distinct peak within the detection limits, it is not possible to fit a reliable lognormal function to the measured mass size distribution. Therefore, neither the total mass concentration nor the mass correction factor can be determined for this sequence.

In both shown cases, the measured rBC mass concentration underestimates the total rBC mass concentration. In other studies (Schwarz et al., 2008a; Spackman et al., 2010), the total rBC mass concentration is derived from the measured mass concentration by scaling with a mass correction factor. This mass correction factor is the ratio between the measured mass concentration and the total mass concentration derived from the lognormal fit. For the BB example in Figure 43, the mass correction factor, the ratio between the shaded part and the total area under the lognormal fit (broken line), would be 1.074. For the PBL sequence, the mass correction factor cannot be determined as the mass median diameter is at or below the lower detection limit of 80 nm.

In order to compare rBC mass concentrations measured during the DC3 campaign to other campaigns, mass correction factors were calculated for each individual flight from the flight's average mass size distribution. The Falcon SP2 data files on the DC3 data base contain both the measured and the total mass concentration (http://data.eol.ucar.edu/master_list/?project=DC3).

Though the mass correction factor gives a good approximation of the total rBC mass concentration, this approach also has a downside. The two examples shown in Figure 43 were both measured during the same flight, but show very different mass size distributions. For the whole flight, the scaling factor is 1.147 on average. This is higher than the 1.074 calculated for the BB sequence, but an underestimation of the factor for the PBL sequence, which cannot be calculated and must be above 2 as the mass size distribution indicates that more than half of the mass size distribution lies below the lower detection limit. Using the BB scaling factor on the boundary layer case would underestimate the total rBC mass concentration while the boundary layer scaling factor would lead to a gross overestimation of the BB total rBC mass concentration. In this work, total rBC mass concentrations are therefore only reported for measurement sequences with a valid lognormal fit to the mass size distribution. This was the case for all BB sequences (compare Figure 63).

As this study focuses on BB, characterized by rBC particles which are mostly larger than 100 nm, using an average scaling factor for each flight or even the whole field campaign data set could lead to a systematic bias leading to an overestimation of rBC mass concentration in BB layers and an underestimation of rBC mass concentrations in sequences dominated by small particles. Instead of the potentially biased total mass concentration time series, only total rBC mass concentrations calculated individually for each sequence, if possible, are shown here.

3.3.4 Delay Time and Coating Thickness

The LEO-fit, described in section 3.2.1, gives a good approximation of optical size and coating thickness of rBC particles. Due to the misalignment of the split detector, quantitative information of coating thickness cannot be retrieved for the DC3 data from the LEO-fit. However, it is still possible to derive qualitative information on rBC particle mixing state from the peak positions of the detector signals, because the evaporating coating produces a different shape of the scattering signal compared to uncoated rBC particles (see also Moteki and Kondo, 2007; Dahlkötter et al., 2014). When an incandescing particle, consisting of a strongly absorbing rBC core with a non-absorbing volatile coating enters the laser beam, it starts to heat up due to light absorption. As the laser intensity increases when the particle approaches the beam center, the scattering signal increases with time. Due to the rising temperature, the volatile coating will eventually start to evaporate and the scattering cross section will shrink. Depending on the material and amount of the coating, the scattering signal can keep increasing towards the center with increasing laser intensity or decrease with decreasing scattering cross section. Figure 44 shows the

signal traces of the scattering and incandescence channel for an uncoated particle (left) and a thickly coated particle (right). The top row shows conceptual sketches of an uncoated (black, left) rBC particle and a coated one (black with light blue coating, right) and their progression through the laser beam, where the coating evaporates (loss of light blue coating in the right column) and the particle eventually incandesces (yellow). Vertical lines in black and red mark the peaks of the scattering and the incandescence signal, respectively. The particle with thick coating (right) has the highest peak of the scattering signal just before the coating starts to evaporate, about 2 µs before the incandescence signal peak. Due to the loss of the coating, the particle size has decreased stronger than the incident laser intensity has increased, resulting in a decrease of the scattering signal. The scattering signal trace of the coated rBC particle shows its highest peak slightly earlier than the peak of the incandescence signal and sometimes a smaller second one coinciding with the incandescence peak. Because of the lower boiling point of the coating material, the rBC core has not heated up enough at this point to produce a signal in the incandescence detector. The core keeps heating up in the laser beam until it incandesces about 2 µs later. A particle without or with only little coating has the peak of the scattering signal before the core starts to evaporate at its maximum temperature, coinciding with the incandescence signal peak.
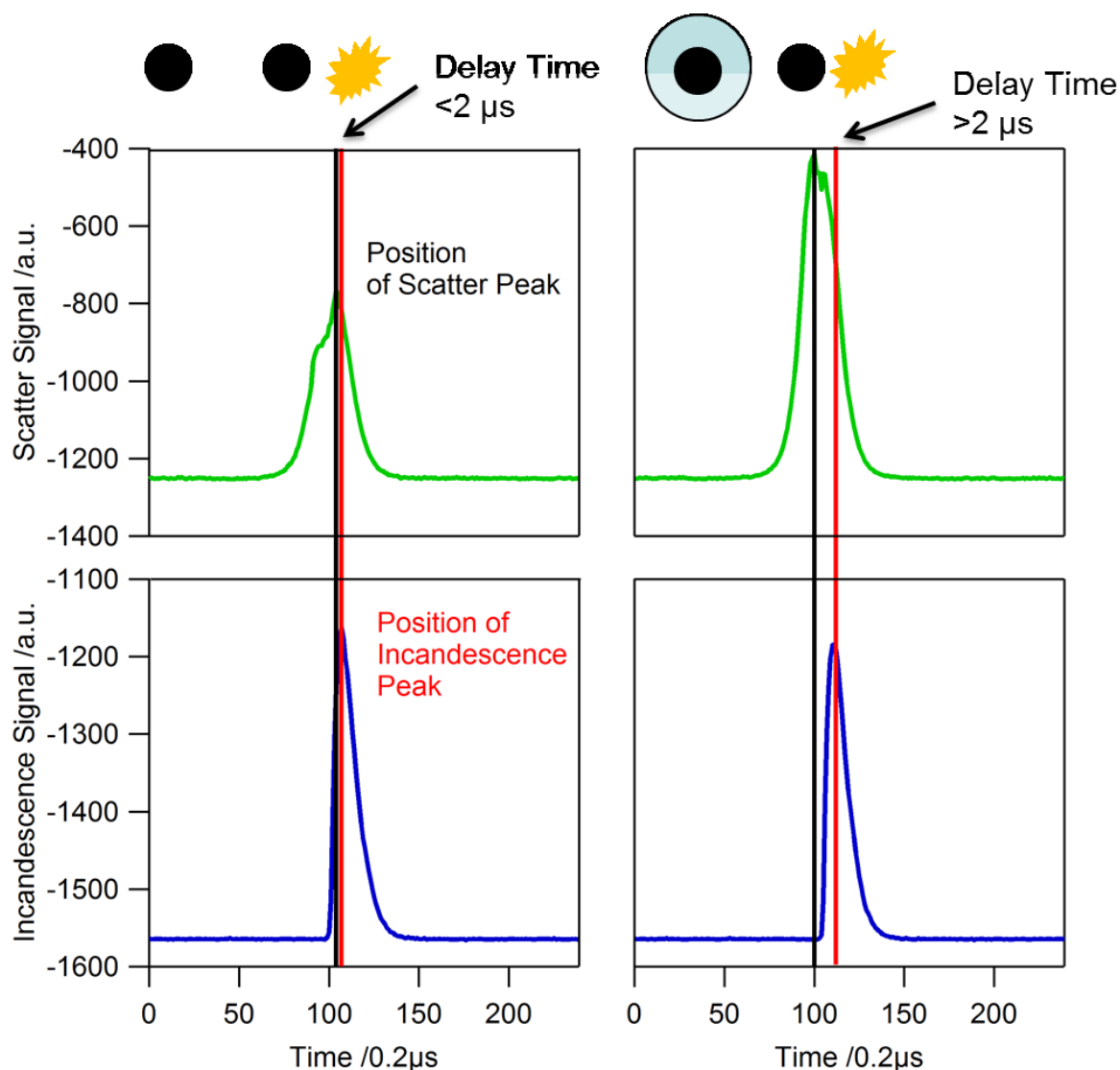
Figure 44: Example signal traces of the scattering (green) and the broadband incandescence (blue) channel for an uncoated (left) and a coted particle (right). The corresponding particle models with and without coating are shown in the top row before (black) and at incandescence (yellow). In the particle models at the top of the figure, the black circle represents the incandescing core, uncoated in the left panel and with a coating in light blue in the right panel. The positions of the peaks are marked in red (incandescence signal) and black (scattering signal). The delay time is the time difference between the two peaks, which is larger for particles with coating.

The delay time between the position of the scattering and the incandescence signal maximum can be used as a qualitative value for coating thickness. Figure 45 shows the relationship between the coating thickness and the delay time for an ambient measurement taken in August 2012 after the realignment of the split detector (see chapter 3.2.1.3). Coated rBC particles with a coating thickness up to 40 nm show a delay time between 0 and 1.5 µs, while particles with a coating above 30 nm show delay times of more

than 2 µs. This gap in the delay time can be used to sort rBC particles into two categories as (thickly) coated and thinly coated or uncoated.
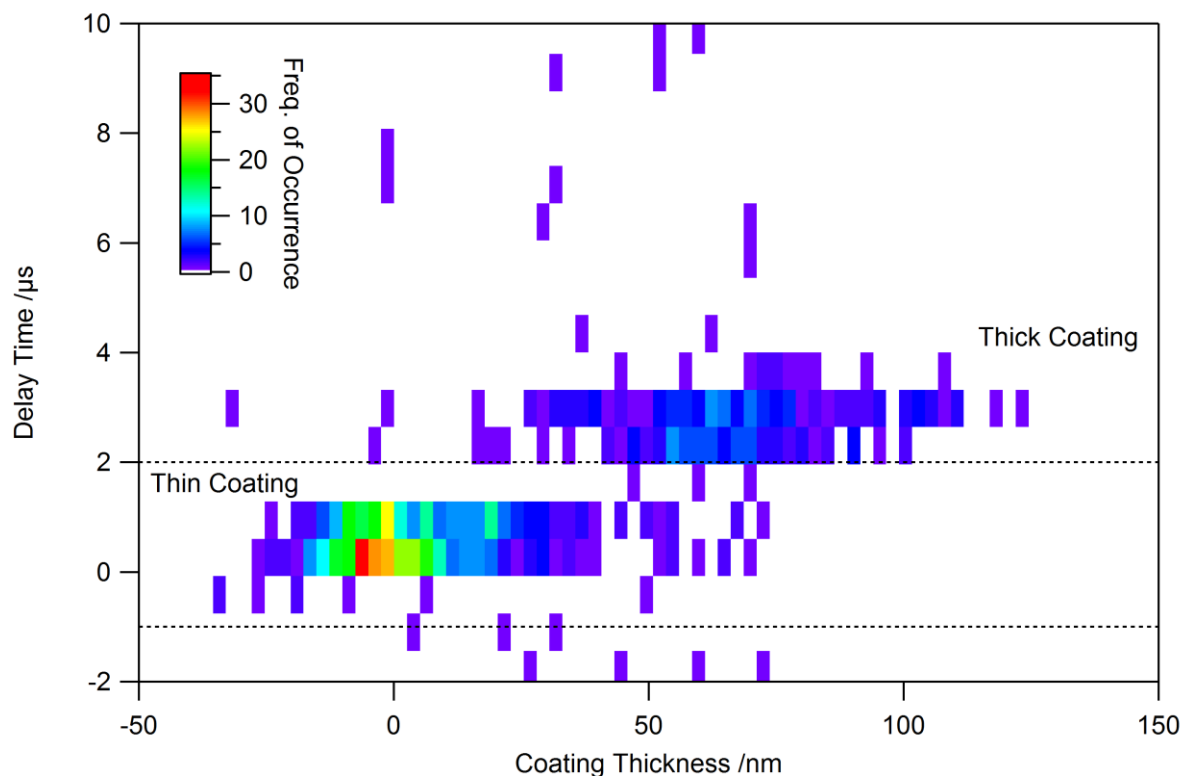

Figure 45: Relationship between delay time and coating thickness. Colors indicate frequency of occurrence with violet for low and red for high. Vertical dashed lines mark the delay time thresholds for thin (-1 to 2 µs) and thick (>2 µs) coatings on rBC cores.

Liu et al. (2010) showed that the average mixing state for the whole detection range of rBC particles can be represented by a narrow size range close to the maximum of the size distribution. To get a comparable average coating thickness distribution, the coating thickness is only given for a small part of the rBC mass size distribution. In this study, particles with an rBC core mass in the range of 4-6 fg, corresponding to a mass equivalent diameter size range of 162-185 nm are shown.

3.3.5 HYSPLIT Backward Trajectories and Dispersion Calculation

HYSPLIT (Hybrid Single Particle Lagrangian Integrated Trajectory Model) is a Lagrangian modelling system for the calculation of air parcel trajectories and the dispersion of trace species. It uses gridded meteorological data of the GFS reanalysis with a horizontal resolution of 1° as input (Draxler and Hess, 1997; Stein et al., 2015). Air parcels are tracked over the grid cells to evaluate how they spread.

Backward trajectories for source identification were calculated with HYSPLIT using the client programmed by Robert Baumann. The trajectories started along the flight path of the Falcon during the

flight sequences in BB layers, which were identified as described in section 3.3.2. For each of these sequences, backward trajectories were calculated going back two to five days. The calculated trajectories were compared to the MODIS fire map in order to find the source fire. For most cases, the backward trajectories indicated specific fires over which the trajectories passed. The trajectory calculation was also used to determine the age of the air mass as time difference between the time of measurement and the approximate time the trajectory passed over the source wildfire. For some cases, the ensemble trajectories spread out in a way that made it impossible to distinguish a certain direction, or spread out over too many fires. If that was the case, the region was used as source name instead of the name of the specific fire.

For the High Park fire, dispersion calculations were run to evaluate the distribution of CO, and therewith rBC particles, downwind of the fire. The fire was assumed to have the size of 350 km², which is roughly the total burned area of the fire, as a circle centered at the fire's location. The maximum plume injection altitude was set to 4000 m. The emissions were set to be constant at a unity value, so all shown dispersion calculation results represent only a relative concentration, not an absolute one. As the modelled trace species was CO, no washout is considered in the model as the model run time of 10 days is shorter than the average residence time of CO in the model.

_____

4 Results and Discussion

During the DC3 campaign, the Falcon encountered biomass burning (BB) layers from several wildfires (see Table 3 and Table 5). Most flight patterns were planned for measuring thunderstorms, but due to the abundance of forest fires, layers containing BB aerosol were often encountered during ascent or descent at the beginning and end of the flights. To demonstrate the characteristics of BB layers at different altitudes, two case studies are shown here. The first case study, June 11, 2012 in chapter 4.1, gives an impression of typical BB layers in the free troposphere. On that day, the highest rBC mass concentrations in the middle troposphere were measured, exceeding 1 µg/m³ at 7 km altitude. This case was also chosen because a coordinated flight between Falcon and DC-8 was conducted on that day, which provides additional data to the Falcon data set. The second case study, June 17, 2012, was selected to represent an example for an upper tropospheric BB layer, measured at 11 km altitude. The situation on this day gave a great opportunity to study the transport mechanisms of an upper tropospheric BB layer in detail as the BB layer was only about one day old when encountered. The chapter continues with an overview of all BB layers measured by the Falcon during DC3 in May and June 2012, focusing on a detailed analysis of the rBC particle properties like mass size distribution and mixing sate. Wildfires emit not only black carbon, but also a wider range of other particle types and trace gases. Here, coarse mode aerosol as a proxy for dust is shown (section 4.4.1). Dust particles can affect the optical properties of aerosol layers due to their large size, which can influence the retrieval of black carbon mass from sun photometer measurements (e.g. Koike et al., 2014), and are considered as efficient ice nuclei (e.g. Gonzi et al., 2011). CO as a tracer for inefficient combustion provides valuable insights into processes that involve cloud processing and wet removal as it is insoluble and survives these processes more or less unchanged. Particles however often undergo strong changes in the same processes. The rBC/CO ratio is therefore a good indicator for such processes and is discussed in section 4.4.2. The last part of this chapter, section 4.5, treats specifically the upper tropospheric BB layers, their extent, transport pathways into the upper troposphere, and their mixing into the UTLS region.

4.1 Case Study: June 11, 2012, as an Example for BB Layers in the Free Troposphere

On June 11, 2012, the DC3 operation area was dominated by a large mesoscale convective system (MCS) over Arkansas and Missouri. Satellite images from the GOES-13 visible channel (Figure 46) show the storm, which was moving southeastwards over Arkansas and Missouri as a large white cloud, extending about 300 km in northwest-southeast direction and more than 500 km in northeast-southwest direction. The image also shows state and country borders in thin yellow lines of which some are named for better orientation.
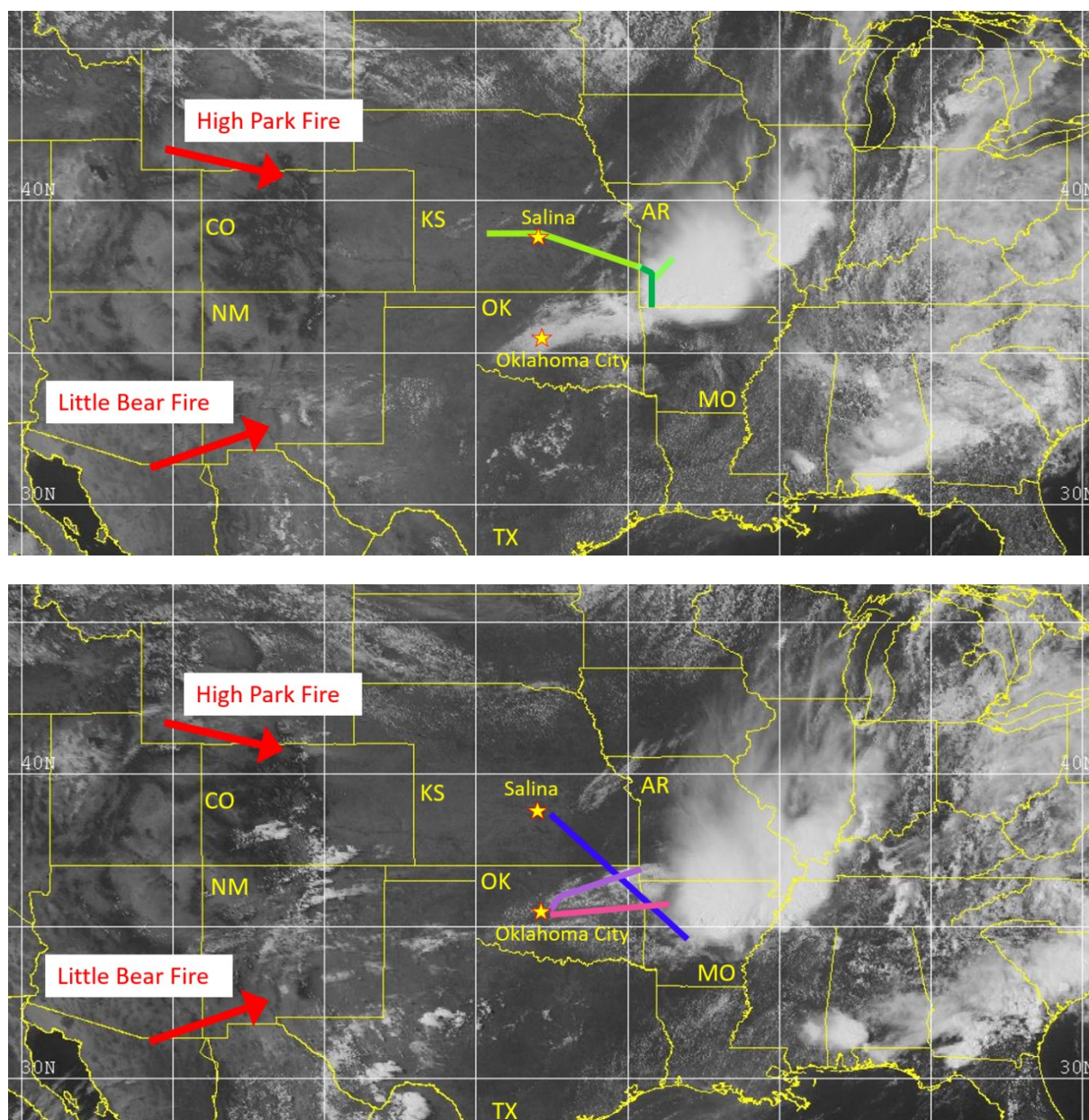
Figure 46: GOES-13 visible channel images of June 11, 2012, 16:40 UTC (top) and 20:40 UTC (bottom). The locations of two major fires in the area on that day, High Park Fire and Little Bear fire, are indicated by red arrows. Colored lines mark parts of flight tracks of the FALCON and DC-8 (see text). National and State borders are marked in yellow, the short names of some States are shown for orientation. The operation base Salina/KS and the refuel airport Oklahoma City/OK are marked by yellow stars.

This day provided a good opportunity to study the influence of a convective system on BB layers. Two large wildfires in Colorado and New Mexico emitting large smoke plumes were already burning for several days and influenced the environment of the MCS. The High Park fire in northern Colorado was

initiated on June 9, 2012 by lightning. A detailed analysis of the evolution of this fire can be found in Coen and Schroeder (2015), where the rapid evolvement of this fire due to local meteorology and topography is discussed. The Little Bear fire in New Mexico was started on June 4, 2012, and was still ongoing. On June 11, the smoke plumes from these two fires extended over a large area in the Midwest. The red arrows in Figure 46 point to the location of the two large fires. The smoke plumes from the fires can be seen in the satellite images in Figure 46 as thin greyish clouds, especially the High Park fire plume.

Two of the DLR Falcon research flights targeted the MCS on that day. Due to the limited reach of the Falcon, a refuel stop in Oklahoma City was necessary. Flight tracks when encountering BB layers are shown as colored lines in Figure 46. The first part of the first flight was a wing-by-wing intercomparison flight with the NASA DC-8. Both aircraft, Falcon and DC-8, met shortly after take-off to fly wing-by-wing on a constant altitude level at 2.2 km in east-west direction through a dense BB aerosol layer located behind the MCS. The top image shows the first part of the flights on June 11 at 16:40 UTC, when the Falcon and the DC-8 flew on the lower level of the intercomparison sequence. Then they climbed out of the aerosol layer to 6.7 km in cleaner background air and continued southeastwards towards the Arkansas/Missouri thunderstorm. The track of the wing-by-wing flight is indicated as a light green colored line in the top panel of Figure 46. They separated after a short time of flying at constant altitude. The Falcon turned northeast and probed the thunderstorm anvil at 11km altitude (marked in Figure 46 in lighter green until the Falcon entered the clouds for anvil profiling). The dark green line marks the flight track of the DC-8 after the two planes separated. The image in the lower panel was taken at a later time (20:40 UTC), when the Falcon took off after refueling in Oklahoma City and ascended towards the storm for the second flight (pink line). The dark violet line marks the flight track when the Falcon descended at the end of the first flight, which was about one and a half hours before the satellite image was taken. The DC-8 targeted a storm over Alabama on that day and returned to Salina around 00 UTC. On the way back from Alabama, at about 23 UTC, the DC-8 passed the western edge of the storm over Missouri. The track of the return flight on the western side of the thunderstorm is added in dark blue in Figure 46.

HYSPLIT backward trajectories show that the smoke layer probed during the intercomparison over Kansas (light green colored flight track) originated from the High Park fire in Colorado, while the backward trajectories for the air mass over Oklahoma and Arkansas (pink and violet colored flight tracks) come from the Little Bear fire in New Mexico. For the ascent from Salina, backward trajectories for the flight track are shown in Figure 47. Below about 4 km altitude, the air mass passed over the High Park fire and had changed little in altitude at the measurement location, visible in Figure 47 as red and orange trajectories. The air mass measured closer to the thunderstorm, at a higher altitude, was influenced by the Little Bear fire.
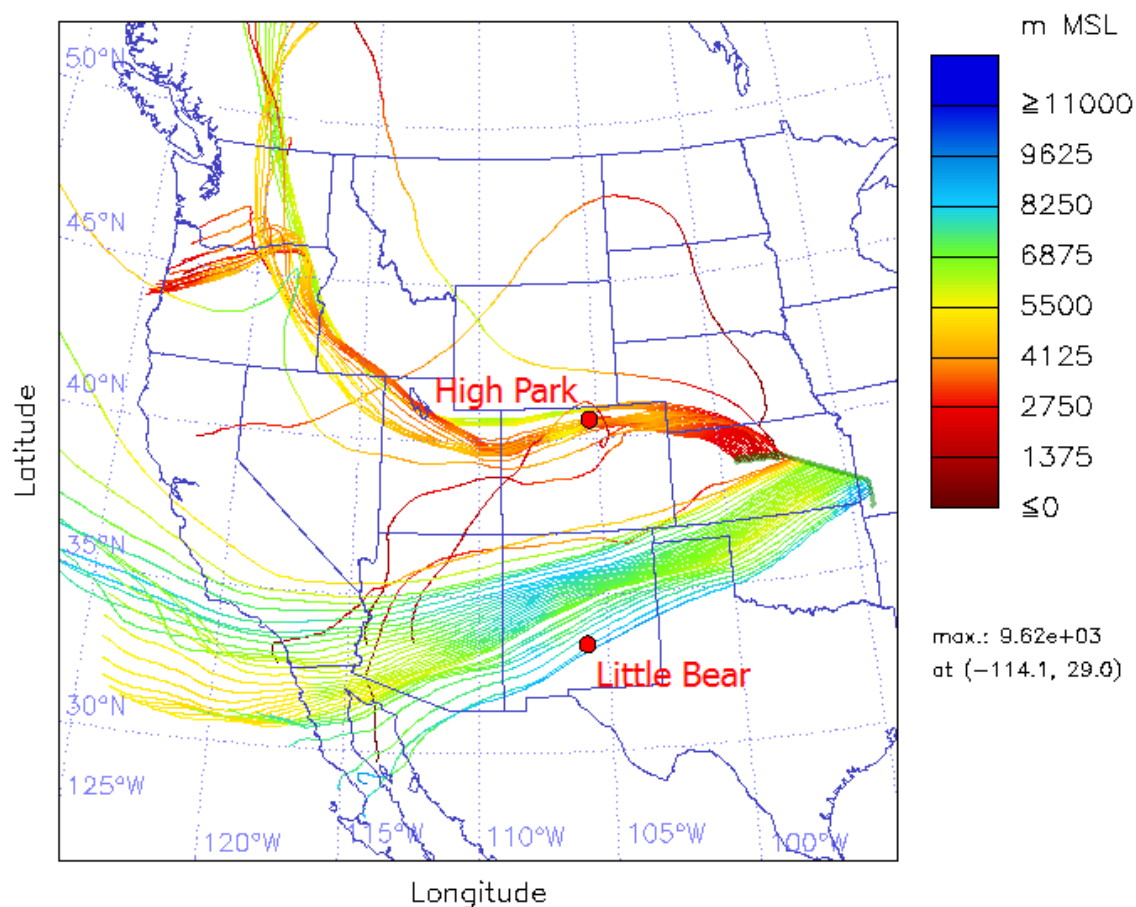
Figure 47: Three days backward trajectories for the ascent and transfer from Salina to the Arkansas thunderstorm, color-coded with trajectory altitude. The two biggest fires on that day, the High Park fire and the Little Bear fire, are marked. The Falcon flight track is marked by a green line, as in Figure 46.

The air mass measured over Oklahoma, on the western side of the storm, passed over the Little Bear fire. HYSPLIT backward trajectories for the ascent after the refuel stop in Oklahoma City are show in Figure 48. According to the trajectories, the air mass that had passed with little change in altitude over the Little Bear fire moved towards Oklahoma. The MCS in Arkansas and Missouri formed downwind of the Little Bear fire.

Figure 48: Three days backward trajectories for the ascent from Oklahoma City (pink line here and in Figure 45) towards the thunderstorm over Arkansas, color-coded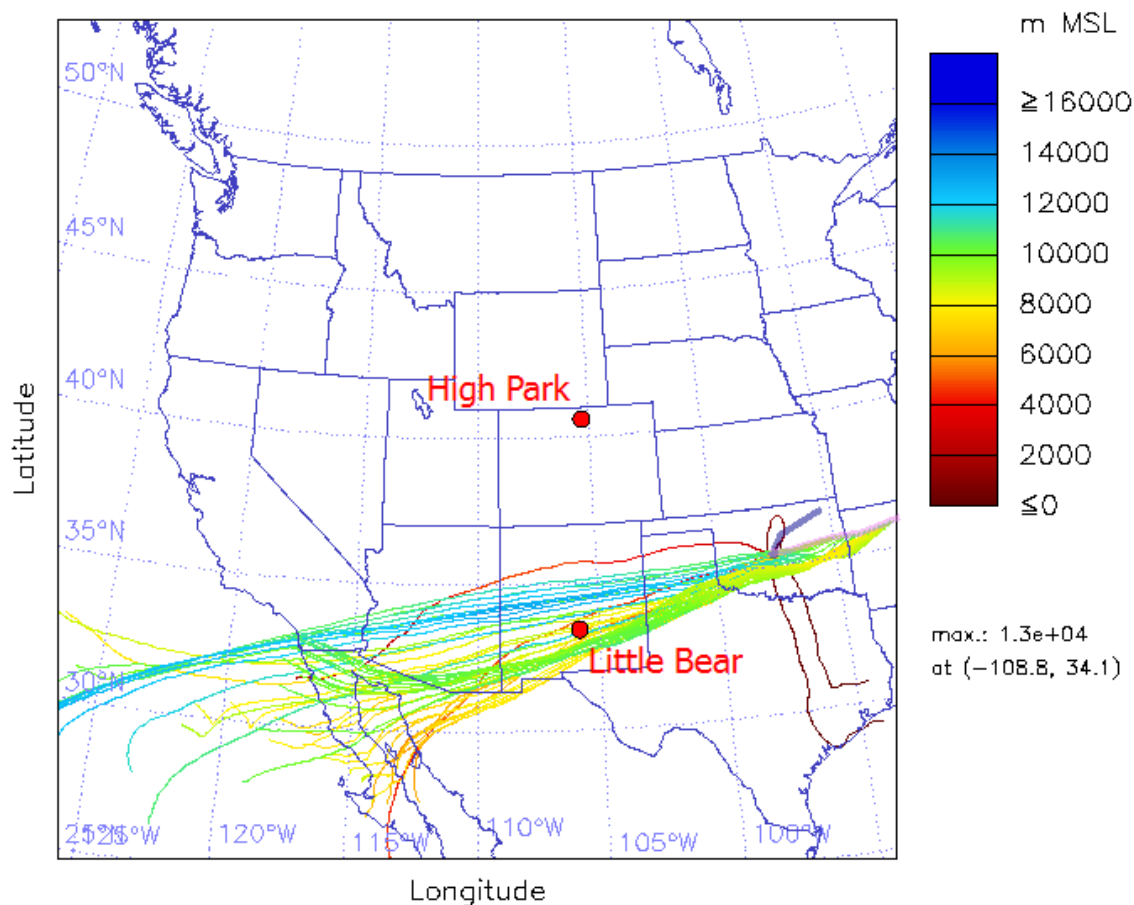 according to trajectory altitude. The two biggest fires on that day, the High Park fire and the Little Bear fire, are marked with red dots. The flight track of the Falcon's decent about one hour earlier is added in dark violet.

Figure 49 and Figure 50 show the aerosol backscatter signal from the DIAL on board of the DC-8 along the flight tracks to and from Alabama. Since this lidar looks both upwards and downwards, the figures show aerosol backscatter both above and below the flight track, which can be seen as a black line in the figures. The green lines at the top of Figure 49 refer to the flight tracks marked in Figure 46. The track marked in light green was the wing-by-wing flight of both DC-8 and Falcon. After both planes separated at an altitude of 7 km, the Falcon probed mainly the rear side of the storm, which moved south-east-wards. Due to its limited reach, the Falcon had to refuel in Oklahoma City in between the measurements. The track descending towards Oklahoma is shown in violet in Figure 46, and the track ascending from Oklahoma City, leading the plane back to the storm, is shown in pink. The back transfer and descent from the storm to Salina was on a similar track as the northwestern part of the DC-8 track in dark blue, but at different altitudes and about half an hour earlier.
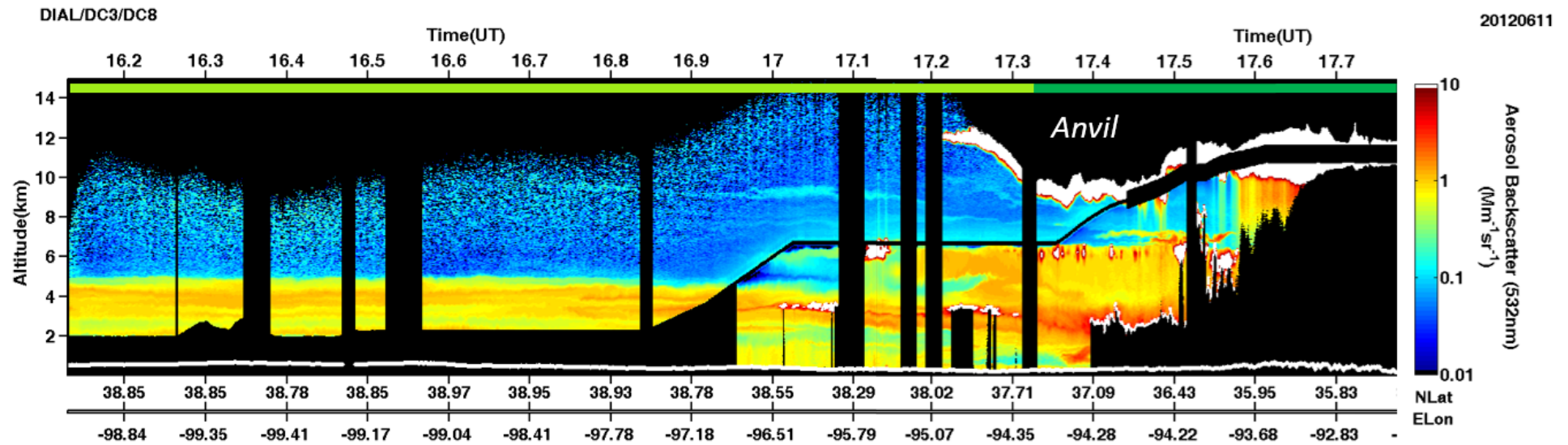
Figure 49: Aerosol backscatter signal at 532 nm from the DIAL onboard of the DC-8 for the first part of the flight. Colored bars in the top of the image refer to the flight track color-coding in Figure 44. The Arkansas thunderstorm is located at the right edge of the image; the anvil is already visible after 17.2 UT above 10 km. (Image courtesy of NASA Langley, Jonathan W. Hair and Marta A. Fenn)
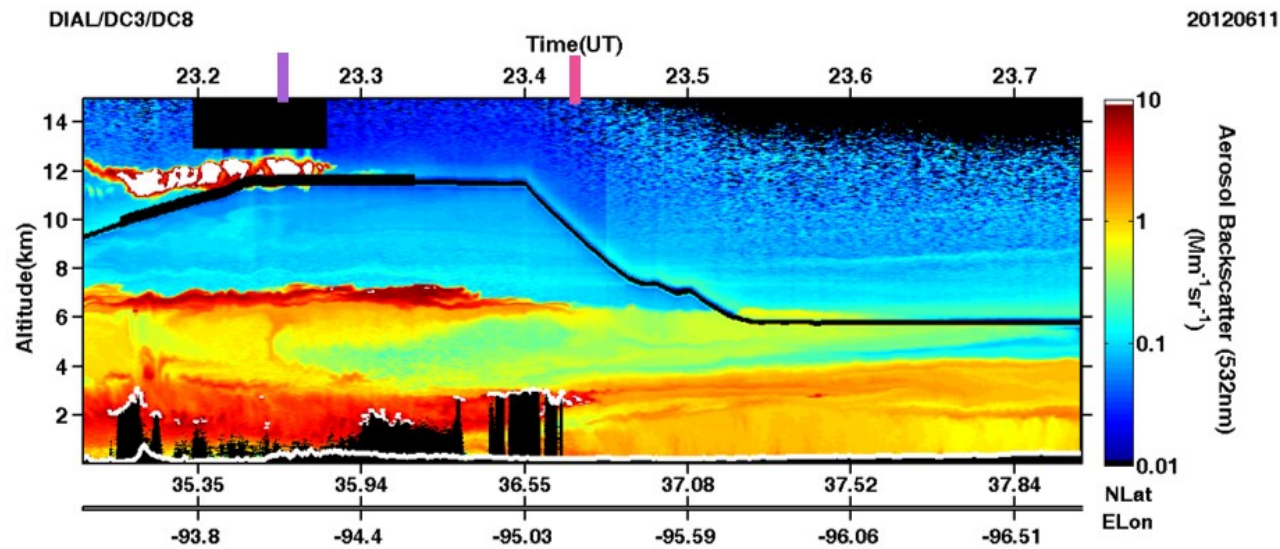
Figure 50: DIAL aerosol backscatter signal at 532 nm for the second part of the DC-8 flight on 11 June 2012. The violet and pink vertical lines mark the crossing of the Falcon aircraft on the descent to and the ascent from Oklahoma. The flight track corresponds to the blue line in Figure 46, with south to the left. The Arkansas thunderstorm is located in front of the page, from the reader's point of view. The edge of the anvil is visible at 12 km. (Image courtesy of NASA Langley, Jonathan W. Hair and Marta A. Fenn)

Figure 51: Vertical profile over Salina/Kansas of the CO concentration, refractory black carbon mass concentration (stp values), the fraction of particles in the size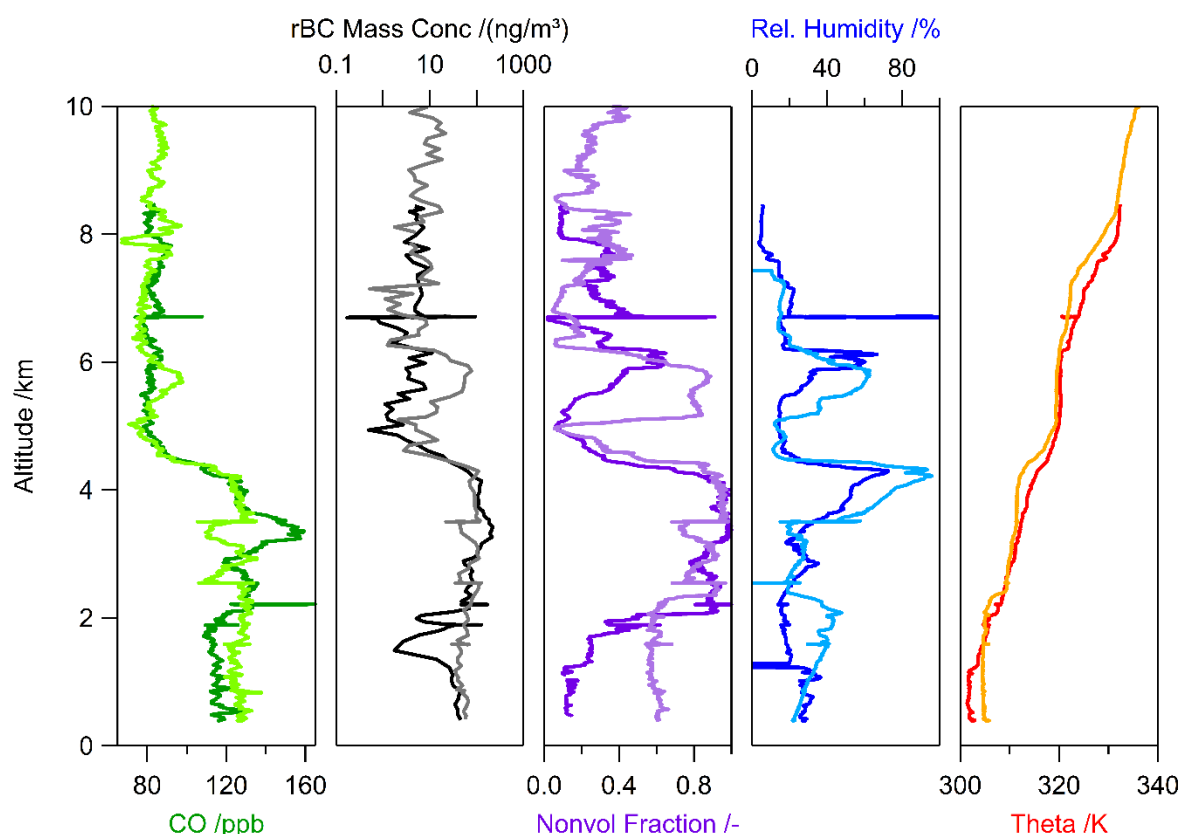 range 10-1000 nm which are not volatile at 250°C, the relative humidity, and the potential temperature (from left to right). Data from the ascent from Salina at the beginning of the first flight are shown in darker colors, and data from the descent to Salina at the end of the second flight are shown in lighter colors.

The lidar images in Figure 49 and Figure 50 show the extended aerosol layer over Salina (left in Figure 49 and right in Figure 50) originating from the High Park fire. The first part of the wing-by-wing sequence was at 2.2 km altitude in the lower part of this layer. The BB aerosol layer extended from the top of the boundary layer at 2 km to 5 km. Figure 51 shows vertical profiles of data measured by the Falcon instrumentation over Salina during ascent of the first flight and the descent at the end of the second flight. Concentrations of rBC mass and CO show that the layer was clearly separated from the boundary layer during ascent which was around noon local time (11:10h – 12:20h local time). The fraction of non-volatile particles is enhanced in the BB aerosol layer to values close to 1. The dominance of non-volatile particles, here mainly black carbon and possibly also dust, indicate a strong influence of BB aerosol over more volatile compounds like sulfate and organics. Data from the descent in the late afternoon (17:34h – 18:22h local time), shown in lighter colors in Figure 51, indicate that the BB layer and the boundary layer have mixed during the afternoon. While CO and rBC mass concentrations remain on a similar level at about 130 ppb and about 100 ng/m³ between 2 and 5 km, CO concentrations in the boundary layer increased and the clear separation between the layers, visible as a dip in concentrations

shortly below 2 km altitude, is replaced by a well-mixed profile in the rBC mass concentrations. The fraction of non-volatile particles in the boundary layer below the BB layer is at about 10% and increases to 60% in the afternoon, but it is still lower below 2 km than in the BB layer between 2 and 5 km. This indicates that BB aerosol was mixed into the boundary layer when the convective boundary layer increased in depth over the day. The sharp upper edge of the layer just below 5 km can be seen both in the lidar image as also in the vertical profile of the in-situ data. The lower edge of the BB layer is more clearly during ascent from Salina (darker colors in Figure 51). Over the course of the day, the convective boundary layer grows into the BB layer above, seen as an increase in thickness of the stably stratified layer of constant potential temperature. The mixing of BB layer air into the PBL leads to an increase in concentrations of CO, rBC mass and a higher fraction of non-volatile particles. Also shown in Figure 51 is the relative humidity, which is low throughout most of the BB layer with a strong increase at the top of the layer. The vertical profile of the potential temperature shows that the BB layer is capped by a strong inversion. That could account for the sharp upper edge, which was also visible by eye from the plane. The static stability in the layer decreases over the day, which is not very surprising considering the convective environment that led to nearly daily evolution of strong convective storms.
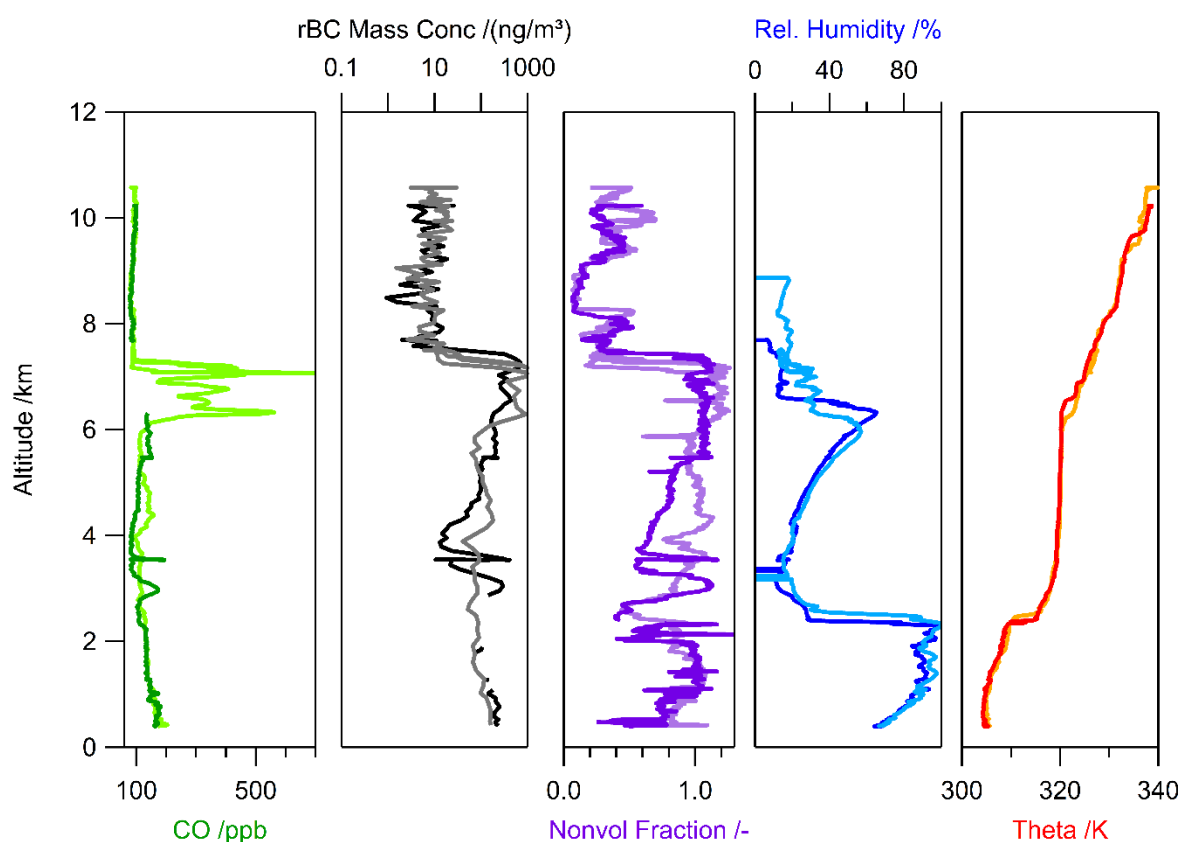

Figure 52: Same as Figure 51, but measured over Oklahoma City/Oklahoma. Data from the descent to Oklahoma City at the end of the first flight are shown in darker colors; data from the ascent from Oklahoma City at the beginning of the second flight are shown in lighter colors.

The vertical profiles in Figure 51 show a second, thinner BB layer at an altitude of 6-7 km above the thick layer below 5km. This layer can also be seen in the lidar image in Figure 49, which also illustrates that the layer increases in thickness, concentrations and altitude when getting closer to the storm at the right edge of Figure 49. This layer is deeper below the anvil, which is visible as white area of strong backscatter and black area where the lidar's laser beam cannot pass through the cloud in the top right part of Figure 49. In this area, close to the storm, the layer extended higher up and looked more filament-like. The structure of this layer is not as dense and compact as the layer between 2 and 5 km over Salina. On the upper level of the intercomparison sequence (17:02 – 17:16 UTC) at 6.7 km altitude, the upper edge of the layer was passed after crossing a small cloud at 17:08 UTC. As all 10 s data points of both ascent and descent were included in Figure 51, sampling both above and within the upper edge of the BB layer result in the strong variations in all values at 6.7 km.

While Figure 51 shows vertical profiles from the rear side of the storm, Figure 52 shows profiles measured by the Falcon at the western side of the storm, taken during descent towards Oklahoma City, and the ascent back to the storm for further measurements. The Falcon flight tracks were crossed at nearly a right angle about two and a half hours later by the DC-8 which passed the west side of the storm on the transfer back from the operation area in Alabama to Salina. In both figures, Figure 50 and Figure 52, a BB layer with high concentrations is visible at about 7 km altitude, originating from the Little Bear fire in New Mexico. This layer is located several km beneath the storm's anvil, which is visible in the top part of Figure 50 at an altitude of 11-12 km. The concentrations of rBC mass and CO in this BB layer were among the highest found in Falcon data of the whole DC3 field campaign. The air mass below this pronounced BB layer is also influenced by BB aerosol as the enhanced non-volatile fraction indicates, but rBC mass concentrations are lower by nearly one order of magnitude than in the BB layer above. Yellow colors in the lidar image (Figure 50) also indicate elevated particle concentrations in this air mass due to entrainment of BB aerosol. As the nearly constant potential temperature indicates, the layer at 2.5-7 km altitude below the thick BB layer is well-mixed, and very dry with relative humidity values going down to 10%.

HYSPLIT backward trajectories for the flight track of the ascent from Oklahoma are shown in Figure 48, corresponding to the pink line in Figure 46, bottom and the vertical profiles in darker colors in Figure 52. The color-coding by altitude shows that the trajectories stay at the same altitude for most of the time. For the BB layer at 7 km altitude, the trajectories pass the Little Bear fire at around 00 UTC on June 11. The smoke plume was thick enough to be detected as a cloud in the GOES images. According to that, the cloud top height of this plume was about 2 km (see Figure A 14, page 192 in the appendix), much lower than the 7 km the layer that was encountered by the Falcon. A possible explanation for this altitude difference could be that the layer of BB aerosol was lifted adiabatically. The MCS downstream of the fire could have acted as an obstacle in the flow, forcing the air to rise.

All in all the case of June 11 presents two interesting BB layers from the High Park fire and from the Little Bear fire. The layer over Salina, originating from the High Park fire, shows characteristics as they were typical for DC3 BB layers directly on top of the boundary layer: well-mixed and with a sharp upper edge. The separation from the PBL underneath vanishes over the day due to the evolution of the convective boundary layer, increasing CO concentrations and the fraction of non-volatile black carbon aerosol at the ground. The intense Little Bear BB layer with rBC mass concentrations exceeding 1 µg/m³ was encountered as elevated layer at an altitude of 7 km. Similar to the High Park fire layer, it is characterized by stable stratification, low relative humidity and high rBC mass concentrations. The similarities and differences between these two layers, and the other BB layers during DC3, will later be discussed in detail with a focus on the properties of rBC particles (see chapter 4.3). The dynamic situation in and especially around the storm seems to influence the vertical distribution of BB layers. Close to the MCS, within the Anvil area, the BB layers reach higher altitudes than the layer farther upwind. Therefore, the interaction between intense thunderstorms and BB layers will be a discussion topic of a later chapter (4.5.2). The layers measured on June 11 were all located in the lower and middle troposphere, not exceeding an altitude of 7.5 km. The next section will take a closer look on a BB layer that was encountered in the upper troposphere.

4.2   Case Study: June 17, 2012, as an Example for a Biomass Burning Layer in the Upper Troposphere

On June 17, 2012, a large frontal system stretched from Arkansas (AR) towards the northwest till Canada. As the satellite image from GOES-13 channel 1 (visible) in Figure 53 shows, was the Midwest mostly cloud free. The frontal system is visible as large white clouds stretching towards the top right corner of Figure 53. The Falcon crossed this system at about 11 km altitude on the flight from Salina (marked by a star in Figure 53) to Syracuse (west of the map in Figure 53). The flight track is shown as a colored line in Figure 53; the color-coding represents the measured rBC mass concentrations.
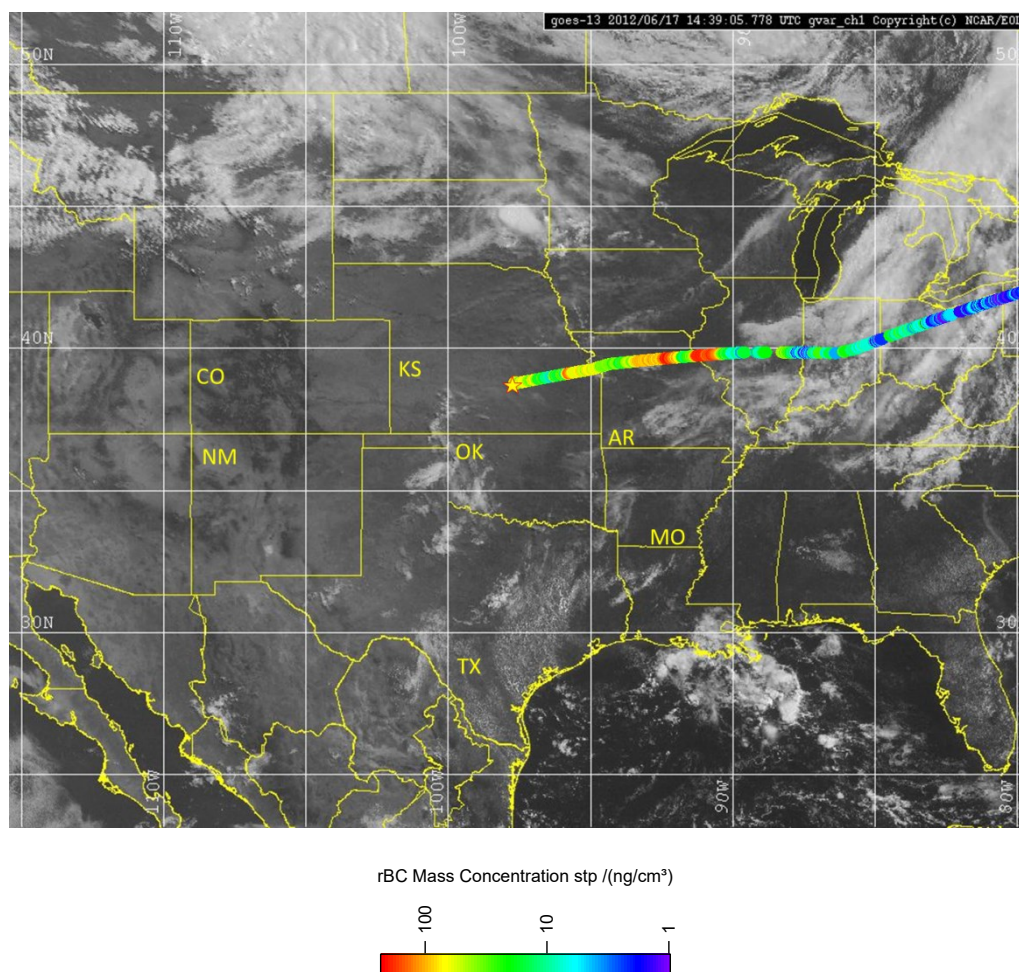
Figure 53: Satellite image from GOES-13, channel 1 (visible) with the flight track of flight 120617a marked. The color coding of the flight track corresponds to the measured rBC concentration. National and state borders are marked in yellow, the short names of some states are shown for orientation. Salina/KS is marked by a yellow star. (time of satellite image 14:39:05 UTC; Falcon position at that time: 39.5483°N/93.2146°W).

High concentrations in rBC mass, up to 200 ng/m³ (orange and red colors), were measured at 11 km altitude over Arkansas and the border to Illinois, exceeding background concentrations of about 1-10 ng/m³ (Schwarz et al., 2013) by more than one order of magnitude. The satellite image was taken at 14:39:05 UTC, the time of the Falcon's first encounter with the 11 km layer over Arkansas. Elevated rBC mass concentrations up to 100 ng/m³ were also found in a weaker layer during ascent between 9 and 11 km altitude, visible as the yellow colored sequence over eastern Kansas.
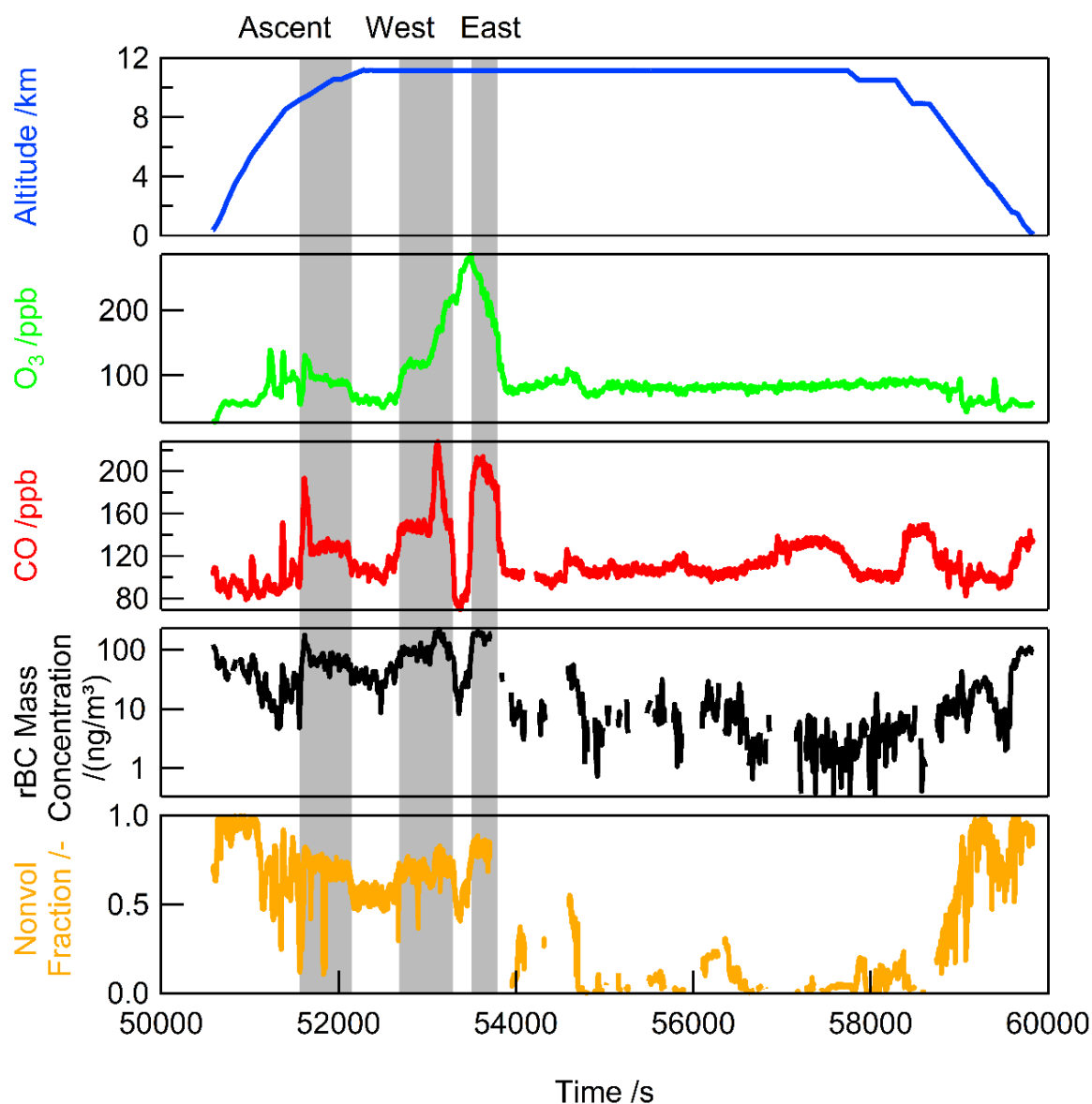
Figure 54: Time series of a selection of data measured during flight 120617a. From top to bottom: altitude, O₃ concentration, CO concentration, rBC mass concentration from SP2, and the fraction of non-volatile particles as ratio between CPC concentrations with and without the thermodenuder in the inlet line. The sequences where pronounced biomass burning layers were found are shaded in grey. The three encounters are referred to as Ascent, East, West, from left to right, see labels at the top of the figure. Data measured inside clouds were removed leading to the missing values in the second part of this flight.

A time series of several measured trace gas and particle concentrations is shown in Figure 54. The time when the Falcon encountered a BB layer is shaded in grey. These layers are characterized by an enhancement in CO (red) and rBC mass concentration (black). Concentrations in CO and rBC mass

were much higher than usually found in the upper troposphere. While the background values for CO concentration are around 80 ppb, maximum values exceed 200 ppb in the layers. The rBC mass concentration in the layers are above 100 ng/m³, values more typical for the polluted boundary layer than for the upper troposphere. Background values for CO, O_3 and rBC mass concentration are shown in Table 11 for comparison. The four listed background sequences were also measured at an altitude around 11 km on flights when the Falcon climbed to cruise altitude to reach the targeted measurement area. The fraction of non-volatile particles (orange) shows a slight increase in the layers. About 60-80% of all particles are non-volatile, a much higher fraction than usually found in the upper troposphere. This indicates a strong influence of the non-volatile black carbon particles on the aerosol composition in the layers. O_3 concentrations show roughly the same shape as CO and rBC mass concentrations in the first BB layer encounter (51565-52149) while all potential correlations in the two encounters at 11 km altitude are masked by the strong O_3 enhancement at around 14:50 h (53400 UTC). This strong increase in O_3 concentrations between the two layer encounters at 11 km altitude points to the presence of a tropopause fold behind the front. After entering the cloudy part of the system, cloud passages led to gaps in the rBC data. However, in between the clouds concentrations of rBC mass were much lower, less than 10 ng/m³, which is close to the expected background concentrations.

Table 11: List of average measurement values of O₃, CO and rBC mass concentration for the three biomass burning layer encounters on June 17. Ascent, East and West refers to the biomass burning sequences during flight 120617a (see Figure 54). Background sequences were measured during other flights at 11 km altitude and are shown for comparison. Values in brackets represent the minimum and maximum measured value in the respective time interval.

	Seconds after Midnight on June 17, 2012	O3 (min/max) /ppb	CO (min/max) /ppb	rBC Mass Concentration (80-450 nm) /(ng/m³)
Ascent	51565-52194	91 (55/131)	131 (96/193)	67
West	52686-53289	142 (80/220)	159 (123/228)	111
East	53504-53795	222 (163/275)	198 (172/212)	185
Background 120530a	70170-71230	107 (92/128)	82 (75/90)	15
Background 120608a	60051-60805	135 (113/165)	80 (74/88)	13
Background 120608b	82425-83587	110 (92/142)	71 (62/85)	6
Background 120614a	64909-65783	105 (83/131)	92 (76/110)	7

HYSPLIT backward trajectories for the three BB encounters marked in Figure 54 are shown in Figure 55, color-coded with age (left) and altitude (right). Active fires on that and the previous day are also marked. Trajectories pass over the High Park fire about 20 hours earlier but stay above 11 km and do not reach down to the lower troposphere, where the fire was located. Since the High Park fire did not produce a pyrocumulus cloud that would reach the upper troposphere on that day (Lang et al., 2014), the BB layer must have reached the upper troposphere in a way that is not captured by the HYSPLIT trajectory model.
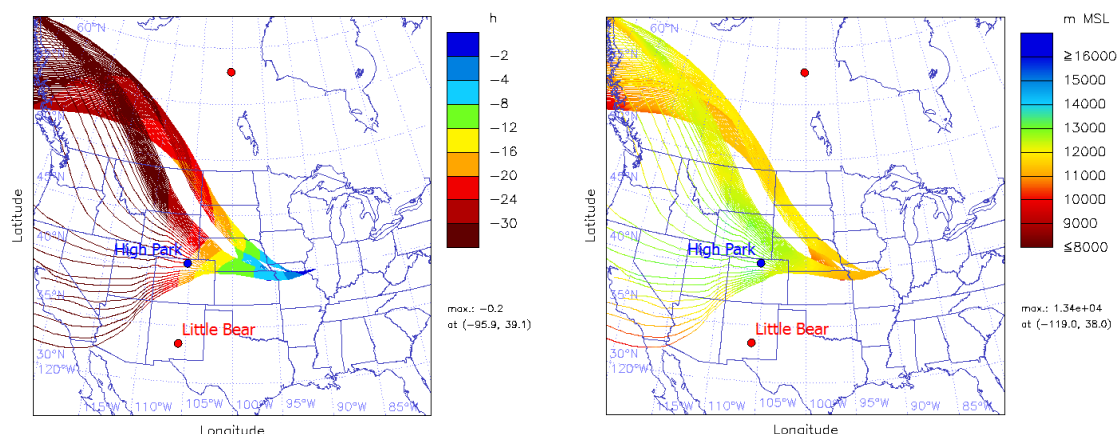
Figure 55: HYSPLIT backward trajectories for the sequences with high rBC mass concentration, color-coded by the time difference to the start time (left) and the trajectory altitude (right). The position of the High Park fire is marked in blue. Two other larger fires that were active on that day are shown as red dots, the Little Bear fire is also labeled.

The development of the frontal system is shown in Figure 56 for the previous 20 hours up to June 17, 14:39:05, which is the same time step as the visible image in Figure 53. Since this period covers the night, thermal infrared images (channel 4) instead of visible images (channel 1) are shown. On the previous day, June 16, 2012, two strong thunderstorms evolved, one over Colorado and the other over Iowa and Missouri. The storms can be identified in Figure 56 by the light green and greyish-black colors, which indicate the cold cloud tops of the convective clouds. With an altitude of 13 km (over Colorado) to 14 km (over Iowa), the storm tops reached even above the tropopause, which was at approximately 10.5 km. , Both storms grew up to tropopause height and developed overshooting tops, visible as grey to white spots in the middle of the green and grey anvil in Figure 56. The remnants of the dissipating storms merged during the night and accompanied the frontal system the Falcon crossed in the morning of June 17.
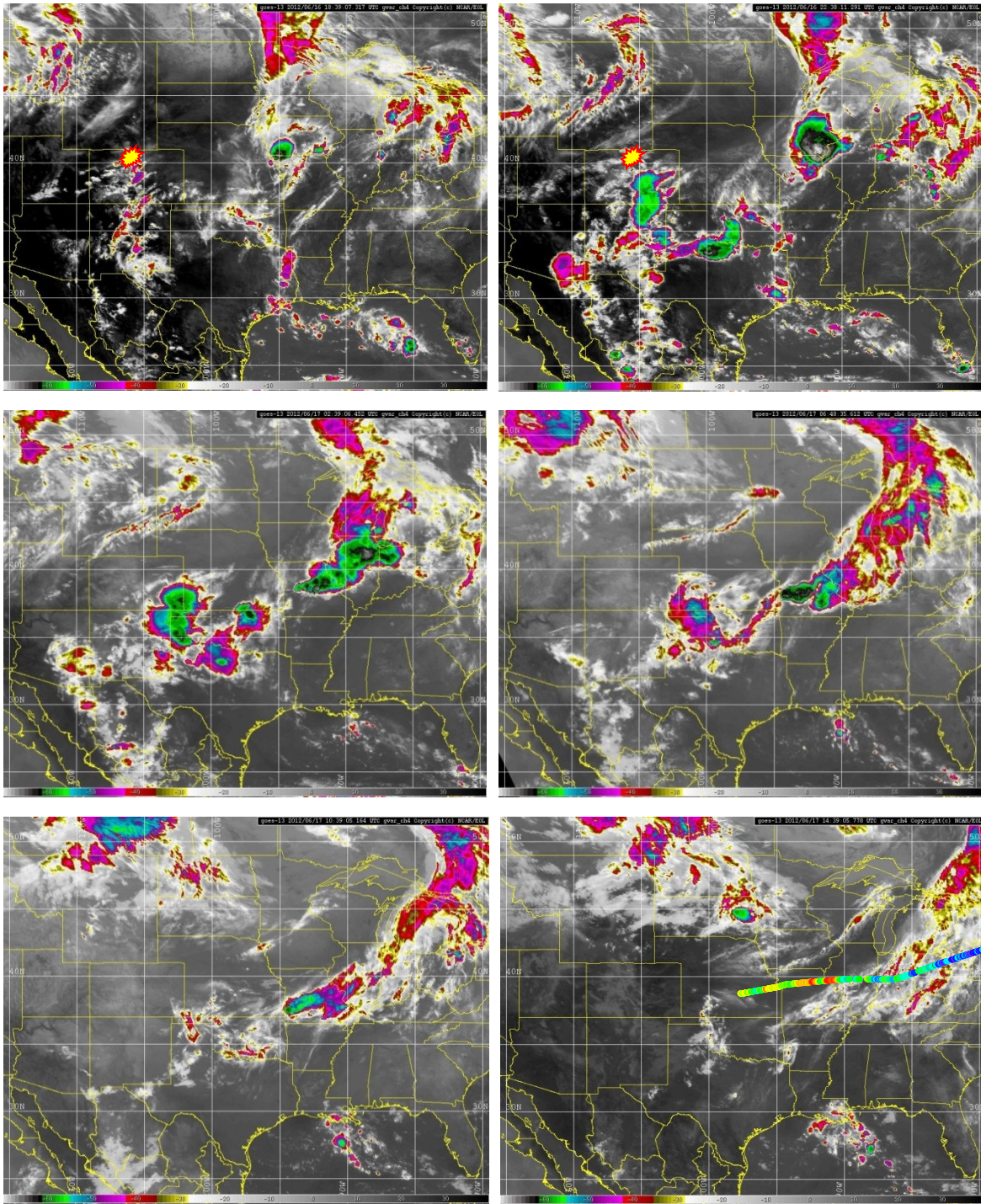
Figure 56: Thermal infrared satellite images from GOES-13, channel 4. A color scale for the temperature is included in the bottom of each image with low temperatures, corresponding to high cloud top altitudes, to the left. Images are shown every four hours starting at June 16, 2012, 18:39 UTC (top left). The bottom right image was taken at June 17, 2012, 14:39 UTC, at the same time step as the visible image in Figure 53. The position of the High Park fire is marked in the first two images as a red-encircled yellow spot. The flight track is marked in the last image color-coded with the rBC mass concentration with the same scale as in Figure 53. (http://catalog.eol.ucar.edu/dc3_2012/)

The BB layers were measured right before the Falcon entered the frontal system, visible as a stretched band of clouds showing pink colors in the last three figures in Figure 56. In the area that is covered by the backward trajectories starting from the flight track (Figure 55), the only larger active fire was the High Park fire. To learn more about the distribution of the High Park fire emissions, the NOAA HYSPLIT model was used to calculate the emission dispersion (see chapter 3.3.5). The resulting distribution of CO from the High Park fire on June 16, 2012 is shown in Figure 57, with the fire marked by a yellow-red dot.
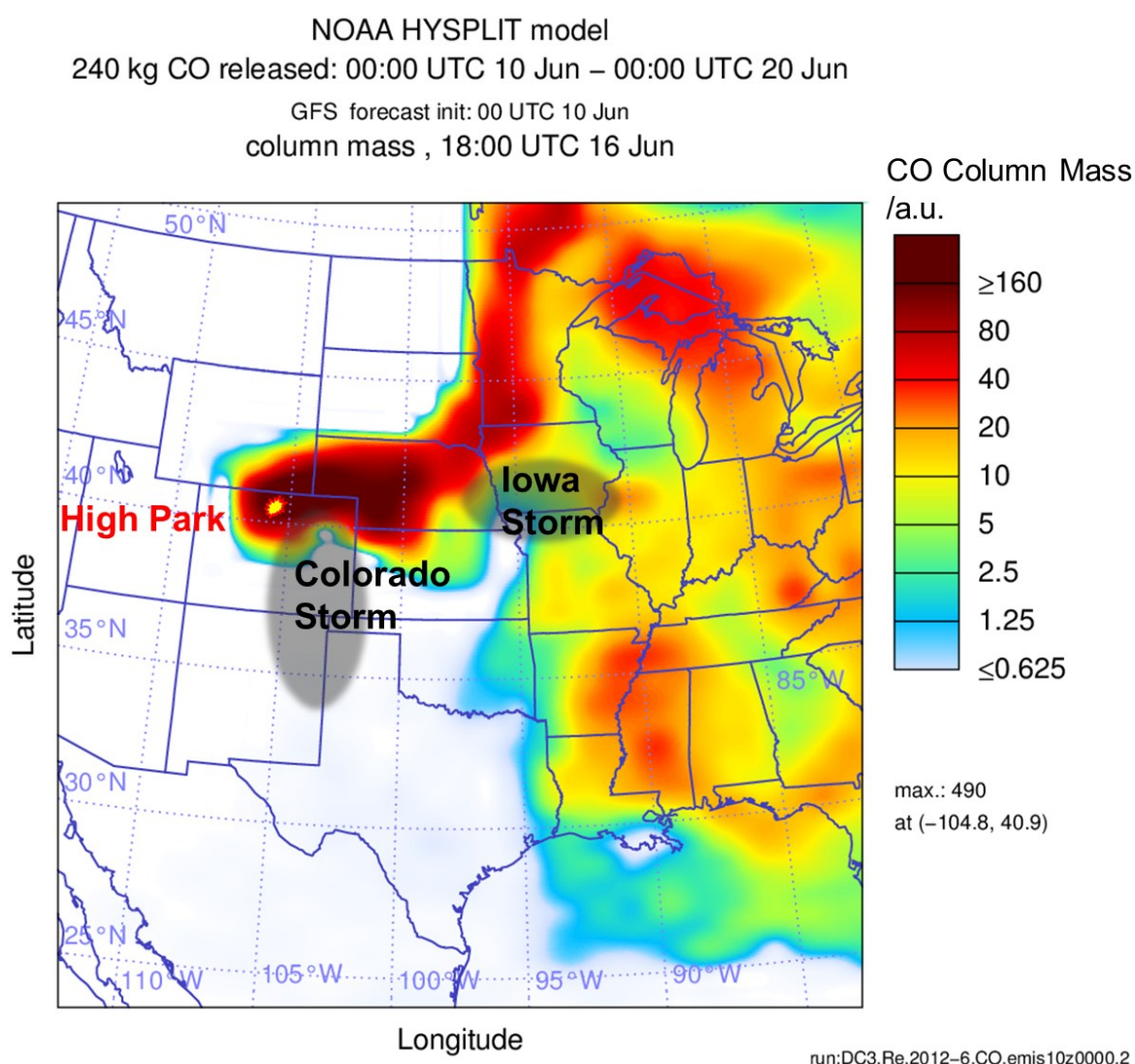

Figure 57: Dispersion of the High Park fire emissions at June 16, 18 UTC, calculated with the HYSPLIT dispersion model stared at June 10, 2012 with constant emission. Grey shaded areas mark the region where thunderstorms developed close to the fire plume (see also Figure 56). The location of the High Park fire is marked by a yellow-red dot.

_____

Similar to the backward trajectories, dispersion calculations do not indicate vertical transport from the lower to the upper troposphere. The altitude, the modelled emissions reach at the position where they were measured, corresponds therefore to the maximum injection height used to set up the calculations. The vertical uplift of the BB layer as observed by the Falcon aircraft must therefore have happened in a way which is not captured by the model. This could be due to the small scale of the process, as the model grid is quite coarse with a horizontal resolution of 1°. Sub-grid scale processes associated with the thunderstorms in this area could account for that. Section 4.5.2 is dedicated to a closer look on this. The horizontal distribution of the High Park fire emissions calculated with the HYSPLIT dispersion tool are shown in Figure 57 for the time around which the two storms developed, that were shown in Figure 56. The dispersion calculations indicate that both thunderstorms developed partly within the fire emissions (see grey shaded areas in Figure 57), possibly influencing the storms' inflow.
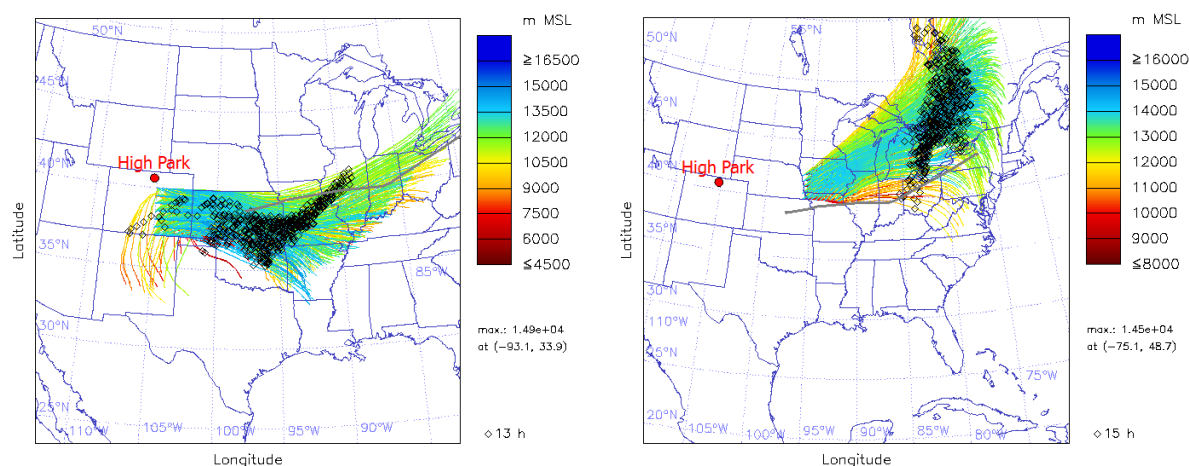
Figure 58: HYSPLIT forward trajectories starting in the anvil region of the Colorado (left) and Iowa (right) thunderstorm. The 120617a flight track is shown in light grey. Black markers indicate the position of the trajectory at the time the biomass burning layers were measured by the Falcon, around 14 UTC on June 17, 2012 (see grey shaded areas in Figure 54).

Forward trajectories from the anvil regions of both storms, started at the time of their largest extent, show that the outflow air mass moved westwards in both cases Forward trajectories from the Colorado storm's anvil region are shown in the left part of Figure 58, the right part shows forward trajectories started from the Iowa storm's anvil region. The trajectories were started at 01 UTC on June 17, approximately 13 hours before the Falcon's encounter with the layers at 11 km altitude. The time of the encounter is marked with black symbols. According to the calculations, the outflow air mass above 11 km altitude was transported westwards and squeezed between the back of the frontal system to the east and the approaching system from the west, both visible in Figure 56. Due to the downward movement behind the front (shown as *dry airstream* in Figure 8), the trajectories indicate a slight

descent, about 1 km, of the air mass, which is also reflected in the elevated O_3 concentrations (see Figure 54) caused by the downward movement of stratospheric air. In the case of the larger Iowa storm, located slightly north of the Falcon flight track, the anvil outflow moves westwards with the frontal system and is likely responsible for the elevated CO concentrations measured during the last third of the flight (see Figure 54 and Figure 58, right).
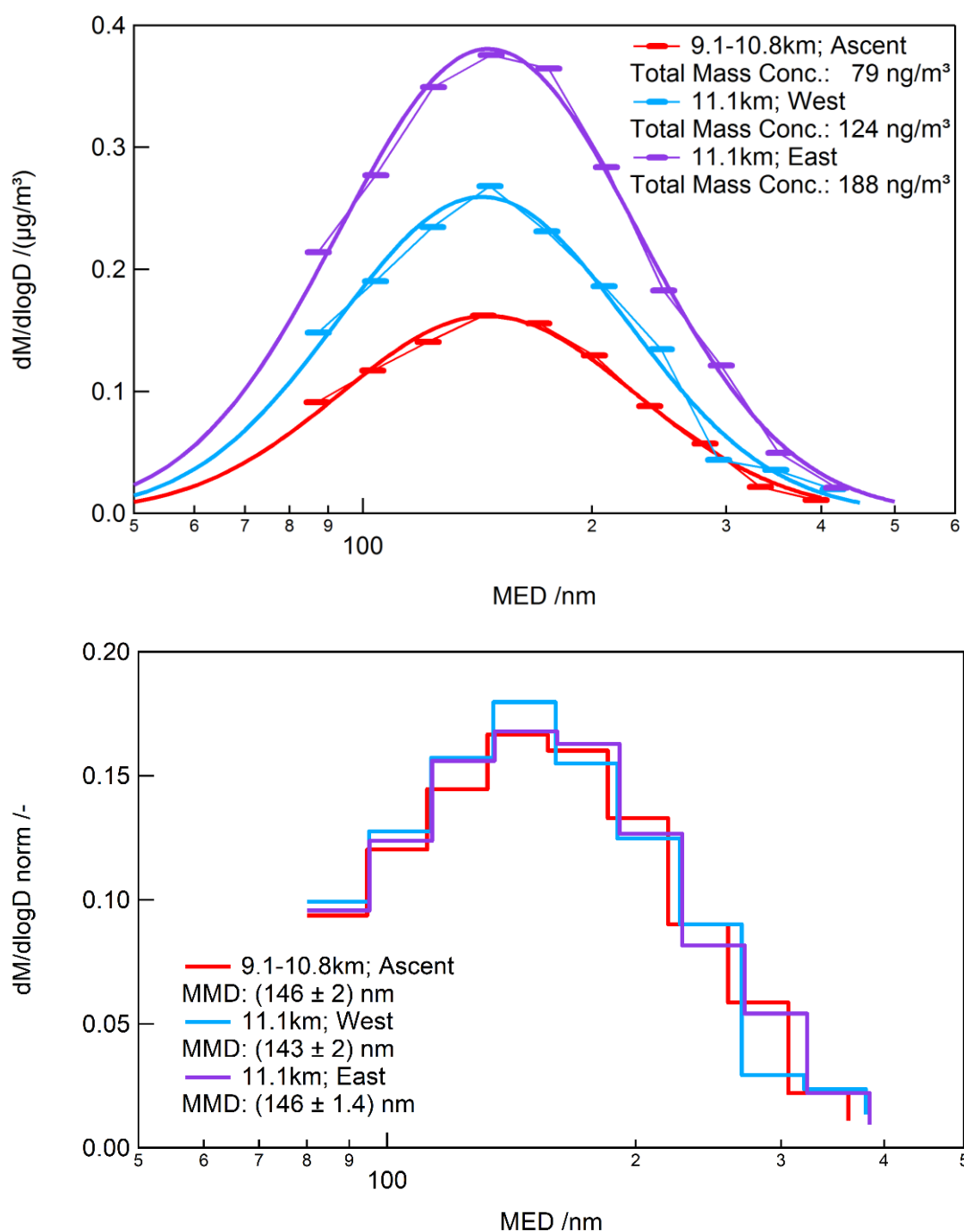
Figure 59: Mass size distribution of rBC in the three biomass burning layers marked in Figure 54. Symbols connected with a thin line in the top panel show the mass size distribution, the thick line is the corresponding lognormal fit, which is also used to determine the total mass concentration of rBC listed in the legend. The bottom panel shows the same mass size distributions as the top panel, normalized with the total concentrations. The legend gives the according mass median diameters of the lognormal fit.

To take a closer look at the rBC particle properties in the BB layers, mass size distributions (as stp concentrations, top, and normalized, bottom) of the rBC particles are shown in Figure 59 for all three BB layers marked in Figure 54. The BB layer measured during ascent at about 9-10 km altitude, shown in red in Figure 59, contained lower total rBC mass concentrations than the two BB layers at 11 km altitude. The shapes of all three mass size distributions are very similar with the mass median diameter of the log-normal fit being 145 nm on average. The geometric sigma of the mass size distribution is also nearly the same for all three layers, with values between 1.55 and 1.58. When comparing the normalized mass size distributions (lower panel of Figure 59), the similarity of the mass size distribution shape is easily seen.

This case study shows that in the BB layers encountered on June 17, CO and rBC mass concentrations were strongly increased compared to the background values. Three layer encounters happened at altitudes between 9 and 11 km behind a frontal system along which strong thunderstorms had developed close to the High Park fire, the source of this layer, the day before. O_3 concentrations at 11 km were enhanced partly due to mixing with stratospheric air. In spite of varying concentrations, the mass size distribution of rBC was nearly the same in all three layer encounters. In chapter 4.3, this similarity is assessed in more detail and compared to the other BB layers found during DC3. The layer was less than one day old but had already been lifted to the upper troposphere, which indicates a very fast transport mechanism. The transport mechanisms are discussed in more detail especially in section 4.5.2 of chapter 4.5, which deals with the upper tropospheric BB layers found during DC3 in general.

4.3 Characteristics of rBC Particles in Biomass Burning Layers during DC3

After showing two flights as examples for BB layers measured during DC3, this chapter extends the previous results to all BB encounters during this campaign. Though most flights performed during the DC3 campaign were dedicated to thunderstorm probing, BB layers were sampled during nearly every flight due to the abundance of wildfires. Table 3 and Table A 3 (page 190) in the appendix gives a summary of all the BB encounters of the Falcon during the DC3 campaign in May and June 2012. In all cases, the fires were burning west of the operating area and the Falcon measured the eastward advected smoke layers. The corresponding backward trajectories for the layers, similar to Figure 47, Figure 48, and Figure 55, can be found in the appendix.
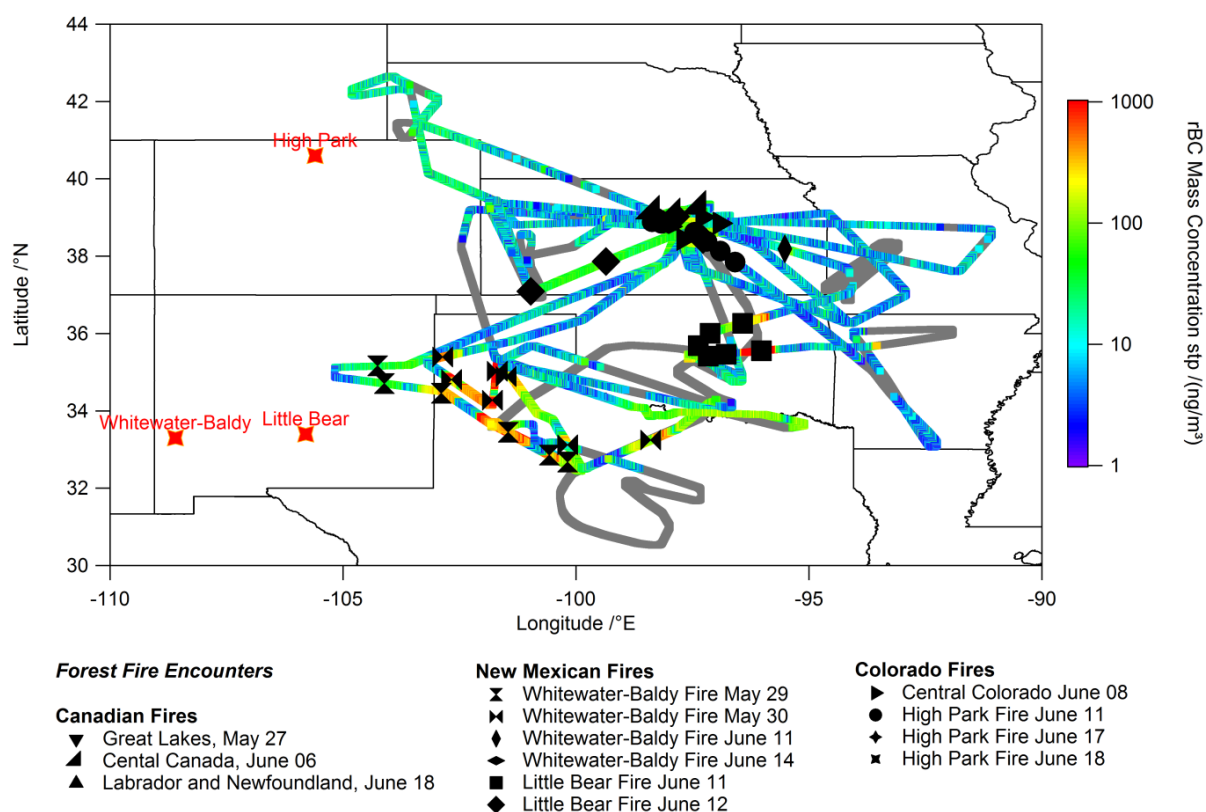
Figure 60: Map of all 13 local flights during the DC3 campaign, color-coded with rBC mass concentration. Grey points indicate flight sequences without valid SP2 data. Each marker type represents a layer on one day and same markers refer to multiple encounters of the same layer on the same day. The same marker types are used to refer to the same fire layer in all following figures in this and the next chapter.

A map of the local flights performed by the Falcon is shown in Figure 60, color-coded with rBC mass concentration. The locations of the tree largest wildfires occurring during the DC3 field campaign period in May and June 2012 are also indicated (red markers). Encounters of BB layers stick out due to the high concentrations of rBC mass (green, yellow and red colors), while the background and the thunderstorm outflow measurements show lower rBC mass concentrations (blue colors). Grey shows the flight track without SP2 data due to cloud passages and data gaps. BB layer encounters during local flights seem to fall into three groups by location on the map, the ones grouped around Salina airport, the Little Bear fire plume encounters over Oklahoma (squares) and the Whitewater-Baldy fire plume encounters over New Mexico and northwestern Texas (sand clocks). Layers located over the operation base airport in Salina/KS were inevitably probed during ascent or descent after take-off and before landing. The case study of June 11, 2012 (section 4.1) showed one of these BB layers originating from the High Park fire (circles in Figure 60), representing a BB layer located directly on top of the boundary layer. These encounters southwest of Salina are marked with circles in Figure 60. BB layers were also

_____

found over Kansas on June 6 (fires in Canada; half squares), June 8 (smaller fires in Colorado; right pointing triangle), June 11 (smaller layer from the Whitewater-Baldy fire that was not mentioned in the case study; upright diamonds), June 12 (Little Bear fire; upright square) and June 14 (Whitewater-Baldy fire; flat diamonds).

The second group of fire encounter locations, a cluster of black squares over Oklahoma, was the Little Bear fire BB layer, probed during descent and ascent for a refuel stop in Oklahoma City on June 11, as described in the case study in section 4.1.

The third group of BB layer encounters are located west of the Whitewater-Baldy fire and were measured during two flights that specifically targeted emissions from this fire, 120529a and 120530a (see also Table 3). Each layer crossings is listed as one encounter and marked accordingly on the map in Figure 60. This leads to a cluster of BB encounters over Texas and New Mexico of upright (May 29) and lying (May 30) sand clocks (black symbols, see legend below figure).
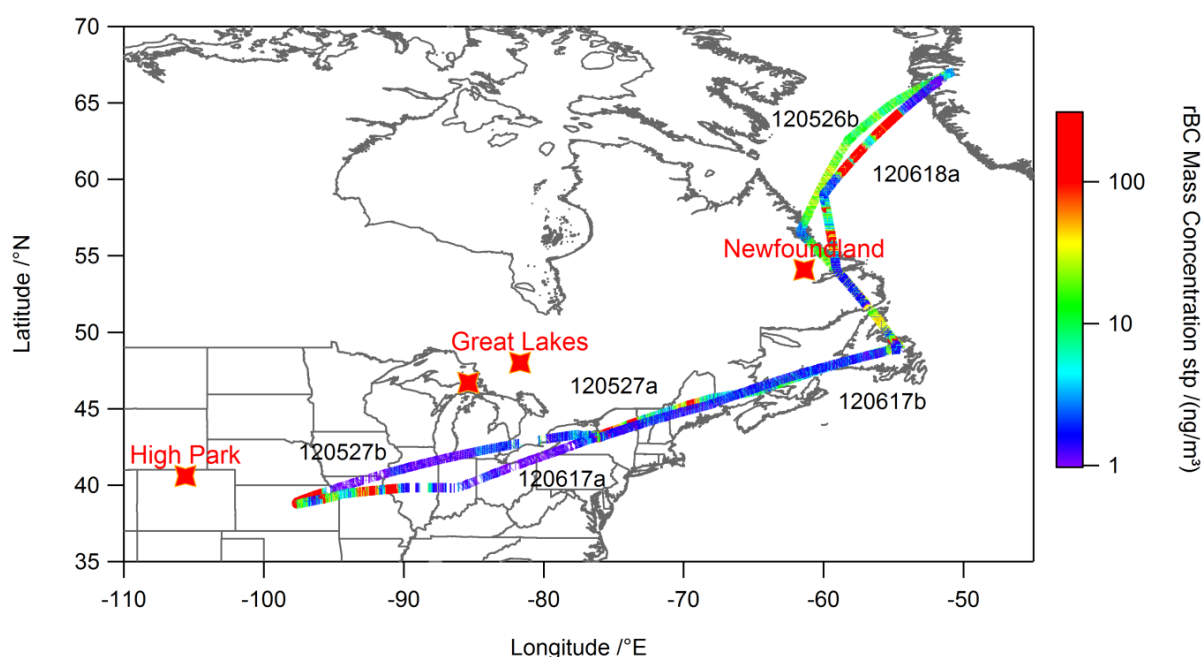
Figure 61: Map of transfer flights over the American continent on May 26/27 (to Salina) and June 17/18 (from Salina), color-coded with rBC mass concentration. Transfer flights between Oberpfaffenhofen and Kangerlussuaq are omitted. Fires from which emissions were measured during these flights are marked with red stars. The corresponding flight numbers are shown next to the flight tracks.

BB layers were also found during the transfer flights. One case, the first back transfer flight from Salina to Syracuse, was already shown as an example for this type of BB layer in the previous section (case June 17, 2012, chapter 4.2). Upper tropospheric BB layers were also found on May 27 east of the Great Lakes and on June 18 between Newfoundland and Greenland. The map in Figure 61 shows the western

_____

half of the transfer flights, between Kangerlussuaq in Greenland and Salina/KS in the U.S.A. (Figure 11 shows all flights). Like in the previous figure, the flight tracks are color-coded by rBC mass concentration. Sequences with high concentrations, shown in reddish colors, appear, from west to east, over Arkansas and Missouri, over the north-eastern USA, and over the Labrador Sea between Labrador and Greenland. Several fires, marked in red, are also shown. During the transfer to the USA, several fires north of the Great Lakes were burning. On the transfer back to Germany, BB layers from the High Park fire influenced large parts of the flights. On leaving Newfoundland, the plume from a fire on the Labrador Peninsula was measured, labeled here as Newfoundland fire.
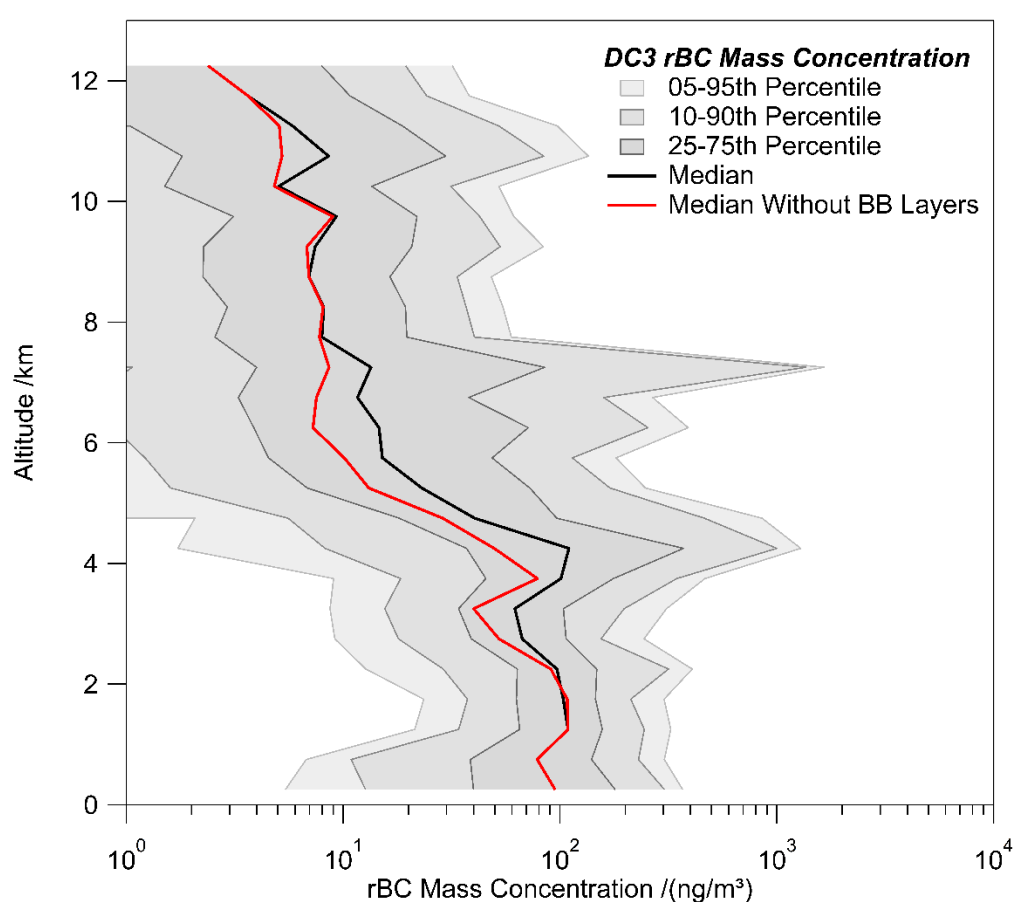
Figure 62: Vertical distribution of rBC mass concentration for all DC3 flights over the American continent. Shown are the median of all data points in black with the corresponding percentiles shaded in grey. The red line shows the median rBC mass concentration profile without the data taken in biomass burning sequences as they are listed in the appendix (Table A 3).
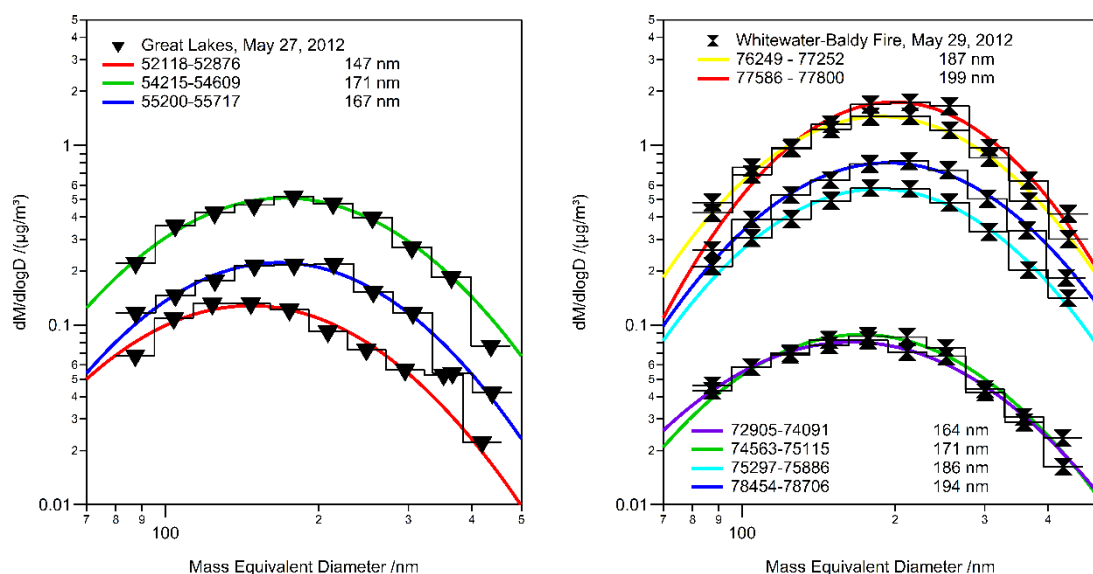
During each flight, the Falcon climbed to altitudes above 11 km and therefore sampled the whole troposphere twice during each flight. The rBC mass concentrations measured by the SP2 during all flights over the American continent are shown in Figure 62. This vertical profile includes all 1 s data points of rBC mass concentration measured on local flights and the transfer flights between
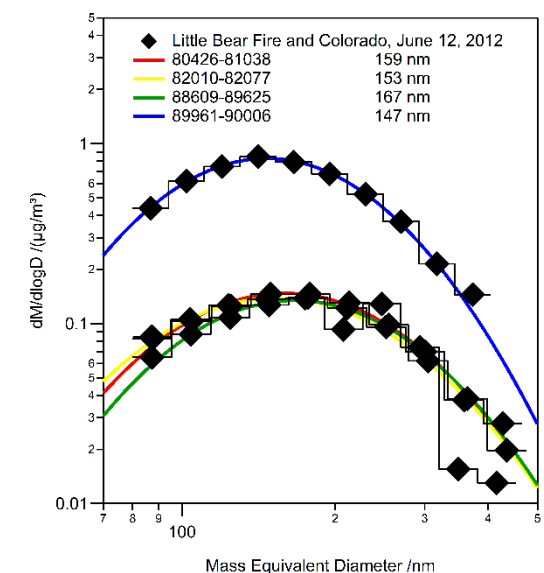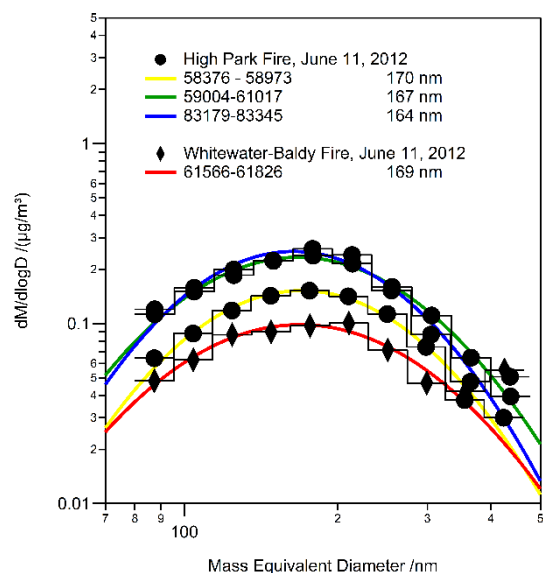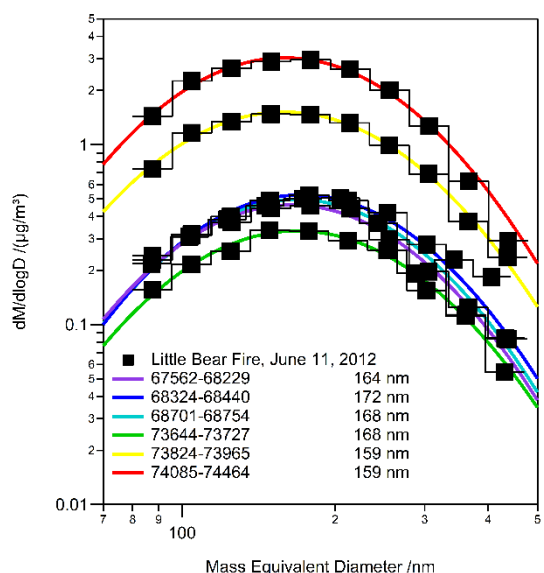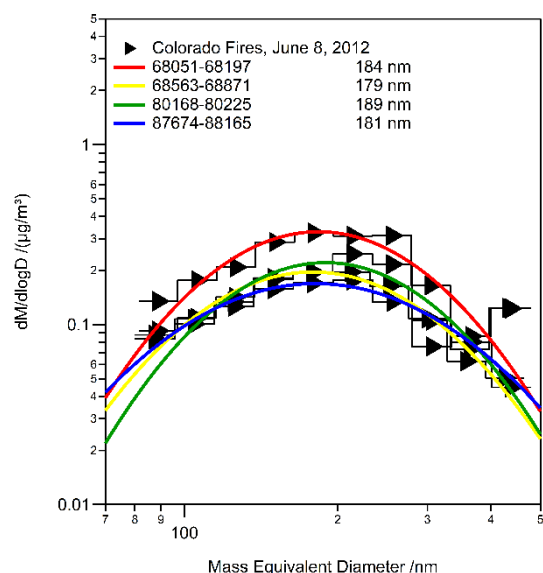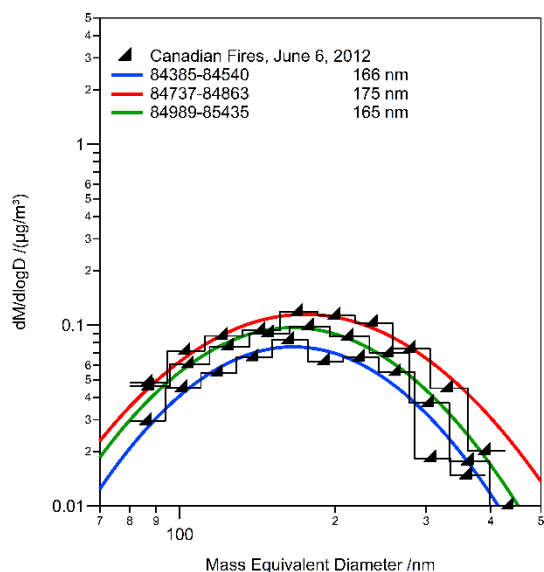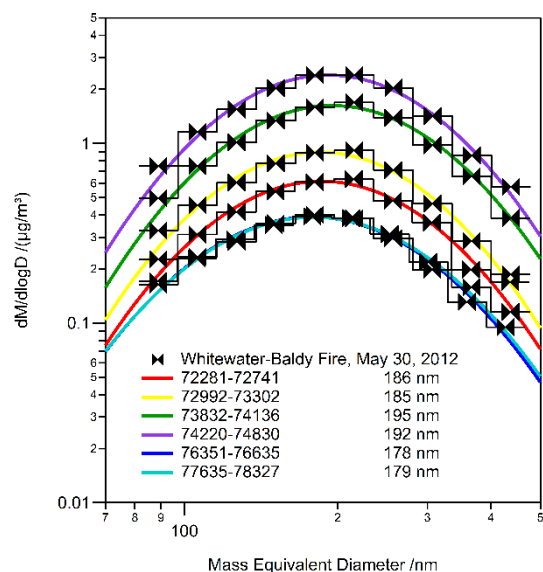
Kangerlussuaq in Greenland and Salina/KS both ways. The amount of data points differs between the altitude bins, because all horizontal flight legs are included, not only sequences of climbing and descending. The highest values, exceeding 1 µg/m³, were found in two strong peaks at 4 and 7 km altitude. A third peak is found at an altitude of 11 km. These three peaks can be attributed to BB layers. The BB layer at 7 km altitude shown in chapter 4.1 from the Little Bear fire is the main reason for the strong peak at that altitude, even influencing the median for all flights. The upper tropospheric BB layer presented in chapter 4.2 from the High Park fire contributes to the 11 km peak. The lowest layers measured during DC3 were located directly on top of the boundary layer, with a thin layer of cleaner air with lower rBC mass concentrations in between and did not reach higher than 5 km altitude. Layers that reached higher than 5 km altitude were thinner in vertical extent, only several hundred meters to less than two kilometers. A layer of cleaner air separated them from the boundary layer below.

To compare the measured profile to the general background situation, all data points taken in identified BB layers were excluded to obtain a background profile, shown in red in Figure 62. When excluding all the BB layers, the median value decreases above 5 km altitude to an average of 10 ng/m³ throughout the middle troposphere. At 12 km altitude, this value decreases further to 2.3 ng/m³, which is still about twice the expected upper tropospheric background of 1 ng/m³ (Schwarz et al., 2013). At 3 to 5 km, the BB-free median still remains influenced by BB that were diluted into the background. This is also the altitude where most BB layers were found, so the influence of very weak BB layers or BB layers that are already diluted into background air can possibly contribute to the background concentrations. Since the measurements were all made on an aircraft, all values measured in the altitude range below 500 m altitude could be biased due to emissions from the airport and nearby cities. These values are therefore more representative of a polluted boundary layer since no dedicated clean boundary layer profiling flight legs were performed during the campaign. Background values for the vertical distribution of rBC mass in the atmosphere over the Pacific region were investigated by Schwarz et al. (2013) over the Pacific during different seasons in the HIPPO (High-performance Instrumented Airborne Platform for Environmental Research Pole-to-Pole Observations) campaigns. In June, the rBC mass concentration of the background is around 13 ng/m³ up to an altitude of about 8 km (350 hPa) and decreases to about 1 ng/m³ above. The DC3 profile shows up to one order of magnitude more rBC than the reported HIPPO background below 5 km altitude. The frequent occurrence of forest fires in 2012 led to an enhancement of rBC mass concentrations throughout the troposphere (Schwarz et al., 2017). No BB layers were found around 8-9 km altitude. This is below the altitude range typical for storm outflow. It is an altitude range that is reached by fire emissions only when pyrocumulus clouds form.

4.3.1 Mass Size Distribution of rBC Particles in Biomass Burning Layers

For each individual encounter with a BB layer shown on the maps in Figure 60 and Figure 61, the rBC mass size distributions are shown in Figure 63, sorted by the fire that emitted the BB layer. For each distribution, the lognormal fit is added in different color and the mass median diameter from the fit is given in the legend.

The sequences span a wide range of rBC mass concentrations and mass median diameters, even for different encounters of the same BB layer. When a layer was encountered several times, this could be at the edges of the layer, where it was more diluted, leading to lower concentrations. This is clearly visible for the Whitewater-Baldy sequences during the BB profiling flights on May 29 and 30. As the flight track led into the plume and out again, measurements were performed both in the edges and in a thicker part of the plume. As the Falcon did not reach the source of the plume, the Whitewater-Baldy wildfire, the maximum concentrations in the plume closer to the fire could be even larger.

dM/dlogD /(µg/m³)

Whitewater-Baldy Fire, May 30, 2012
72281-72741   186 nm
72992-73302   185 nm
73832-74136   195 nm
74220-74830   192 nm
76351-76635   178 nm
77635-78327   179 nm

Mass Equivalent Diameter /nm

Canadian Fires, June 6, 2012
84385-84540   166 nm
84737-84863   175 nm
84989-85435   165 nm

dM/dlogD /(µg/m³)

Mass Equivalent Diameter /nm

dM/dlogD /(µg/m³)

Colorado Fires, June 8, 2012
68051-68197   184 nm
68563-68871   179 nm
80168-80225   189 nm
87674-88165   181 nm

Mass Equivalent Diameter /nm

dM/dlogD /(µg/m³)

Little Bear Fire, June 11, 2012
67562-68229   164 nm
68324-68440   172 nm
68701-68754   168 nm
73644-73727   168 nm
73824-73965   159 nm
74085-74464   159 nm

Mass Equivalent Diameter /nm

dM/dlogD /(µg/m³)

High Park Fire, June 11, 2012
58376 - 58973   170 nm
59004-61017   167 nm
83179-83345   164 nm

Whitewater-Baldy Fire, June 11, 2012
61566-61826   169 nm

Mass Equivalent Diameter /nm

dM/dlogD /(µg/m³)

Little Bear Fire and Colorado, June 12, 2012
80426-81038   159 nm
82010-82077   153 nm
88609-89625   167 nm
89961-90006   147 nm

Mass Equivalent Diameter /nm

Figure 63: rBC mass size distributions for biomass burning sequences sorted by the fires from which the layers originated. The source fire is given in the top left corner of every panel. The step curves with symbols give the measured rBC mass size distributions, the colored line represents the corresponding lognormal fit to the measured distribution. The legend lists all fire encounters by the time interval of the measurement and the mass median diameter from the lognormal fit. (Colors have no other significance than to distinguish between different encounters of the same BB layer.)

Variations can be seen in the mass median diameter especially for the encounters of the BB layers on May 27 from the fires at the Great Lakes. The BB layer from the Little Bear fire on June 12, encountered three times, shows only little variation in rBC mass concentration and mass median diameter. As shown for the June 17 case, size distributions measured during different encounters with the same BB layer

show similar rBC mass size distributions. The rBC mass median diameters are also similar between the High Park fire layer encounters on June 7 and June 18. On both days, the BB layers were located in the upper troposphere (chapter 4.2).

Log-normal functions were fitted to all the mass size distribution shown in Figure 63 to condense the information contained in the mass size distribution and make comparison plots less confusing. These parameters are shown for all DC3 BB sequences probed by the Falcon in Figure 64. The panels show, from left to right, the mass median diameter (MMD), the total rBC mass concentration and the geometric standard deviation (GSD) of the mass size distribution for the average altitude of each layer. As in Figure 63, same markers represent the same layer, listed with marker type on the right side of the figure.
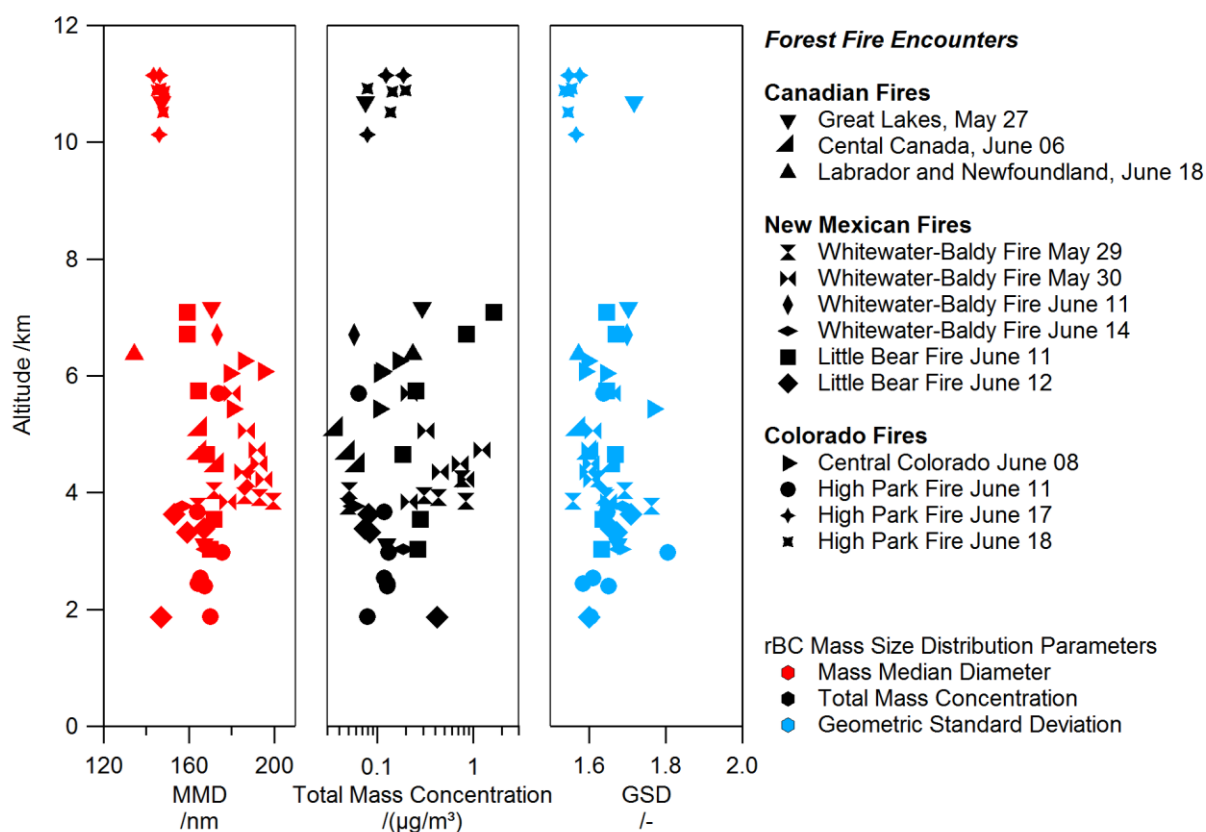
Figure 64: Properties of the rBC mass size distribution of all DC3 biomass burning layers probed by the Falcon: MMD (left), total rBC mass concentration from log-normal fit (middle) and GSD of the log-normal rBC mass size distribution (right) at the layer-averaged altitude. The different layers are identified as individual markers listed on the right.

As mentioned before, the layers were found between the boundary layer and 8 km altitude, and between 10 and 11 km altitude, with a distinct gap at 8-9 km altitude. Layers above 9 km altitude are referred to as upper tropospheric layers in the following. The mass concentration and mass size distribution of rBC

particles in the layers throughout the free troposphere show a high variability in size distribution and concentration, as shown in Figure 64. In contrast to the high variability in mass size distribution found in layers below 8 km, the layers at 11 km show little to no variation in mass size distribution. All 10-11 km layers have a mass median diameter of around 145 nm, which is at the low end of the range of values found in the mid-tropospheric layers. The GSDs of the rBC mass size distribution in these sequences are also smaller than most of the size distributions measured below 8 km altitude. The measured distributions indicate a tendency of more narrow rBC mass size distributions at smaller diameters at altitudes around 10-11 km compared to layers below 8 km.

Previous measurements of rBC mass size distributions in BB layers found values for the MMD at the upper range of the values here. During the ARCTAS-B campaign in Canada, Kondo et al. (2011a) found a MMD of 207±31 nm for rBC mass size distributions in aged BB aerosol from Siberia and Kazakhstan, and 187±10 nm in Canadian BB layers. Similar MMDs, 193±16 nm, were also found in fresher plumes during ARCTAS-Carb in California (Sahu et al., 2012). An even larger MMD of 210 nm was observed by Schwarz et al. (2008a) in a BB plume over Texas. All these measurements were made below 8 km altitude. The GSD of the rBC mass size distribution in this plume was at 1.43, much lower than in all observed BB cases during DC3. Background measurements of rBC during the HIPPO campaign (Schwarz et al., 2010b) showed a nearly constant MMD of about 182 nm in remote air masses over the Pacific, indicating a steady-state mass size distribution with an MMD between the typical MMDs in fresh emissions and aged BB. The MMDs observed here in the layers below 8 km altitude vary around this value with higher values in dense plumes and lower values in layers that possibly mixed with PBL air. Mass median diameters of rBC observed in the DC3 BB layers were generally at the low end of observed MMDs in other campaigns. Especially the low MMDs of around 145 nm found in the upper tropospheric BB layers stand out as much lower than the values found below 8 km in Figure 64. The GSD values of the upper tropospheric layers are also on the low side of observed values. Both GSD and MMD values change during coagulation processes in an ageing aerosol population. A comparison of both parameters can therefore indicate if variations between different layers are a result of different sources or ageing processes.
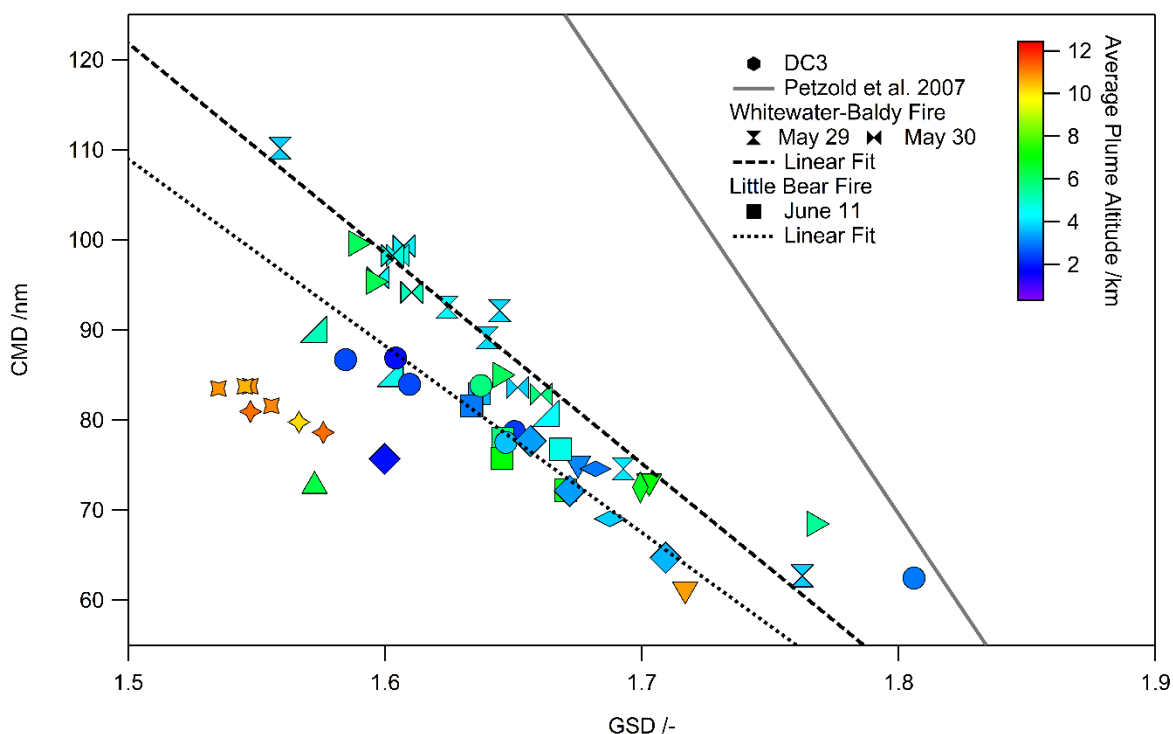
Figure 65: Relationship between count median diameter (CMD) and geometric standard deviation (GSD) for all DC3 biomass layer rBC size distributions (symbols, same as in Figure 64). The grey line is taken from Petzold et al. (2007) and refers to complete particles while the symbols and the dashed lines refer to rBC cores only. The short dashed line is derived from the Little Bear plume on June 11 and the long dashed line from the Whitewater-Baldy plume on May 29 and 30. Different symbols represent the different layers, see the legend displayed in previous figures. Color-coding refers to average layer altitude.

The GSD and the count median diameter (CMD) of the rBC mass size distributions are compared for all Falcon DC3 BB sequences in Figure 65. The color-coding represents the layer altitude with blue colors for sequences close to the boundary layer and orange colors for upper tropospheric layers. The symbol type refers to the different sources, and are the same as in the previous Figure 64. The figure shows clearly that these parameters are not completely independent from each other but follow a linear trend. For two cases, the Whitewater-Baldy fire (May 29 and 30) and the Little Bear fire (June 11), linear fits are added to the figure.

The relationship between width and median diameter of the mass size distribution changes if the aerosol sample undergoes various processes in the atmosphere. According to Hinds (1999), coagulation of particles with a lognormal size distribution will narrow the distribution and shift it to larger diameters. In a coordinate system as in Figure 65, a coagulating size distribution would move from the bottom right corner to the top left corner in this process. As coagulation processes are influenced by particle size and

concentration, competing processes will, in the end, lead to a stable, self-preserving size distribution (Hinds, 1999). Dentener et al. (2006) and Petzold et al. (2007) studied and parameterized the change in size distribution of forest fire plumes due to ageing. They found a linear relationship between particle size distributions of BB plumes of different age. This ratio is shown in Figure 65 as a grey line. It must be noted here that the ratio from Dentener and Petzold refers to complete particles, measured by optical methods while the markers, derived from the DC3 BB cases, represent rBC particle cores only. Therefore, it is not surprising that diameters for the DC3 data are smaller than the complete particles as additional coating material volume is not taken into account. Both data sets have the linear relationship between CMD and GSD in common, however, the relationship derived from the DC3 data shows a less steep increase of the CMD with decreasing GSD. A possible reason for this might be that in layers containing larger rBC cores these cores have also a thicker coating. The complete particle size could not be derived from the DC3 SP2 data (see chapter 3.2.1.3), so it is not possible for this data set to derive the corresponding CMD for the complete particles.

Washout processes, on the other hand, would predominantly remove the larger particles and the size distribution would become narrower and have a smaller median diameter. So, the size distribution would move from the top right to the bottom left. While most BB layers group along the two dashed black lines, a small group is located further to the bottom left. Most of these are the upper tropospheric layers, identifiable by their orange color. The upper tropospheric layers therefore show a different kind of rBC size distribution than the layers below 8 km. This indicates that ageing was not the dominant process leading to the size distribution found in the upper tropospheric layers. Cloud processing or washout could play a role as these processes act more on larger particles than on smaller ones.

The comparisons shown so far in this chapter make it clear that the upper tropospheric BB layers show a very different rBC mass size distribution compared to the BB layers encountered between the top of the boundary layer and 8 km. This makes it worthwhile to compare the rBC mass size distributions in these upper tropospheric BB layers in comparison to distributions found in the upper troposphere outside of these layers, e.g. in the background and in the outflow regions of thunderstorm anvils. Since the estimated rBC mass size distribution parameters found in the upper tropospheric layers show only little variations, they are compared to other encounters of BB layers in the upper troposphere to see whether similar size distributions are an effect of the source only, or of processes happening during transport.

Figure 66 shows rBC mass size distributions measured at 11 km altitude. Blue, red and orange colors mark the BB layers found in the upper troposphere, while measurements in cloud-free thunderstorm outflow are colored in green. Though the Falcon spent much time in thunderstorm outflow, this was mostly within anvil clouds. To avoid biases from cloud artefacts induced by the aerosol inlet, only four sequences, measured out of clouds (cases 120605a, 120605b, and 120606a) and in cloud-free aged outflow (case 120608a), are shown here. A more detailed list of these sequences can be found in the

appendix (Table A 4). Background concentrations measured on different days are shown in black for comparison. These are the same background sequences as listed in Table 11 for comparison with the June 17 case.
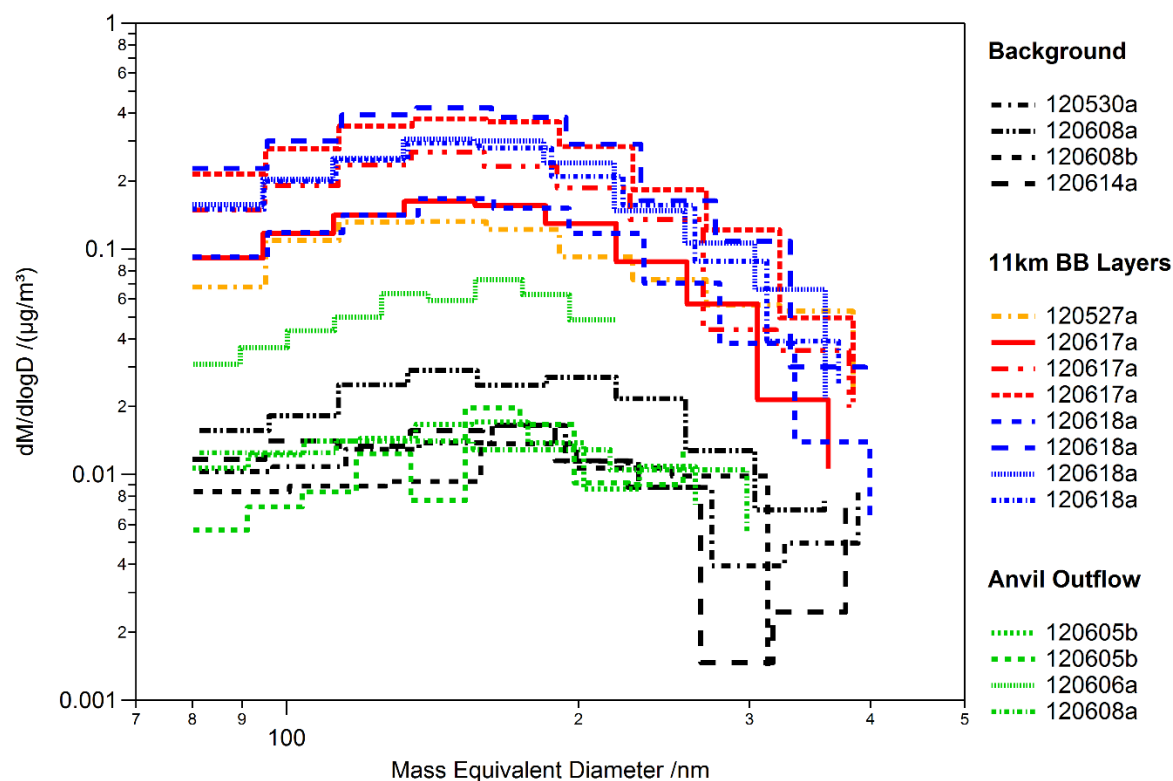

Figure 66: rBC mass size distributions measured in the upper troposphere in biomass burning layers and in thunderstorm outflow out of clouds compared to background mass size distributions.

Mass concentrations of rBC in BB layers are more than one order of magnitude larger than rBC mass concentrations found in the surrounding background. Thunderstorm outflow and background concentrations are very similar in size and shape. All background concentrations were measured over the mid-west in an area that was strongly influenced by thunderstorms with large convection cells evolving nearly every day. Thunderstorm outflow therefore had an influence on the background concentration in the upper troposphere during DC3 (Barth et al., 2015; Huntrieser et al., 2016b). This is reflected in the similarity between thunderstorm outflow and background rBC mass size distributions. One exception is the thunderstorm outflow case from the flight 120606a, which was measured at the edge of a strong convective system over Colorado. At that time, north of the thunderstorm the Cheyenne fires were active which likely influenced the aerosol concentration in and around the storm.

As shown in Figure 64 and Figure 65, the rBC mass size distributions in upper tropospheric BB layers are shifted to smaller diameters compared to the BB layers below 8 km. The similarity to the distributions in thunderstorm outflow, which was subject to washout of particles before being emitted

from the thunderstorm cloud, indicates that cloud processing might be a process leading to the observed distribution in the upper tropospheric BB layers. This decrease in rBC MMD was also observed in pollution layers from Tokyo that were transported off the Japanese coast, which can only be explained by wet removal that preferably washes out the larger particles (Moteki et al., 2012). The large difference in concentrations between BB layers and anvil outflow sequence with very low rBC mass concentrations indicate that anvil outflow experienced much stronger washout than the observed upper tropospheric BB layers.
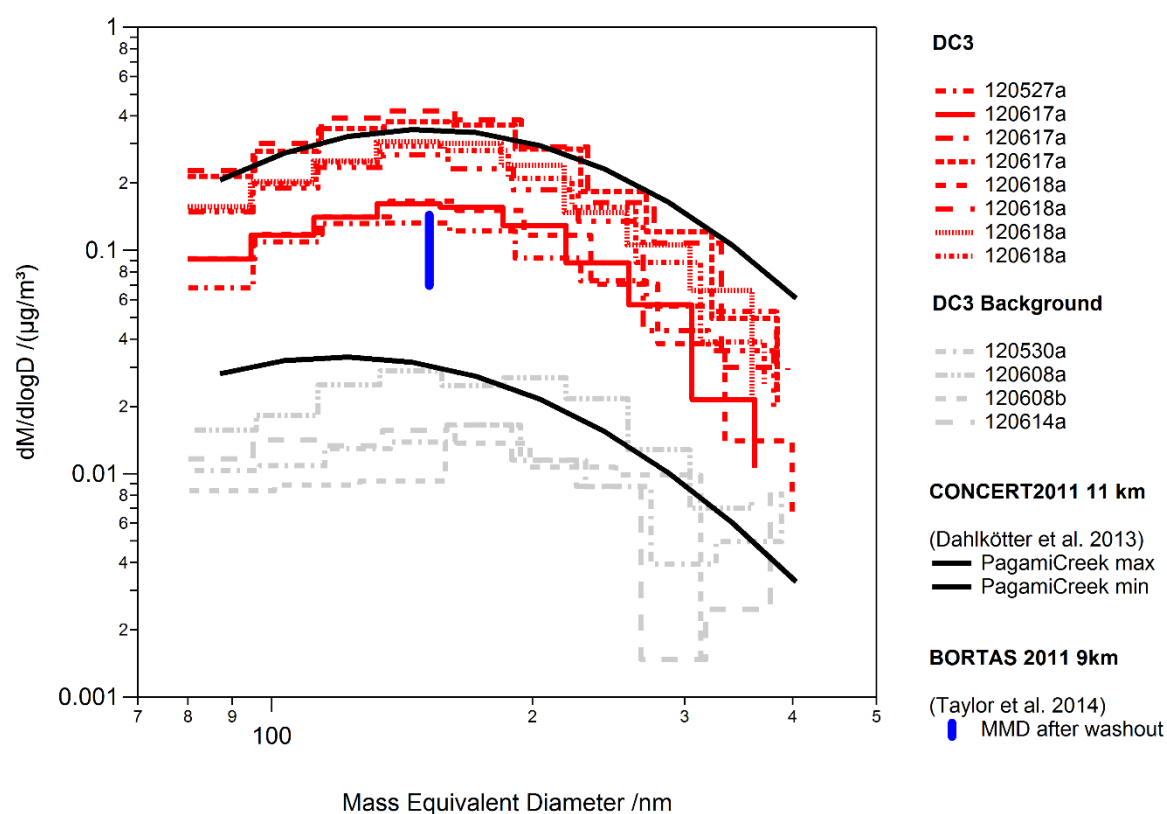
Figure 67: rBC mass size distributions in upper tropospheric biomass burning layers (same as in Figure 66) compared to literature values. The DC3 background sequences are shown in light grey.

Previous measurements of rBC in upper tropospheric BB layers are shown in Figure 67. The rBC mass size distribution found during DC3 during the Falcon transfer flights, as shown in Figure 66, are shown in red. Black lines mark the upper and lower limit of rBC mass size distributions found by Dahlkötter et al. (2014) in a Canadian BB layer over Europe during the CONCERT 2011 field campaign. The layer originated from a single fire, the Pagami Creek fire and was transported over the Atlantic where it was observed over Northern Germany about six days later. The maximum distribution is nearly the same as the distributions observed in the Falcon DC3 BB layers with higher concentration while the minimum distribution lies below the lowest distribution found in the Falcon DC3 layers. Taylor et al. (2014) show

one example of BB measured during the BORTAS campaign in 2011 at an altitude of 9 km. As they only report normalized rBC mass size distribution, only the median diameter is shown here, as a vertical blue line.

All these layers have nearly identical rBC mass size distributions, only varying in concentration, even if they originate from different fires in different years. The comparison of upper tropospheric BB layers from four different fires, three of them measured during DC3, seems to indicate a certain rBC mass size distribution which is typical for the upper troposphere. The layers were measured at very different distances from the source and had different ages, ranging from one (120617a DC3 case) to ten days (Pagami Creek layer) and still show the same size distribution. This suggests that upper tropospheric BB layers have a stable steady-state rBC mass size distribution (see e.g. Hinds, 1999). Due to the extended lifetime of aerosol in the upper troposphere, they could dilute into the background and influence the background rBC size distribution. This would also explain the similarity between the rBC mass size distribution shape in the background and in the layers (see Figure 66).

This section showed some of the characteristics of mass size distributions of rBC cores in DC3 BB layers probed by the Falcon. These layers can be separated roughly by altitude into two types, layers in the free troposphere below 8 km and layers in the upper troposphere (10-11 km). For both types, concentrations of rBC mass were enhanced by up to two orders of magnitude compared to the background (below 8 km: up to 2000ng/m³ in layers and 10 ng/m³ in background; in the upper troposphere about 100 ng/m³ in layers and around 1 ng/m³ in the background). Comparisons with literature values showed that the rBC particles in the DC3 BB layers had slightly smaller MMDs than found in previous studies, but are mostly still within given uncertainties. Perhaps the DC3 layers were emitted under different fire conditions or were younger than the Siberian layers in the Arctic. While the variations in size distribution parameters can be attributed to different stages for aging for the mid-tropospheric layers, cloud processing or wet removal seems to be a relevant process influencing the upper tropospheric layers. A comparison of the nearly uniform mass size distribution shape with other measurements over Canada and Europe suggests that rBC in BB layers in the upper troposphere has a nearly uniform mass size distribution with an MMD of about 145 nm, independent of age.

4.3.2 Mixing State of rBC Particles in the DC3 Biomass Burning Layers

As shown in the previous section, ageing and cloud processing both have a strong influence on the mass size distribution of the rBC cores. The rBC-containing particles consist not only of the core, but often also of a coating that surrounds the rBC core. Ageing and cloud processing also influence this coating, so the mixing state of the rBC particles should also reflect the processes acting on the BB aerosol population. Coatings on rBC particles also enhance the light absorption of the particles (Schwarz et al., 2008b). Due to the abundance of weakly or non-absorbing materials in BB layers, rBC particles can

acquire thick coatings of material which would contribute less to absorption if not condensed on the highly absorbing rBC material. Coatings on hydrophobic rBC cores can also increase these particles' hygroscopicity. In BB layers from prescribed fires in Wyoming, nearly all particles above 100 nm could act as cloud nuclei due to their chemical composition (Pratt et al., 2011).

Coating thickness is also considered an indicator of aged particles. Wildfires emit, besides black carbon, large amounts of organics. These can condense and coagulate to form secondary organic aerosol (see e.g. Kondo et al., 2011a). Organics can also condense on the already existing rBC cores where they are found as coatings. This condensation happens very fast and thick coatings on rBC particles can be found close to the source within minutes after emission. Akagi et al. (2012) found an increase in coated particle fraction from 55% to nearly 80% in a Californian chaparral fire plume within only one hour after release. As all BB layers in this study were measured several hours to days downwind of the respective fires, a high fraction of thickly coated particles would be expected.

The usual approach to study the coatings on rBC particles is to compare the optical size and the incandescent mass equivalent size of rBC particles, as described in chapter 3.2.1.3. Due to the second crossing problem in the split detector, the optical size of rBC particles cannot be determined reliably in that way. The approach chosen here, described in chapter 3.3.4, only gives a fraction of rBC particles coated thickly compared to the total number of particles. For the Falcon measurements, the mixing state of rBC particles is given qualitatively here as the relation of the number of particles in the size range 4-6 fg with delay times larger than 1.5 µs to the total number of particles in this size range. Figure 68 shows the fraction of thickly coated particles with altitude for all DC3 BB layers probed by the Falcon (black) and the DC-8 (grey) and compares them with values found in thunderstorm outflow sequences out of clouds (red hexagons, same sequences as in Figure 66) and the planetary boundary layer (yellow hexagons). Blue circles mark PBL measurement cases when a BB layer was situated on top of the PBL but the layers were still distinguishable by a sharp increase in rBC mass concentration. For the data from the NOAA group, measured on board of the DC-8, the grey stars indicate the fraction of rBC particles in the size range of 4-6 fg with a coating thicker than 30 nm.
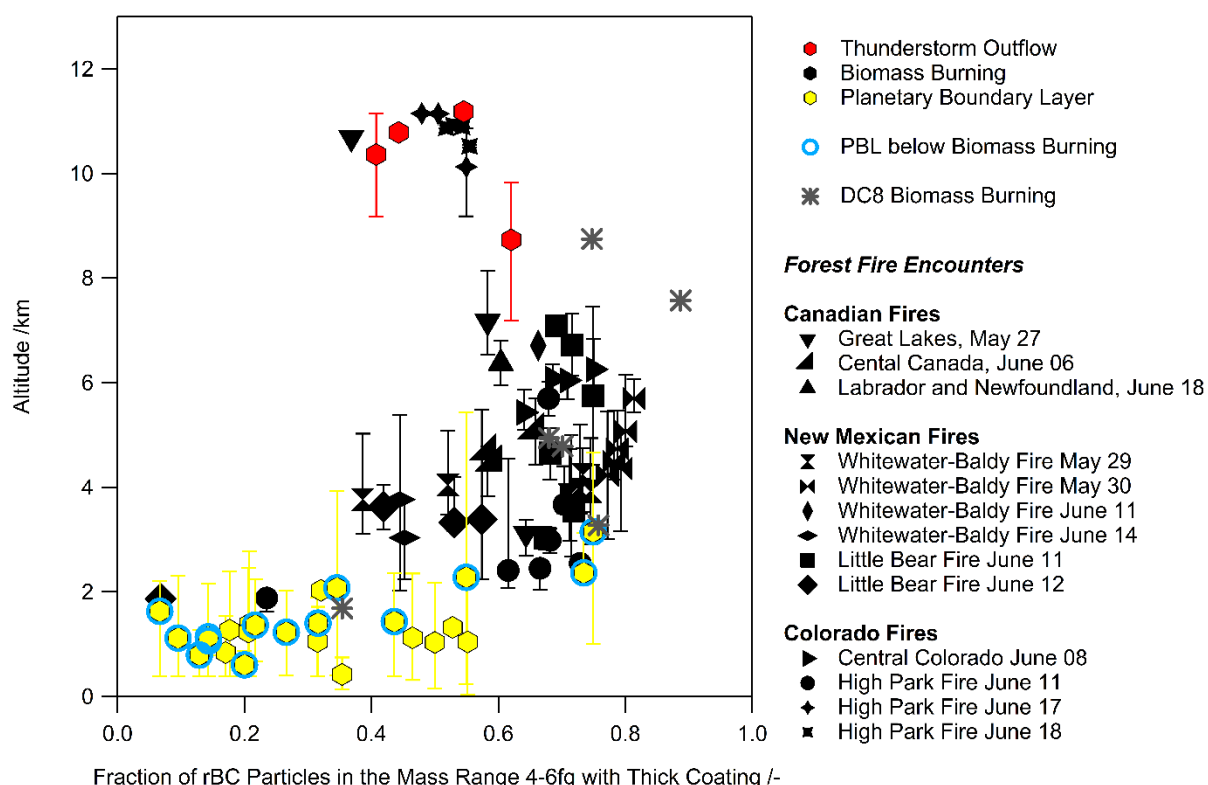
Figure 68: Fraction of 4-6fg rBC particles with thick coating for biomass burning layers (black and grey), planetary boundary layer (yellow) and thunderstorm outflow sequences (red). Different layers are indicated by different markers. Black markers indicate Falcon measurements of biomass burning, grey stars represent data measured by NOAA on board of the DC-8. PBL sequences that had biomass burning layers on top are encircled in blue. Vertical error bars represent the altitude of the sequence with the marker placed at the average altitude of the sequence.

As Figure 68 shows, about 70% of the rBC-containing particles with cores of 4-6 fg have a thick coating in the BB layers found at 3-8 km. This fraction decreases below 4 km, probably due to mixing with air from the boundary layer or sampling of fresher BB layers. Two cases of thin BB layers located directly on top of the boundary layer contain only very few thickly coated particles, less than 30%. These layers are probably strongly influenced by the underlying boundary layer with fresh, uncoated rBC particles. One example is the Little Bear fire sequence measured on June 12 (square diamond). This sequence was measured directly on top of the well mixed boundary layer and boundary layer air from below might already have been mixed in, but not yet to an extent which would have made both layers indistinguishable. During other encounters, this layer reached higher up and showed a higher fraction of coated particles. The measurements from the SP2 onboard of the DC-8 aircraft show about the same pattern as the Falcon measurements.

PBLs with a thickness of more than 2000 m associated with BB aerosol layers located above also show a large fraction of thickly coated particles. In these cases, BB aerosol containing thickly coated rBC particles might have been mixed into the PBL from above while the convective boundary layer evolved during the day.

For the layers around 11 km altitude, this fraction is lower and only half of the particles in this size range are thickly coated. The 11 km BB layers lie in the same range of fractions of thickly coated particles as it is found in thunderstorm outflow, and at the lower end of the range of coatings found in mid-tropospheric BB layers.

Considering that the BB layers at 11 km are older or of similar age as the mid-tropospheric layers, a high fraction of thickly coated particles would be expected. For a case of an upper tropospheric BB layer over Central Europe, transported over the Atlantic from North America, Dahlkötter et al. (2014) report coatings thicker than 30 nm for nearly all rBC particles. The higher fraction of thickly coated particles in that layer is probably caused by the age of the layer which gave the rBC particles more time to acquire coatings.

The lower fraction of thickly coated particles in the upper tropospheric BB layers compared to the ones in the middle troposphere suggests that processes during the transport favored the removal of thickly coated particles. Processes that remove the coating from rBC particles, or the complete coated rBC particles could be cloud processing or wet removal. Since rBC particles coated with a hydrophilic material are better cloud condensation nuclei than uncoated rBC particles, these would predominantly form cloud droplets and, consequently, might rain out first. This is supported by the thunderstorm outflow data, which show the same fraction of thickly coated particles, however, rBC mass concentrations are considerably lower.

A comparison of rBC mass size distribution and coated fraction shows that the thickly coated fraction is higher in layers that contain rBC particles with a larger mass median diameter (Figure 69, top).The lower part of Figure 69 displays the correlation between coated fraction and total rBC mass concentration. Here it also seems that BB layers with a high rBC ass concentration also tend to contain more particles with thick coating. Layers with a large fraction of thickly coated particles contain, however, not always mainly large rBC particles in a high mass concentration. The two cases with a much lower fraction of thickly coated particles, below 30%, are both thin layers located right on top of the boundary layer and were probably already mixed with boundary layer air to some degree (see also Figure 68).
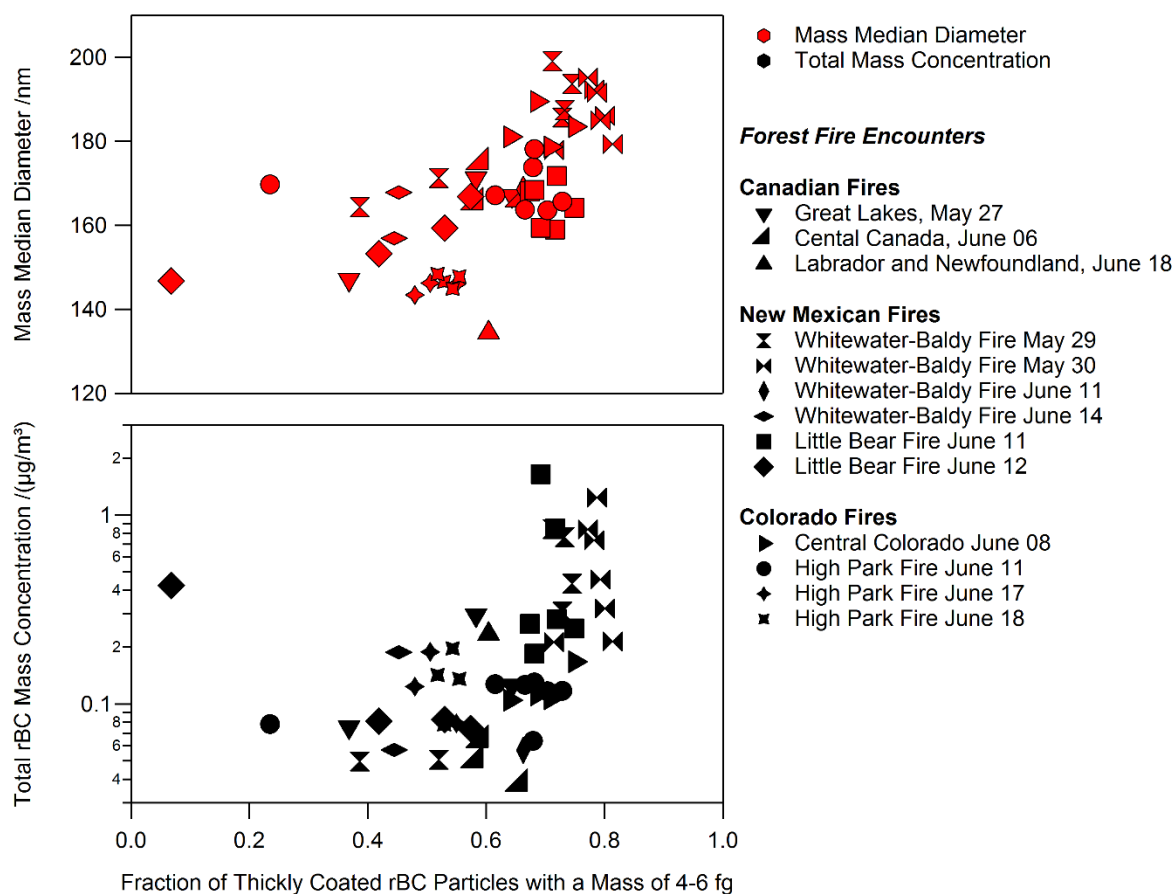
Figure 69: Relationship between mass median diameter (top) and total rBC mass concentration (bottom) and the fraction of thickly coated particles.

The BB sequences in which more than half the rBC particles in the 4-6 fg range have a thick coating are also the sequences where large particles are found at high concentrations. Layers with high concentrations have both larger particles and more thickly coated particles, consistent with coagulation theories (Hinds, 1999). Aerosol populations with higher concentrations coagulate faster and should therefore contain larger particles compared to a population with lower concentration after the same time interval. The higher fraction of thickly coated particles in layers with larger rBC particles and more rBC mass indicates that these layers also contain more secondary organic aerosol and corresponding precursors, which often make up the coating on rBC cores. These substances were probably emitted together with the rBC particles. Therefore, from the beginning these fire plumes contained large concentrations of both rBC cores and possible coating material which favors coagulation, leading to larger rBC cores. As both larger particles and thicker coatings enhance the absorption of radiation in a BB layer, the co-occurrence of both could even increase this effect.

The fraction of thickly coated rBC particles in DC3 BB layers is around 60-70% for most cases, consistent with literature values for the coated fraction of rBC particles in a fire plume after several

hours (Akagi et al., 2012). Layers on top of the boundary layer tend to contain a lower fraction of thickly coated particles, probably due to mixing with PBL air. Upper tropospheric layers also tend to be on the lower side when looking at the coated fraction, similar to the rBC mass size distribution that was discussed in the previous section. While the content of thickly coated particles is lower than the average for layers below 8 km, still about half of all rBC particles are covered by a more than 30 nm thick layer of volatile materials. As this coating can affect absorption and hygroscopicity of rBC particles, it should be taken into account when modelling aerosols and their interaction with atmospheric processes in the upper troposphere.

As detailed in this chapter, rBC particles in the mid-tropospheric DC3 BB layers tend to be large and have a thick coating, consistent with previous observations. The upper tropospheric BB layers, however, differ in properties. They all have a nearly uniform rBC mass size distribution and only about half of all rBC particles contain coatings with more than 30 nm thickness. This seems to be caused by wet removal processes during vertical transport and can already be observed in layers when they are less than one day old. To identify these processes, chapter 4.5 will look closer at the involved vertical transport mechanisms. Besides rBC particles, wildfires emit a wide range of other substances. While this chapter focused on the rBC particles in BB layers only, the next chapter discusses the distribution two co-emitted species (coarse-mode dust particles and carbon monoxide) that also play important roles in atmospheric processes.

4.4 Properties of Co-Emitted Species in the Biomass Burning Layers: Dust Particles and CO Concentration

In this section, coarse mode dust particles and CO in DC3 BB layers serve as examples in discussing other species in the layer besides rBC.

4.4.1 Dust Content in DC3 Biomass Burning Layers

Mixtures of dust with BB aerosols are often found when air masses containing e.g. Saharan dust and air masses from BB regions interact, for example in the Mediterranean region (Ancellet et al., 2016) or off the African coast (Weinzierl et al., 2011). Mineral dust can also be contained in BB layers originating from fires in dry areas (e.g. Nisantzi et al., 2014; Dahlkötter et al., 2014). It is usually found in the coarse mode of the multi-modal aerosol size distribution (e.g. Weinzierl et al., 2009).
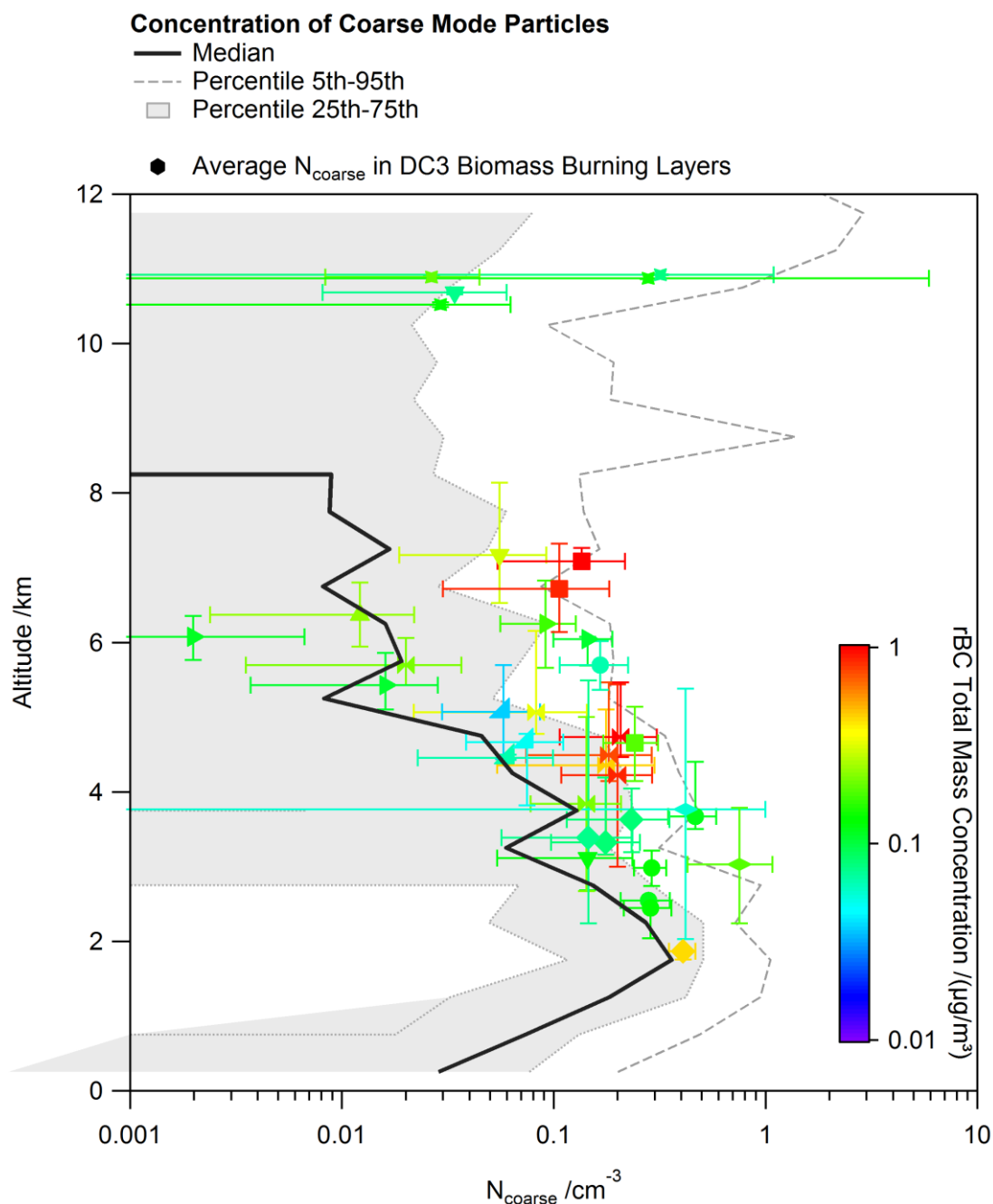
Figure 70: Average number concentration of particles larger than 2 μm in DC3 biomass burning layers compared to the median profile of all data. The 5th and 25th percentile are only shown when above zero. Different symbols indicate different layers, see previous figures for legend. Color-coding represents total rBC mass concentration. Horizontal error bars correspond to one standard deviation of the averaged concentration and vertical bars give the vertical range where the layer was measured.

The area where the DC3 fires were located experienced a period of unusual drought in that year (Hoerling et al., 2014). It is therefore possible that soil dust was mobilized in the heat and turbulence of

the strong wildfires like the Whitewater-Baldy fire. The number concentration of particles larger than 2 µm is used as a proxy for dust particle number concentration to evaluate the dust content of the DC3 BB layers. These concentrations were derived from measurements with the FSSP-100 cloud probe. Figure 70 shows the median vertical profile of the number concentration of coarse mode particles larger than 2 µm (N_{coarse}) for all flights over the North American continent (thick black line). Cloud passages were removed to avoid a bias from cloud droplets and ice crystals in the same size range. In general, the concentration of coarse mode particles (>2 µm) decreases with altitude. A possible reason for this might be that the larger dust particles sink fast and do not reach high altitudes due to their weight. A striking feature is the "nose" of higher concentrations at 2 km altitude and the decrease in concentrations towards the ground. As the source of the particles is at the ground, this indicates that the particles were not emitted locally but transported from their source to the measurement area.

Average concentrations of coarse mode particles in the Falcon-probed DC3 BB layers are added as colored markers. In most BB layers, the average coarse mode particle concentrations lie above the median of the profile for the whole campaign, reaching nearly 1 cm^{-3} in some cases. These concentrations are, unsurprisingly, on the lower side of the range of values found in Saharan dust layers over Morocco (0.5-10 cm^{-3}, with an average of 3 cm^{-3} (Weinzierl et al., 2009)). However, these Saharan dust layers often reach only up to 5 km altitude (Ansmann et al., 2011; Weinzierl et al., 2011) while the DC3 BB layers still show coarse mode concentrations up to 0.1 cm^{-3} at an altitude of 7 km.

BB layers with high rBC mass concentrations, marked by the reddish color coding in Figure 70, tend to have higher concentrations of large particles. While most layers contain average large particle concentrations above the median of all measurements, especially layers with high rBC mass concentrations also contain more dust. It is possible that in a stronger fire, that emitted more rBC, turbulence is also stronger, leading to an increased mobilization of large particles. The highest concentrations of large particles are found in layers with average rBC mass concentrations, measured on June 11 and June 14, that origin from the two largest fires, the Whitewater-Baldy fire encounters (lying diamonds for June 14 measurements) and one of the High Park fire plume encounters on June 11 (circles for June 11 measurements). On June 11, the large concentrations of dust particles could also be influenced by strong gust fronts from the thunderstorms. The gust front on May 30 (lying sand clocks) passed the airport at Lubbock/TX shortly after the Falcon had landed, carrying enough dust to strongly decrease the visibility (Figure 71).

Figure 71: Photograph taken on May 30, 01:38 UTC, shortly after landing in Lubbock. Due to the dust storm, the airport buildings in the background are hardly visible. A wing of the Falcon can be seen in the front. (Photograph taken by Roland Welser, DLR)

The measurements made on the back transfer flight on June 18 (thick lying crosses) in parts still contain large particles at 11 km altitude. Generally, concentrations of dust particles in BB layers were in many cases higher than the median observed during DC3 (thick black line in Figure 70). Especially in thunderstorm outflow, mineral dust signatures were higher than background values, indicating that dust particles were transported efficiently through the troposphere in the thunderstorms (Corr et al., 2016). This could also influence the concentration of coarse mode dust particles in the upper troposphere, if the upper tropospheric BB layers were influenced by thunderstorm outflow. This is a possible explanation for the vertical transport of the layer measured on June 17 (standing crosses in Figure 70), that was shown as example case in chapter 4.2.

Vertical transport in convection would also imply cloud processing and therewith removal of particles. To investigate these processes further, the next section focuses on the ratios between rBC particles and the non-soluble trace gas CO, which is not processed in clouds.

_____

4.4.2 CO in Biomass Burning Layers as an Indicator for Atmospheric Processes

The correlation between rBC and trace gases like CO can give ideas of the type of combustion and processes acting on the emitted plume. CO is, like rBC, a product of incomplete combustion. Even if CO is considered a short-lived trace gas, it has a much longer residence time in the atmosphere than rBC particles. CO is removed from the atmosphere mostly due to reaction with OH, resulting in an atmospheric lifetime of CO of about 30-90 days (Seinfeld and Pandis, 2016). In contrast to that, one of the main removal processes for rBC particles in the atmosphere is washout through cloud processing. Therefore the ratio between the rBC mass concentration and CO concentration depends on the burning type and will decrease due to rBC removal when the air parcel undergoes cloud processing.
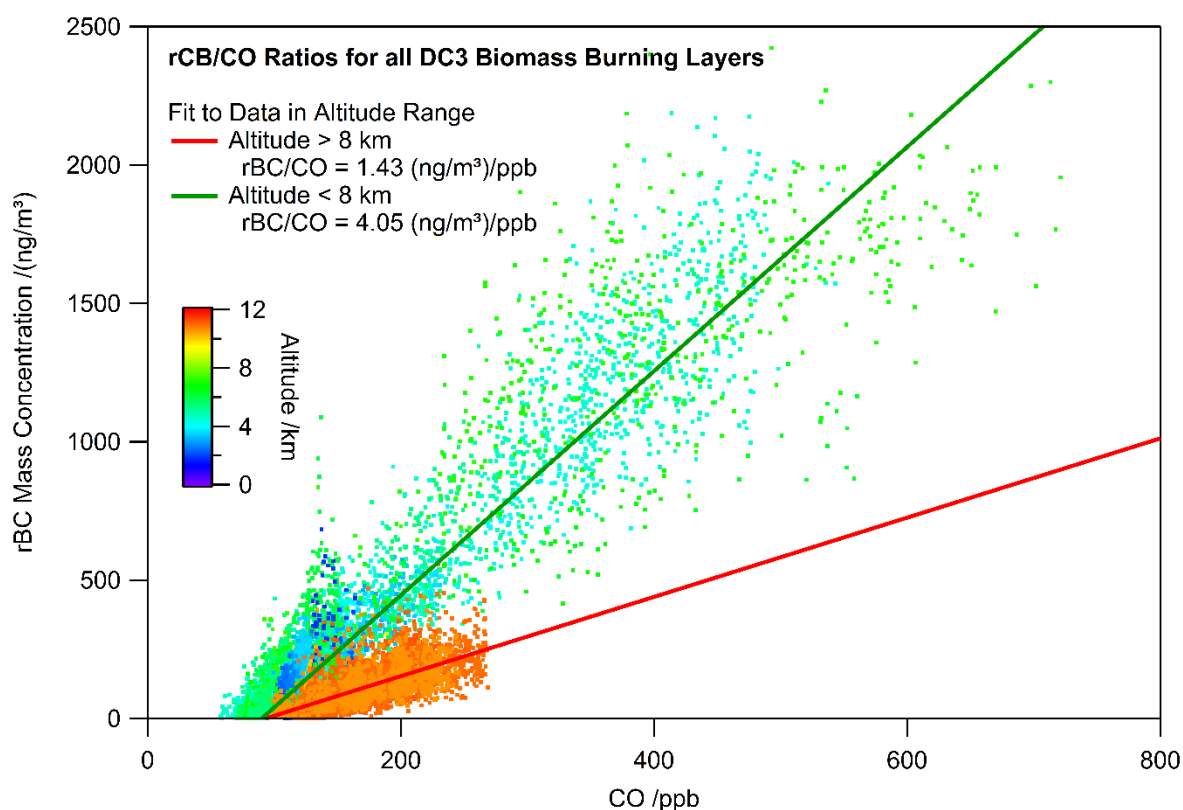

Figure 72: Correlation between CO and rBC mass concentrations and average rBC/CO ratio for all DC3 biomass burning layers, separated by altitude into layers below and above 8 km.

For a first idea of rBC/CO ratios in the BB layers during DC3, 1 s averages of rBC mass and CO concentrations measured after May 30, 2012 are displayed on a scatterplot in Figure 72, color-coded by altitude. Only data points measured in BB layers during DC3 are shown in this plot, other data points are not included Correlations fall into two groups, the lower and mid tropospheric layers in blue and green, and the upper tropospheric layers in orange to red colors. For a closer analysis, the layers are separated by altitude into layers below and layers above 8 km. This is the altitude, where no BB layers

were found, as e.g. the vertical profiles of the rBC mass size distribution parameters in the BB layers show (Figure 64). Layers below and above 8 km differ in properties, as detailed in the previous chapters. To get an average rBC/CO correlation, linear fits were applied to the data, separately for BB layers below (green line) and above (red line) 8 km altitude. Clearly, the upper tropospheric layers also differ in rBC/CO ratio, besides the differences in size distribution and mixing state, as discussed in the previous sections. The ratio of the rBC mass concentration to the CO concentration is 1.43 (ng/m³)/ppb in the BB layers below 8 km altitude, nearly three times higher than in the upper tropospheric ones, with 1.43 (ng/m³)/ppb.

The rBC/CO ratio and the CO concentration can be used to calculate a theoretical concentration of rBC mass that would be contained in the upper tropospheric BB layers, assuming that the ratio between CO and rBC mass concentration remains the same during the transport into the upper troposphere, with the same values as in the lower troposphere. In the layers below 8 km, the rBC/CO ratio is around 4 (ng/m³)/ppb, while the 11 km BB layers have an rBC/CO ratio of 1.4 (ng/m³)/ppb. With an average CO concentration in the upper tropospheric layers of 172 ppb, the rBC/CO ratio of the lower tropospheric BB layers would give an rBC mass concentration of 330 ng/m³. This is two to three times the concentration actually found in BB layers at 11 km altitude, which is between 60 and 180 ng/m³.

When assuming that the layers found in the upper troposphere had similar concentrations and size distributions as the layers found in the lower and middle troposphere, 50 to 80% of the rBC mass was removed during transport. These numbers are derived from the measured range of mass. As the mass size distribution of the upper tropospheric BB layers is shifted to smaller sizes compared to those below 8 km, the upper tropospheric BB layers contain a higher fraction of particles below the detection limit. Therefore, these numbers are an upper estimate of the removed mass fraction. The remaining rBC mass concentrations of 70 to 200 ng/m³ in the layers are still ten to hundred times larger than the concentrations found in the upper tropospheric background or in thunderstorm outflow (~1-10 ng/m³).

For the DC3 thunderstorms, Barth et al. (2016) and Bela et al. (2016) investigated scavenging efficiencies of several soluble trace gases. For formaldehyde, nitric acid, methyl hydrogen peroxide and sulfur dioxide, the fraction that was removed due to cloud processing varies between 40 and 90% (Bela et al., 2016). This is similar to the ratio between rBC particle mass concentration in BB layers below and above 8 km.

For a more detailed analysis of the single layers, the same linear fits as in Figure 72 were made for each individual BB encounter. With that method, the ratio is derived from total concentrations without the subtraction of background values. As the comparison of the rBC measurements with data from other years show (Schwarz et al., 2017), the background was heavily influenced by BB emissions. This can lead to slightly lower values of the rBC/CO ratio compared to ΔrBC/ΔCO ratios. Figure 73 shows the

rBC/CO ratios for all the BB layers found during the DC3 campaign as black filled symbols with the marker shapes referring to the different BB layers as before. Values for rBC/CO ratios found in the literature are added as colored open diamonds in the same colors as the corresponding legend at the top of the figure. Vertical error bars represent the altitude range at which the values were reported. The horizontal error bars are standard deviations given in the publication. As the values reported by Schwarz et al. (2008a) and Spackman et al. (2008) were retrieved from corrected total rBC mass concentration, the correction factor was removed from the data for better comparability (similar to the approach of McMeeking et al., 2010).
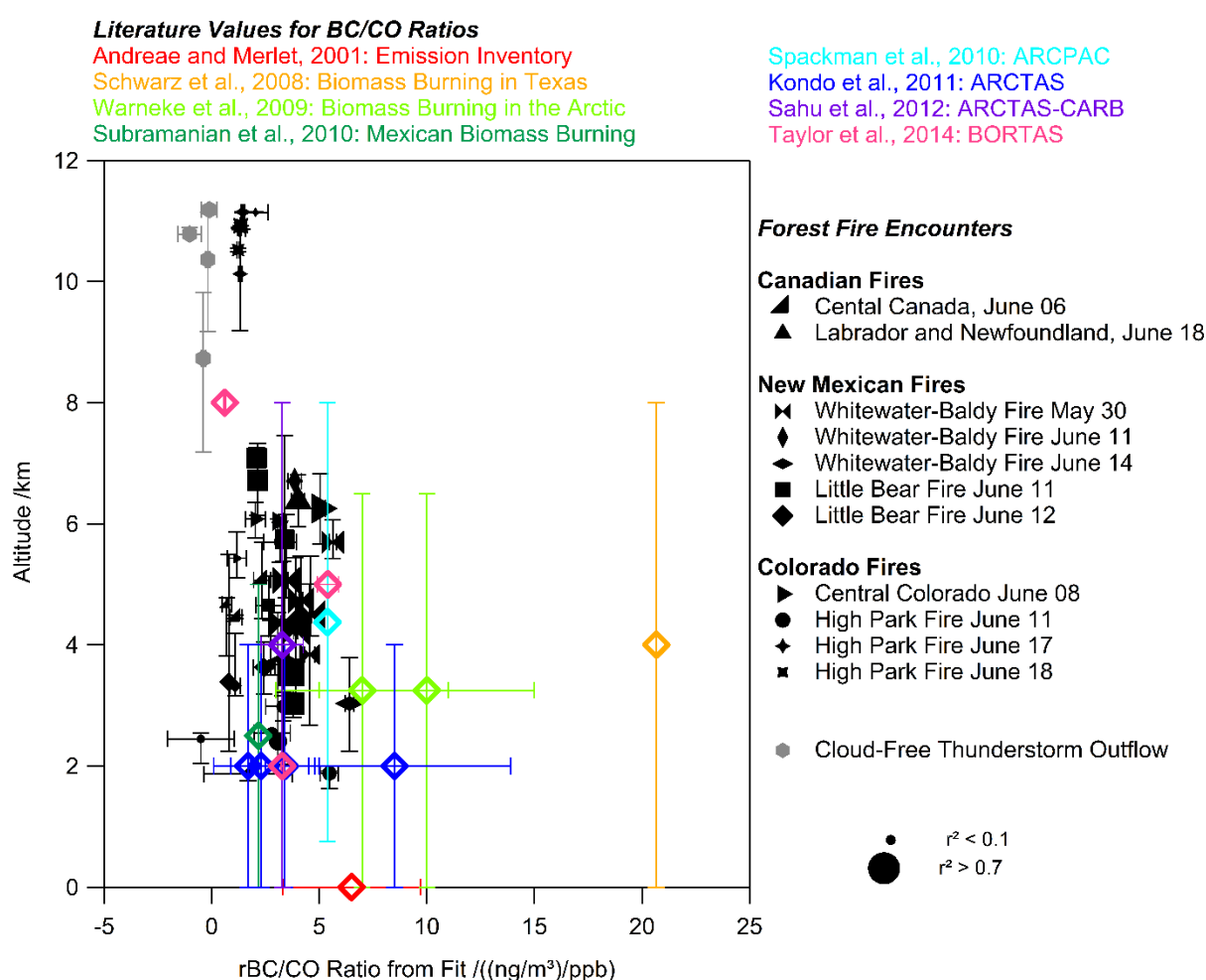
Figure 73: rBC/CO ratios from the DC3 biomass burning layers (filled symbols, legend to the right) compared to literature values (diamonds, colored according to source list at the top).

The DC3 values lie at the lower end of literature values for rBC/CO ratios in BB. The measured ratios are slightly lower than the emission inventory value for burning of extratropical forests given by Andreae and Merlet (2001), but most of them are still within the given uncertainty range. The literature values span a large geographical distance from subtropics to the Arctic. Geographically closest is the rBC/CO

ratio found by Schwarz et al. (2008a) in a fresh BB plume in Texas. This is also the highest reported value, indicating that the fresh plume in Texas contained more rBC mass relative to CO than all other layers which were measured several hours to days downwind of the fire. Other examples of rBC/CO ratios in BB plumes close to the DC3 region are BB plumes over California (Sahu et al., 2012), Mexico (Subramanian et al., 2010) and eastern Canada (Taylor et al., 2015). These values are in the same range as the DC3 values. Aged biomass layers that were transported to the Arctic are in a similar range or slightly higher than the DC3 values. Shown are average values from the ARCTAS campaign (Kondo et al., 2011a) and the ARCPAC campaign (Warneke et al., 2009; Spackman et al., 2010). The study by Kondo et al. (2011a) also reported that the observed BC/CO ratio decreased with an increase in accumulated precipitation along the backward trajectory for BB layers from Asia observed over Canada.

Most DC3 BB layers in the lower and middle troposphere were at the lower end but within the range of literature values. A reason for the lower emission of rBC in relation to CO could be the efficient burning of the dry fuel, since the region suffered from a severe drought (Hoerling et al., 2014). In some of the layers, the correlation between rBC and CO was close to zero, with an r^2 value below 0.5. Most BB layers in the lower and middle troposphere show rBC/CO ratios between 2 and 5 (Figure 73). The BB layers on June 6 and June 12 have lower rBC/CO ratios, around 1, with low r^2 values. These BB layers also show lower concentrations in rBC mass (compare Figure 64). The low concentration of rBC could be a result of mixing with background air, which would also explain the low correlation between rBC and CO. The negative value of the short encounter of the BB layer from the High Park fire on June 11 is probably caused by mixing with boundary layer air, as already shown in the previous sections, which led to the entrainment of an air mass with more CO in relation to rBC mass concentrated in a smaller size range.

The upper tropospheric BB layers had a lower rBC/CO ratio, with r^2 values between 0.1 and 0.6, than most of the lower and middle tropospheric layers. The overall pattern is similar to the relation derived from the whole entity of BB measurements (Figure 72). Upper tropospheric BB layers show a lower rBC/CO ratio, about 1.4, than most layers in the middle troposphere where the rBC/CO ratio in layers with more reliable ratios ($r^2 > 0.5$) are around 4 with a spread from 2 to 6, similar to the average value of 4.05, derived from all BB encounters (Figure 72).

CO is emitted at the ground into the boundary layer and can be brought to the upper troposphere by thunderstorms. Concentrations were often enhanced in thunderstorm outflow during DC3. The rBC/CO ratio is independent of dilution but changes with processes influencing the removal of one of the substances, mainly rBC particles. It is therefore interesting to compare this ratio for BB layers with values found in the boundary layer, the upper tropospheric background and in thunderstorm outflow.

Figure 74 shows the same rBC ratios as Figure 73 for the BB layers with altitude (black) in different symbols for the different layers. Values found in the boundary layer (yellow), thunderstorm outflow (red) and in the upper tropospheric background (green) are also shown. Generally, the boundary layer shows similar ratios between rBC and CO concentration as the BB layers in the middle troposphere. BB layers often lay on top of the boundary layer, so both layers mixed into each other due to convection in the course of the day. This led to high concentrations of BB aerosol in the boundary layer as well as elevated concentrations of freshly emitted, uncoated rBC particles in the BB layer while it was still distinguishable as a different layer (see also previous section 4.3.2). The downward mixing of these elevated layers due to the evolution of the convective boundary layer over the day can cause an influence of BB aerosol at the ground even far downwind of the wildfire.
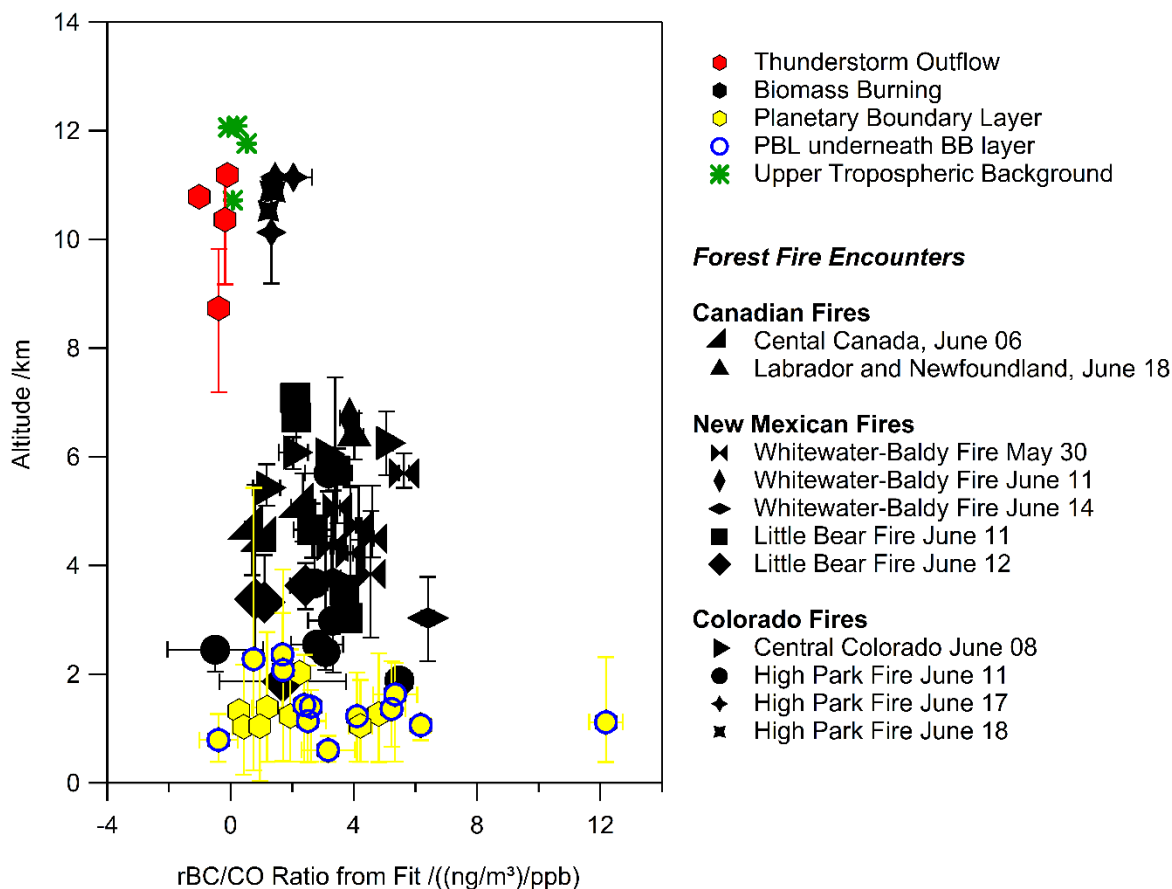
Figure 74: Ratio of rBC mass to CO concentration from fit at different altitudes for measurements in thunderstorm outflow (red), in the planetary boundary layer (yellow) and in biomass burning layers. The different layers are identified with the same markers as in the previous figures. PBL measurements that were influenced by biomass burning are marked with blue circles. The background value sequences are listed in Table 11, the thunderstorm outflow sequences are listed in the appendix (Table A 4).

The highest ratio of rBC/CO, 12 (ng/m³)/ppb, was found on June 8 in the boundary layer. On that day, small agricultural fires were burning close to the Salina airport, as it was observed from the plane during take-off. The mixing of boundary layer air with these fresh BB emissions might lead to a higher rBC/CO ratio, which is more similar to the observations of Schwarz et al. (2008a) and Warneke et al. (2009)than the BB layers above the boundary layer (Figure 73).

In the upper troposphere, rBC and CO are not well correlated in thunderstorm outflow and background air, with ratios around 0 and r² values below 0.05. The thunderstorm outflow and background sequences are the same as in previous chapters. In thunderstorm outflow, correlations between rBC and CO are generally low (due to washout) and in some cases even negative. The background was influenced by the wide spread of the thunderstorm outflow (Huntrieser et al., 2016b), so it is not astonishing that these values are similar to the outflow values.

Correlations between rBC and CO in the upper tropospheric BB layers are higher than in the background and thunderstorm outflow, and more reliable. The lower ratios compared to layers in the middle troposphere, indicate a removal of rBC particles, most likely due to cloud processing that does not remove CO. The comparison with thunderstorm outflow shows that the removal processes are much weaker than cloud processing and washout in thunderstorms updrafts. The comparison of rBC mass concentrations in thunderstorm outflow and upper tropospheric BB layers (section 4.3.1) shows that the layers contain a hundred times more rBC mass than the outflow. This leads to the conclusion that the upper tropospheric BB layers experienced processes that led to a removal of larger and thickly coated rBC particles somewhere between their emission and their arrival in the upper troposphere. The mass size distributions suggest wet removal processes while the rBC/CO ratios indicate that these processes are weaker than in thunderstorm cores. This makes it also interesting to look closer at the transport processes involved in lifting the layers up to 11 km altitude. The next chapter will therefore discuss the properties of the upper tropospheric BB layers, which are different to layers in the middle troposphere, as illustrated in the previous sections.

4.5 Biomass Burning Layers in the Upper Troposphere

While the previous sections showed all BB layers probed by the Falcon during DC3 and compared the aerosol characteristics of these layers at different altitudes, this section focuses on the layers in the upper troposphere. In order to classify the influence of upper tropospheric BB layers and their role as source for black carbon in the upper troposphere in general, it is necessary to estimate the total extent of the upper tropospheric BB layers, since aircraft measurements can provide only a snapshot of the atmosphere. Vertical transport processes that are involved in bringing the BB layers into the upper troposphere are also discussed in this chapter, focusing on vertical transport in a convective environment. The last part of this chapter gives an overview of the O3 concentrations measured in the upper tropospheric BB layers and discusses their sources.

4.5.1 Extent of the Upper Tropospheric Biomass Burning Layers

The Falcon flew in total about 1175 km in upper tropospheric BB layers, which was about 10% of the total distance flown on the part of the transfer flights between Salina and Greenland. During one of the transfer flights to Salina (120527a) and during two of the flights back (120617a and 120618a), BB layers were measured, partly over very long distances. These flights were planned solely for the purpose to get from Oberpfaffenhofen to Salina, and back again after the measurement campaign. All these encounters happened at cruise altitude during transfer, and are therefore not biased towards BB sampling by flight planning, as e.g. the BB flights (120529a and 120530a) were. While only 2% of the flight time on the transfer from Kangerlussuaq to Salina were in one upper tropospheric BB layer (flight 120527a), the

_____

Falcon spent 19% of back transfer from Salina to Kangerlussuaq in upper tropospheric BB layers, mainly on flight 120618a (Gander-Kangerlussuaq). The map in Figure 61 shows the location of these BB layer encounters. The BB layers were optically thick enough to be seen by the eye from the side during the flight. Figure 75 shows the view from the Falcon cockpit on June 18 over the Labrador Sea. The BB layers stretch as thin layers at the horizon.
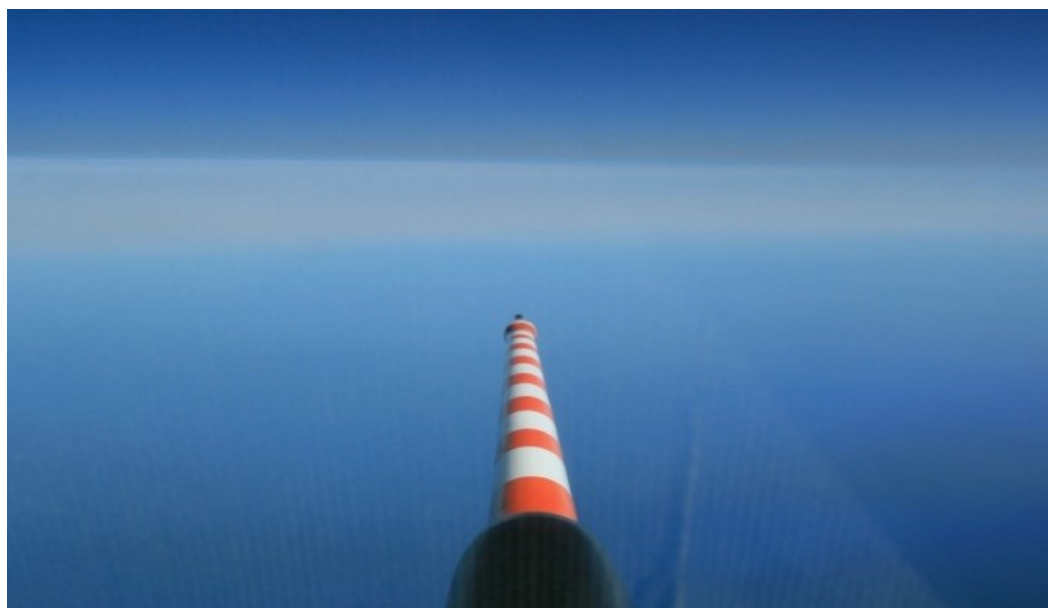
Figure 75: Picture taken from the Falcon cockpit during the transfer flight 120618a from Gander to Kangerlussuaq. The biomass burning layer is visible as thin brownish layers against the horizon. The red and white nose boom of the Falcon can be seen in the center of the picture. (Photograph taken by Bernadett Weinzierl)

On average, each of the encounters lasted for nearly 170 km, calculated as the average distance between start and end position of the Falcon penetration. This extension is larger than the average size of rBC-containing layers of 85-155 km found by Weigum et al. (2012) during three HIPPO campaigns. However, this average layer size for the HIPPO campaign includes layers measured at all altitudes with most of them situated between 2 and 9 km, and only few of them in the upper troposphere. The difference could also be due to the different flight patterns in the HIPPO campaign and during the DC3 transfer. While the DC3 transfer consisted mainly of straight flight legs in the upper troposphere at constant altitude (see, for example, the time series of the first back transfer flight, 120617a, Figure 54), the focus of the HIPPO campaigns was on atmospheric profiling, ascending and descending with only few constant altitude legs in between (Weigum et al., 2012).

The Falcon did not probe the layers in all directions so from the measurements only, it is difficult to judge their extent. The HYSPLIT dispersion model was used to calculate the distribution of CO emitted

by the High Park fire, to serve as a proxy for the distribution of rBC. It must be considered, however, that CO is not washed out in the model, so cloud processing of rBC particles cannot be represented. Model CO was emitted from a column with a base area corresponding to the burned area of the wildfire (~ 350 km²) reaching from the ground to 4000 m altitude. The simulation ran with continuous emissions from June 9 to June 20 2012. Two snapshots, corresponding to the times of the transfer flights 120617a (Figure 76) and 120618a (Figure 77), are shown, with the flight path superimposed in black. The BB sequences are marked in white. The HYSPLIT backward trajectories for the BB encounters, which were used to identify the source fire of the layers, are shown in the appendix (Figure A 3 to Figure A 13). On June 17, the upper tropospheric layer was about one day old. The layer measured over the Labrador Sea on June 18 was encountered about three days after emission. Properties of rBC particles in the June 18 layers were very similar to those in the June 17 ones, described in chapter 4.2, in spite of their different age, as the comparisons in the previous sections of this chapter illustrated.
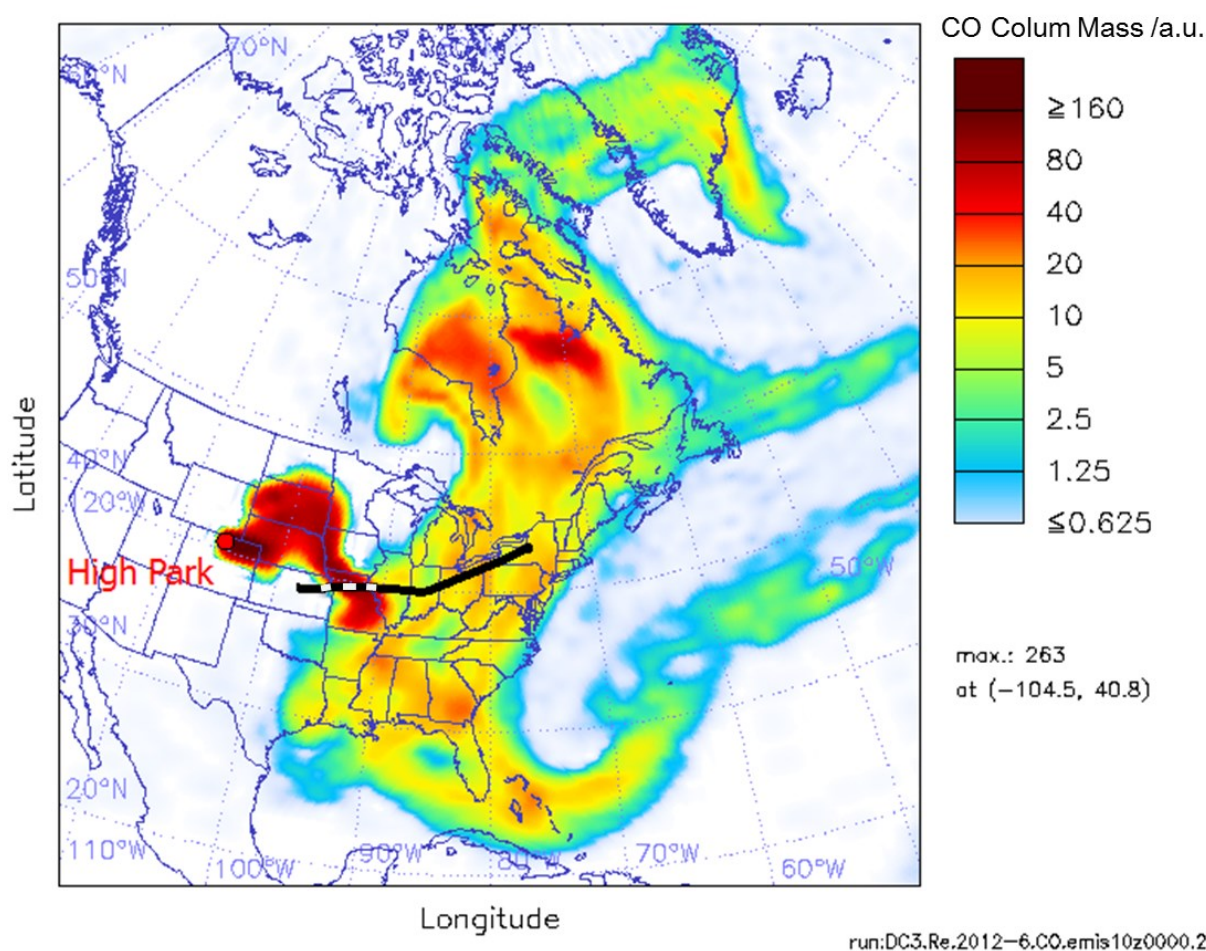

Figure 76: Dispersion of the total column CO mass for the High Park fire on June 17. The flight track of flight 120617a is shown in black and the flight sequences in biomass burning layers at 11 km altitude are marked in white. The flight distances covered during the three upper tropospheric layer encounters were 111 km (ascent) 132 km (west) and 68 km (east).
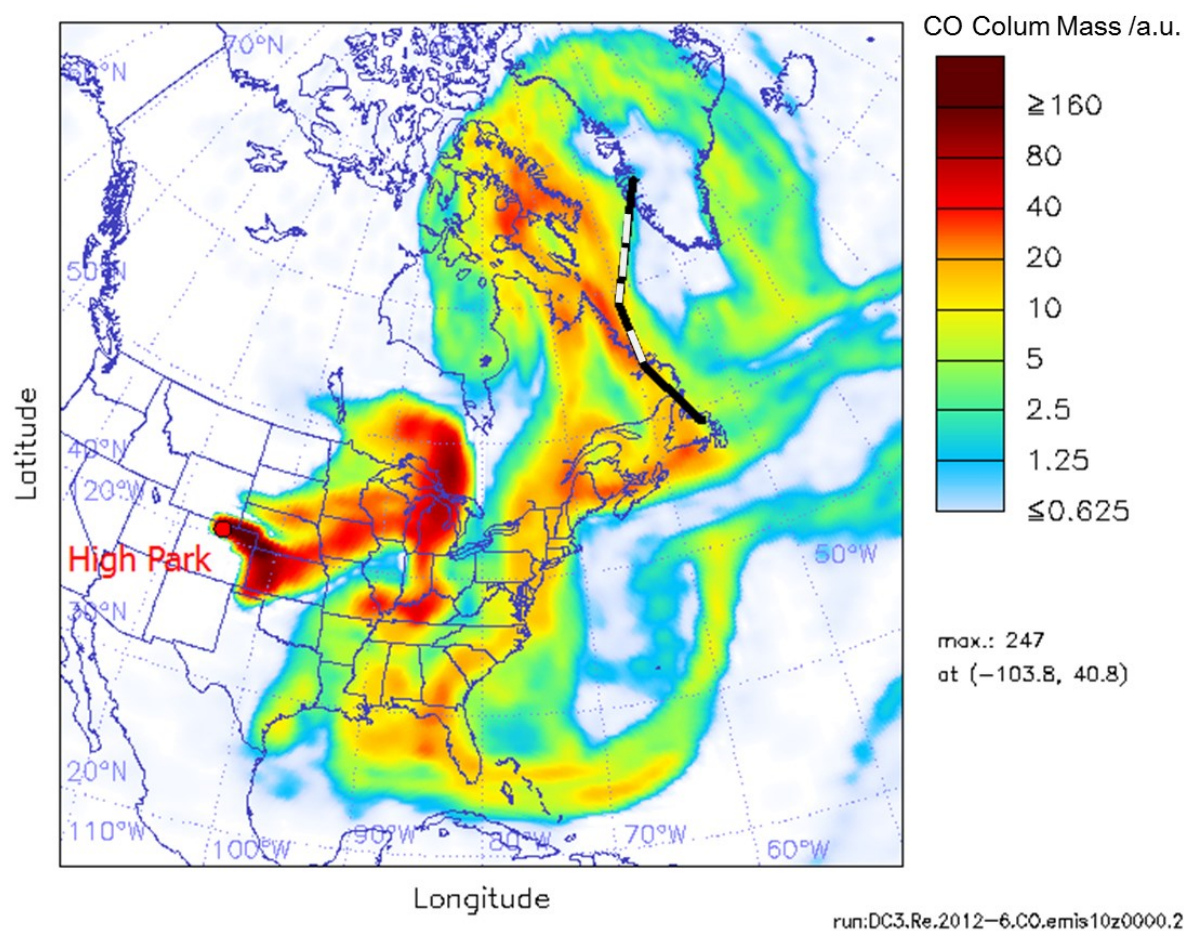
Figure 77: Same as Figure 76, but for June 18 and flight 120618a. The flight distances covered during the four upper tropospheric biomass burning layers encounters was, from south to north, 406 km, 85 km, 107 km, and 237 km.

The horizontal distribution of the HYSPLIT dispersion calculations show the June 17 BB layer, in the same place as it was measured (Figure 76). It shows the transport of the High Park fire BB layer towards the area, where the Falcon crossed the BB layer, but it appears in the model only up to an altitude of 4 km, not the 11 km the layer was measured at. As the dispersion model captures horizontal transport very well but cannot always resolve uplift processes far below the model grid scale, the vertical redistribution of air masses by the thunderstorm over Colorado on the previous day might not be captured. The two crossings of 132 km (west) and 68 km (east) are probably a lower estimate of the layer extent as it was crossed at its most narrow part, and the layer was separated by a stratospheric inversion (see chapter 4.2).

In case of the BB layer measurements on June 18, the dispersion calculations (Figure 77) indicate that the layer was touched along its longest extending side several times, resulting in the four layer encounters derived from the time series. The sum of these encounters, 835 km, could serve as an estimate

of the layer's elongation. This is certainly an upper limit of the horizontal layer extent as, according to the HYSPLIT calculation, the Falcon flew along the direction of the greatest extent of the layer.

To estimate the total rBC content of such an upper tropospheric layer, it is necessary to approximate its extent. Only one of the upper tropospheric BB layers was completely crossed in the vertical direction. The BB layer from the High Park fire encountered on June 17 during ascent stretched from 9.2 km altitude to 10.8 km, resulting in a thickness of 1.6 km. This is in the same range as thicknesses of upper tropospheric layers from thunderstorm outflow, 0.3-2 km (Huntrieser et al., 2016a). With an average extent in both horizontal directions of 170 km, the volume of the layer would be about $46 \cdot 10^3$ km³. For a lower estimate of 70 km and an upper estimate of 840 km, the layer volume would be $7.8 \cdot 10^3$ km³ and $1129 \cdot 10^3$ km³. The average ambient total rBC mass concentration in the upper tropospheric layers is about 38 ng/m³. With these assumptions, this would give approximately 1.8 Mg of rBC for the average case and 0.3 Mg and 43 Mg for the upper and lower estimations.

In a case study on one Canadian wildfire BB layer over Europe, Dahlkötter et al. (2014) estimated the total rBC mass in this layer to be 25 Mg. This amount is larger than the average estimation here, but still within the range of the upper estimate. These calculations give examples for the contribution of BB layers to rBC in the upper troposphere. To evaluate this contribution, the rBC content of BB layers is compared to aviation emissions as these are the only local source of rBC in the upper troposphere. Besides thunderstorms, fast vertical transport happens in warm conveyor belts (WCB). However, WCBs over the northern Atlantic are more frequently in the winter months (Eckhardt et al., 2004), when North American fire activity is low.

Depending on the estimation method the amount of black carbon emitted directly into the upper troposphere by aircraft at cruise altitude is 6000 Mg/yr (Bond et al., 2013) to 14500 Mg/yr (Stettler et al., 2013), which corresponds to 16 to 40 Mg per day globally. When comparing these numbers, it must be noted that the aviation-related emissions correspond to all aircraft worldwide on one day. The rBC mass in one BB layer on one day was emitted by only one fire of a large amount of wildfires burning simultaneously all over the world (see e.g. the MODIS fire maps at http://rapidfire.sci.gsfc.nasa.gov/cgi-bin/imagery/firemaps.cgi). In addition, thousands of thunderstorms are active globally per day and a considerable number of them might transport smoke emissions to the UT. Depending on the estimated extent, one upper tropospheric BB layer might contain a tenth to two times the rBC mass that it is emitted by aviation worldwide in one day.

4.5.2 Vertical Transport of Biomass Burning Aerosol in the Vicinity of a Thunderstorm

Several different transport mechanisms could be responsible for the uplift of the BB layers to the upper troposphere. In chapter 2.2, various types of vertical transport were briefly described. The mass size

distributions of rBC particles in the upper tropospheric BB layers indicate that cloud processing and wet removal were involved in the transport process, as discussed in chapter 4.3. The case study of the upper tropospheric BB layer from the High Park fire on June 17 (chapter 4.2) was found in the remnants of a strong thunderstorm which was located behind a frontal system.

Pyroconvection has been identified as the cause of rapid vertical transport of BB layers to the region of the upper troposphere and lower stratosphere for previous cases (e.g. Jost et al., 2004; Dahlkötter et al., 2014). In both studies, a large pyroconvective cloud was located directly above the fire location. This was not the case for the High Park fire. The study by Lang et al. (2014), which looked at lightning in the BB smoke plumes from the Colorado fires during DC3, found that pyroconvection reaching higher than 8 km over the High Park fire occurred only on one day, June 13. On that day, the plume was transported westwards over the Great Lakes and did not reach the DC3 operation area in the following days (see trajectories in Figure A 15, page 193). On the days when the BB layers probed on June 17 and 18 were emitted from the High Park fire (June 16 and June 15, respectively), the plume reached only up to around 6-8 km altitude. Therefore, a different process must have causes the uplift to the upper troposphere than pyroconvection, unlike the cases described by Jost et al. (2004) and Dahlkötter et al. (2014). While pyroconvection was rarely observed during DC3, deep convection was a nearly daily phenomenon during the campaign (Barth et al., 2015; Huntrieser et al., 2016b). In addition to the well-known updrafts inside the thunderstorm, Huntrieser et al. (2016b) describe additional upward transport pathways of air from the boundary layer and lower troposphere at the outer edge of thunderstorms. A more detailed description, based on airborne trace gas in-situ observations, can be found in Huntrieser et al. (2016a). This upward transport at the thunderstorm edge is plotted schematically as yellow arrows in Figure 78. Air from the lower troposphere is transported upwards at the edge of the thunderstorm to the region just below the anvil outflow. In the area beneath the outflow, descending stratospheric masses that wrap around the outflow (red) and ascending boundary layer air masses (yellow) can mix (Huntrieser et al., 2016b). This air mass is then rich in both O_3 from the stratosphere (maybe also from photochemical O_3 production) and also in CO and rBC from the boundary layer.
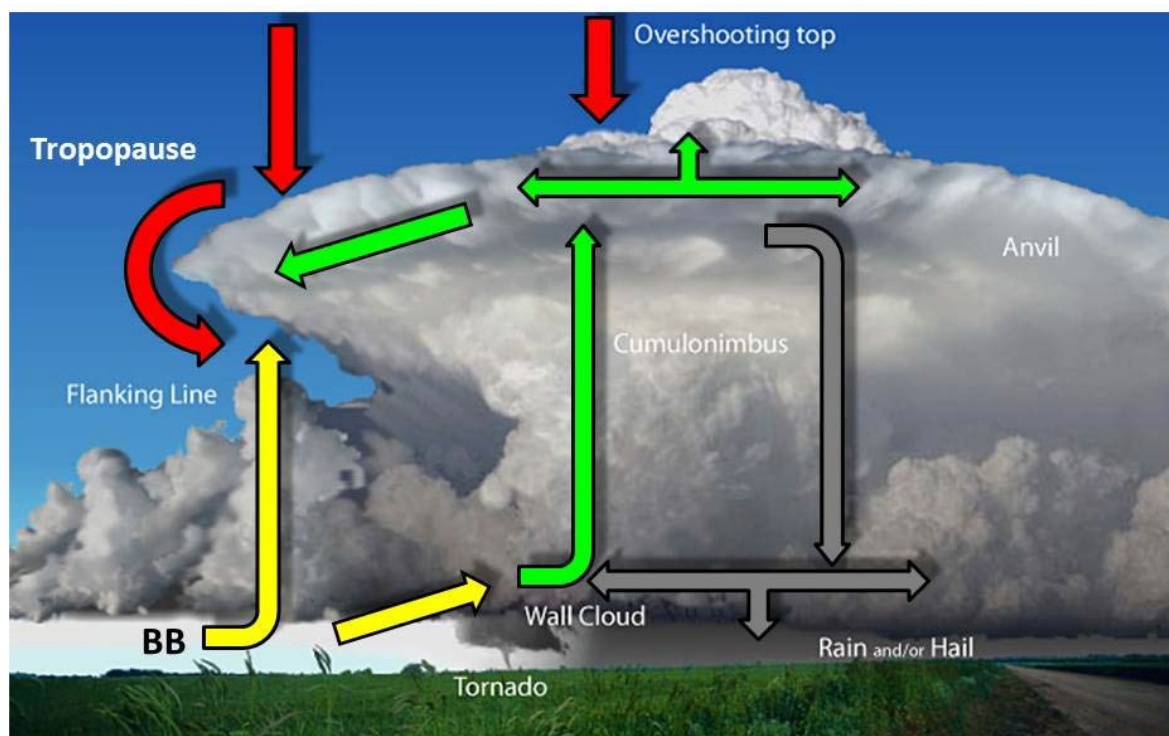
Figure 78: Sketch of circulations in and around an isolated severe thunderstorm (from Huntrieser et al., 2016b; storm image credit: NOAA National Weather Service, http://www.weather.gov/jetstream/tstrmtypes). Green arrows mark the updrafts and main outflow inside the storm, grey arrows indicate downdrafts. Red arrows symbolize the downward mixing of stratospheric air (Pan et al., 2014) and yellow arrows the upward transport of biomass burning and boundary layer air.

The comparison between rBC mass size distributions in upper tropospheric BB layers and thunderstorm outflow shows that washout was dominant in the main anvil outflow. Concentrations of rBC mass were about one order of magnitude lower in the outflow than in the lofted BB layers, indicating that most rBC was removed with the downdrafts inside the storm (section 4.3.1). However, the upper tropospheric BB layers show also signatures of cloud processing and wet removal, though to a lesser extent than anvil outflow. As severe thunderstorms are often surrounded by smaller cumulus congestus clouds (Emanuel, 1994), which are also shown in Figure 78 (flanking line), cloud processing and wet removal of the BB aerosol could also have happened in these. The air mass transported to the upper troposphere would then contain less large particles and fewer particles with thick coating, compared to the layers below 8 km, in accordance with what was found in the upper tropospheric BB layers (as described in section 4.3). Though the wet removal reduces the rBC mass in the transported air mass, this removal is less strong than in the thunderstorm cores, as the comparison of rBC mass size distributions and rBC/CO ratios between upper tropospheric BB layers and anvil outflow shows (see section 4.3.1 and section 4.4.2).

The case of the upper tropospheric BB layer from the High Park fire on June 17, 2012, (chapter 4.2) as well as the layers measured on June 18, 2012, shows both high O_3 concentration and rBC mass concentrations distinctly above the background levels. O_3 concentrations were also elevated in aged thunderstorm outflow, as the discussion in Huntrieser et al. (2016a) details. However, rBC mass concentration (included here as outflow case "120608") were much lower than in the upper tropospheric BB layers measured during the transfer flights. In that outflow case, no large wildfire smoke plumes were close by and removal processes reduced the rBC mass concentration to background level (details in Huntrieser et al., 2016a).

As both wildfires and thunderstorms were frequent during the DC3 measurement period in May and June 2012, it might be possible that upper tropospheric BB layers could occur more frequently than just the three cases that were measured by the Falcon (120527a, 120617a,120618a). So far, in-situ measurements of rBC in upper tropospheric BB layers are sparse (Dahlkötter et al., 2014; Taylor et al., 2014). Considering vertical transport by thunderstorms as a potential source for BB aerosol in the upper troposphere, a simple approximation can be made by roughly quantifying the number of thunderstorms that possibly interacted with the smoke plumes from the extended wildfires during DC3. Comparing cloud top heights and visible images derived from GOES satellite data gives 17 days of a 30 day period around the Falcon DC3 field campaign (May 25 to June 23) on which large thunderstorms evolved downwind of wildfires with large smoke plumes (visible on GOES-13 channel 1 images). On about half of the days in this period, thunderstorms had the potential to transport large amounts of BB aerosol to the upper troposphere. This rough estimate indicates that upper tropospheric BB layers can be more than just episodic occurrences in the Great Plains area in early summer.

The Falcon crossed the Atlantic on the same route as during the DC3 transfers also in the summers of the two following years, 2013 and 2014, for entirely different campaigns. While no BB layers were encountered during the two flights in 2014, the 2013 transfer was in the middle of a long-range transport event where massive amounts of BB aerosol was transported from North America to Europe (Trickl et al., 2015). Mattis et al. (2008) also find a seasonal peak in the occurrence of aerosol layers from North America over Leipzig that coincides with the North American summer burning season. These measurements with the Falcon give therefore the impression that events of large rBC transport in the upper troposphere over the Atlantic maybe a common feature during the summer season.

4.5.3 Mixing of Upper Tropospheric Biomass Burning Layers with Stratospheric Air

In the transport processes shown in the previous section, lifted air from the lower tropopause can be mixed with stratospheric air in and outside of the anvil region of the convective storm (Huntrieser et al., 2016a). Thereby, O_3-rich air would be entrained into the air parcel, increasing the concentration of O_3.

_____

However, O₃ can also be produced in BB layers by photochemistry. Under the influence of solar radiation, photolysis of precursor species produces O radicals that form O_3 with ambient oxygen molecules (Seinfeld and Pandis, 2016). These precursors, nitrogen oxides, CO, and organic carbons, are emitted from wildfires in large amounts and can lead to the production of O_3 in the smoke plumes downwind of the fires, globally resulting in about 170 Tg or 3.5% of tropospheric O_3 production per year (Jaffe and Wigder, 2012).
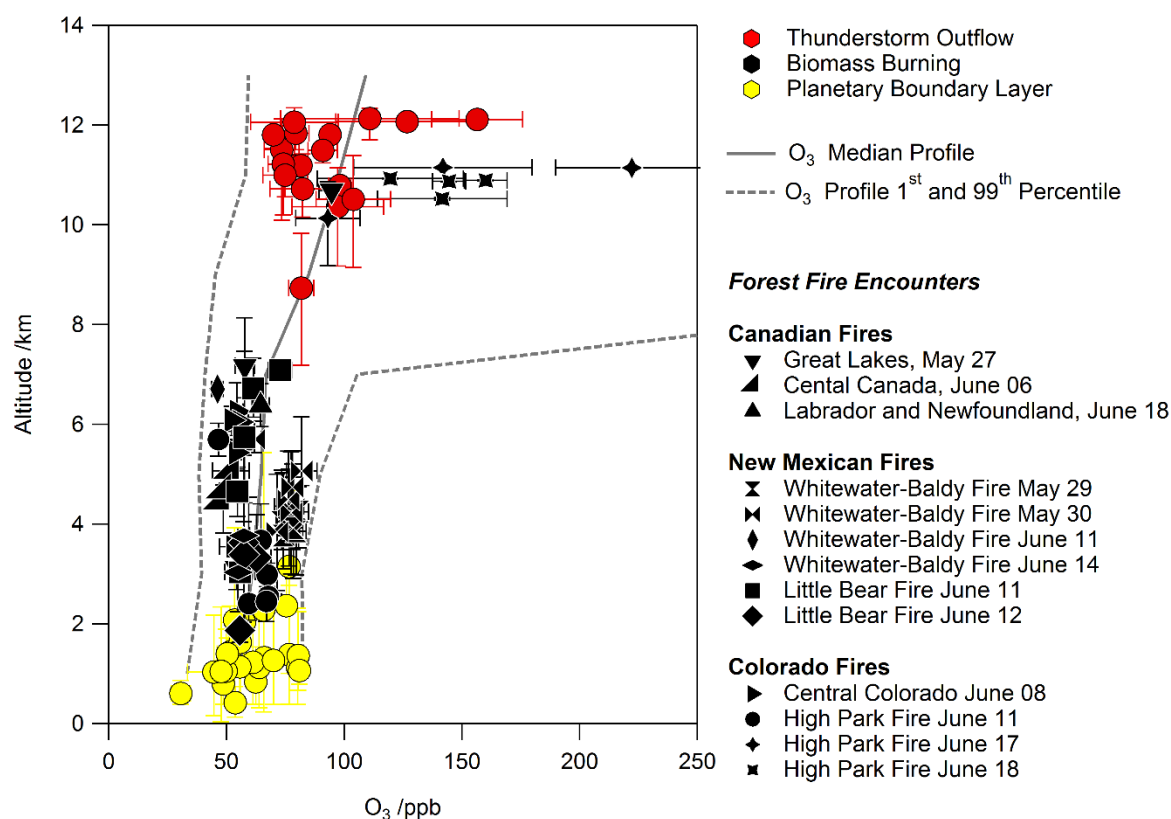

Figure 79: Vertical distribution of the concentration of O₃ concentrations for flight sequences in the boundary layer (yellow), in biomass burning layers (black) and in thunderstorm outflow (red). Vertical error bars represent the vertical extent of the measurements, which may not represent the vertical extent of the corresponding air layer. Horizontal error bars represent the standard deviation of O₃ concentrations in the corresponding sequence. The grey line represents the median of all O3 measurements during DC3, with the 1ˢᵗ and 99ᵗʰ percentiles marked by dashed grey lines.

Figure 79 shows the O_3 concentrations for all BB layers probed by the Falcon during DC3. Boundary layer and thunderstorm outflow values are added for comparison. The previous sections already discussed the differences in rBC particle properties between the layers below and above 8 km. The striking similarity of rBC mass size distributions is not the only feature that distinguishes these upper tropospheric layers from those below 8 km. Another difference between the BB layers below and above

---

8 km altitude are the strongly enhanced O_3 concentrations, especially in the High Park fire layers on June 17, 2012.

Below 8 km, the O_3 concentration found in BB layers lies between 40 and 90 ppb, slightly higher than background concentrations (about 30-60 ppb over the North Atlantic, Kumar et al., 2013). The higher values seem to be typical for BB layers of an age of several days with photochemical production of O_3. For example, Parrington et al. (2013) found similar concentrations in Canadian forest fire plumes during the BORTAS campaign in 2011. O_3 concentrations in this range are also reported by Real et al. (2007) from the ICARTT/ITOP campaign for a BB layer measured at different ages up to 10 days during long-range transport. The Whitewater-Baldy fire plume, measured on May 29 and 30, contains the largest O_3 concentrations, with all encounters clustered around 70-85 ppb. BB layers from other fires at that altitude, like those from the Canadian fires or the Little Bear BB layers, have slightly lower O_3 concentrations. This could be an effect of slightly different burning conditions leading to an increased emission of O_3 precursors, in the Whitewater-Baldy fire, which covered a larger area than the other fires. High concentrations of co-emitted O_3 precursors could also contribute to O_3 production and the elevated O_3 concentrations. On both days, May 29 and 30, the BB layers were probed during the afternoon, around 3pm local time, while the other layers were probed at an earlier or later time of the day. The stronger insolation at that time of the day could also have been a factor in increasing O_3 production. The layers with the highest O_3 content were encountered on June 17 during the late morning, at an altitude of about 11 km.

Above 8 km altitude, the average O_3 concentrations found in thunderstorm outflow and in upper tropospheric BB layers during DC3 range from 70 ppb to more than 200 ppb (see also Huntrieser et al., 2016b). Even the lowest value lies above the average level found in BB layers below 8 km. Considering that the High Park fire BB layer measured on June 17 was only about one day old, this would result in a production rate of more than 150 ppb/day, which is twenty times higher than the 7-8 ppb/day given in literature (Pickering et al., 1996). These high O_3 concentrations cannot be a product of photochemical production in BB layers alone, making mixing with stratospheric air, as described in Huntrieser et al. (2016a) the most likely source for such a high O_3 concentration in the upper tropospheric BB layers. The measurements on June 17 (Figure 54) and June 18, 2012 (not shown) indicate an increase in O_3 concentrations right after leaving the BB layer with high rBC concentrations. The high concentrations found already in the fresher layer on June 17 indicate that the mixing of O_3-rich air must have happened very soon in the transport process, enhancing O_3 concentrations by about a factor of 2. As the lifetime of particles is longer in the stratosphere than in the troposphere, a transport of BB layers into the tropopause region increases their lifetime and therewith their effect on radiation and climate.

5   Summary and Conclusion

The DC3 campaign gave a unique opportunity to study many BB layers in the whole vertical extent of the troposphere since 2012 was a very intense fire year. Many strong thunderstorms were active in the study area during the DC3 field campaign, that had the potential to rapidly transport the BB emissions to the upper troposphere, where the lifetime of many trace species is longer and their effect on radiation and climate increases.

This work reports mainly rBC measurements made with an SP2 on board of the DLR Falcon aircraft. The SP2 is an ideal instrument to measure rBC particles in the accumulation mode, where the majority of rBC mass from BB is found. To acquire good and reliable data from the SP2, it is necessary to validate the alignment and calibration regularly, as described in chapter 3.2. Regular measurements of particles of known size and optical properties, like PSL, are required to monitor laser performance. It was demonstrated here that the performance of the SP2's scattering detector can be further improved by correcting for the detectors temperature dependency. The calibration of the incandescence channels is a crucial factor in deriving reliable values for rBC particle mass, making it necessary to verify the calibration regularly. If no adjustments to the detector system were made, like changing the detector gain settings, calibrations performed within an interval of about 1-2 months match well while a drift of nearly 20% can be observed within an interval of one year, as it was demonstrated in this work. A crucial parameter for the SP2's performance for determining rBC optical size and coating thickness is the split point. Here, it was shown that alignment procedures for the split detector are different for different versions of the split detector, as the newer one, which was also employed during DC3, produces an artificial electronic peak. The standard check procedure do not capture these differences due to this artificial peak, compromising the split point quality during DC3, as described in section 3.2.1.3. Therefore, a different data treatment was necessary to derive information on rBC particle mixing state. The delay time between the scattering and the incandescence signal peak is increased by the time, a thick coating needs to evaporate in the laser beam and can therefore be used to differentiate between rBC particles with thick and those with thin or no coating.

Though the DC3 field campaign focused on studying thunderstorms, the abundance of wildfires, especially to the west of the operation area, caused the presence of BB layers throughout most of the campaign. Since 2012 was characterized by an extraordinarily strong fire season, wildfire emissions even influenced the rBC mass concentrations in the atmospheric background over the Central US. The average vertical profile of rBC mass concentrations measured during DC3 is much higher than profiles measured in other years (Schwarz et al., 2017). BB layers were encountered at different altitudes throughout the troposphere, with a gap at 8-9 km, where no BB layers were observed. This study investigated the properties of rBC particles in those BB layers and their representativeness and

comparability. Of special interest were vertical transport processes that led to the contrast between BB layers in the upper troposphere and those below 8 km altitude, mainly due to washout of larger, coated rBC particles.

In the free troposphere, the BB layers were located mainly between the top of the boundary layer and 8 km. Two typical BB layers as they were found frequently during DC3 in the free troposphere were shown in detail in the case study of June 11, 2012. The BB layers on June 11 contained high concentrations of rBC mass, up to 1 μg/m³, and their vertical extent was around 1-2 km. One of the layers was situated directly on top of the boundary layer while the other was measured at about 7 km altitude. Both BB layers were dry, with the relative humidity going down to nearly 10%, stably stratified and had a sharp upper edge connected to a capping inversion. The BB layers were advected horizontally without major changes in altitude. When the BB layers approached thunderstorms further downwind from the source, the layer reached higher, up to altitudes of 7 km, as detailed in the case study of June 11 (chapter 4.1). The thunderstorm could have acted here as a barrier forcing the BB layer to rise. In general, the BB layers measured below 8 km altitude showed strong variations in rBC mass concentration, from less than 0.1 μg/m³ to more than 2 μg/m³. The mass size distribution of rBC particles also varied strongly between different BB layers, even if they originated from the same wildfire and were measured on the same day. The observed MMDs (140-200 nm) were on the low side of the range found in other measurements of rBC in biomass burning layers, e.g. average values of 187$\pm$10 nm over Canada (Kondo et al., 2011a) or 193$\pm$16 nm over California (Sahu et al., 2012). The parameters of the mass size distribution of rBC in the DC3 BB layers, MMD and GSD, have an approximately linear relationship which is typical for particle ageing. The fitted slope is lower than the one found by Dentener et al. (2006) and Petzold et al. (2007) since they included whole particles and all aerosol types while here, only the rBC cores are considered. In lofted BB layers in the middle troposphere, about 60-80% of the rBC particles were thickly coated, which is in the range of literature values (about 70%, Akagi et al., 2012). BB layers directly on top of the boundary layer showed in some cases a lower fraction, less than 50%, of thickly coated particles. Fresh pollution with a high fraction of uncoated rBC particles is entrained into the BB layer when the convective boundary layer increases in depth over the day and grows into the BB layer above.

The concentration of super micron particles was enhanced in most BB layers, to 0.1-1 cm⁻³, with the median concentrations during DC3 being about one order of magnitude lower, 0.3-0.001 cm⁻³, depending on altitude. In some cases, coarse mode concentrations reached 1 cm⁻³, comparable to values typical for Saharan dust layers measured during the SAMUM campaigns (0.5-1 cm⁻³, Weinzierl et al., 2009). As the Great Plains suffered from a drought in 2012 (Hoerling et al., 2014), the soil was dry and could easily be mobilized by wind and turbulence in strong wildfires and thunderstorm gust fronts, which might explain the increased concentrations in super micron particles.

While rBC particles in BB layers below 8 km altitude show properties that are fairly similar to literature values, the situation for BB layers measured above 8 km latitude is different. The BB layers found in the upper troposphere have a vertical extent of about one kilometer, and can stretch horizontally over distances of several tens to about 1000 km. The mass concentration of rBC particles was strongly enhanced to more than 0.2 µg/m³ in the upper tropospheric BB layers, which is about hundred times higher than background concentrations (about 0.001 µg/m³ at 11 km altitude, Schwarz et al., 2017). In contrast to the strong variability in rBC mass size distributions in BB layers below 8 km altitude, rBC particles in UT-BB layers show a nearly uniform mass size distribution, independent of source and age. The rBC mass size distribution was slightly narrower in the layers above 9 km with a geometric standard deviation of 1.5 compared to the 1.5 to 1.8 found below 9 km, and mass median diameters were about 145 nm. This mass size distribution is not only similar to the distributions found in the upper tropospheric background and in thunderstorm outflow, but also in a BB layer over Canada (Taylor et al., 2014) and a BB layer over Europe from a Canadian wildfire in 2011 (Dahlkötter et al., 2014). The recurrence of this nearly uniform size distribution in the upper troposphere associated with BB layers indicates that this is a steady-state distribution reached after similar atmospheric processes. The fraction of thickly coated particles in the upper tropospheric BB layers was about 50%, which is lower than in elevated layers in the middle troposphere.

The measured rBC properties were different between BB layers observed at different altitude, with strong variations found below 8 km altitude and nearly uniform rBC mass size distributions in the upper troposphere. This distinctive altitude dependence of rBC particle properties indicates that processes during vertical transport influenced rBC mass size distribution and particle mixing state. To investigate the processes during vertical transport, CO was used as a tracer as it can indicated cloud processing, which removes hydrophilic rBC particles and leaves the non-soluble trace gas CO behind. A comparison between the rBC/CO ratios found in DC3 BB layers, 4 (ng/m³)/ppb on average, and literature values shows that the estimated values from DC3 for the layers below 8 km are within, but on the low end of values from other studies, ranging from 1.7 (ng/m³)/ppb (Kondo et al., 2011a) to 20 (ng/m³)/ppb (Schwarz et al., 2008a). In the upper tropospheric BB layers, the rBC/CO ratio was lower, 1.43 (ng/m³)/ppb on average, indicating that the upper tropospheric BB layers contain only half to a third of the rBC mass expected from the CO concentration.

The shift in rBC mass size distribution to smaller diameters in upper tropospheric BB layers can also be attributed to washout during transport. As larger particles and particles coated with hydrophilic substances tend to activate in clouds better than small ones, uncoated particles, the larger particles will be washed out preferentially (e.g. Moteki et al., 2012). As coated rBC particles are often better cloud condensation nuclei than uncoated ones, cloud processing can also explain the reduced fraction of thickly coated rBC particles in the upper tropospheric BB layers. The resulting rBC mass size

distribution is then narrower with the peak at smaller sizes, as found in the upper troposphere. A similar rBC mass size distribution was also n found in thunderstorm anvil outflow and in the upper tropospheric background, though it must be noted that the latter was likely influenced by thunderstorm outflow, too. The comparison of rBC mass concentrations and rBC/CO ratio in upper tropospheric BB layers and anvil outflow indicate that washout in anvil outflow was stronger than washout processes experienced by the upper tropospheric BB layers during transport. In one case study, June 17, 2012, an upper tropospheric BB layer and its transport pathways were analyzed in detail (chapter 4.2). The BB layer was located in the upper troposphere behind a frontal system and contained rBC mass concentrations about hundred times higher than in the background, with a similar rBC mass size distribution as in all cases of upper tropospheric BB layers found during DC3. Analyzing the meteorological situation led to the conclusion that the BB layer was injected into the upper troposphere by a large, overshooting thunderstorm located right to the south of the High Park fire. This vertical transport was not captured by backward trajectories and dispersion calculations of the High Park fire plume, possibly because the model grid was too coarse to correctly resolve all involved processes.
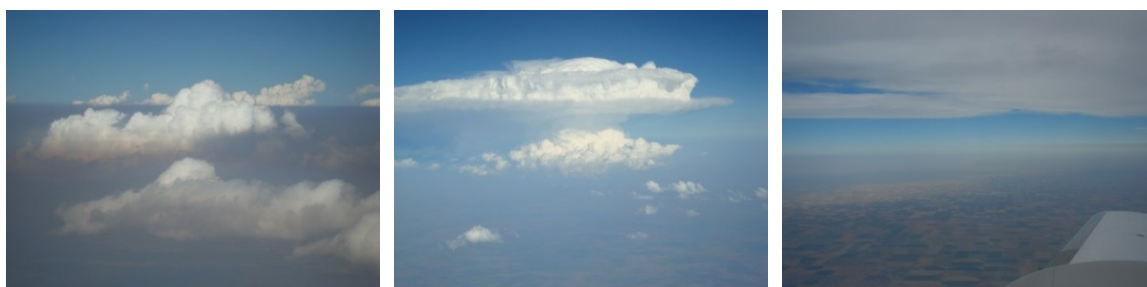
Figure 80: Development of a large, overshooting thunderstorm in a biomass burning environment. From left to right: Evolving cumulus clouds in the thick, brownish biomass burning layer, towering cumulonimbus cloud with large anvil, dissipating clouds from the dissolving thunderstorm cell. (Photographs on the left and in the middle taken by Roland Welser, DLR; see also Huntrieser et al., 2016b; Photograph on the right taken by Daniel Fütterer, DLR)

Figure 80 shows the development of such a large-scale, overshooting thunderstorms in a BB environment episodically in three stages. The cumulus clouds start to grow in the top part of the BB layer, seen as brownish air layer with a sharp upper edge (left). The growing towers make their way to the tropopause, where the anvil forms. In the Midwest, the tropopause sometimes has a double structure (Homeyer et al., 2014), leading to the two-layer anvil seen in Figure 80 (middle). The third picture shows the dissipating stage and the reduced visibility due to the high particle concentrations caused by the wildfire emissions.
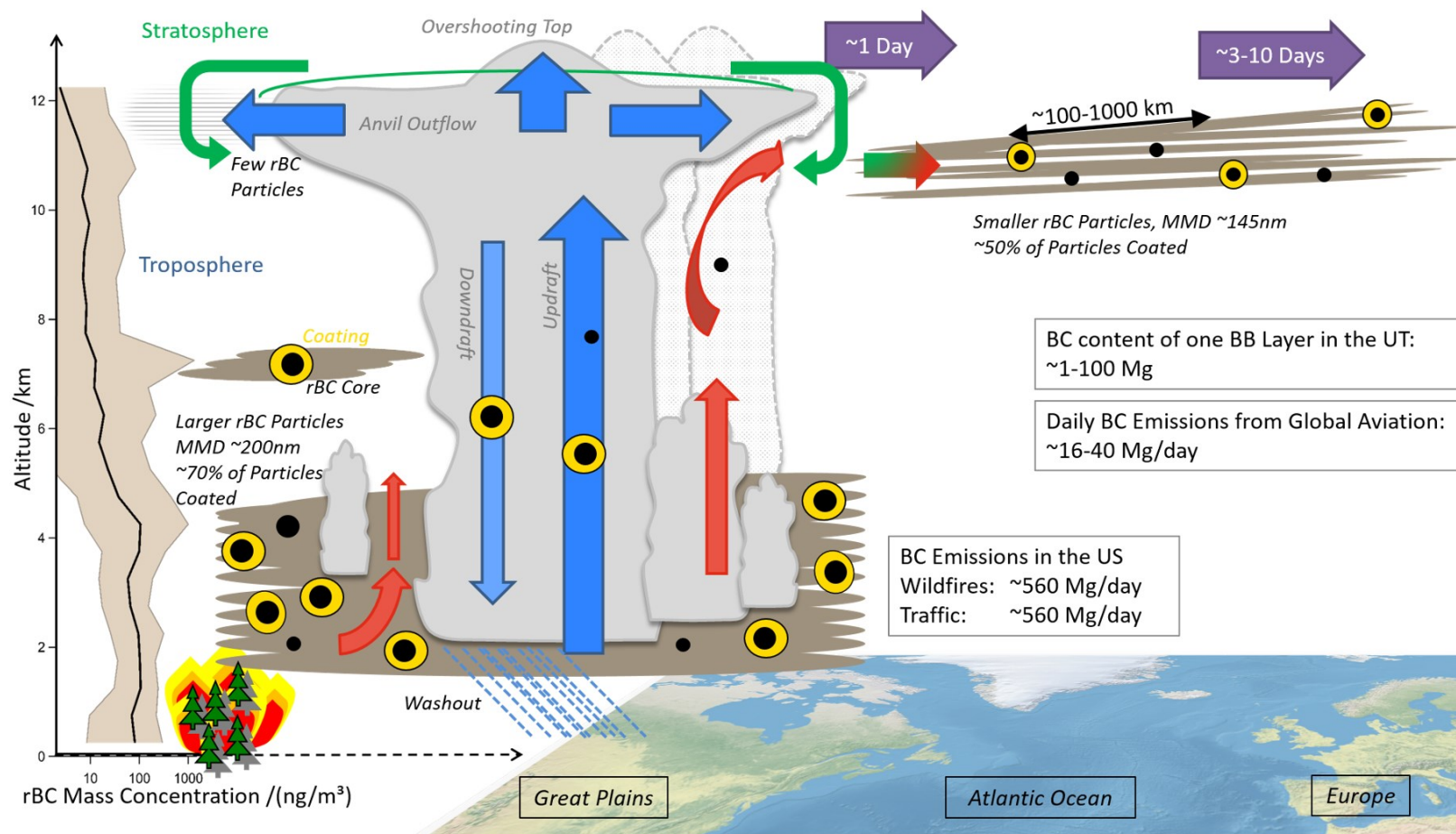
Figure 81: Sketch of biomass burning aerosol transport from its source, large wildfires in the Midwest, ascent associated with large-scale, overshooting thunderstorm, and long-range transport over the Atlantic to Europe. The layers are shown in brownish colors and the mass median diameter of the rBC mass size distribution and the mixing state are given. (Aircraft emissions: Bond et al., 2013; Stettler et al., 2013; US BC emissions: EPA, 2012)

A schematic sketch of the fully developed thunderstorm from Figure 80 (middle) is also depicted in Figure 81, to give an overview of the vertical transport pathways of BB layers associated with large-scale thunderstorm. Figure 81 illustrates the complete transport pathway of BB layers from their source regions in New Mexico and Colorado to the North Atlantic and even further downwind to Europe with a sketch of the vertical transport associated with a large, overshooting thunderstorm (the cloud rim is marked by a thin grey line). Such a mature thunderstorm in the Great Plains can have a large vertical extent of several hundreds of kilometers and often appears not as isolated thunderstorms but form large-scale MCS or squall lines (as the thinner grey lines in the background suggest). The "classic" thunderstorm circulation with strong updrafts and downdrafts, a large anvil and an overshooting top ("bubble" on top) is represented by thick, blue arrows (as described in chapter 2.2.3). The vertical distribution of rBC mass concentrations during DC3 is shown at the left side of Figure 81. Wildfires burning west of the Great Plains emit a large mass of large, thickly coated BC particles, (bottom left corner of Figure 81). The emissions form extended BB layers, indicated by brownish areas. The rBC particles in the BB layers are drawn as black circles, their mixing state as light blue coatings. The BB layers initially have a sharp upper edge (as in Figure 80, left) and rise during westward advective transport in altitude. Large-scale thunderstorms can develop over the Great Plains in the BB layers (see Figure 80, middle). The storm's overshooting top forces stratospheric air to evade to the sides, where it is mixed downward at the anvil's rim, shown here as green arrows (Pan et al., 2014). Additional upward transport at the outer edge causes air to rise outside of the main updrafts (red arrows). Comparison of rBC and trace gas data indicates that this air mass also undergoes cloud processing during transport, but less rBC mass is washed out than in the anvil outflow. The air mass mixes with the stratospheric air at the anvil edge (Huntrieser et al., 2016a; 2016b). This mixed air, containing stratospheric air as well as BB from the lower troposphere (shown here as a multi-colored arrow in red, green and blue), moves downstream with the dissolving anvil. This air mass, which contains both O3-rich stratospheric air and the cloud-processed BB air, forms thin, outstretched layers in the UTLS region. During the transport, the fraction of coated rBC particles increases in the upper tropospheric BB layers. In the BB layers measured on the western side of the Atlantic, on May 27, June 17 and June 18, about half of the rBC particles had thick coatings while in a layer that was transported over the Atlantic, nearly all particles were thickly coated (Dahlkötter et al., 2014).

The high concentrations of O_3 in the upper tropospheric BB layers indicate O_3-rich transported downward from the stratosphere mixed into these layers. During DC3, O_3 concentrations in BB layers below 8 km were in a range between 40 and 90 ppb, with the higher values measured in the early afternoon. These values are typical for O_3 concentrations in BB layers of around 40-80 ppb in Canadian boreal biomass burning plumes (Parrington et al., 2013) due to photochemical O_3 production of 7-8 ppb/day (Pickering et al., 1996). In upper tropospheric BB layers, O_3 concentrations can exceed values

of 200 ppb, indicating mixing with stratospheric air. The tops of the larger storms overshoot the tropopause, pushing the stratospheric air above the storm to the sides. At the anvil edge, stratospheric air can mix with tropospheric air from the edge of the thunderstorm.

To classify the contributions of BB in comparison to other sources, numbers for the emission from industry and traffic in the US and from global aviation are added. Estimates of the total rBC content of the upper tropospheric BB layers make it clear that the vertical transport of BB aerosol is an important source for rBC in the UTLS region besides anthropogenic emissions from aircraft that are also emitted at this altitude. Since all these examples of upper tropospheric BB layers have undergone cloud processing, though to a weaker extent than thunderstorm outflow air masses, the resulting size distribution after washout seems to remain stable, and similar to the distribution found in the upper tropospheric background over the Great Plains. Due to the long lifetime in the upper troposphere, dispersing upper tropospheric BB layers could contribute to the background rBC in the UTLS region.

This vertical transport associated with thunderstorms, as shown in Figure 81, is not well captured by the HYSPLIT model. Subsequently, the injection of BB aerosol into the upper troposphere and lower stratosphere could be underestimated. However, an evaluation of AerCOM models in comparison with rBC measurements revealed a high overestimation of the model BC in the upper troposphere (Schwarz et al., 2013; 2017), probably due to the underestimation of washout during vertical transport. Washout is an important process influencing the mass size distribution and concentration in the upper tropospheric BB layers, as shown here. These upper tropospheric BB layers contain rBC in a nearly uniform mass size distribution with a MMD of 145 nm, which is a smaller diameter than the MMD of about 200 nm usually found in aged BB layers. Underestimating washout would lead to too high concentrations of too large rBC particles in the upper troposphere. To improve the modeled upper tropospheric rBC content, cloud-resolving models would be necessary to better capture the rapid mesoscale transport. These models must be run with appropriate resolution as too coarse grid points could result in the vertical transport not being captured appropriately (e.g. Raut et al., 2017). Most studies show that black carbon in Europe and the Arctic related to biomass burning in North America originates from sources in Canada and Alaska (Petzold et al., 2007; Dahlkötter et al., 2014; Ancellet et al., 2016). Here, I showed that wildfires farther south, in the central US, can also contribute to black carbon in the upper troposphere. The change in rBC size distribution during vertical transport, to smaller sizes, might also make it worthwhile to model radiative transfer in such upper tropospheric BB layers, as the change in size distribution could also effects the optical properties of the layer.

References

Akagi, S. K., Yokelson, R. J., Wiedinmyer, C., Alvarado, M. J., Reid, J. S., Karl, T., Crounse, J. D., and Wennberg, P. O.: Emission factors for open and domestic biomass burning for use in atmospheric models, Atmospheric Chemistry and Physics, 11, 4039-4072, 10.5194/acp-11-4039-2011, 2011.

Akagi, S. K., Craven, J. S., Taylor, J. W., McMeeking, G. R., Yokelson, R. J., Burling, I. R., Urbanski, S. P., Wold, C. E., Seinfeld, J. H., Coe, H., Alvarado, M. J., and Weise, D. R.: Evolution of trace gases and particles emitted by a chaparral fire in California, Atmospheric Chemistry and Physics, 12, 1397-1421, 10.5194/acp-12-1397-2012, 2012.

AMAP: AMAP Assessment 2015: Black carbon and ozone as Arctic climate forcers. Arctic Monitoring and Assessment Programme (AMAP), Arctic Monitoring and Assessment Programme (AMAP), Oslo, Norway (www.amap.no), Oslo, Norway, vii + 116 pp pp., 2015.

Ancellet, G., Pelon, J., Totems, J., Chazette, P., Bazureau, A., Sicard, M., Di Iorio, T., Dulac, F., and Mallet, M.: Long-range transport and mixing of aerosol sources during the 2013 North American biomass burning episode: analysis of multiple lidar observations in the western Mediterranean basin, Atmospheric Chemistry and Physics, 16, 4725-4742, 10.5194/acp-16-4725-2016, 2016.

Andreae, M. O., Artaxo, P., Fischer, H., Freitas, S. R., Gregoire, J. M., Hansel, A., Hoor, P., Kormann, R., Krejci, R., Lange, L., Lelieveld, J., Lindinger, W., Longo, K., Peters, W., de Reus, M., Scheeren, B., Dias, M., Strom, J., van Velthoven, P. F. J., and Williams, J.: Transport of biomass burning smoke to the upper troposphere by deep convection in the equatorial region, Geophysical Research Letters, 28, 951-954, 10.1029/2000gl012391, 2001.

Andreae, M. O., and Merlet, P.: Emission of trace gases and aerosols from biomass burning, Global Biogeochemical Cycles, 15, 955-966, 10.1029/2000gb001382, 2001.

Ansmann, A., Petzold, A., Kandler, K., Tegen, I., Wendisch, M., Muller, D., Weinzierl, B., Muller, T., and Heintzenberg, J.: Saharan Mineral Dust Experiments SAMUM-1 and SAMUM-2: what have we learned?, Tellus Series B-Chemical and Physical Meteorology, 63, 403-429, 10.1111/j.1600-0889.2011.00555.x, 2011.

Aquila, V., Hendricks, J., Lauer, A., Riemer, N., Vogel, H., Baumgardner, D., Minikin, A., Petzold, A., Schwarz, J. P., Spackman, J. R., Weinzierl, B., Righi, M., and Dall'Amico, M.: MADE-in: a new aerosol microphysics submodel for global simulation of insoluble particles and their mixing state, Geoscientific Model Development, 4, 325-355, 10.5194/gmd-4-325-2011, 2011.

Arakawa, A., and Schubert, W. H.: Interaction of a Cumulus Cloud Ensemble with the Large-Scale Environment, Part I, Journal of the Atmospheric Sciences, 31, 674-701, 10.1175/1520-0469(1974)031<0674:ioacce>2.0.co;2, 1974.

Arnott, W. P., Moosmuller, H., Rogers, C. F., Jin, T. F., and Bruch, R.: Photoacoustic spectrometer for measuring light absorption by aerosol: instrument description, Atmospheric Environment, 33, 2845-2852, 1999.

Barbero, R., Abatzoglou, J. T., Larkin, N. K., Kolden, C. A., and Stocks, B.: Climate change presents increased potential for very large fires in the contiguous United States, International Journal of Wildland Fire, 24, 892-899, 10.1071/wf15083, 2015.

Barth, M. C., Cantrell, C. A., Brune, W. H., Rutledge, S. A., Crawford, J. H., Huntrieser, H., Carey, L. D., MacGorman, D., Weisman, M., Pickering, K. E., Bruning, E., Anderson, B., Apel, E., Biggerstaff,

M., Campos, T., Campuzano-Jost, P., Cohen, R., Crounse, J., Day, D. A., Diskin, G., Flocke, F., Fried, A., Garland, C., Heikes, B., Honomichl, S., Hornbrook, R., Huey, L. G., Jimenez, J. L., Lang, T., Lichtenstern, M., Mikoviny, T., Nault, B., O'Sullivan, D., Pan, L. L., Peischl, J., Pollack, I., Richter, D., Riemer, D., Ryerson, T., Schlager, H., St Clair, J., Walega, J., Weibring, P., Weinheimer, A., Wennberg, P., Wisthaler, A., Wooldridge, P. J., and Ziegler, C.: The Deep Convective Clouds and Chemistry (DC3) Field Campaign, Bulletin of the American Meteorological Society, 96, 1281-1309, 10.1175/bams-d-13-00290.1, 2015.

Barth, M. C., Bela, M. M., Fried, A., Wennberg, P. O., Crounse, J. D., St. Clair, J. M., Blake, N. J., Blake, D. R., Homeyer, C. R., Brune, W. H., Zhang, L., Mao, J., Ren, X., Ryerson, T. B., Pollack, I. B., Peischl, J., Cohen, R. C., Nault, B. A., Huey, L. G., Liu, X., and Cantrell, C. A.: Convective Transport and Scavenging of Peroxides by Thunderstorms Observed over the Central U.S. during DC3, Journal of Geophysical Research: Atmospheres, 10.1002/2015JD024570, 2016.

Baumgardner, D., Brenguier, J. L., Bucholtz, A., Coe, H., DeMott, P., Garrett, T. J., Gayet, J. F., Hermann, M., Heymsfield, A., Korolev, A., Krämer, M., Petzold, A., Strapp, W., Pilewskie, P., Taylor, J., Twohy, C., Wendisch, M., Bachalo, W., and ChuangP.: Airborne instruments to measure atmospheric aerosol particles, clouds and radiation: A cook's tour of mature and emerging technology, Atmospheric Research, 102, 10-29, 10.1016/j.atmosres.2011.06.021, 2011.

Baumgardner, D., Popovicheva, O., Allan, J., Bernardoni, V., Cao, J., Cavalli, F., Cozic, J., Diapouli, E., Eleftheriadis, K., Genberg, P. J., Gonzalez, C., Gysel, M., John, A., Kirchstetter, T. W., Kuhlbusch, T. A. J., Laborde, M., Lack, D., Muller, T., Niessner, R., Petzold, A., Piazzalunga, A., Putaud, J. P., Schwarz, J., Sheridan, P., Subramanian, R., Swietlicki, E., Valli, G., Vecchi, R., and Viana, M.: Soot reference materials for instrument calibration and intercomparisons: a workshop summary with recommendations, Atmospheric Measurement Techniques, 5, 1869-1887, 10.5194/amt-5-1869-2012, 2012.

Bela, M. M., Barth, M. C., Toon, O. B., Fried, A., Homeyer, C. R., Morrison, H., Cummings, K. A., Li, Y., Pickering, K. E., Allen, D., Yang, Q., Wennberg, P. O., Crounse, J. D., St. Clair, J. M., Teng, A. P., O'Sullivan, D., Huey, L. G., Chen, D., Liu, X., Blake, D., Blake, N., Apel, E., Hornbrook, R. S., Flocke, F., Campos, T., and Diskin, G.: Wet Scavenging of Soluble Gases in DC3 Deep Convective Storms Using WRF-Chem Simulations and Aircraft Observations, Journal of Geophysical Research: Atmospheres, 10.1002/2015JD024623, 2016.

Binder, H., Boettcher, M., Joos, H., and Wernli, H.: The Role of Warm Conveyor Belts for the Intensification of Extratropical Cyclones in Northern Hemisphere Winter, Journal of the Atmospheric Sciences, 73, 3997-4020, 10.1175/jas-d-15-0302.1, 2016.

Birch, M. E., and Cary, R. A.: Elemental carbon-based method for monitoring occupational exposures to particulate diesel exhaust, Aerosol Science and Technology, 25, 221-241, 10.1080/02786829608965393, 1996.

Bisiaux, M. M., Edwards, R., McConnell, J. R., Curran, M. A. J., Van Ommen, T. D., Smith, A. M., Neumann, T. A., Pasteris, D. R., Penner, J. E., and Taylor, K.: Changes in black carbon deposition to Antarctica from two high-resolution ice core records, 1850-2000 AD, Atmospheric Chemistry and Physics, 12, 4107-4115, 10.5194/acp-12-4107-2012, 2012.

Bohren, C. F., and Huffman, D. R.: Absorption and Scattering of Light by Small Particles, John Wiley & Sons, Inc., 530 pp., 1998.

Bond, T. C., Anderson, T. L., and Campbell, D.: Calibration and intercomparison of filter-based measurements of visible light absorption by aerosols, Aerosol Science and Technology, 30, 582-600, 10.1080/027868299304435, 1999.

Bond, T. C., and Bergstrom, R. W.: Light absorption by carbonaceous particles: An investigative review, Aerosol Science and Technology, 40, 27-67, 10.1080/02786820500421521, 2006.

Bond, T. C., Doherty, S. J., Fahey, D. W., Forster, P. M., Berntsen, T., DeAngelo, B. J., Flanner, M. G., Ghan, S., Karcher, B., Koch, D., Kinne, S., Kondo, Y., Quinn, P. K., Sarofim, M. C., Schultz, M. G., Schulz, M., Venkataraman, C., Zhang, H., Zhang, S., Bellouin, N., Guttikunda, S. K., Hopke, P. K., Jacobson, M. Z., Kaiser, J. W., Klimont, Z., Lohmann, U., Schwarz, J. P., Shindell, D., Storelvmo, T., Warren, S. G., and Zender, C. S.: Bounding the role of black carbon in the climate system: A scientific assessment, Journal of Geophysical Research: Atmospheres, 118, 5380-5552, 10.1002/jgrd.50171, 2013.

Boucher, O., Randall, D., Artaxo, P., Bretherton, C., Feingold, G., Forster, P., Kerminen, V.-M., Kondo, Y., Liao, H., Lohmann, U., Rasch, P., Satheesh, S. K., Sherwood, S., Stevens, B., and Zhang, X. Y.: Clouds and Aerosols, in: Climate

Change 2013: The Physical Science Basis. Contribution of Working Group I to the Fifth Assessment Report of the

Intergovernmental Panel on Climate Change, edited by: Stocker, T. F., Qin, D., Plattner, G.-K., Tignor, M., Allen, S. K., J. Boschung, Nauels, A., Xia, Y., Bex, V., and Midgley, P. M., Cambridge University Pres, Cambridge, United Kingdom and

New York, NY, USA, 571-657, 2013.

Bougiatioti, A., Bezantakos, S., Stavroulas, I., Kalivitis, N., Kokkalis, P., Biskos, G., Mihalopoulos, N., Papayannis, A., and Nenes, A.: Biomass-burning impact on CCN number, hygroscopicity and cloud formation during summertime in the eastern Mediterranean, Atmospheric Chemistry and Physics, 16, 7389-7409, 10.5194/acp-16-7389-2016, 2016.

Bowman, D., Balch, J. K., Artaxo, P., Bond, W. J., Carlson, J. M., Cochrane, M. A., D'Antonio, C. M., DeFries, R. S., Doyle, J. C., Harrison, S. P., Johnston, F. H., Keeley, J. E., Krawchuk, M. A., Kull, C. A., Marston, J. B., Moritz, M. A., Prentice, I. C., Roos, C. I., Scott, A. C., Swetnam, T. W., van der Werf, G. R., and Pyne, S. J.: Fire in the Earth System, Science, 324, 481-484, 10.1126/science.1163886, 2009.

Bowman, D., Balch, J., Artaxo, P., Bond, W. J., Cochrane, M. A., D'Antonio, C. M., DeFries, R., Johnston, F. H., Keeley, J. E., Krawchuk, M. A., Kull, C. A., Mack, M., Moritz, M. A., Pyne, S., Roos, C. I., Scott, A. C., Sodhi, N. S., and Swetnam, T. W.: The human dimension of fire regimes on Earth, Journal of Biogeography, 38, 2223-2236, 10.1111/j.1365-2699.2011.02595.x, 2011.

Brown, W. K., and Wohletz, K. H.: Derivation of the Weibull distribution based on physical principles and its connection to the Rosin–Rammler and lognormal distributions, Journal of Applied Physics, 78, 2758-2763, 10.1063/1.360073, 1995.

Burton, S. P., Hair, J. W., Kahnert, M., Ferrare, R. A., Hostetler, C. A., Cook, A. L., Harper, D. B., Berkoff, T. A., Seaman, S. T., Collins, J. E., Fenn, M. A., and Rogers, R. R.: Observations of the spectral dependence of linear particle depolarization ratio of aerosols using NASA Langley airborne High Spectral Resolution Lidar, Atmospheric Chemistry and Physics, 15, 13453-13473, 10.5194/acp-15-13453-2015, 2015.

Burtscher, H., Baltensperger, U., Bukowiecki, N., Cohn, P., Huglin, C., Mohr, M., Matter, U., Nyeki, S., Schmatloch, V., Streit, N., and Weingartner, E.: Separation of volatile and non-volatile aerosol fractions by thermodesorption: instrumental development and applications, Journal of Aerosol Science, 32, 427-442, 10.1016/s0021-8502(00)00089-6, 2001.

Byers, H. R., and Braham, R. R.: Thunderstorm Structure and Circulation, Journal of Meteorology, 5, 71-86, 10.1175/1520-0469(1948)005<0071:tsac>2.0.co;2, 1948.

Carlson, T. N., Benjamin, S. G., Forbes, G. S., and Li, Y. F.: Elevated Mixed Layers in the Regional Severe Storm Environment: Conceptual Model and Case Studies, Monthly Weather Review, 111, 1453-1473, 10.1175/1520-0493(1983)111<1453:emlitr>2.0.co;2, 1983.

Clewell, A. F.: Forest Development 44 Years after Fire Exclusion in Formerly Annually Burned Oldfield Pine Woodland, Florida, Castanea, 79, 147-167, 10.2179/14-010, 2014.

Coen, J. L., and Schroeder, W.: The High Park fire: Coupled weather-wildland fire model simulation of a windstorm-driven wildfire in Colorado's Front Range, Journal of Geophysical Research: Atmospheres, 120, 2014JD021993, 10.1002/2014JD021993, 2015.

Cohen, J. D.: Preventing disaster - Home ignitability in the wildland-urban interface, Journal of Forestry, 98, 15-21, 2000.

Corr, C. A., Ziemba, L. D., Scheuer, E., Anderson, B. E., Beyersdorf, A. J., Chen, G., Crosbie, E., Moore, R. H., Shook, M., Thornhill, K. L., Winstead, E., Lawson, R. P., Barth, M. C., Schroeder, J. R., Blake, D. R., and Dibb, J. E.: Observational evidence for the convective transport of dust over the Central United States, Journal of Geophysical Research: Atmospheres, 121, 1306-1319, 10.1002/2015jd023789, 2016.

Costabile, F., Angelini, F., Barnaba, F., and Gobbi, G. P.: Partitioning of Black Carbon between ultrafine and fine particle modes in an urban airport vs. urban background environment, Atmospheric Environment, 102, 136-144, 10.1016/j.atmosenv.2014.11.064, 2015.

Cross, E. S., Onasch, T. B., Ahern, A., Wrobel, W., Slowik, J. G., Olfert, J., Lack, D. A., Massoli, P., Cappa, C. D., Schwarz, J. P., Spackman, J. R., Fahey, D. W., Sedlacek, A., Trimborn, A., Jayne, J. T., Freedman, A., Williams, L. R., Ng, N. L., Mazzoleni, C., Dubey, M., Brem, B., Kok, G., Subramanian, R., Freitag, S., Clarke, A., Thornhill, D., Marr, L. C., Kolb, C. E., Worsnop, D. R., and Davidovits, P.: Soot Particle Studies Instrument Inter-Comparison Project Overview, Aerosol Science and Technology, 44, 592-611, 10.1080/02786826.2010.482113, 2010.

Dahlkötter, F., Gysel, M., Sauer, D., Minikin, A., Baumann, R., Seifert, P., Ansmann, A., Fromm, M., Voigt, C., and Weinzierl, B.: The Pagami Creek smoke plume after long-range transport to the upper troposphere over Europe - aerosol properties and black carbon mixing state, Atmospheric Chemistry and Physics, 14, 6111-6137, 10.5194/acp-14-6111-2014, 2014.

Damoah, R., Spichtinger, N., Forster, C., James, P., Mattis, I., Wandinger, U., Beirle, S., Wagner, T., and Stohl, A.: Around the world in 17 days - hemispheric-scale transport of forest fire smoke from Russia in May 2003, Atmospheric Chemistry and Physics, 4, 1311-1321, 2004.

DeMott, P. J., Chen, Y., Kreidenweis, S. M., Rogers, D. C., and Sherman, D. E.: Ice formation by black carbon particles, Geophysical Research Letters, 26, 2429-2432, 10.1029/1999gl900580, 1999.

Dentener, F., Kinne, S., Bond, T., Boucher, O., Cofala, J., Generoso, S., Ginoux, P., Gong, S., Hoelzemann, J. J., Ito, A., Marelli, L., Penner, J. E., Putaud, J. P., Textor, C., Schulz, M., van der Werf, G. R., and Wilson, J.: Emissions of primary aerosol and precursor gases in the years 2000 and 1750 prescribed data-sets for AeroCom, Atmospheric Chemistry and Physics, 6, 4321-4344, 2006.

Doswell, C. A.: Severe Convective Storms—An Overview, in: Severe Convective Storms, edited by: Doswell, C. A., American Meteorological Society, Boston, MA, 1-26, 2001.

Draxler, R. R., and Hess, G.: Description of the HYSPLIT4 modeling system, 1997.

Droplet Measurement Technologies, I.: Single Particle Soot Photomenter (SP2) Operator Manual, DOC-0171 Revision E ed., edited by: Droplet Measurement Technologies, I., Boulder, Colorado, USA, 2010.

Eckbreth, A. C.: Effects of laser-modulated particulate incandescence on Raman scattering diagnostics, Journal of Applied Physics, 48, 4473-4479, 10.1063/1.323458 1977.

Eckhardt, S., Stohl, A., Wernli, H., James, P., Forster, C., and Spichtinger, N.: A 15-year climatology of warm conveyor belts, Journal of Climate, 17, 218-237, 10.1175/1520-0442(2004)017<0218:aycowc>2.0.co;2, 2004.

Emanuel, K. A.: Atmospheric Convection, Oxford University Press New York, 1994.

EPA: Report to Congress on Black Carbon, Department of the Interior, Environment, and Related Agencies Appropriations Act, 2010, United States Environmental Protection Agency, 351, 2012.

Fan, J. W., Leung, L. R., Rosenfeld, D., Chen, Q., Li, Z. Q., Zhang, J. Q., and Yan, H. R.: Microphysical effects determine macrophysical response for aerosol impacts on deep convective clouds, Proceedings of the National Academy of Sciences of the United States of America, 110, E4581-E4590, 10.1073/pnas.1316830110, 2013.

Fiebig, M.: Das troposphärische Aerosol in mittleren Breiten - Mikrophysik, Optik und Klimaantrieb am Beispiel der Feldstudie LACE 98, Fakultät für Physik, Ludwig-Maximilians-Universität München, Deutsches Zentrum für Luft- und Raumfahrt e.V.; Bibliotheks- und Informationswesen; Köln, 259 pp., 2001.

Frey, W., Schofield, R., Hoor, P., Kunkel, D., Ravegnani, F., Ulanovsky, A., Viciani, S., D'Amato, F., and Lane, T. P.: The impact of overshooting deep convection on local transport and mixing in the tropical upper troposphere/lower stratosphere (UTLS), Atmospheric Chemistry and Physics, 15, 6467-6486, 10.5194/acp-15-6467-2015, 2015.

Fromm, M., Bevilacqua, R., Servranckx, R., Rosen, J., Thayer, J. P., Herman, J., and Larko, D.: Pyro-cumulonimbus injection of smoke to the stratosphere: Observations and impact of a super blowup in northwestern Canada on 3–4 August 1998, Journal of Geophysical Research: Atmospheres, 110, n/a-n/a, 10.1029/2004JD005350, 2005.

Fromm, M., Torres, O., Diner, D., Lindsey, D., Hull, B. V., Servranckx, R., Shettle, E. P., and Li, Z.: Stratospheric impact of the Chisholm pyrocumulonimbus eruption: 1. Earth-viewing satellite perspective, Journal of Geophysical Research: Atmospheres, 113, 16, 10.1029/2007jd009153, 2008.

Fromm, M., Lindsey, D. T., Servranckx, R., Yue, G., Trickl, T., Sica, R., Doucet, P., and Godin-Beekmann, S. E.: The Untold Story of Pyrocumulonimbus, Bulletin of the American Meteorological Society, 91, 1193-1209, 10.1175/2010bams3004.1, 2010.

Gao, R. S., Schwarz, J. P., Kelly, K. K., Fahey, D. W., Watts, L. A., Thompson, T. L., Spackman, J. R., Slowik, J. G., Cross, E. S., Han, J. H., Davidovits, P., Onasch, T. B., and Worsnop, D. R.: A novel method for estimating light-scattering properties of soot aerosols using a modified single-particle soot photometer, Aerosol Science and Technology, 41, 125-135, Doi 10.1080/02786820601118398, 2007.

Goncalves, W. A., Machado, L. A. T., and Kirstetter, P. E.: Influence of biomass aerosol on precipitation over the Central Amazon: an observational study, Atmospheric Chemistry and Physics, 15, 6789-6800, 10.5194/acp-15-6789-2015, 2015.

Gonzi, S., Feng, L., and Palmer, P. I.: Seasonal cycle of emissions of CO inferred from MOPITT profiles of CO: Sensitivity to pyroconvection and profile retrieval assumptions, Geophysical Research Letters, 38, 5, 10.1029/2011gl046789, 2011.

Groß, S., Esselborn, M., Weinzierl, B., Wirth, M., Fix, A., and Petzold, A.: Aerosol classification by airborne high spectral resolution lidar observations, Atmospheric Chemistry and Physics, 13, 2487-2505, 10.5194/acp-13-2487-2013, 2013.

Guo, J. P., Deng, M. J., Lee, S. S., Wang, F., Li, Z. Q., Zhai, P. M., Liu, H., Lv, W. T., Yao, W., and Li, X. W.: Delaying precipitation and lightning by air pollution over the Pearl River Delta. Part I: Observational analyses, Journal of Geophysical Research: Atmospheres, 121, 6472-6488, 10.1002/2015jd023257, 2016.

Gysel, M., Laborde, M., Olfert, J. S., Subramanian, R., and Grohn, A. J.: Effective density of Aquadag and fullerene soot black carbon reference materials used for SP2 calibration, Atmospheric Measurement Techniques, 4, 2851-2858, DOI 10.5194/amt-4-2851-2011, 2011.

Gysel, M.: in, SP2 scattering detector angular weighting function ed., 2012.

Gysel, M., Laborde, M., Corbin, J. C., Mensah, A. A., Keller, A., Kim, J., Petzold, A., and Sierau, B.: Technical Note: The single particle soot photometer fails to detect PALAS soot nanoparticles, Atmospheric Measurement Techniques, 5, 3099-3107, 10.5194/amt-5-3099-2012, 2012.

Hair, J. W., Hostetler, C. A., Cook, A. L., Harper, D. B., Ferrare, R. A., Mack, T. L., Welch, W., Izquierdo, L. R., and Hovis, F. E.: Airborne High Spectral Resolution Lidar for profiling aerosol optical properties, Applied Optics, 47, 6734-6752, 10.1364/ao.47.006734, 2008.

Hansen, A. D. A., Rosen, H., and Novakov, T.: The aethalometer — An instrument for the real-time measurement of optical absorption by aerosol particles, Science of The Total Environment, 36, 191-196, 10.1016/0048-9697(84)90265-1, 1984.

Hansen, J., Sato, M., and Ruedy, R.: Radiative forcing and climate response, Journal of Geophysical Research: Atmospheres, 102, 6831-6864, 10.1029/96jd03436, 1997.

Hansen, J., and Nazarenko, L.: Soot climate forcing via snow and ice albedos, Proceedings of the National Academy of Sciences of the United States of America, 101, 423-428, 10.1073/pnas.2237157100, 2004.

Harrold, T. W.: Mechanisms influencing the distribution of precipitation within baroclinic disturbances, Quarterly Journal of the Royal Meteorological Society, 99, 232-251, 10.1002/qj.49709942003, 1973.

Hatch, T., and Choate, S. P.: Statistical description of the size properties of non uniform particulate substances, Journal of the Franklin Institute, 207, 369-387, 10.1016/S0016-0032(29)91451-4, 1929.

Heidenreich, R. D., Hess, W. M., and Ban, L. L.: A Test Object and Criteria for High Resolution Electron Microscopy, Journal of Applied Crystallography, 1, 1-19, 1968.

Heimerl, K.: Characterisation of the DLR Single Particle Soot Photometer and its Sensitivity to Different Absorbing Aerosol Types, Diplom, Fakultät für Physik, Ludwig-Maximilians-Universität München, 87 pp., 2011.

Heimerl, K., Weinzierl, B., Minikin, A., Sauer, D., Fütterer, D., Lichtenstern, M., Schlager, H., Schwarz, J. P., Markovic, M. Z., Perring, A. E., Fahey, D. W., and Huntrieser, H.: Biomass burning layers measured with an airborne Single Particle Soot Photometer (SP2) during the Deep Convective Clouds

and Chemistry (DC3) experiment, Abstract A41B-0043 presented at 2013 Fall Meeting, AGU, San Francisco, CA, 2013.

Hill, A. A., and Dobbie, S.: The impact of aerosols on non-precipitating marine stratocumulus. II: The semi-direct effect, Quarterly Journal of the Royal Meteorological Society, 134, 1155-1165, 10.1002/qj.277, 2008.

Hill, A. S. G.: Measurement of the optical densities of smoke stains of filter papers, Transactions of the Faraday Society, 32, 1125-1131, 1936.

Hinds, W. C.: Aerosol Technology. Properties, Behavior, and Measurement of Airborne Particles, 1999.

Hinds, W. C.: Physical and Chemical Processes in Aerosol Systems, in: Aerosol Measurement, John Wiley & Sons, Inc., 31-40, 2011.

Hoerling, M., Eischeid, J., Kumar, A., Leung, R., Mariotti, A., Mo, K., Schubert, S., and Seager, R.: Causes and Predictability of the 2012 Great Plains Drought, Bulletin of the American Meteorological Society, 95, 269-282, 10.1175/bams-d-13-00055.1, 2014.

Hofmann, W.: Modelling inhaled particle deposition in the human lung—A review, Journal of Aerosol Science, 42, 693-724, 10.1016/j.jaerosci.2011.05.007, 2011.

Holton, J. R., and Hakim, G. J.: An Introduction to Dynamic Meteorology, Fifth Edition ed., Elsevier Inc., Oxford, UK, 532 pp., 2013.

Homeyer, C. R., Pan, L. L., and Barth, M. C.: Transport from convective overshooting of the extratropical tropopause and the role of large-scale lower stratosphere stability, Journal of Geophysical Research: Atmospheres, 119, 2220-2240, 10.1002/2013jd020931, 2014.

Hoose, C., and Möhler, O.: Heterogeneous ice nucleation on atmospheric aerosols: a review of results from laboratory experiments, Atmospheric Chemistry and Physics, 12, 9817-9854, 10.5194/acp-12-9817-2012, 2012.

Houze, R. A.: Cloud Dynamics, 2nd Edition, Cloud Dynamics, 2nd Edition, Elsevier Academic Press Inc, San Diego, 1-432 pp., 2014.

Huang, X. F., Gao, R. S., Schwarz, J. P., He, L. Y., Fahey, D. W., Watts, L. A., McComiskey, A., Cooper, O. R., Sun, T. L., Zeng, L. W., Hu, M., and Zhang, Y. H.: Black carbon measurements in the Pearl River Delta region of China, Journal of Geophysical Research: Atmospheres, 116, Doi 10.1029/2010jd014933, 2011.

Hulst, H. C. v. d.: Light scattering by small particles, Dover Publications, New York, 470 p. pp., 1981.

Huntrieser, H., Schlager, H., Lichtenstern, M., Stock, P., Hamburger, T., Holler, H., Schmidt, K., Betz, H. D., Ulanovsky, A., and Ravegnani, F.: Mesoscale convective systems observed during AMMA and their impact on the NOx and O-3 budget over West Africa, Atmospheric Chemistry and Physics, 11, 2503-2536, 10.5194/acp-11-2503-2011, 2011.

Huntrieser, H., Lichtenstern, M., Scheibe, M., Aufmhoff, H., Schlager, H., Pucik, T., Minikin, A., Weinzierl, B., Heimerl, K., Fütterer, D., Rappenglück, B., Ackermann, L., Pickering, K. E., Cummings, K. A., Biggerstaff, M. I., Betten, D. P., Honomichl, S., and Barth, M. C.: On the origin of pronounced O3 gradients in the thunderstorm outflow region during DC3, Journal of Geophysical Research: Atmospheres, n/a-n/a, 10.1002/2015JD024279, 2016a.

Huntrieser, H., Lichtenstern, M., Scheibe, M., Aufmhoff, H., Schlager, H., Pucik, T., Minikin, A., Weinzierl, B., Heimerl, K., Pollack, I. B., Peischl, J., Ryerson, T. B., Weinheimer, A. J., Honomichl, S., Ridley, B. A., Biggerstaff, M. I., Betten, D. P., Hair, J. W., Butler, C. F., Schwartz, M. J., and Barth, M. C.: Injection of lightning-produced NOx, water vapor, wildfire emissions, and stratospheric air to the UT/LS as observed from DC3 measurements, Journal of Geophysical Research: Atmospheres, 121, 6638-6668, 10.1002/2015jd024273, 2016b.

IPCC: Climate Change 2013: The Physical Science Basis. Contribution of Working Group I to the Fifth Assessment Report of the Intergovernmental Panel on Climate Change, edited by: Stocker, T. F., D. Qin, G.-K. Plattner, M. Tignor, S.K. Allen, J. Boschung, A. Nauels, Y. Xia, V. Bex and P.M. Midgley, Cambridge University Press, Cambridge, United Kingdom and New York, NY, USA, 1535 pp., 2013.

Jaenicke, R.: Atmospheric Aerosols and Global Climate, Journal of Aerosol Science, 11, 577-588, 10.1016/0021-8502(80)90131-7, 1980.

Jaffe, D. A., and Wigder, N. L.: Ozone production from wildfires: A critical review, Atmospheric Environment, 51, 1-10, 10.1016/j.atmosenv.2011.11.063, 2012.

Janssen, N. A. H., Hoek, G., Simic-Lawson, M., Fischer, P., van Bree, L., ten Brink, H., Keuken, M., Atkinson, R. W., Anderson, H. R., Brunekreef, B., and Cassee, F. R.: Black Carbon as an Additional Indicator of the Adverse Health Effects of Airborne Particles Compared with PM10 and PM2.5, Environmental Health Perspectives, 119, 1691-1699, 10.1289/ehp.1003369, 2011.

John, W.: Size Distribution Characteristics of Aerosols, in: Aerosol Measurement, John Wiley & Sons, Inc., 41-54, 2011.

Jolly, W. M., Cochrane, M. A., Freeborn, P. H., Holden, Z. A., Brown, T. J., Williamson, G. J., and Bowman, D.: Climate-induced variations in global wildfire danger from 1979 to 2013, Nature Communications, 6, 11, 10.1038/ncomms8537, 2015.

Jost, H. J., Drdla, K., Stohl, A., Pfister, L., Loewenstein, M., Lopez, J. P., Hudson, P. K., Murphy, D. M., Cziczo, D. J., Fromm, M., Bui, T. P., Dean-Day, J., Gerbig, C., Mahoney, M. J., Richard, E. C., Spichtinger, N., Pittman, J. V., Weinstock, E. M., Wilson, J. C., and Xueref, I.: In-situ observations of mid-latitude forest fire plumes deep in the stratosphere, Geophysical Research Letters, 31, 5, 10.1029/2003gl019253, 2004.

Kaiser, J. C., Hendricks, J., Righi, M., Riemer, N., Zaveri, R. A., Metzger, S., and Aquila, V.: The MESSy aerosol submodel MADE3 (v2.0b): description and a box model test, Geoscientific Model Development, 7, 1137-1157, 10.5194/gmd-7-1137-2014, 2014.

Kandler, K., Schutz, L., Deutscher, C., Ebert, M., Hofmann, H., Jäckel, S., Jaenicke, R., Knippertz, P., Lieke, K., Massling, A., Petzold, A., Schladitz, A., Weinzierl, B., Wiedensohler, A., Zorn, S., and Weinbruch, S.: Size distribution, mass concentration, chemical and mineralogical composition and derived optical parameters of the boundary layer aerosol at Tinfou, Morocco, during SAMUM 2006, Tellus Series B-Chemical and Physical Meteorology, 61, 32-50, 10.1111/j.1600-0889.2008.00385.x, 2009.

Kaspari, S. D., Schwikowski, M., Gysel, M., Flanner, M. G., Kang, S., Hou, S., and Mayewski, P. A.: Recent increase in black carbon concentrations from a Mt. Everest ice core spanning 1860-2000 AD, Geophysical Research Letters, 38, Doi 10.1029/2010gl046096, 2011.

Kaspari, S. D., Skiles, S. M., Delaney, I., Dixon, D., and Painter, T. H.: Accelerated glacier melt on Snow Dome, Mount Olympus, Washington, USA, due to deposition of black carbon and mineral dust from

wildfire, Journal of Geophysical Research: Atmospheres, 120, 2793-2807, 10.1002/2014jd022676, 2015.

Kaufman, Y. J., Fraser, R. S., and Mahoney, R. L.: Fossil Fuel and Biomass Burning Effect on Climate— Heating or Cooling?, Journal of Climate, 4, 578-588, 10.1175/1520-0442(1991)004<0578:FFABBE>2.0.CO;2, 1991.

Koch, D., Schulz, M., Kinne, S., McNaughton, C., Spackman, J. R., Balkanski, Y., Bauer, S., Berntsen, T., Bond, T. C., Boucher, O., Chin, M., Clarke, A., De Luca, N., Dentener, F., Diehl, T., Dubovik, O., Easter, R., Fahey, D. W., Feichter, J., Fillmore, D., Freitag, S., Ghan, S., Ginoux, P., Gong, S., Horowitz, L., Iversen, T., Kirkev, aring, g, A., Klimont, Z., Kondo, Y., Krol, M., Liu, X., Miller, R., Montanaro, V., Moteki, N., Myhre, G., Penner, J. E., Perlwitz, J., Pitari, G., Reddy, S., Sahu, L., Sakamoto, H., Schuster, G., Schwarz, J. P., Seland, Ø., Stier, P., Takegawa, N., Takemura, T., Textor, C., van Aardenne, J. A., and Zhao, Y.: Evaluation of black carbon estimations in global aerosol models, Atmospheric Chemistry and Physics, 9, 9001-9026, 10.5194/acp-9-9001-2009, 2009.

Koch, D., and Del Genio, A. D.: Black carbon semi-direct effects on cloud cover: review and synthesis, Atmospheric Chemistry and Physics, 10, 7685-7696, 10.5194/acp-10-7685-2010, 2010.

Koike, M., Moteki, N., Khatri, P., Takamura, T., Takegawa, N., Kondo, Y., Hashioka, H., Matsui, H., Shimizu, A., and Sugimoto, N.: Case study of absorption aerosol optical depth closure of black carbon over the East China Sea, Journal of Geophysical Research: Atmospheres, 119, 122-136, 10.1002/2013jd020163, 2014.

Kondo, Y., Matsui, H., Moteki, N., Sahu, L., Takegawa, N., Kajino, M., Zhao, Y., Cubison, M. J., Jimenez, J. L., Vay, S., Diskin, G. S., Anderson, B., Wisthaler, A., Mikoviny, T., Fuelberg, H. E., Blake, D. R., Huey, G., Weinheimer, A. J., Knapp, D. J., and Brune, W. H.: Emissions of black carbon, organic, and inorganic aerosols from biomass burning in North America and Asia in 2008, Journal of Geophysical Research: Atmospheres, 116, Doi 10.1029/2010jd015152, 2011a.

Kondo, Y., Sahu, L., Moteki, N., Khan, F., Takegawa, N., Liu, X., Kolke, M., and Miyakawa, T.: Consistency and Traceability of Black Carbon Measurements Made by Laser-Induced Incandescence, Thermal-Optical Transmittance, and Filter-Based Photo-Absorption Techniques, Aerosol Science and Technology, 45, 295-312, 10.1080/02786826.2010.533215, 2011b.

Kreidenweis, S. M., Koehler, K., DeMott, P. J., Prenni, A. J., Carrico, C., and Ervens, B.: Water activity and activation diameters from hygroscopicity data - Part I: Theory and application to inorganic salts, Atmospheric Chemistry and Physics, 5, 1357-1370, 2005.

Kulkarni, P., Baron, P. A., and Willeke, K.: Aerosol Measurement: Principles, Techniques, and Applications, 3rd ed., John Wiley & Sons, Inc., Hoboken, New Jersey, 883 pp., 2011.

Kumar, A., Wu, S., Weise, M. F., Honrath, R., Owen, R. C., Helmig, D., Kramer, L., Martin, M. V., and Li, Q.: Free-troposphere ozone and carbon monoxide over the North Atlantic for 2001-2011, Atmospheric Chemistry and Physics, 13, 12537-12547, 10.5194/acp-13-12537-2013, 2013.

Laborde, M., Mertes, P., Zieger, P., Dommen, J., Baltensperger, U., and Gysel, M.: Sensitivity of the Single Particle Soot Photometer to different black carbon types, Atmospheric Measurement Techniques, 5, 1031-1043, 10.5194/amt-5-1031-2012, 2012a.

Laborde, M., Schnaiter, M., Linke, C., Saathoff, H., Naumann, K. H., Mohler, O., Berlenz, S., Wagner, U., Taylor, J. W., Liu, D., Flynn, M., Allan, J. D., Coe, H., Heimerl, K., Dahlkotter, F., Weinzierl, B., Wollny, A. G., Zanatta, M., Cozic, J., Laj, P., Hitzenberger, R., Schwarz, J. P., and Gysel, M.: Single

Particle Soot Photometer intercomparison at the AIDA chamber, Atmospheric Measurement Techniques, 5, 3077-3097, 10.5194/amt-5-3077-2012, 2012b.

Lack, D. A., Cappa, C. D., Cross, E. S., Massoli, P., Ahern, A. T., Davidovits, P., and Onasch, T. B.: Absorption Enhancement of Coated Absorbing Aerosols: Validation of the Photo-Acoustic Technique for Measuring the Enhancement, Aerosol Science and Technology, 43, 1006-1012, 10.1080/02786820903117932, 2009.

Lang, T. J., Rutledge, S. A., Dolan, B., Krehbiel, P., Rison, W., and Lindsey, D. T.: Lightning in Wildfire Smoke Plumes Observed in Colorado during Summer 2012, Monthly Weather Review, 142, 489-507, 10.1175/mwr-d-13-00184.1, 2014.

Lee, A. K. Y., Willis, M. D., Healy, R. M., Wang, J. M., Jeong, C. H., Wenger, J. C., Evans, G. J., and Abbatt, J. P. D.: Single-particle characterization of biomass burning organic aerosol (BBOA): evidence for non-uniform mixing of high molecular weight organics and potassium, Atmospheric Chemistry and Physics, 16, 5561-5572, 10.5194/acp-16-5561-2016, 2016a.

Lee, S., Ghim, Y. S., Kim, S. W., and Yoon, S. C.: Effect of biomass burning and regional background aerosols on CCN activity derived from airborne in-situ measurements, Atmospheric Environment, 44, 5227-5236, 10.1016/j.atmosenv.2010.08.044, 2010.

Lee, S. S., Guo, J. P., and Li, Z. Q.: Delaying precipitation by air pollution over the Pearl River Delta: 2. Model simulations, Journal of Geophysical Research: Atmospheres, 121, 11739-11760, 10.1002/2015jd024362, 2016b.

Liu, C. T., and Zipser, E. J.: Global distribution of convection penetrating the tropical tropopause, Journal of Geophysical Research: Atmospheres, 110, 12, 10.1029/2005jd006063, 2005.

Liu, C. T., Zipser, E. J., and Nesbitt, S. W.: Global distribution of tropical deep convection: Different perspectives from TRMM infrared and radar data, Journal of Climate, 20, 489-503, 10.1175/jcli4023.1, 2007.

Liu, D., Flynn, M., Gysel, M., Targino, A., Crawford, I., Bower, K., Choularton, T., Juranyi, Z., Steinbacher, M., Huglin, C., Curtius, J., Kampus, M., Petzold, A., Weingartner, E., Baltensperger, U., and Coe, H.: Single particle characterization of black carbon aerosols at a tropospheric alpine site in Switzerland, Atmospheric Chemistry and Physics, 10, 7389-7407, DOI 10.5194/acp-10-7389-2010, 2010.

Liu, N. N., and Liu, C. T.: Global distribution of deep convection reaching tropopause in 1year GPM observations, Journal of Geophysical Research: Atmospheres, 121, 3824-3842, 10.1002/2015jd024430, 2016.

Maddox, R. A.: Mesoscale Convective Complexes, Bulletin of the American Meteorological Society, 61, 1374-1387, 10.1175/1520-0477(1980)061<1374:mcc>2.0.co;2, 1980.

Mahowald, N. M., Engelstaedter, S., Luo, C., Sealy, A., Artaxo, P., Benitez-Nelson, C., Bonnet, S., Chen, Y., Chuang, P. Y., Cohen, D. D., Dulac, F., Herut, B., Johansen, A. M., Kubilay, N., Losno, R., Maenhaut, W., Paytan, A., Prospero, J. A., Shank, L. M., and Siefert, R. L.: Atmospheric Iron Deposition: Global Distribution, Variability, and Human Perturbations, Annual Review of Marine Science, 1, 245-278, 10.1146/annurev.marine.010908.163727, 2009.

Markovic, M. Z.: in, Size-dependent density of the NOAA-sample of fullerene soot ed., 2012.

Matsui, H., Kondo, Y., Moteki, N., Takegawa, N., Sahu, L. K., Zhao, Y., Fuelberg, H. E., Sessions, W. R., Diskin, G., Blake, D. R., Wisthaler, A., and Koike, M.: Seasonal variation of the transport of black carbon aerosol from the Asian continent to the Arctic during the ARCTAS aircraft campaign, Journal of Geophysical Research: Atmospheres, 116, 19, 10.1029/2010jd015067, 2011.

Mattis, I., Muller, D., Ansmann, A., Wandinger, U., Preissler, J., Seifert, P., and Tesche, M.: Ten years of multiwavelength Raman lidar observations of free-tropospheric aerosol layers over central Europe: Geometrical properties and annual cycle, Journal of Geophysical Research: Atmospheres, 113, 19, 10.1029/2007jd009636, 2008.

McMeeking, G. R., Hamburger, T., Liu, D., Flynn, M., Morgan, W. T., Northway, M., Highwood, E. J., Krejci, R., Allan, J. D., Minikin, A., and Coe, H.: Black carbon measurements in the boundary layer over western and northern Europe, Atmospheric Chemistry and Physics, 10, 9393-9414, DOI 10.5194/acp-10-9393-2010, 2010.

McMeeking, G. R., Good, N., Petters, M. D., McFiggans, G., and Coe, H.: Influences on the fraction of hydrophobic and hydrophilic black carbon in the atmosphere, Atmospheric Chemistry and Physics, 11, 5099-5112, DOI 10.5194/acp-11-5099-2011, 2011.

McMeeking, G. R., Fortner, E., Onasch, T. B., Taylor, J. W., Flynn, M., Coe, H., and Kreidenweis, S. M.: Impacts of nonrefractory material on light absorption by aerosols emitted from biomass burning, Journal of Geophysical Research: Atmospheres, 119, 12272-12286, 10.1002/2014jd021750, 2014.

Melton, L. A.: Soot diagnostics based on laser heating, Applied Optics, 23, 2201-2208, 10.1364/AO.23.002201, 1984.

Mie, G.: Beiträge zur Optik trüber Medien, speziell kolloidaler Metallösungen, Annalen der Physik, 330, 377-445, 10.1002/andp.19083300302, 1908.

Moosmüller, H., Chakrabarty, R. K., and Arnott, W. P.: Aerosol light absorption and its measurement: A review, Journal of Quantitative Spectroscopy & Radiative Transfer, 110, 844-878, 10.1016/j.jqsrt.2009.02.035, 2009.

Moteki, N., and Kondo, Y.: Effects of mixing state on black carbon measurements by laser-induced incandescence, Aerosol Science and Technology, 41, 398-417, Doi 10.1080/02786820701199728, 2007.

Moteki, N., Kondo, Y., Miyazaki, Y., Takegawa, N., Komazaki, Y., Kurata, G., Shirai, T., Blake, D. R., Miyakawa, T., and Koike, M.: Evolution of mixing state of black carbon particles: Aircraft measurements over the western Pacific in March 2004, Geophysical Research Letters, 34, Doi 10.1029/2006gl028943, 2007.

Moteki, N., Kondo, Y., Takegawa, N., and Nakamura, S.: Directional dependence of thermal emission from nonspherical carbon particles, Journal of Aerosol Science, 40, 790-801, DOI 10.1016/j.jaerosci.2009.05.003, 2009.

Moteki, N., and Kondo, Y.: Dependence of Laser-Induced Incandescence on Physical Properties of Black Carbon Aerosols: Measurements and Theoretical Interpretation, Aerosol Science and Technology, 44, 663-675, Doi 10.1080/02786826.2010.484450, 2010.

Moteki, N., Kondo, Y., Oshima, N., Takegawa, N., Koike, M., Kita, K., Matsui, H., and Kajino, M.: Size dependence of wet removal of black carbon aerosols during transport from the boundary layer to the free troposphere, Geophysical Research Letters, 39, 10.1029/2012gl052034, 2012.

Moteki, N., Adachi, K., Ohata, S., Yoshida, A., Harigaya, T., Koike, M., and Kondo, Y.: Anthropogenic iron oxide aerosols enhance atmospheric heating, Nature Communications, 8, 11, 10.1038/ncomms15329, 2017.

Murphy, D. M., Cziczo, D. J., Hudson, P. K., Thomson, D. S., Wilson, J. C., Kojima, T., and Buseck, P. R.: Particle Generation and Resuspension in Aircraft Inlets when Flying in Clouds, Aerosol Science and Technology, 38, 401-409, 10.1080/02786820490443094, 2004.

Naeher, L. P., Brauer, M., Lipsett, M., Zelikoff, J. T., Simpson, C. D., Koenig, J. Q., and Smith, K. R.: Woodsmoke health effects: A review, Inhalation Toxicology, 19, 67-106, 10.1080/08958370600985875, 2007.

Nisantzi, A., Mamouri, R. E., Ansmann, A., and Hadjimitsis, D.: Injection of mineral dust into the free troposphere during fire events observed with polarization lidar at Limassol, Cyprus, Atmospheric Chemistry and Physics, 14, 12155-12165, 10.5194/acp-14-12155-2014, 2014.

Ogren, J. A., and Charlson, R. J.: Elemental carbon in the atmosphere: cycle and lifetime, Tellus B, 35B, 241-254, 10.1111/j.1600-0889.1983.tb00027.x, 1983.

Ogura, Y., and Phillips, N. A.: Scale Analysis of Deep and Shallow Convection in the Atmosphere, Journal of the Atmospheric Sciences, 19, 173-179, 10.1175/1520-0469(1962)019<0173:SAODAS>2.0.CO;2, 1962.

Ohata, S., Schwarz, J. P., Moteki, N., Koike, M., Takami, A., and Kondo, Y.: Hygroscopicity of materials internally mixed with black carbon measured in Tokyo, Journal of Geophysical Research: Atmospheres, 121, 362-381, 10.1002/2015jd024153, 2016.

Oshima, N., Koike, M., Zhang, Y., and Kondo, Y.: Aging of black carbon in outflow from anthropogenic sources using a mixing state resolved model: 2. Aerosol optical properties and cloud condensation nuclei activities, Journal of Geophysical Research: Atmospheres, 114, 17, 10.1029/2008jd011681, 2009a.

Oshima, N., Koike, M., Zhang, Y., Kondo, Y., Moteki, N., Takegawa, N., and Miyazaki, Y.: Aging of black carbon in outflow from anthropogenic sources using a mixing state resolved model: Model development and evaluation, Journal of Geophysical Research: Atmospheres, 114, 17, 10.1029/2008jd010680, 2009b.

Palmer, P. I., Parrington, M., Lee, J. D., Lewis, A. C., Rickard, A. R., Bernath, P. F., Duck, T. J., Waugh, D. L., Tarasick, D. W., Andrews, S., Aruffo, E., Bailey, L. J., Barrett, E., Bauguitte, S. J. B., Curry, K. R., Di Carlo, P., Chisholm, L., Dan, L., Forster, G., Franklin, J. E., Gibson, M. D., Griffin, D., Helmig, D., Hopkins, J. R., Hopper, J. T., Jenkin, M. E., Kindred, D., Kliever, J., Le Breton, M., Matthiesen, S., Maurice, M., Moller, S., Moore, D. P., Oram, D. E., O'Shea, S. J., Owen, R. C., Pagniello, C., Pawson, S., Percival, C. J., Pierce, J. R., Punjabi, S., Purvis, R. M., Remedios, J. J., Rotermund, K. M., Sakamoto, K. M., da Silva, A. M., Strawbridge, K. B., Strong, K., Taylor, J., Trigwell, R., Tereszchuk, K. A., Walker, K. A., Weaver, D., Whaley, C., and Young, J. C.: Quantifying the impact of BOReal forest fires on Tropospheric oxidants over the Atlantic using Aircraft and Satellites (BORTAS) experiment: design, execution and science overview, Atmospheric Chemistry and Physics, 13, 6239-6261, 10.5194/acp-13-6239-2013, 2013.

Pan, L. L., Homeyer, C. R., Honomichl, S., Ridley, B. A., Weisman, M., Barth, M. C., Hair, J. W., Fenn, M. A., Butler, C., Diskin, G. S., Crawford, J. H., Ryerson, T. B., Pollack, I., Peischl, J., and Huntrieser, H.: Thunderstorms enhance tropospheric ozone by wrapping and shedding stratospheric air, Geophysical Research Letters, 41, 7785-7790, 10.1002/2014gl061921, 2014.

Parrington, M., Palmer, P. I., Lewis, A. C., Lee, J. D., Rickard, A. R., Di Carlo, P., Taylor, J. W., Hopkins, J. R., Punjabi, S., Oram, D. E., Forster, G., Aruffo, E., Moller, S. J., Bauguitte, S. J. B., Allan, J. D., Coe, H., and Leigh, R. J.: Ozone photochemistry in boreal biomass burning plumes, Atmospheric Chemistry and Physics, 13, 7321-7341, 10.5194/acp-13-7321-2013, 2013.

Petzold, A., Schloesser, H., Sheridan, P. J., Arnott, W. P., Ogren, J. A., and Virkkula, A.: Evaluation of multiangle absorption photometry for measuring aerosol light absorption, Aerosol Science and Technology, 39, 40-51, 10.1080/027868290901945, 2005.

Petzold, A., Weinzierl, B., Huntrieser, H., Stohl, A., Real, E., Cozic, J., Fiebig, M., Hendricks, J., Lauer, A., Law, K., Roiger, A., Schlager, H., and Weingartner, E.: Perturbation of the European free troposphere aerosol by North American forest fire plumes during the ICARTT-ITOP experiment in summer 2004, Atmospheric Chemistry and Physics, 7, 5105-5127, 2007.

Petzold, A., Ogren, J. A., Fiebig, M., Laj, P., Li, S. M., Baltensperger, U., Holzer-Popp, T., Kinne, S., Pappalardo, G., Sugimoto, N., Wehrli, C., Wiedensohler, A., and Zhang, X. Y.: Recommendations for reporting "black carbon" measurements, Atmos. Chem. Phys., 13, 8365-8379, 10.5194/acp-13-8365-2013, 2013.

Pickering, K. E., Thompson, A. M., Wang, Y. S., Tao, W. K., McNamara, D. P., Kirchhoff, V., Heikes, B. G., Sachse, G. W., Bradshaw, J. D., Gregory, G. L., and Blake, D. R.: Convective transport of biomass burning emissions over Brazil during TRACE A, Journal of Geophysical Research: Atmospheres, 101, 23993-24012, 10.1029/96jd00346, 1996.

Planck, M.: Über das Gesetz der Energieverteilung im Normalspectrum, Annalen der Physik, 4, 553-563, 1901.

Pratt, K. A., Murphy, S. M., Subramanian, R., DeMott, P. J., Kok, G. L., Campos, T., Rogers, D. C., Prenni, A. J., Heymsfield, A. J., Seinfeld, J. H., and Prather, K. A.: Flight-based chemical characterization of biomass burning aerosols within two prescribed burn smoke plumes, Atmospheric Chemistry and Physics, 11, 12549-12565, 10.5194/acp-11-12549-2011, 2011.

Prospero, J. M., Ginoux, P., Torres, O., Nicholson, S. E., and Gill, T. E.: Environmental characterization of global sources of atmospheric soil dust identified with the Nimbus 7 Total Ozone Mapping Spectrometer (TOMS) absorbing aerosol product, Reviews of Geophysics, 40, 31, 10.1029/2000rg000095, 2002.

Ramanathan, V., and Carmichael, G.: Global and regional climate changes due to black carbon, Nature Geoscience, 1, 221-227, 10.1038/ngeo156, 2008.

Raut, J. C., Marelle, L., Fast, J. D., Thomas, J. L., Weinzierl, B., Law, K. S., Berg, L. K., Roiger, A., Easter, R. C., Heimerl, K., Onishi, T., Delanoe, J., and Schlager, H.: Cross-polar transport and scavenging of Siberian aerosols containing black carbon during the 2012 ACCESS summer campaign, Atmospheric Chemistry and Physics, 17, 10969-10995, 10.5194/acp-17-10969-2017, 2017.

Real, E., Law, K. S., Weinzierl, B., Fiebig, M., Petzold, A., Wild, O., Methven, J., Arnold, S., Stohl, A., Huntrieser, H., Roiger, A., Schlager, H., Stewart, D., Avery, M., Sachse, G., Browell, E., Ferrare, R., and Blake, D.: Processes influencing ozone levels in Alaskan forest fire plumes during long-range transport over the North Atlantic, Journal of Geophysical Research: Atmospheres, 112, 19, 10.1029/2006jd007576, 2007.

Reid, J. S., Lagrosas, N. D., Jonsson, H. H., Reid, E. A., Sessions, W. R., Simpas, J. B., Uy, S. N., Boyd, T. J., Atwood, S. A., Blake, D. R., Campbell, J. R., Cliff, S. S., Holben, B. N., Holz, R. E., Hyer, E. J., Lynch, P., Meinardi, S., Posselt, D. J., Richardson, K. A., Salinas, S. V., Smirnov, A., Wang, Q., Yu, L.,

and Zhang, J.: Observations of the temporal variability in aerosol properties and their relationships to meteorology in the summer monsoonal South China Sea/East Sea: the scale-dependent role of monsoonal flows, the Madden-Julian Oscillation, tropical cyclones, squall lines and cold pools, Atmospheric Chemistry and Physics, 15, 1745-1768, 10.5194/acp-15-1745-2015, 2015.

Reischl, G. P.: The Relationship of Input and Output Aerosol Characteristcs for an Ideal Differential Mobility Analyser Particle Standard, Journal of Aerosol Science, 22, 297-312, 10.1016/s0021-8502(05)80008-4, 1991.

Remer, L. A., Kaufman, Y. J., Tanre, D., Mattoo, S., Chu, D. A., Martins, J. V., Li, R. R., Ichoku, C., Levy, R. C., Kleidman, R. G., Eck, T. F., Vermote, E., and Holben, B. N.: The MODIS aerosol algorithm, products, and validation, Journal of the Atmospheric Sciences, 62, 947-973, 10.1175/jas3385.1, 2005.

Sahu, L. K., Kondo, Y., Moteki, N., Takegawa, N., Zhao, Y., Cubison, M. J., Jimenez, J. L., Vay, S., Diskin, G. S., Wisthaler, A., Mikoviny, T., Huey, L. G., Weinheimer, A. J., and Knapp, D. J.: Emission characteristics of black carbon in anthropogenic and biomass burning plumes over California during ARCTAS-CARB 2008, Journal of Geophysical Research: Atmospheres, 117, 20, 10.1029/2011jd017401, 2012.

Samset, B. H., and Myhre, G.: Climate response to externally mixed black carbon as a function of altitude, Journal of Geophysical Research: Atmospheres, 120, 2913-2927, 10.1002/2014jd022849, 2015.

Schemm, S., Wernli, H., and Papritz, L.: Warm Conveyor Belts in Idealized Moist Baroclinic Wave Simulations, Journal of the Atmospheric Sciences, 70, 627-652, 10.1175/jas-d-12-0147.1, 2013.

Schultz, D. M.: Reexamining the cold conveyor belt, Monthly Weather Review, 129, 2205-2225, 10.1175/1520-0493(2001)129<2205:rtccb>2.0.co;2, 2001.

Schultz, M. G., Heil, A., Hoelzemann, J. J., Spessa, A., Thonicke, K., Goldammer, J. G., Held, A. C., Pereira, J. M. C., and van het Bolscher, M.: Global wildland fire emissions from 1960 to 2000, Global Biogeochemical Cycles, 22, 17, 10.1029/2007gb003031, 2008.

Schumann, U.: Atmospheric Physics Background – Methods – Trends, Springer Heidelberg New York Dordrecht London, 2012.

Schwarz, J. P., Gao, R. S., Fahey, D. W., Thomson, D. S., Watts, L. A., Wilson, J. C., Reeves, J. M., Darbeheshti, M., Baumgardner, D. G., Kok, G. L., Chung, S. H., Schulz, M., Hendricks, J., Lauer, A., Karcher, B., Slowik, J. G., Rosenlof, K. H., Thompson, T. L., Langford, A. O., Loewenstein, M., and Aikin, K. C.: Single-particle measurements of midlatitude black carbon and light-scattering aerosols from the boundary layer to the lower stratosphere, Journal of Geophysical Research: Atmospheres, 111, 10.1029/2006jd007076, 2006.

Schwarz, J. P., Gao, R. S., Spackman, J. R., Watts, L. A., Thomson, D. S., Fahey, D. W., Ryerson, T. B., Peischl, J., Holloway, J. S., Trainer, M., Frost, G. J., Baynard, T., Lack, D. A., de Gouw, J. A., Warneke, C., and Del Negro, L. A.: Measurement of the mixing state, mass, and optical size of individual black carbon particles in urban and biomass burning emissions, Geophysical Research Letters, 35, 10.1029/2008gl033968, 2008a.

Schwarz, J. P., Spackman, J. R., Fahey, D. W., Gao, R. S., Lohmann, U., Stier, P., Watts, L. A., Thomson, D. S., Lack, D. A., Pfister, L., Mahoney, M. J., Baumgardner, D., Wilson, J. C., and Reeves, J. M.: Coatings and their enhancement of black carbon light absorption in the tropical atmosphere, Journal of Geophysical Research: Atmospheres, 113, 10.1029/2007jd009042, 2008b.

Schwarz, J. P., Spackman, J. R., Gao, R. S., Perring, A. E., Cross, E., Onasch, T. B., Ahern, A., Wrobel, W., Davidovits, P., Olfert, J., Dubey, M. K., Mazzoleni, C., and Fahey, D. W.: The Detection Efficiency of the Single Particle Soot Photometer, Aerosol Science and Technology, 44, 612-628, 10.1080/02786826.2010.481298, 2010a.

Schwarz, J. P., Spackman, J. R., Gao, R. S., Watts, L. A., Stier, P., Schulz, M., Davis, S. M., Wofsy, S. C., and Fahey, D. W.: Global-scale black carbon profiles observed in the remote atmosphere and compared to models, Geophysical Research Letters, 37, n/a-n/a, 10.1029/2010gl044372, 2010b.

Schwarz, J. P., Samset, B. H., Perring, A. E., Spackman, J. R., Gao, R. S., Stier, P., Schulz, M., Moore, F. L., Ray, E. A., and Fahey, D. W.: Global-scale seasonally resolved black carbon vertical profiles over the Pacific, Geophysical Research Letters, 40, 5542-5547, 10.1002/2013gl057775, 2013.

Schwarz, J. P., Perring, A. E., Markovic, M. Z., Gao, R. S., Ohata, S., Langridge, J., Law, D., McLaughlin, R., and Fahey, D. W.: Technique and theoretical approach for quantifying the hygroscopicity of black-carbon-containing aerosol using a single particle soot photometer, Journal of Aerosol Science, 81, 110-126, 10.1016/j.jaerosci.2014.11.009, 2015.

Schwarz, J. P., Weinzierl, B., Samset, B. H., Dollner, M., Heimerl, K., Markovic, M. Z., Perring, A. E., and Ziemba, L.: Aircraft Measurements of Black Carbon Vertical Profiles Show Upper Tropospheric Variability and Stability, Geophysical Research Letters, 44, 1132-1140, 10.1002/2016gl071241, 2017.

Sedlacek, A. J., III, Lewis, E. R., Kleinman, L., Xu, J., and Zhang, Q.: Determination of and evidence for non-core-shell structure of particles containing black carbon using the Single-Particle Soot Photometer (SP2), Geophysical Research Letters, 39, 10.1029/2012gl050905, 2012.

Seinfeld, J. H., and Pandis, S. N.: Atmospheric chemistry and physics : from air pollution to climate change, Third edition. ed., John Wiley & Sons, Inc., Hoboken, New Jersey, xxvi, 1120 pages pp., 2016.

Shiraiwa, M., Kondo, Y., Iwamoto, T., and Kita, K.: Amplification of Light Absorption of Black Carbon by Organic Coating, Aerosol Science and Technology, 44, 46-54, 10.1080/02786820903357686, 2010.

Simmonds, P. G., Manning, A. J., Derwent, R. G., Ciais, P., Ramonet, M., Kazan, V., and Ryall, D.: A burning question. Can recent growth rate anomalies in the greenhouse gases be attributed to large-scale biomass burning events?, Atmospheric Environment, 39, 2513-2517, 10.1016/j.atmosenv.2005.02.018, 2005.

Slowik, J. G., Cross, E. S., Han, J. H., Davidovits, P., Onasch, T. B., Jayne, J. T., WilliamS, L. R., Canagaratna, M. R., Worsnop, D. R., Chakrabarty, R. K., Moosmuller, H., Arnott, W. P., Schwarz, J. P., Gao, R. S., Fahey, D. W., Kok, G. L., and Petzold, A.: An inter-comparison of instruments measuring black carbon content of soot particles, Aerosol Science and Technology, 41, 295-314, 10.1080/02786820701197078, 2007.

Small, J. D., Chuang, P. Y., Feingold, G., and Jiang, H. L.: Can aerosol decrease cloud lifetime?, Geophysical Research Letters, 36, 5, 10.1029/2009gl038888, 2009.

Soja, A. J., Cofer, W. R., Shugart, H. H., Sukhinin, A. I., Stackhouse, P. W., McRae, D. J., and Conard, S. G.: Estimating fire emissions and disparities in boreal Siberia (1998-2002), Journal of Geophysical Research: Atmospheres, 109, 25, 10.1029/2004jd004570, 2004.

Sokolik, I. N., and Toon, O. B.: Incorporation of mineralogical composition into models of the radiative properties of mineral aerosol from UV to IR wavelengths, Journal of Geophysical Research: Atmospheres, 104, 9423-9444, 10.1029/1998jd200048, 1999.

Solomon, D. L., Bowman, K. P., and Homeyer, C. R.: Tropopause-Penetrating Convection from Three-Dimensional Gridded NEXRAD Data, Journal of Applied Meteorology and Climatology, 55, 465-478, 10.1175/jamc-d-15-0190.1, 2016.

Sommers, W. T., Loehman, R. A., and Hardy, C. C.: Wild land fire emissions, carbon, and climate: Science overview and knowledge needs, Forest Ecology and Management, 317, 1-8, 10.1016/j.foreco.2013.12.014, 2014.

Spackman, J. R., Schwarz, J. P., Gao, R. S., Watts, L. A., Thomson, D. S., Fahey, D. W., Holloway, J. S., de Gouw, J. A., Trainer, M., and Ryerson, T. B.: Empirical correlations between black carbon aerosol and carbon monoxide in the lower and middle troposphere, Geophysical Research Letters, 35, 10.1029/2008gl035237, 2008.

Spackman, J. R., Gao, R. S., Neff, W. D., Schwarz, J. P., Watts, L. A., Fahey, D. W., Holloway, J. S., Ryerson, T. B., Peischl, J., and Brock, C. A.: Aircraft observations of enhancement and depletion of black carbon mass in the springtime Arctic, Atmospheric Chemistry and Physics, 10, 9667-9680, 10.5194/acp-10-9667-2010, 2010.

Spracklen, D. V., Carslaw, K. S., Poschl, U., Rap, A., and Forster, P. M.: Global cloud condensation nuclei influenced by carbonaceous combustion aerosol, Atmospheric Chemistry and Physics, 11, 9067-9087, 10.5194/acp-11-9067-2011, 2011.

Stein, A. F., Draxler, R. R., Rolph, G. D., Stunder, B. J. B., Cohen, M. D., and Ngan, F.: NOAA'S HYSPLIT Atmospheric Transport and Dispersion Modeling System, Bulletin of the American Meteorological Society, 96, 2059-2077, 10.1175/bams-d-14-00110.1, 2015.

Stephens, M., Turner, N., and Sandberg, J.: Particle identification by laser-induced incandescence in a solid-state laser cavity, Applied Optics, 42, 3726-3736, 10.1364/AO.42.003726, 2003.

Stephens, S. L., and Ruth, L. W.: Federal forest-fire policy in the United States, Ecological Applications, 15, 532-542, 10.1890/04-0545, 2005.

Stettler, M. E. J., Boies, A. M., Petzold, A., and Barrett, S. R. H.: Global Civil Aviation Black Carbon Emissions, Environmental Science & Technology, 47, 10397-10404, 10.1021/es401356v, 2013.

Stohl, A.: A 1-year Lagrangian "climatology" of airstreams in the Northern Hemisphere troposphere and lowermost stratosphere, Journal of Geophysical Research: Atmospheres, 106, 7263-7279, 10.1029/2000jd900570, 2001.

Stull, R. B.: An Introduction to Boundary Layer Meteorology, Kluwer Academic Publishers, Dordrecht, The Netherlands, 666 pp., 1988.

Subramanian, R., Kok, G. L., Baumgardner, D., Clarke, A., Shinozuka, Y., Campos, T. L., Heizer, C. G., Stephens, B. B., de Foy, B., Voss, P. B., and Zaveri, R. A.: Black carbon over Mexico: the effect of atmospheric transport on mixing state, mass absorption cross-section, and BC/CO ratios, Atmospheric Chemistry and Physics, 10, 219-237, 10.5194/acp-10-219-2010, 2010.

Taylor, J. W., Allan, J. D., Allen, G., Coe, H., Williams, P. I., Flynn, M. J., Le Breton, M., Muller, J. B. A., Percival, C. J., Oram, D., Forster, G., Lee, J. D., Rickard, A. R., Parrington, M., and Palmer, P. I.: Size-dependent wet removal of black carbon in Canadian biomass burning plumes, Atmospheric Chemistry and Physics, 14, 13755-13771, 10.5194/acp-14-13755-2014, 2014.

Taylor, J. W., Allan, J. D., Liu, D., Flynn, M., Weber, R., Zhang, X., Lefer, B. L., Grossberg, N., Flynn, J., and Coe, H.: Assessment of the sensitivity of core/shell parameters derived using the single-particle

soot photometer to density and refractive index, Atmospheric Measurement Techniques, 8, 1701-1718, 10.5194/amt-8-1701-2015, 2015.

Trickl, T., Vogelmann, H., Flentje, H., and Ries, L.: Stratospheric ozone in boreal fire plumes - the 2013 smoke season over central Europe, Atmospheric Chemistry and Physics, 15, 9631-9649, 10.5194/acp-15-9631-2015, 2015.

Twomey, S.: The Influence of Pollution on the Shortwave Albedo of Clouds, Journal of the Atmospheric Sciences, 34, 1149-1152, 10.1175/1520-0469(1977)034<1149:tiopot>2.0.co;2, 1977.

van der Werf, G. R., Randerson, J. T., Giglio, L., Collatz, G. J., Mu, M., Kasibhatla, P. S., Morton, D. C., DeFries, R. S., Jin, Y., and van Leeuwen, T. T.: Global fire emissions and the contribution of deforestation, savanna, forest, agricultural, and peat fires (1997-2009), Atmospheric Chemistry and Physics, 10, 11707-11735, 10.5194/acp-10-11707-2010, 2010.

van der Werf, G. R., Randerson, J. T., Giglio, L., van Leeuwen, T. T., Chen, Y., Rogers, B. M., Mu, M., van Marle, M. J. E., Morton, D. C., Collatz, G. J., Yokelson, R. J., and Kasibhatla, P. S.: Global fire emissions estimates during 1997–2016, Earth Syst. Sci. Data, 9, 697-720, 10.5194/essd-9-697-2017, 2017.

van Poppel, L. H., Friedrich, H., Spinsby, J., Chung, S. H., Seinfeld, J. H., and Buseck, P. R.: Electron tomography of nanoparticle clusters: Implications for atmospheric lifetimes and radiative forcing of soot, Geophysical Research Letters, 32, 4, 10.1029/2005gl024461, 2005.

Warneke, C., Bahreini, R., Brioude, J., Brock, C. A., de Gouw, J. A., Fahey, D. W., Froyd, K. D., Holloway, J. S., Middlebrook, A., Miller, L., Montzka, S., Murphy, D. M., Peischl, J., Ryerson, T. B., Schwarz, J. P., Spackman, J. R., and Veres, P.: Biomass burning in Siberia and Kazakhstan as an important source for haze over the Alaskan Arctic in April 2008, Geophysical Research Letters, 36, 6, 10.1029/2008gl036194, 2009.

Weigum, N. M., Stier, P., Schwarz, J. P., Fahey, D. W., and Spackman, J. R.: Scales of variability of black carbon plumes over the Pacific Ocean, Geophysical Research Letters, 39, 10.1029/2012gl052127, 2012.

Weinzierl, B., Petzold, A., Esselborn, M., Wirth, M., Rasp, K., Kandler, K., Schutz, L., Koepke, P., and Fiebig, M.: Airborne measurements of dust layer properties, particle size distribution and mixing state of Saharan dust during SAMUM 2006, Tellus Series B-Chemical and Physical Meteorology, 61, 96-117, 10.1111/j.1600-0889.2008.00392.x, 2009.

Weinzierl, B., Sauer, D., Esselborn, M., Petzold, A., Veira, A., Rose, M., Mund, S., Wirth, M., Ansmann, A., Tesche, M., Gross, S., and Freudenthaler, V.: Microphysical and optical properties of dust and tropical biomass burning aerosol layers in the Cape Verde region-an overview of the airborne in situ and lidar measurements during SAMUM-2, Tellus Series B-Chemical and Physical Meteorology, 63, 589-618, 10.1111/j.1600-0889.2011.00566.x, 2011.

Westerling, A. L., Gershunov, A., Brown, T. J., Cayan, D. R., and Dettinger, M. D.: Climate and wildfire in the western United States, Bulletin of the American Meteorological Society, 84, 595-+, 10.1175/bams-84-5-595, 2003.

Whitby, K. T., Husar, R. B., and Liu, B. Y. H.: The aerosol size distribution of Los Angeles smog, Journal of Colloid and Interface Science, 39, 177-204, 10.1016/0021-9797(72)90153-1, 1972.

Whitby, K. T.: The physical characteristics of sulfur aerosols, Atmospheric Environment (1967), 12, 135-159, 10.1016/0004-6981(78)90196-8, 1978.

Wilcox, E. M., Thomas, R. M., Praveen, P. S., Pistone, K., Bender, F. A. M., and Ramanathan, V.: Black carbon solar absorption suppresses turbulence in the atmospheric boundary layer, Proceedings of the National Academy of Sciences of the United States of America, 113, 11794-11799, 10.1073/pnas.1525746113, 2016.

Wooster, M. J., Roberts, G., Perry, G. L. W., and Kaufman, Y. J.: Retrieval of biomass combustion rates and totals from fire radiative power observations: FRP derivation and calibration relationships between biomass consumption and fire radiative energy release, Journal of Geophysical Research: Atmospheres, 110, 24, 10.1029/2005jd006318, 2005.

Wotawa, G., and Trainer, M.: The Influence of Canadian Forest Fires on Pollutant Concentrations in the United States, Science, 288, 324-328, 10.1126/science.288.5464.324 2000.

Yamaguchi, T., Feingold, G., Kazil, J., and McComiskey, A.: Stratocumulus to cumulus transition in the presence of elevated smoke layers, Geophysical Research Letters, 42, 8, 10.1002/2015gl066544, 2015.

Zhang, R., Khalizov, A. F., Pagels, J., Zhang, D., Xue, H., and McMurry, P. H.: Variability in morphology, hygroscopicity, and optical properties of soot aerosols during atmospheric processing, Proceedings of the National Academy of Sciences, 105, 10291-10296, 2008.

Zimmerman, G. T., and Laven, R. D.: Effects of Forest Fuel Smoke on Dwarf Mistletoe Seed Germination, Great Basin Naturalist, 47, 652-659, 1987.

Web pages:

http://www.globalfiredata.org   accessed 16.12.2017

http://www.eol.ucar.edu/field_projects/dc3   accessed 16.12.2017

http://catalog.eol.ucar.edu/dc3_2012/   accessed 16.12.2017

http://rapidfire.sci.gsfc.nasa.gov/cgi-bin/imagery/firemaps.cgi   accessed 16.12.2017

https://worldview.earthdata.nasa.gov/   accessed 16.12.2017

http://data.eol.ucar.edu/master_list/?project=DC3   accessed 16.12.2017

https://www-calipso.larc.nasa.gov/   accessed 16.12.2017

https://www.nasa.gov/centers/armstrong/aircraft/DC-8/index.html   accessed 16.12.2017

http://www.weather.gov/jetstream/life   accessed 16.12.2017

Appendix

A large variety of calibration data was compared to evaluate both the quality of the data from the DC3 campaign and the SP2's performance over time. With the 8-channel upgrade, some of the parameters changed, which made performance monitoring even more important. Table A 1 lists all the calibrations that were included in the alignment, calibration and performance description in chapter 3.2.

Table A 1: Calibration data, dates of calibration, and differences in instrument setup to previous calibration for the alignment and calibration steps shown in chapter 3.2.

Calibration Date	Performed Calibration	Comments/Differences to Previous Calibration
22.03.2012	Fullerene Soot Calibration	Change of Gain
30.03.2012	Split Detector Alignment	
02.04.2012	Fullerene Soot Calibration	
05.06.2012	Fullerene Soot Calibration	
21.06.2012	Laser Beam Alignment	Output Coupler Adjustment
	Fullerene Soot Calibration	
02.07.2012	Laser Intensity Verification	
05.07.2012	Fullerene Soot Calibration	
02.08.2012	Fullerene Soot Calibration	
13.02.2013	Sample Flow Calibration	Change of Gain;
07.02.2014	Chamber Position Alignment	Upgrade to 8-Channel SP2; Output Coupler Adjustment
10.02.2014	Fullerene Soot Calibration	
21.02.2014	Fullerene Soot Calibration	
16.04.2014	Fullerene Soot Calibration	
23.04.2014	Chamber Position Alignment	Output Coupler Adjustment
24.04.2014	Laser Beam and Output Coupler Alignment	

	Fullerene Soot Calibration	
20.05.2014	Sample Flow Calibration	
07.07.2014	Fullerene Soot Calibration	
20.08.2014	Chamber Position Alignment	Output Coupler Adjustment
	Fullerene Soot Calibration	
26.08.2014	Fullerene Soot Calibration	
28.08.2014	Split Detector Alignment	
	Fullerene Soot Calibration	
14.01.2015	Fullerene Soot Calibration	
09.09.2015	Chamber Position Alignment	Output Coupler Adjustment
	Fullerene Soot Calibration	
17.09.2015	Fullerene Soot Calibration	

An additional performance check of the split detector, as described in chapter 3.2.1.3, is, to compare the first, negative split signal peak of non-incandescing particles with the peak height of the scattering channel. A large spread would indicate an unstable split point.
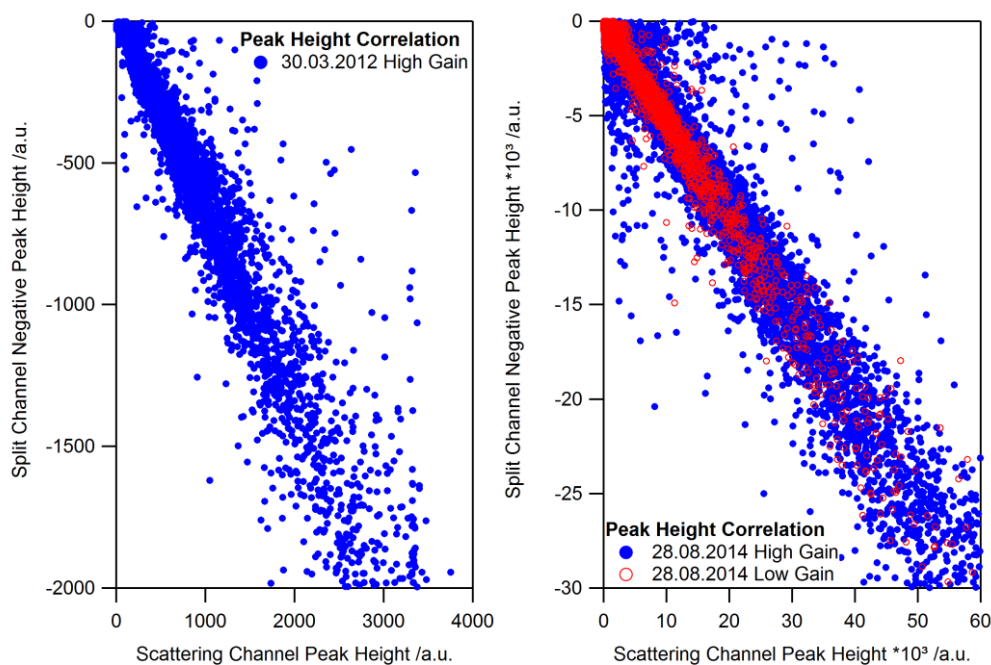
Figure A 1:Correlation between the peak height of the scattering signal and the negative peak height of the split detector signal of non-incandescing particles. Left: Ambient air sample measured during the DC3 preparation. Right: Ambient air sample measured with the August 2014 alignment.

Chapter 3.2.2 showed the necessary steps for obtaining the calibration coefficients for the incandescence channels for the 4-channel SP2. The calibration coefficients for the 8-channel version are listed in Table A 2 for the measurement campaigns in which the DLR's SP2 was involved, with the corresponding figures following on the next pages (Figure A 2).

Table A 2: Calibration coefficients for the 8-channel SP2 in 2014 and 2015. Corresponding figures with calibration curves follow on the next pages.

	BBHG offset	BBHG slope	BBLG offset	BBLG slope	NBHG offset	NBHG slope	NBLG offset	NBLG slope
ML-Cirrus	0.19 ± 0.07	0.000181 ± 0.000004	0.15 (fixed)	0.00202 ± 0.00002	0.1 ± 0.1	0.000225 ± 0.000006	0.15 (fixed)	0.00223 ± 0.00002
ACCESS-II	0.179 ± 0.06	0.000196 ± 0.000003	0.16 (fixed)	0.00207 ± 0.00001	0.24 ± 0.09	0.000234 ± 0.000003	0.3 ± 0.3	0.00229 ± 0.00002
ACRIDICON	0.15 ± 0.03	0.000183 ± 0.000002	0.15 (fixed)	0.00193 ± 0.00002	0.04 ± 0.09	0.000225 ± 0.000005	0.3 (fixed)	0.00200 ± 0.00002
ECLIF	0.21 ± 0.04	0.000152 ± 0.000002	0.16 (fixed)	0.001662 ± 0.00001	0.3 ± 0.1	0.000178 ± 0.000006	0.14 ± 0.06	0.00185 ± 0.00001

Calibration Date

- ◆ 140210
- ▲ 140221
- ◥ 140224
- ◆ 140416
- ■ 140424
- ◆ 140707
- ✳ 140820
- ⋈ 140826
- ◀ 140828
- ▶ 150114
- ⟂ 150909
- ▼ 150917

Calibration Curves

—— March/April 2014 (ML-Cirrus)
—— May 2014 (ACCESS-II)
—— September/October 2014 (ACRIDICON)
—— September/October 2015 (ECLIF)
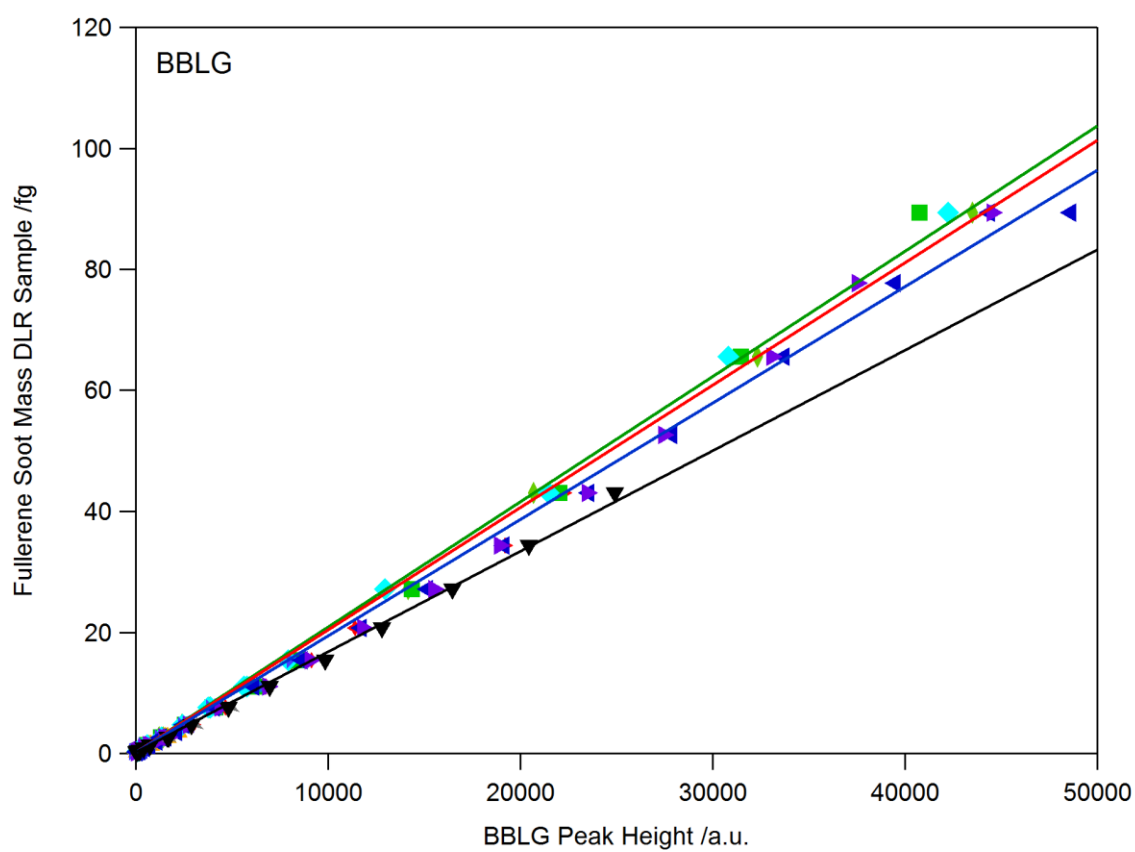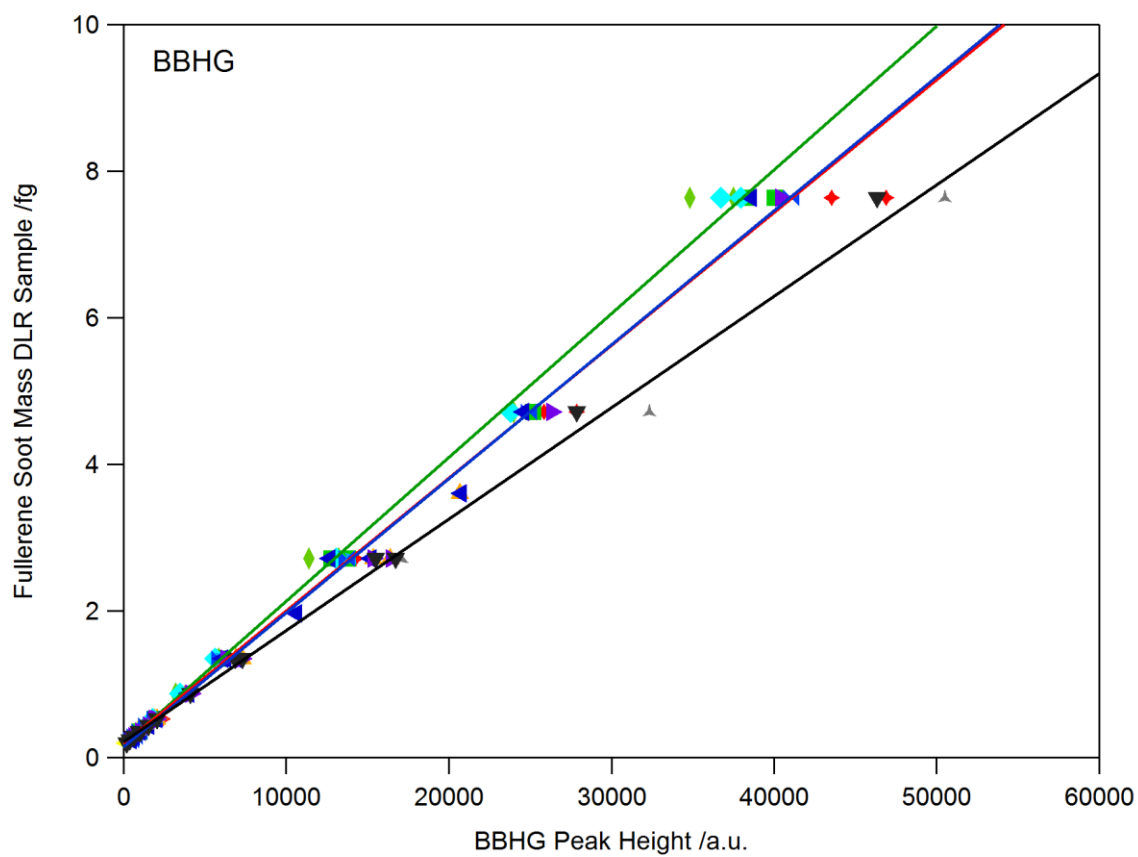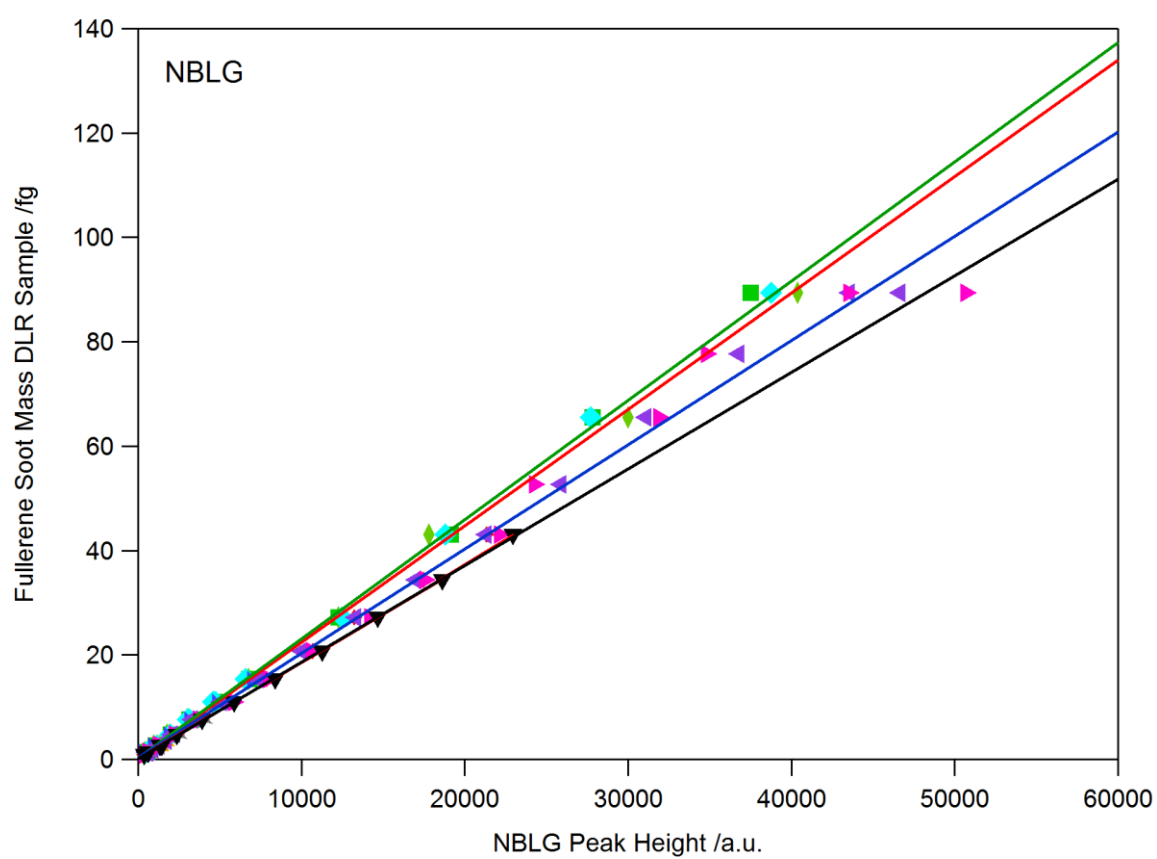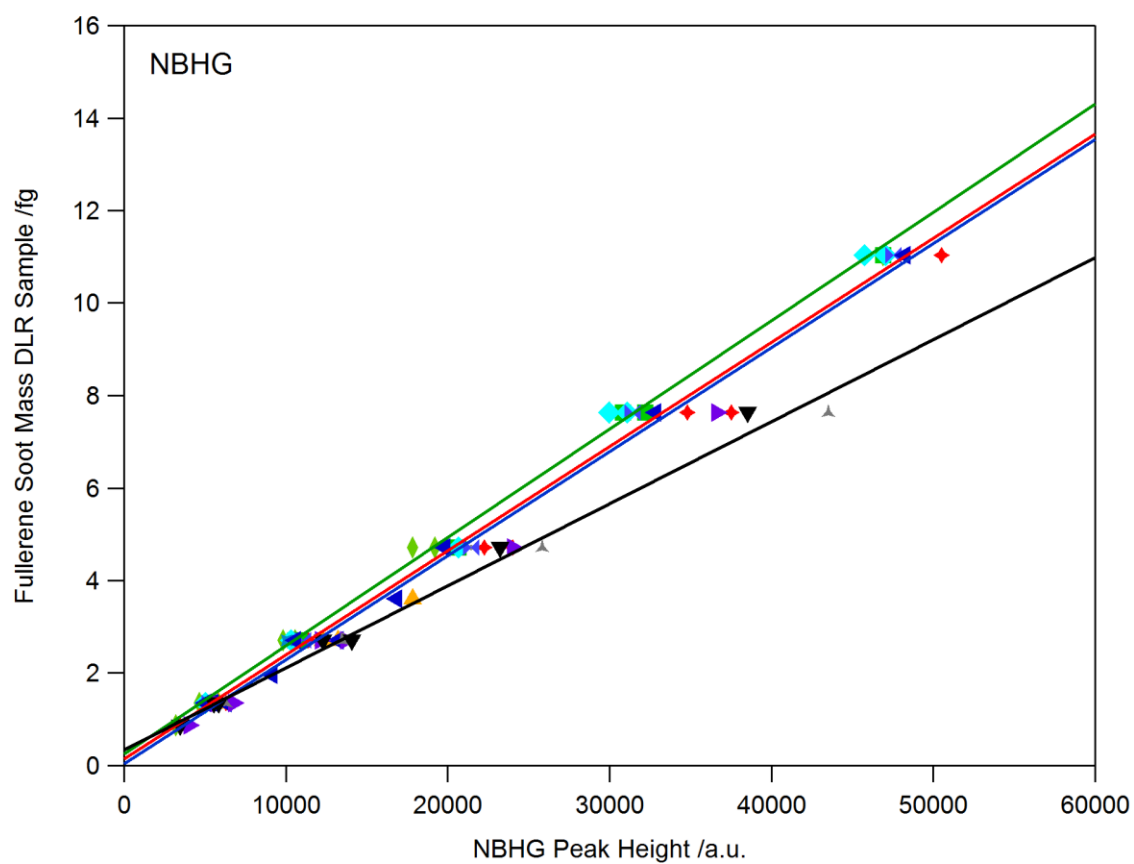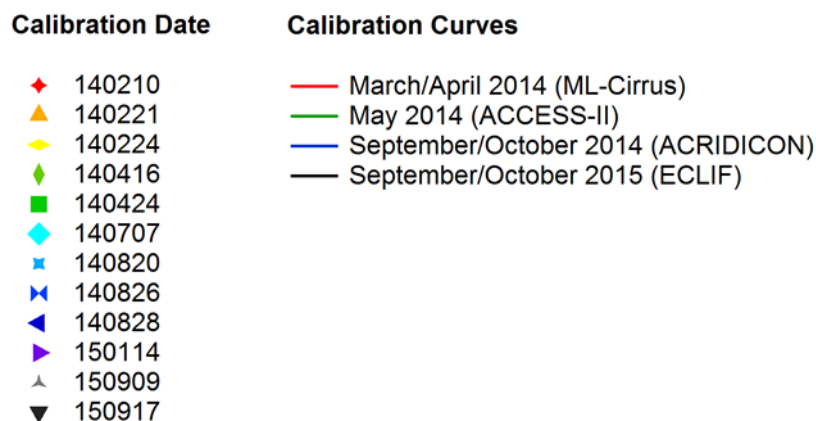
Figure A 2: Calibration curves for 8-channel SP2 since January 2015. Legend for all four panels at the bottom

To determine the origin of the biomass burning layers during DC3, backward trajectories for the BB encounters were compared with the MODIS fire map. The backward trajectories for all encounters, color-coded with altitude, are shown in the following figures (Figure A 3 to Figure A 13) together with the corresponding flight track in grey. The identified source fires are marked as red circles. All encounters are listed in Table A 3.
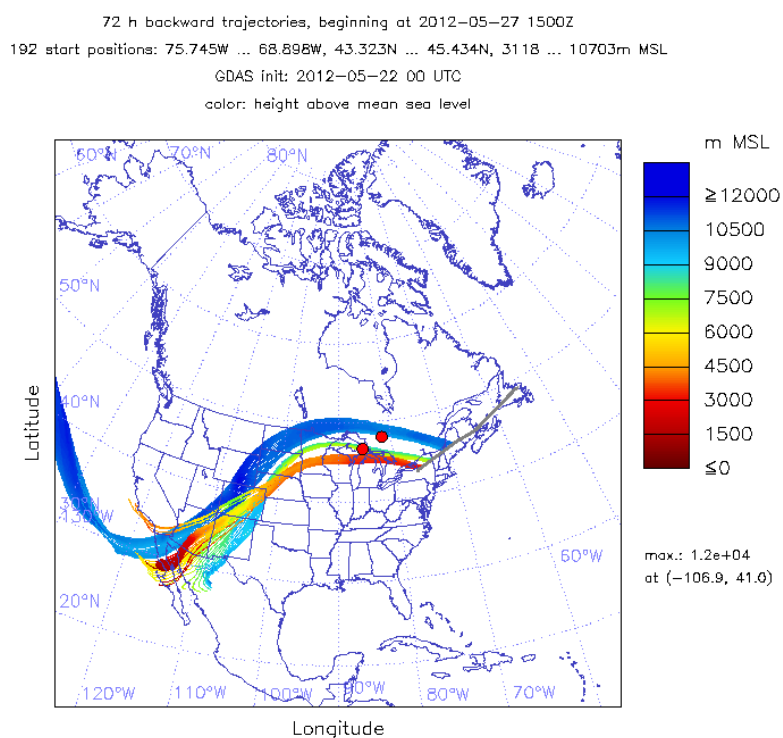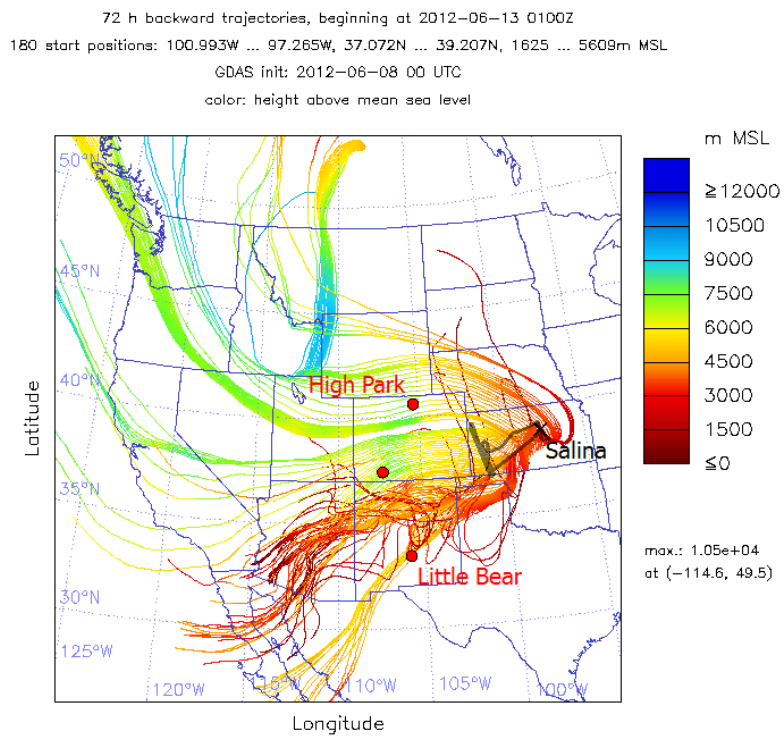

Figure A 3: Backward trajectories for BB encounters during flight 120527a (▼)
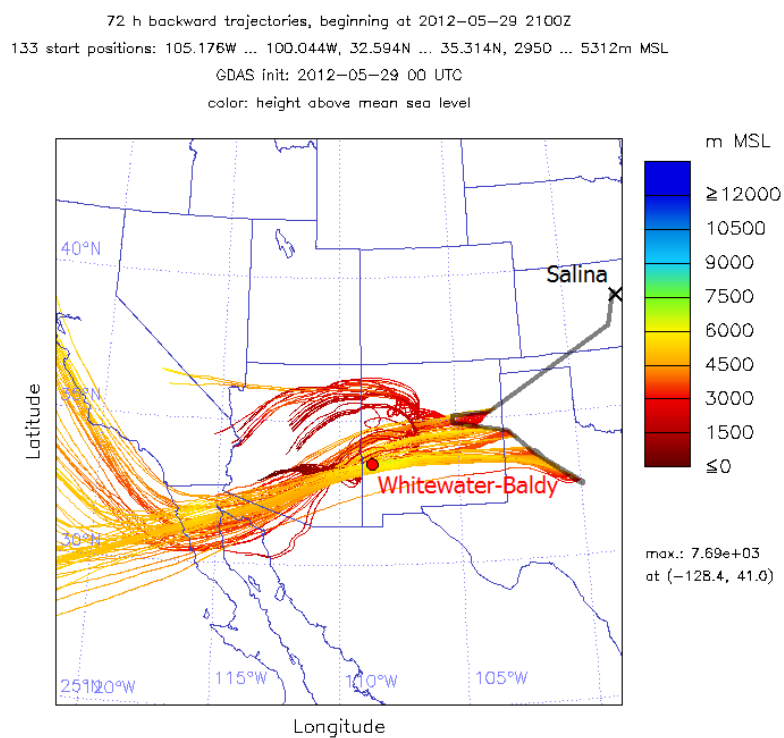
Figure A 4: Backward trajectories for BB encounters during flight 120529a (⧖)
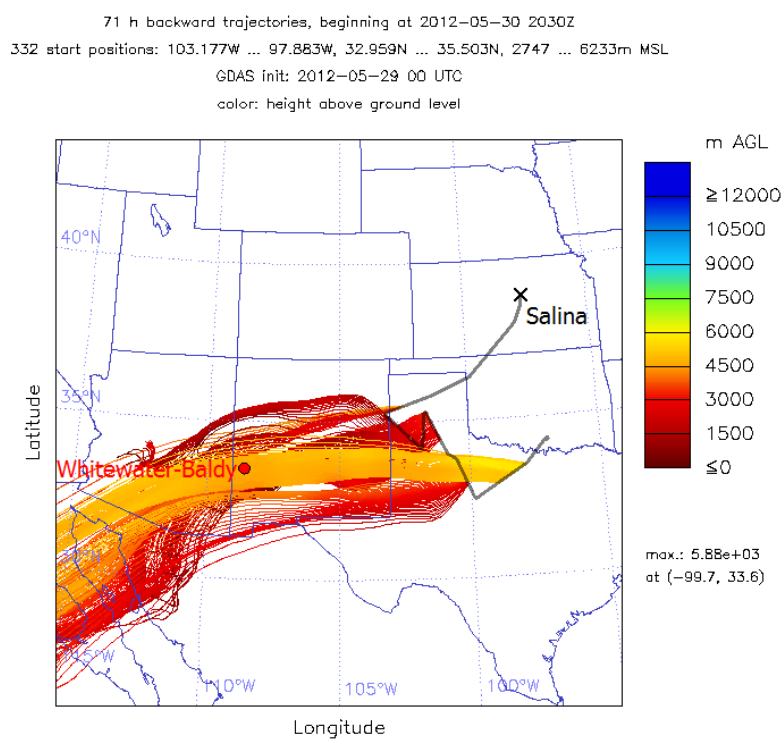
Figure A 5: Backward trajectories for BB encounters during flight 120539a (⋈)
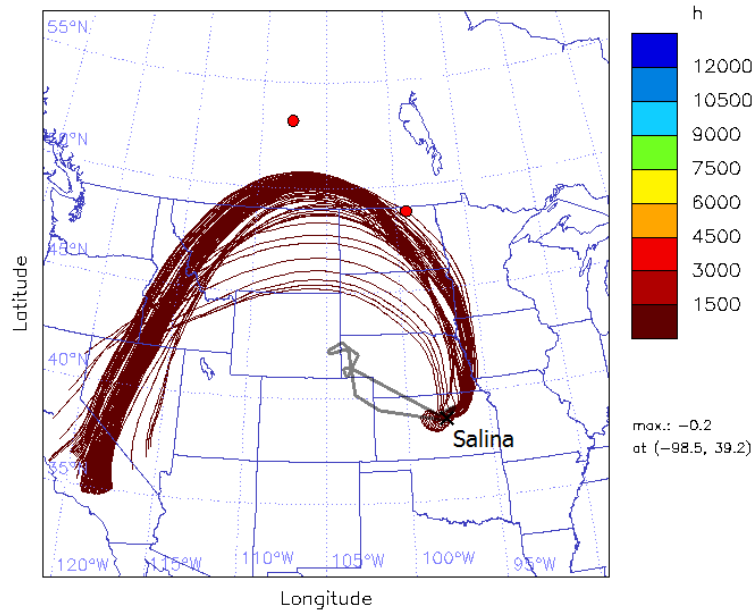
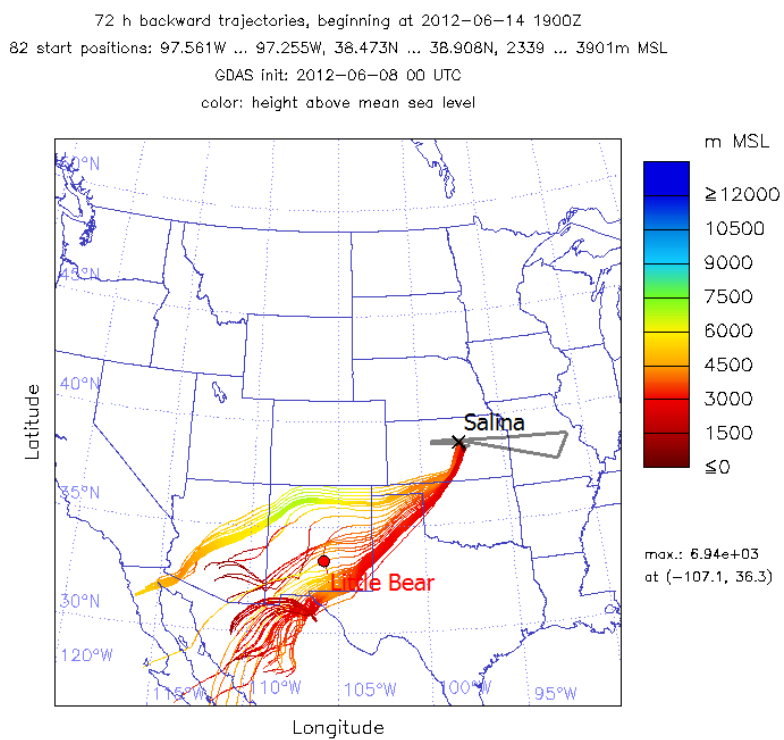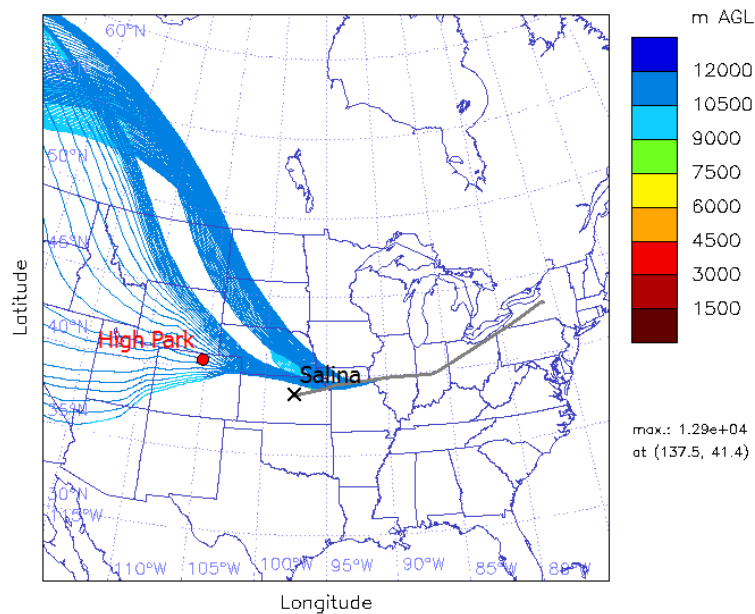*Figure A 6: Backward trajectories for BB encounters during flight 120606a (◀)*
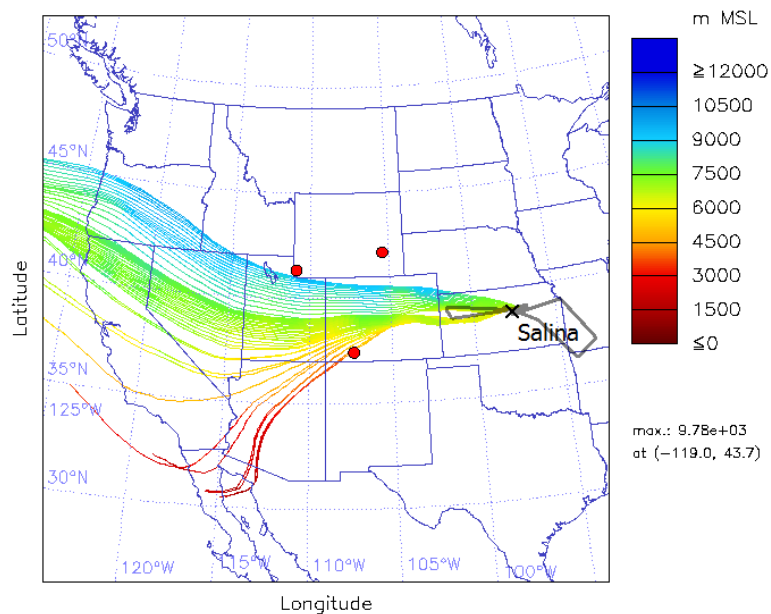
Figure A 7: Backward trajectories for BB encounters during flight 1206068a (▶)

71 h backward trajectories, beginning at 2012-06-11 1630Z
392 start positions: 99.362W ... 95.301W, 35.668N ... 38.965N, 384 ... 7606m MSL
GDAS init: 2012-06-08 00 UTC
color: height above mean sea level
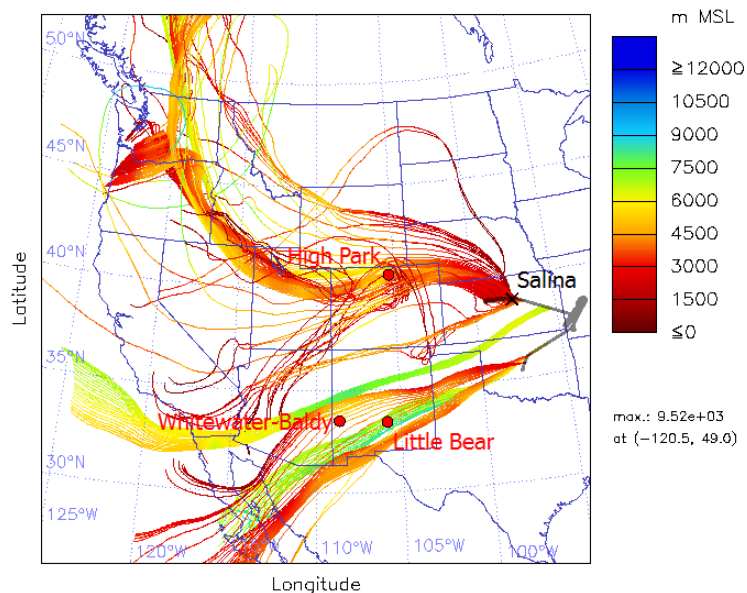
Figure A 8: Backward trajectories for BB encounters during flight 120611a (Little Bear:■; High Park: ●; Whitewater-Baldy:◆)

72 h backward trajectories, beginning at 2012-06-11 2100Z
132 start positions: 97.507W ... 95.76W, 35.403N ... 38.663N, 2238 ... 7204m MSL
GDAS init: 2012-06-08 00 UTC
color: height above mean sea level
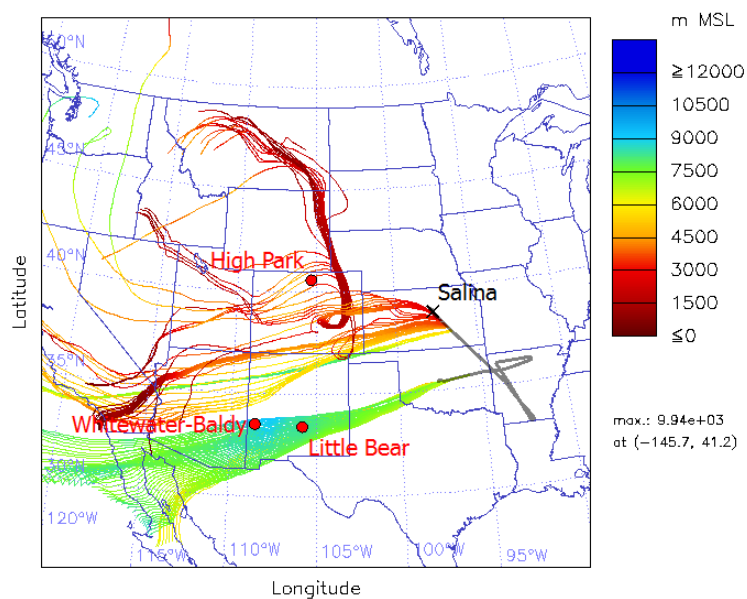
Figure A 9: Backward trajectories for BB encounters during flight 120611b (Little Bear:■; High Park: ●)

72 h backward trajectories, beginning at 2012-06-13 0100Z
180 start positions: 100.993W ... 97.265W, 37.072N ... 39.207N, 1625 ... 5609m MSL
GDAS init: 2012-06-08 00 UTC
color: height above mean sea level

Figure A 10: Backward trajectories for BB encounters during flight 120612a (◆)

72 h backward trajectories, beginning at 2012-06-14 1900Z
82 start positions: 97.561W ... 97.255W, 38.473N ... 38.908N, 2339 ... 3901m MSL
GDAS init: 2012-06-08 00 UTC
color: height above mean sea level

Figure A 11: Backward trajectories for BB encounters during flight 120614a (◆)

71 h backward trajectories, beginning at 2012-06-17 1430Z
150 start positions: 95.894W ... 90.515W, 39.08N ... 39.781N, 9093 ... 11153m MSL
GDAS init: 2012-06-15 00 UTC
color: height above ground level

Figure A 12: Backward trajectories for BB encounters during flight 120617a (✦)

120 h backward trajectories, beginning at 2012-06-18 1400Z
458 start positions: 59.972W ... 54.54W, 49.435N ... 64.379N, 5788 ... 10928m MSL
GDAS init: 2012-06-15 00 UTC
color: height above mean sea level
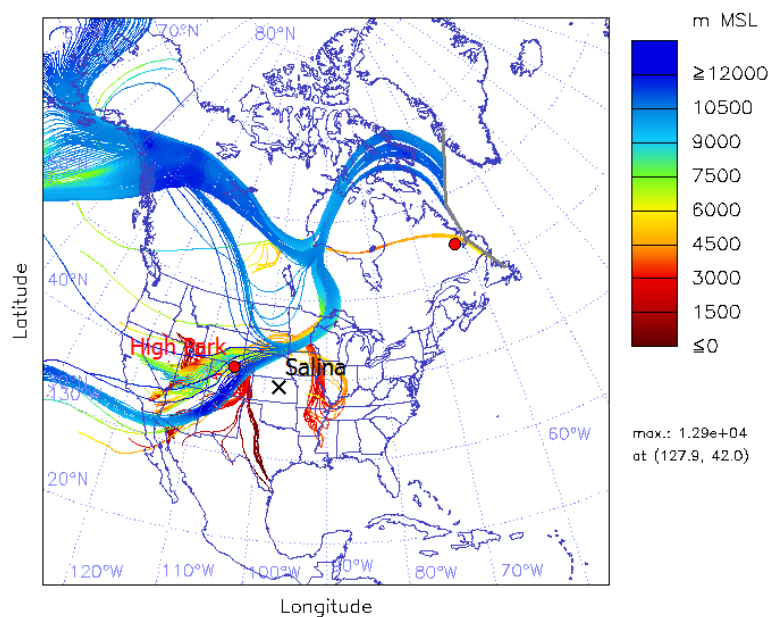
Figure A 13: Backward trajectories for BB encounters during flight 120618a (High Park:✖; Labrador and Newfoundland: ▲)

Table A 3: List of BB encounters during DC3

Flight Number	Start Time /UTC	End Time /UTC	rBC/CO ratio /(ng/(m³ppb))	Average Altitude /m	Estimated Plume Age /h	Plume Origin	Fraction with Thick Coating	Total rBC Mass Concentration µg/m³	GSD	MMD /nm
120527a	52118	52876		10683	8	Great Lakes	0.37	0.075	1.72	147
120527a	54215	54609		7168	12	Great Lakes	0.58	0.295	1.70	171
120527a	55200	55717		3114	22	Great Lakes	0.64	0.125	1.68	167
120529a	72905	74091		3766	12	WWB	0.39	0.050	1.76	164
120529a	74563	75115		4040	10	WWB	0.52	0.051	1.69	171
120529a	75297	75886		3952	20	WWB	0.73	0.308	1.64	186
120529a	76249	77252		4243	14	WWB	0.73	0.764	1.62	187
120529a	77586	77800		3853	18	WWB	0.71	0.842	1.56	199
120529a	78454	78706		3921	18	WWB	0.75	0.433	1.64	194
120530a	72281	72741	3.47	5064	18	WWB	0.80	0.319	1.61	186
120530a	72992	73302	3.28	4356	24	WWB	0.79	0.455	1.60	185
120530a	73832	74136	3.90	4226	24	WWB	0.77	0.839	1.61	195
120530a	74220	75451	4.60	4493	24	WWB	0.78	0.735	1.60	192
120530a	76351	76635	4.55	3840	20	WWB	0.71	0.213	1.65	178
120530a	77635	78327	5.63	5697	18	WWB	0.81	0.214	1.66	179
120606a	84385	84540	2.35	5070	34	CAN	0.66	0.038	1.57	166
120606a	84737	84863	1.12	4453	34	CAN	0.59	0.064	1.66	175
120606a	84989	85435	0.70	4668	34	CAN	0.58	0.050	1.60	165
120608a	68051	68197	5.05	6252	24	CO	0.75	0.167	1.60	184
120608a	68563	68871	3.08	6043	24	CO	0.71	0.106	1.64	179
120608b	80168	80225	2.04	6078	26	CO	0.69	0.111	1.59	189
120608b	87674	88165	1.17	5430	20	CO	0.64	0.105	1.77	181
120611a	58376	58973	5.48	1881	12	HP	0.23	0.078	1.60	170

120611a	59004	61017	3.08	2407	12	HP	0.62	0.127	1.65	167
120611a	61566	61826	3.86	6707	22	WWB	0.66	0.057	1.70	169
120611a	67562	68229	3.39	5744	24	LB	0.75	0.251	1.65	164
120611a	68324	68440	3.69	3548	24	LB	0.72	0.282	1.64	172
120611a	68701	68754	3.80	3030	24	LB	0.67	0.265	1.63	168
120611b	73644	73727	2.66	4654	24	LB	0.68	0.185	1.67	168
120611b	73824	73965	2.14	6718	20	LB	0.72	0.848	1.67	159
120611b	74085	74464	2.09	7085	20	LB	0.69	1.648	1.65	159
120611b	82235	82316	3.17	5696	20	CO	0.68	0.064	1.64	174
120611b	82471	82783	2.72	3670	20	CO	0.70	0.117	1.65	164
120611b	82909	82968	3.32	2983	20	CO	0.68	0.130	1.81	178
120611b	83095	83157	2.81	2544	20	CO	0.73	0.117	1.61	166
120611b	83179	83345	-0.50	2449	24	HP	0.67	0.126	1.58	164
120612a	80426	81038	1.10	3322	30	CO/LB	0.53	0.083	1.67	159
120612a	82010	82077	2.44	3628	24	LB	0.42	0.081	1.71	153
120612a	88609	89625	0.80	3386	18	CO	0.57	0.074	1.66	167
120612a	89961	90006	1.69	1867			0.07	0.423	1.60	147
120614a	59473	59747	3.33	3765	32	LB	0.44	0.057	1.69	157
120614a	67636	68444	6.41	3032	34	LB/CO	0.45	0.188	1.68	168
120617a	51565	52149	1.33	10126	22	HP	0.55	0.079	1.57	146
120617a	52686	53289	1.45	11146	20	HP	0.48	0.124	1.55	143
120617a	53504	53795	2.04	11141		HP	0.51	0.188	1.58	146
120618a	42084	42168	4.02	6373	16	CAN/NFLA	0.60	0.234	1.57	134
120618a	46294	48444	1.35	10924	65	HP	0.53	0.078	1.56	147
120618a	49370	49810	1.29	10889	50	HP	0.54	0.196	1.54	145
120618a	49958	50522	1.44	10873	50	HP	0.52	0.142	1.55	148
120618a	50708	51952	1.23	10521	30	HP	0.55	0.136	1.55	148

Thick BB plumes can be detected by the cloud top height algorithm, showing the altitude they rose to.
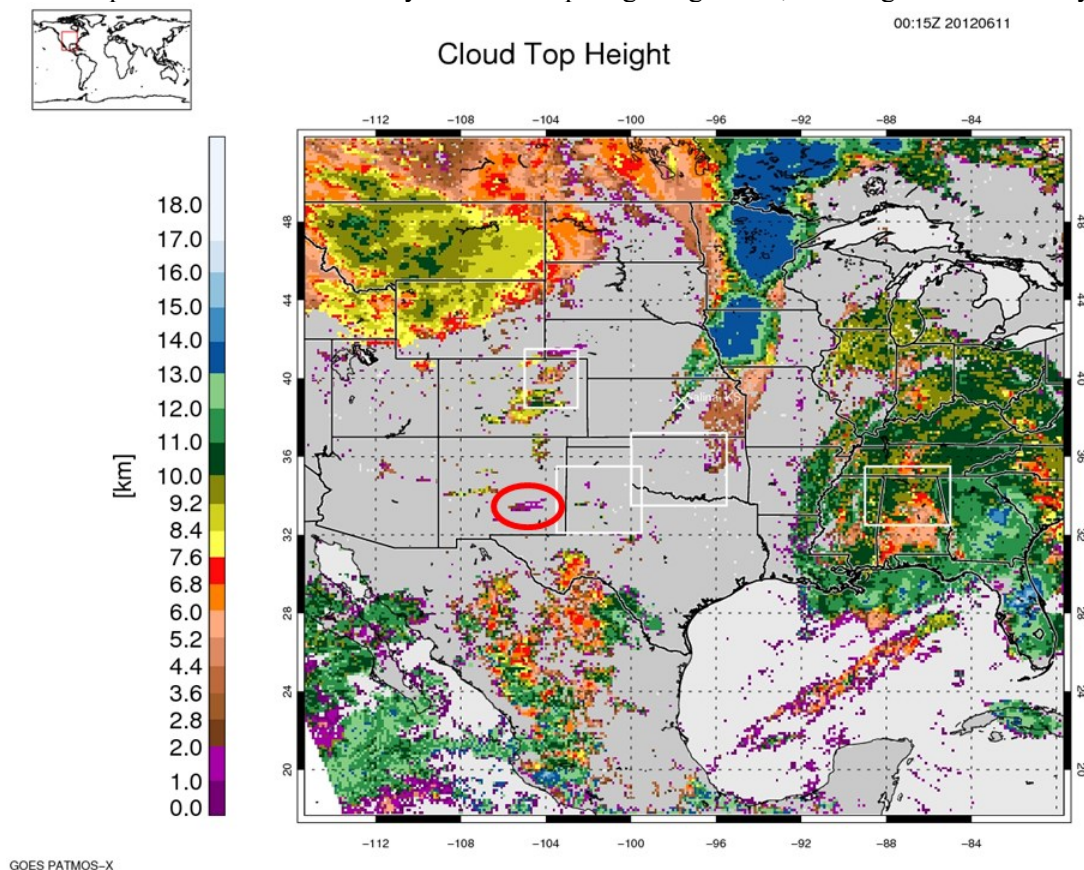
Figure A 14: Cloud top height from GOES-PATMOS-X at June 11, 00:15 UTC, the approximate time of emission of the Little Bear Fire plume measured on June 11 over Oklahoma, according to HYSPLIT trajectories. The Little Bear plume is encircled in red.

Four sequences of cloud-free anvil outflow were shown as reference for comparison with UT-BB layes and backgrounds. These are listed in Table A 4.

Table A 4: Table of thunderstorm outflow sequences out of clouds shown in Chapter 4.

Flight Number	Time /UTC	CO /ppb	O3 /ppb	rBC mass /ng/m³	CPC Concentration /cm⁻³
120605b	80862 – 81386	107	82	7.1	16445.7
120605b	82385 – 82563	110	82	5.9	4168.99
120606a	80114 – 80356	106	98	31	992.704
120608a	65921 – 67251	100	97	7.6	13575.8

To evaluate the influence of pyroconvection on the measured UT-BB layers, forward trajectories for the only case of pyroconvection over the High park fire are shown in Figure A 15.
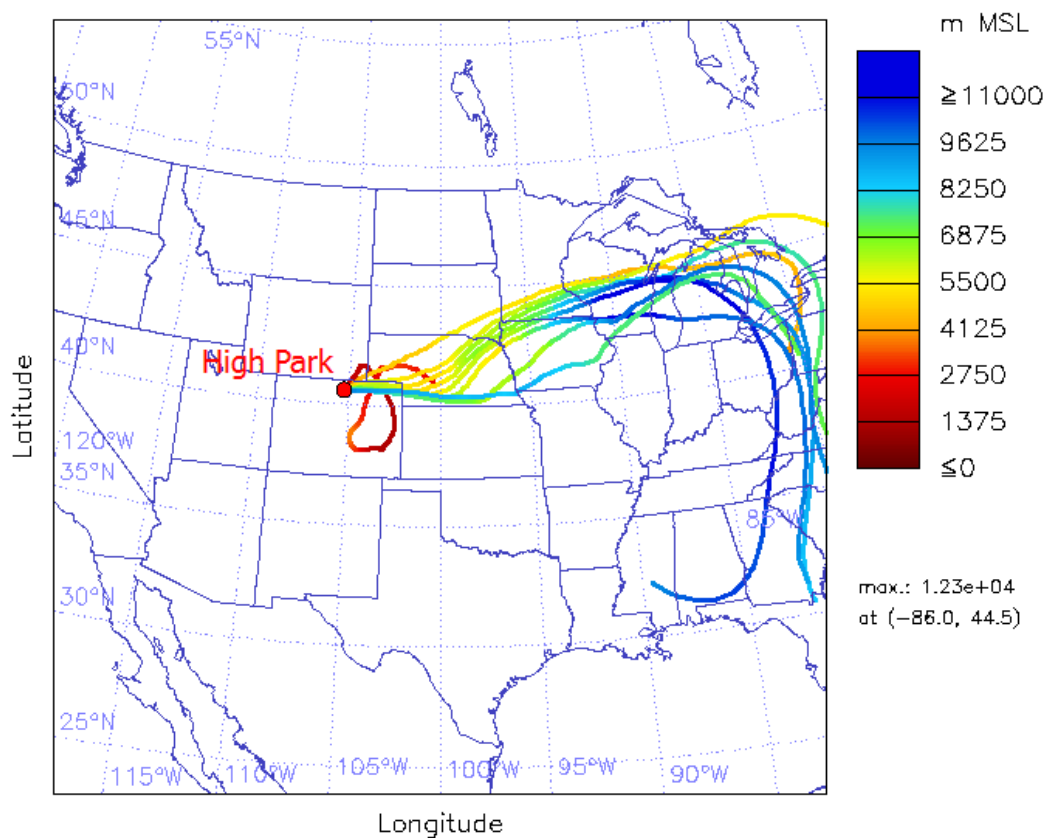
Figure A 15:Forward trajectories from the High Park fire on June 13, 2012, starting from altitudes between 100 m and 9 km to represent the transport from the pyroconvective cloud on that day.

List of Abbreviations

Abbreviation	Long Form
a.u.	Arbitrary Units
ACCESS	Arctic Climate Change Economy and Society
AMAP	Arctic Monitoring and Assessment Programme (www.amap.no)
APD	Avalanche Photodiode
AR	Arkansas
ARCPAC	Aerosol, Radiation, and Cloud Processes affecting Arctic Climate
ARCTAS	Arctic Research of the Composition of the Troposphere from Aircraft and Satellite
BBHG	Broadband high gain incandescence channel
BBLG	Broadband low gain incandescence channel
BORTAS	Quantifying the impact of BOReal forest fires on Tropospheric oxidants over the Atlantic using Aircraft and Satellite
CALIOP	Cloud-Aerosol Lidar with Orthogonal Polarization
CALIPSO	Cloud-Aerosol Lidar and Infrared Pathfinder Satellite Observation
CAN	Canada
CAPE	Convective Available Potential Energy
CCB	Cold Conveyor Belt
CO	Colorado
CPC	Condensation Particle Counter
CPSA	Condensation Particle Size Analyzer
DC3	Deep convective Clouds and Chemistry field experiment in 2012
DIAL	Differential Absorption Lidar
DLR	Deutsches Zentrum für Luft- und Raumfahrt e.V. (German Aerospace Center)
DMT	Droplet Measurement Technologies, Inc.
EOSDIS	Earth Observing System Data and Information System

EPA	United States Environmental Protection Agency
FSSP-100	Forward Scattering Spectrometer Probe 100
FSSP-300	Forward Scattering Spectrometer Probe 300
GOES	Geostationary Operational Environmental Satellite
GPS	Global Positioning System
HIPPO	High-performance Instrumented Airborne Platform for Environmental Research Pole-to-Pole Observations
HYSPLIT	Hybrid Single Particle Lagrangian Integrated Trajectory Model
ICARTT/ITOP	International Consortium for Atmospheric Research on Transport and Transformation / Intercontinental Transport of Ozone and Precursors
IPCC	Intergovernmental Panel on Climate Change
KS	Kansas
LEO-fit	Leading-edge-only-fit, used to determine a particle's size from the first part of the scattering signal only
LFC	Level of Free Convection
Lidar	Light detection and Ranging
LZB	Level of Zero Buoyancy
MCS	Mesoscale Convective system
MED	Mass Equivalent Diameter
MODIS	Moderate Resolution Imaging Spectroradiometer
MO	Missouri
Nd:YAG	Neodymium-doped Yttrium-Aluminium-Garnet laser crystal
NASA	National Aeronautics and Space Administration
NBHG	Narrowband high gain incandescence channel
NBLG	Narrowband low gain incandescence channel
NIST	National Institute of Standards and Technology
NOAA	National Oceanic and Atmospheric Administration

NSF	National Science Foundation
OK	Oklahoma
OPC	Optical Particle Counter
PBL	Planetary boundary layer
PCASP	Passive Cavity Aerosol Spectrometer Probe
PMT	Photomultiplier tube
PSAP	Particle Soot Absorption Photometer
PSL	Polystyrene Latex spheres
rBC	refractory Black Carbon (as measured by the SP2)
SCHG	Scattering high gain channel
SCLG	Scattering low gain channel
SP2	Single Particle Soot Photometer
SPAT	Split Detector Alignment software, provided by DMT
SPHG	Split detector high gain channel
SPLG	Split detector low gain channel
stp	Standard temperature (273.15 K) and pressure (1013.25 hPa)
TX	Texas
UHSAS	Ultra-High Sensitivity Aerosol Spectrometer, Droplet Measurement Technologies, Boulder/Colorado, USA
UT	Upper Troposphere
UTLS	Region of the upper troposphere and lower stratosphere
WCB	Warm Conveyor Belt
WY	Wyoming

List of Symbols

Symbol	Description	Units
a	Particle radius	µm or nm
B	Blackbody radiation according to Planck's law	W/(m²·nm·sr)
c	Speed of light (2.9979·10⁸ m/s)	m/s
C_{abs}	Absorption cross section of a particle	m²
C_{ext}	Extinction cross section of a particle	m²
$C_{geometric}$	Geometrical cross section of a particle	m²
c_p	specific heat of dry air at constant pressure	J/(gK)
Cs	Specific heat of a particle	J/(gK)
C_{sca}	Scattering cross section of a particle	m²
CMD	Count median diameter of a lognormal distribution	µm or nm
D_{MED}	Mass equivalent diameter of a particle	nm
D_{opt}	Optical diameter of a particle	µm or nm
d	Particle diameter	µm or nm
g	Acceleration of gravity (9.807m/s² as a standard value)	m/s²
GSD	Geometric standard deviation of a lognormal distribution	dimensionless
h	Planck's constant (6,626·10⁻³⁴ Js)	Js
h_N	Nusselt number	W/cm²K
H_v	Latent heat of vaporization	J/mol

I_i	Incident irradiance of electromagnetic radiation	W/m²
k_B	Boltzmann's constant ($1.381 \cdot 10^{-23}$ J/K)	J/K
M	Mass concentration of particles	µg/m³ or ng/m³
m	Refractive index	dimensionless
m_P	Mass of a particle	g
MMD	Mass median diameter of a lognormal particle distribution	µn or nm
N	Number concentration of particles	cm⁻³
N_{coarse}	Number concentration of coarse mode aerosol larger than 2 µm	cm⁻³
p	Pressure	Pa
p_0	Reference pressure	Pa
Q_{abs}	Absorption efficiency of a particle	dimensionless
Q_{ext}	Extinction efficiency of a particle	dimensionless
Q_{sca}	Scattering efficiency of a particle	dimensionless
R	Gas constant (8.314 J/(mol·K))	J/(mol·K)
$R(\lambda)$	wavelength-dependent filter transmission	dimensionless
t	Time	s
T	Temperature	K
T_0	Reference temperature	K
W_{abs}	Energy rate absorbed in a volume	W
W_{ext}	Energy rate extinguished in a volume	W

W_{sca}	Energy rate scattered out of a volume	W
W_v	Molecular weight of the incandescing particle's vapor	g/mol
x	Size parameter	dimensionless
z	Altitude	m
ΔC_{sca}	Differential scattering cross section	m²
$\Delta\Omega$	Solid angle of view of a detector in the SP2	sr
ε	Emissivity	dimensionless
θ	Potential temperature	K
λ	Wavelength of light	μm or nm
ρ	Density of the particle	kg/m³
σ_{sb}	Stefan-Boltzmann constant ($5.67\cdot10^{-8}$ W/(m²K))	W/m²K

Values for fundamental physical constants were taken from Seinfeld and Pandis (2016)

Acknowledgements

_____